

# UC Riverside

## UC Riverside Electronic Theses and Dissertations

### Title

New Directions in Dark Sector Model Building: From Flat to Warped Spacetime

### Permalink

<https://escholarship.org/uc/item/9s33r6kw>

### Author

Chaffey, Ian

### Publication Date

2022

### Copyright Information

This work is made available under the terms of a Creative Commons Attribution License, available at <https://creativecommons.org/licenses/by/4.0/>

Peer reviewed|Thesis/dissertation

UNIVERSITY OF CALIFORNIA  
RIVERSIDE

New Directions in Dark Sector Model Building: From Flat to Warped Spacetime

A Dissertation submitted in partial satisfaction  
of the requirements for the degree of

Doctor of Philosophy

in

Physics

by

Ian William Peter Chaffey

September 2022

Dissertation Committee:

Dr. Philip Tanedo, Chairperson

Dr. Hai-Bo Yu

Dr. Yanou Cui

Copyright by  
Ian William Peter Chaffey  
2022

The Dissertation of Ian William Peter Chaffey is approved:

---

---

---

Committee Chairperson

University of California, Riverside

## Acknowledgments

I would like to thank my advisor Philip Tanedo for all of the advice and support as well as significantly contributing the work that forms the basis of this dissertation. I would like thank Sylvain Fichet for helpful discussions and contributing to a significant portion of this dissertation. I would like to thank Hai-Bo Yu for several helpful discussions and insight.

The text of this dissertation, in part, is a reprint of the material as it appears in “Vector Self-Interacting Dark Matter”, Phys. Rev. D 101, 075005, 3 April 2020 and “Continuum Mediated Self-Interacting Dark Matter”, Journal of High Energy Physics, 1 June 2021. The coauthor Philip Tanedo listed in those publications directed and supervised research which forms the basis for this dissertation. The coauthor Sylvain Fichet provided technical expertise, assisted with calculations, and contributed to the writing of the manuscript “Continuum Mediated Self-Interacting Dark Matter” which forms the basis for this dissertation.

To my wife Meghan Neureither and our dog Lemon Neureither-Chaffey for all the  
love and support.

# ABSTRACT OF THE DISSERTATION

New Directions in Dark Sector Model Building: From Flat to Warped Spacetime

by

Ian William Peter Chaffey

Doctor of Philosophy, Graduate Program in Physics

University of California, Riverside, September 2022

Dr. Philip Tanedo, Chairperson

We present four dark sector models with novel phenomena beyond the weakly-interacting massive particle paradigm. We present a model of spin-1 dark matter charged under a  $U(1)$  gauge symmetry, resulting from the spontaneous symmetry breaking of an  $SU(2)$  dark sector. The dark matter is subject thermal freeze out and direct detection constraints while simultaneously meeting self-interaction targets for small scale structure anomalies. We present a model of pseudo-Goldstone boson dark matter based of the same symmetry structure. The pseudo-Goldstone boson dark matter satisfies thermal freeze out and direct detection constraints while satisfying self-interaction targets as well. We expand the self-interacting dark matter framework to the case of a continuum of mediators and present a model of continuum-mediated self-interacting dark matter. The model is described holographically by brane localized dark matter interacting with a bulk scalar in a slice of 5D anti-de Sitter space. The long-range scattering potential follows a non-integer power law, resulting in a self-scattering cross section that depends on a non-integer power of the dark matter relative velocity as well as Sommerfeld enhancement which exhibits a pattern

of resonances determined by the non-integer power. The novel power laws introduced by the continuum mediator present new possibilities self-interacting dark matter phenomenology. We expand the dark photon framework to the case where the dark photon is a continuum of states, modeled as a bulk spin-1 field interacting with brane-localized matter in a 5D slice of anti-de Sitter space. We derive a simple formula for recasting existing dark photon bounds for our model. We consider a model of brane-localized dark matter which freezes out by annihilating into holographic dark photons, and present targets for the dark matter mass and coupling to the holographic dark photon. We conclude that even though a definitive signal for dark matter remains unseen, there are several possibilities for model building and future study which may provide further insight into the microscopic nature of dark matter.



# Contents

<b>List of Figures</b>	<b>xii</b>
<b>List of Tables</b>	<b>xvii</b>
<b>1 Introduction</b>	<b>1</b>
<b>2 Vector Self-Interacting Dark Matter</b>	<b>4</b>
2.1 Introduction and Context . . . . .	4
2.2 Particles and Symmetries . . . . .	7
2.2.1 General, Renormalizable Lagrangian . . . . .	8
2.2.2 Spectrum, Symmetry, Stability . . . . .	9
2.3 Symmetry Breaking . . . . .	11
2.3.1 Would-be Goldstones . . . . .	12
2.3.2 Gauge Boson Masses . . . . .	12
2.3.3 Higgs Mechanism and Leftover Goldstones . . . . .	13
2.3.4 Symmetry Breaking with $\lambda, \lambda'$ . . . . .	13
2.3.5 Symmetry Breaking with $\lambda, \lambda', \mu$ . . . . .	14
2.3.6 Symmetry Breaking with $\lambda, \lambda', \lambda'', \mu$ . . . . .	17
2.3.7 Qualitative Behavior . . . . .	17
2.3.8 Vacuum Stability . . . . .	18
2.4 Feynman Rules for Light States . . . . .	18
2.5 Relic Abundance and Annihilation . . . . .	20
2.5.1 Sommerfeld Enhancement . . . . .	24
2.5.2 Bound State Formation . . . . .	24
2.6 Relating Dark Matter and Dark Pion Masses . . . . .	25
2.7 Self-Interacting Dark Matter . . . . .	28
2.8 Portal Interactions . . . . .	31
2.9 Conclusions . . . . .	35
<b>3 Vector Portal Pseudo-Goldstone Dark Matter</b>	<b>39</b>
3.1 Introduction . . . . .	39
3.2 Symmetry Structure . . . . .	42

3.2.1	Lagrangian and Symmetry Breaking Potential . . . . .	43
3.2.2	Spontaneous Symmetry Breaking . . . . .	43
3.2.3	Explicit Symmetry Breaking . . . . .	44
3.2.4	Particle Spectrum . . . . .	45
3.3	Particles and Mass Spectrum . . . . .	47
3.3.1	Gauge Boson Masses . . . . .	48
3.3.2	vevs and Scalar Boson Masses . . . . .	49
3.4	Feynman Rules for Dark Sector States . . . . .	51
3.5	Relic Abundance . . . . .	53
3.6	Self-Interactions . . . . .	56
3.7	Portal Interactions . . . . .	59
3.8	Conclusion . . . . .	62
<b>4</b>	<b>Continuum Mediated Self-Interacting Dark Matter</b>	<b>64</b>
4.1	Introduction . . . . .	64
4.2	Preliminary Observations . . . . .	67
4.3	Continuum-Mediated Self-Interactions from AdS . . . . .	70
4.3.1	Geometry and Action . . . . .	70
4.3.2	Effective Field Theory Consistency . . . . .	72
4.3.3	Model Parameters . . . . .	73
4.3.4	Mediator Propagator and Spectrum . . . . .	75
4.3.5	Qualitative Description of 4D Near-Conformal Theory . . . . .	77
4.4	Phenomenological Constraints . . . . .	78
4.4.1	Cosmological Dark Radiation . . . . .	78
4.4.2	Fifth Force . . . . .	79
4.4.3	Deviations from the Standard Model . . . . .	79
4.5	The Continuum-Mediated Potential . . . . .	80
4.5.1	Spectral Representation . . . . .	81
4.5.2	Propagator Asymptotics . . . . .	82
4.5.3	Potential, $\alpha < 1$ . . . . .	85
4.5.4	Potential, $\alpha = 1$ . . . . .	86
4.5.5	Validation of Potential . . . . .	90
4.6	Astrophysical Phenomenology . . . . .	91
4.6.1	Review of Self-Interacting Dark Matter Cross Sections . . . . .	91
4.6.2	Analytical Behavior of a Continuum Mediator . . . . .	95
4.6.3	Numerical Methodology and Results . . . . .	99
4.6.4	Comparison to Astrophysical Data . . . . .	102
4.6.5	Comment on Annihilation and Relic Abundance . . . . .	105
4.7	Continuum-Mediated Sommerfeld Enhancement . . . . .	106
4.8	Conclusion . . . . .	109
<b>5</b>	<b>Holographic Dark Photon</b>	<b>112</b>
5.1	Introduction . . . . .	113
5.1.1	Outline . . . . .	117
5.1.2	Summary of Results . . . . .	118

5.2	A Broken $U(1)$ in $\text{AdS}_{d+1}$ . . . . .	121
5.2.1	Geometry . . . . .	122
5.2.2	Action and Gauge Fixing . . . . .	122
5.2.3	Spontaneous Symmetry Breaking . . . . .	125
5.2.4	On Backreaction and IR brane . . . . .	128
5.3	Propagators and Boundary Effective Action . . . . .	129
5.3.1	Vector Sector . . . . .	129
5.3.2	Scalar Sector . . . . .	131
5.3.3	Boundary Effective Action . . . . .	133
5.4	The Landscape of Broken $U(1)$ in AdS . . . . .	137
5.4.1	WKB Approximation . . . . .	138
5.4.2	$\alpha \geq \frac{d}{2}$ . . . . .	139
5.4.3	$\alpha < \frac{d}{2}$ . . . . .	141
5.5	A Holographic Continuum Dark Photon . . . . .	146
5.5.1	Definition . . . . .	147
5.5.2	Dressing the Photon . . . . .	148
5.5.3	Benchmark Continuum Models . . . . .	149
5.5.4	Spectral Density and Phase Space . . . . .	151
5.5.5	Simplified Continuum Models . . . . .	155
5.5.6	Continuum Phase Space . . . . .	156
5.5.7	A Recasting Formula for Continuum Models . . . . .	157
5.5.8	Cutoff scales . . . . .	159
5.6	Finite Temperature and a Cosmological Scenario . . . . .	159
5.6.1	Feeding the Bulk Black Hole . . . . .	162
5.6.2	The Transition Time/Temperature . . . . .	164
5.6.3	Ultracold Hidden Sector Freeze-out Scenario . . . . .	166
5.6.4	Dark Photon Radiation . . . . .	168
5.6.5	UV Brane-Localized Dark Matter . . . . .	170
5.7	Phenomenological Comments and Cross Sections . . . . .	175
5.7.1	Decay Width and Bulk Oscillations . . . . .	175
5.7.2	Holographic Dark Photon Processes . . . . .	176
5.7.3	Phenomenological Signatures and Plots . . . . .	179
5.8	On the Goldstone Equivalence Theorem in AdS . . . . .	182
5.8.1	A Bulk Equivalence Theorem . . . . .	184
5.8.2	A Boundary Equivalence Theorem . . . . .	185
5.9	$U(1)$ Breaking in the Holographic CFT . . . . .	186
5.9.1	$U(1)$ breaking . . . . .	187
5.9.2	Properties of the $U(1)$ Current . . . . .	188
5.9.3	Comparison to AdS . . . . .	190
5.9.4	Summary . . . . .	192
5.10	Conclusions . . . . .	192

**6 Conclusions** **196**

**Bibliography** **198**

<b>A</b>	<b>Vector Self-Interacting Dark Matter</b>	<b>217</b>
A.1	Goldstones and Pions: an Abelian Example . . . . .	217
A.1.1	Gauging a Subgroup Combination . . . . .	218
A.1.2	Gauging a Vectorlike Combination . . . . .	219
A.1.3	Which Goldstone is Which? . . . . .	219
A.1.4	Gauging an Axial Combination . . . . .	220
A.1.5	Gauging both Vector and Axial Symmetry . . . . .	221
A.1.6	Global Vector and Axial Goldstones . . . . .	222
A.2	SIDM Methodology . . . . .	222
<b>B</b>	<b>Continuum Mediated Self-Interacting Dark Matter</b>	<b>226</b>
B.1	AdS/CFT with UV brane . . . . .	226
B.1.1	The Two Branches . . . . .	226
B.1.2	The Two Branches with a UV brane . . . . .	228
B.2	Derivation of Gapless $\alpha = 1$ Potential . . . . .	229
B.3	Validity of the Born Approximation . . . . .	230
B.4	Classical Transfer Cross Section . . . . .	232
B.4.1	Velocity Scaling in the Small Mass Gap/High Velocity Limit . . . . .	233
B.4.2	Low Velocity Classical Regime . . . . .	234
B.5	Sommerfeld Enhancement from a $1/r^2$ Potential . . . . .	235
B.6	Self-Interacting Dark Matter Numerical Method . . . . .	237
<b>C</b>	<b>Holographic Dark Photon</b>	<b>241</b>
C.1	Gauge Parameter Boundary Conditions . . . . .	241
C.2	A WKB Method for Near-AdS Background . . . . .	242
C.2.1	Matching to the Solution Near the Turning Point . . . . .	245
C.2.2	UV Brane-to-Brane Propagator . . . . .	246
C.3	Holographic Dark Photon Model Detailed Calculation . . . . .	247
C.3.1	Exact Result from Dressing . . . . .	248
C.3.2	Equivalence with Holographic Field Redefinition . . . . .	250

# List of Figures

2.1	Model spectrum. Mass eigenstates are black lines, charged (neutral) Goldstones are blue (green) lines, radial Higgs modes are red lines. Mixing into mass eigenstates indicated by thin lines. . . . .	11
2.2	The $W$ relic abundance from thermal freeze out as a function of the $W$ mass and fine structure constant. We plot lines where the $W$ saturates the entire dark matter density (solid/blue) or only a 10% (dash-dotted/green) or 1% fraction (dotted/red). We take $\lambda = \lambda' = 4\pi$ , $\lambda'' = 0$ and $\mu = f$ . The shaded region is excluded in order to prevent dark matter decay. . . . .	20
2.3	Diagrams contributing to $W^+W^- \rightarrow AA$ annihilation. Not shown: crossed ( $u$ -channel) diagrams and annihilation to scalars. . . . .	22
2.4	Shaded regions correspond to values of the dark fine structure constant $\alpha_X = g^2/4\pi$ and the pion mass $m_\pi \approx \mu f$ that (i) do not overclose the universe [solid lines], (ii) have a stable $W$ [dashed lines], and (iii) have a stable vacuum [dotted lines]. Colors correspond to choices of $f = 700$ GeV (green, lower-left), $f = 1400$ GeV (teal, middle), $f = 2800$ GeV (magenta, upper-right). We take $\lambda'' = 0$ for simplicity. LEFT: $\lambda = \lambda' = 1$ . RIGHT: $\lambda = \lambda' = 4\pi$ . . .	26
2.5	Self-interaction cross section as a function of average velocity in our model compared to inferred cross sections for a set of dwarf galaxies, low surface brightness (LSB) spiral galaxies, and galaxy clusters from Ref. [200]. <b>Benchmark models:</b> the solid/red curve are a fit to the inferred cross sections from astrophysical data. The $W^\pm$ are required to have a sub-GeV mass in order to agree with the cluster scale observations [187]. The dash-dotted/green curve corresponds to a fit to the low-velocity data points while maintaining a GeV scale mass. Both benchmark models are subject to the requirement that $\alpha_X$ is large enough for the $W^\pm$ to saturate the dark matter relic abundance; see Fig. 2.2. <b>Illustrative unphysical examples:</b> the dotted/blue line assumes a <i>purely repulsive potential</i> and reproduces the best fit curve from Ref. [200] using the same model parameters. The dashed/yellow line corresponds to the same model parameters but including both attractive and repulsive potentials. . .	37
2.6	Constraints on the effective dark matter–proton coupling, $c_p^2$ , from direct detection experiments XENON 1T [13] and DarkSide 50 [5]. . . . .	38

3.1	Model spectrum. Mass eigenstates are black lines, charged (neutral) Goldstones are blue (green) lines, radial Higgs modes are red lines. Mixing into mass eigenstates indicated by thin lines. . . . .	47
3.2	Diagrams contributing to $\pi^+\pi^- \rightarrow AA$ annihilation. Not shown: crossed ( $u$ -channel) diagrams and annihilation to scalars. . . . .	53
3.3	The $\pi$ relic abundance as a function of the $\pi$ mass and dark fine structure constant/dark Higgs doublet coupling (Left/Right). The solid (purple/blue), dash-dotted (teal/orange), and dotted (red/green) curves represent when the $\pi$ saturate the dark matter relic abundance for $\lambda' = 10^{-3}/\alpha_X = 10^{-4}$ , $10^{-2}/10^{-3}$ , and $10^{-1}/10^{-2}$ respectively. The corresponding solid (purple/blue), dash-dotted (teal/orange), and dotted (red/green) vertical lines bound the regions in which the vacuum/ $\pi$ are unstable. The shaded triangular regions denote where the $\pi$ /vacuum is unstable. . . . .	54
3.4	Numerical results for the dark matter self-interaction cross section in our model compared to cross sections for a set of dwarf galaxies, low surface brightness (LSB) spiral galaxies, and galaxy clusters from Ref. [200]. The solid/dashed (blue/orange) curves corresponding to benchmarks with symmetric relic abundances, are compared to the dotted (green) curve corresponding to the benchmark model from Ref. [200] with an asymmetric relic abundance. The benchmarks we present are identical to those found for spin-1 dark matter in Ref. [69] with the replacements $m_W \rightarrow m_\pi$ and $\alpha_X \rightarrow \alpha_\pi$ . . . . .	58
3.5	Constraints on the effective dark matter–proton coupling, $c_p^2$ , from direct detection experiments XENON 1T [13, 14] and DarkSide 50 [5]. . . . .	62
4.1	Schematic description of the continuum-mediated self-interacting dark matter scenario. . . . .	70
4.2	Absolute potential $ V(r) $ plotted to validate the continuum-mediated potential with a mass gap (black) against a sum over $n_{\max}$ Kaluza–Klein modes (colored). The potential with $n_{\max}$ KK modes is valid for separations larger than $r \gtrsim m_{n_{\max}}^{-1}$ . The disagreement at long separations between the blue and black lines represents our numerical error and does not change the quantitative behavior of integrals over the potential. Also shown: the non-integer power law limit (dashed gray) that is realized in the gap-less limit $m_1 \rightarrow 0$ . . . . .	89
4.3	Regimes of self-interacting dark matter. The horizontal axis measures whether the ladder of mediator exchanges can be approximated by a single mediator exchange. The vertical axis is a measure of the velocity. The figures of merit are scaled by the ratio of the dark matter mass to the mediator mass (or mass gap) so that the regimes are limits relative to unity. The perturbative regime is described by the Born approximation over the range of all velocities, whereas the non-perturbative regime is separated into a classical regime at high velocities and a resonant regime at low velocities. Blue: asymptotic velocity scaling of the transfer cross section $\sigma_T$ in the continuum-mediated scenario. No simple scaling exists in the resonant regime. The standard case of a single 4D mediator corresponds to $\alpha = 1$ . . . . .	92

4.4	Velocity dependence of the transfer cross section in the Born regime. Comparison between the Born approximation and (blue/solid) and the numerical result from a sum of partial waves (orange/dashed). The results asymptotically scale like $v^{-4\alpha}$ at large velocity (green). . . . .	96
4.5	Comparison of the numerically calculated transfer cross section to the analytic approximations introduced in Figure 4.3. The general behavior displays distinct regimes, similar to that of a single mediator, see e.g. Ref. [293, Fig. 2]. The blue line is the numerical solution. Orange (dashed)/green (dotted) lines correspond to analytic Born/classical approximations valid in their respective regimes; (4.62) and (4.67) . . . . .	100
4.6	Transfer cross section as a function of relative dark matter velocity $v$ (left) and bulk mass parameter $\alpha$ (right). The plots demonstrate the presence of resonances and anti-resonances. Vertical markers identify parameters used in the opposite plot. . . . .	102
4.7	Velocity dependence of the thermally averaged transfer cross section. The parameters are chosen to be reasonably fit astronomical data. A benchmark 4D self-interacting dark matter model with a scalar mediator is shown for comparison. The data points for velocities $v \sim 30 - 200$ km/s are determined from the observed rotation curves of dwarf (red) and low-surface brightness galaxies (blue) respectively; points for velocities $v \gtrsim 10^3$ km/s correspond to galaxy clusters (green) and are determined from stellar line-of-sight velocity dispersion data [200]. . . . .	103
4.8	Velocity dependence of the thermally averaged transfer cross section, analogous to Figure 4.7, for a range of $\mu$ and $m_\chi$ choices to demonstrate the behavior with respect to these parameters. . . . .	105
4.9	Sommerfeld enhancement of the $\ell = 0$ partial wave for a range of $\alpha$ and the ratio $\mu/m_\chi$ . Our approximation of the potential breaks down near $\alpha = 1$ and hence this region is removed. . . . .	106
4.10	Sommerfeld enhancement of the $\ell = 0$ partial wave as a function of $\alpha$ . . . . .	107
5.1	The set up for $\alpha > d/2$ (Left) and $\alpha < d/2$ (Right). The scalar vev profile as well as the location of the UV brane are shown for both cases. For $\alpha < d/2$ , an backreaction occurs in the IR due to the non-negligible scalar vev profile. . . . .	121
5.2	The holographic continuum dark photon mediates interactions on the UV brane. . . . .	147
5.3	Examples of the spectral density for $\alpha = 1$ . The location of the pole is shifted away from the gap depending on the values of $c_{UV}$ and $r_{UV}/R$ . . . . .	153
5.4	Examples of the spectral density for $\alpha = 2$ . The width of the resonance is determined by the value of $m_A$ relative to $R^{-1}$ . . . . .	154
5.5	Respective geometries for thermal phase with the AdS black hole (Left) and the gapped phase when the background is truncated by an IR brane (Right). . . . .	160
5.6	Target values of $\alpha_\chi$ and $m_\chi$ for non-relativistic freeze out in the case $\alpha = 1$ . We consider a mass gap $m_A = 100$ MeV and AdS curvature $R^{-1} = 10^3$ TeV. . . . .	171
5.7	Target values of $\alpha_\chi$ and $m_\chi$ for non-relativistic freeze out in the case $\alpha = 2$ . We consider a bulk mass $m_A = 1$ GeV and AdS curvature $R^{-1} = 10^3$ TeV. . . . .	172

- 5.8 We recast constraints on invisibly decaying dark photons according to our formula for  $\alpha = 1$  and  $R = 10^{-18} \text{ GeV}^{-1}$ . There are bounds from BaBar and Belle II projections at large masses [163]. The solid green curve corresponds to a projected luminosity of 0.04%, the dashed green curve corresponds to 1% luminosity, the dotted green curve to 10%, and the dash-dotted green curve to 100%. Note that projections greater than 0.04% are purely speculative and require a detailed analysis. There are bounds due to stellar cooling from the Sun, HB stars, and RG stars [263]. At low masses there are bounds from fifth force experiments searching for deviations to the Coulomb potential [25], as well as from CMB spectral distortions[246]. We take  $r_{UV}/R = 1$  and  $c_{UV} = 10^3$  so that the pole mass remains above the gap scale and does not contribute. . . . . 180
- 5.9 We recast constraints on invisibly decaying dark photons according to our formula for  $\alpha = 1$  and  $R = 1 \text{ TeV}^{-1}$ . There are bounds from BaBar and Belle II projections at large masses [163]. The solid green curve corresponds to a projected luminosity of 0.04%, the dashed green curve corresponds to 1% luminosity, the dotted green curve to 10%, and the dash-dotted green curve to 100%. Note that projections greater than 0.04% are purely speculative and require a detailed analysis. There are bounds due to stellar cooling from the Sun, HB stars, and RG stars [263]. At low masses there are bounds from fifth force experiments searching for deviations to the Coulomb potential [25], as well as from CMB spectral distortions[246]. We take  $r_{UV}/R = 1$  and  $c_{UV} = 10^3$  so that the pole mass remains above the gap scale and does not contribute. . . . . 181
- 5.10 We recast constraints on invisibly decaying dark photons according to our formula for  $\alpha = 2$  and  $R = 1 \text{ TeV}^{-1}$ . There are bounds from BaBar, LEP, and Belle II projections at large masses [163]. The solid green curve corresponds to a projected luminosity of 0.04%, the dashed green curve corresponds to 1% luminosity, the dotted green curve to 10%, and the dash-dotted green curve to 100%. Note that projections greater than 0.04% are purely speculative and require a detailed analysis. There are bounds due to stellar cooling from the Sun, HB stars, and RG stars [263]. At low masses there are bounds from fifth force experiments searching for deviations to the Coulomb potential [25], as well as from the resonant conversion of CMB photons into dark photons[246]. We take  $r_{UV}/R = 1$  and  $c_{UV} = 0$ . . . . . 182



5.11	We recast constraints on invisibly decaying dark photons according to our formula for $\alpha = 2$ and $R = 1 \text{ TeV}^{-1}$ . There are bounds from BaBar and Belle II projections at large masses [163]. The solid green curve corresponds to a projected luminosity of 0.04%, the dashed green curve corresponds to 1% luminosity, the dotted green curve to 10%, and the dash-dotted green curve to 100%. Note that projections greater than 0.04% are purely speculative and require a detailed analysis. There are bounds due to stellar cooling from the Sun, HB stars, and RG stars [263]. At low masses there are bounds from fifth force experiments searching for deviations to the Coulomb potential [25], as well as from the resonant conversion of CMB photons into dark photons[246]. We take $r_{UV}/R = 1$ and $c_{UV} = 0$ . . . . .	183
A.1	Fields $a$ and $b$ acquire unequal vacuum expectation values $f_a > f_b$ . The Goldstone excitations with respect to a transformation by parameter $\theta$ have correspondingly different magnitudes, $\delta\varphi_a > \delta\varphi_b$ . The Goldstone, $\delta\varphi_V$ , for a vectorial transformation where $\theta_a = \theta_b$ is thus <i>not</i> orthogonal to the corresponding Goldstone, $\delta\varphi_A$ for an axial transformation where $\theta_a = -\theta_b$ . . . . .	220

# List of Tables

2.1	Benchmark models: a model realizing self-interacting dark matter targets (SIDM, solid/ <b>red</b> in Fig. 2.5) and a model that realizes thermal freeze out with a weak-scale dark matter mass (WIMP-like, dash-dotted/ <b>green</b> in Fig. 2.5). The SIDM benchmark corresponds to $g = 4.2 \times 10^{-3}$ , $v = 46$ MeV, $f = 15$ GeV. The WIMP-like benchmark corresponds to $g = 0.11$ , $v = 107$ MeV, and $f = 535$ GeV. The maximum pion mass for $\lambda = \lambda' = 1$ and $\lambda = \lambda' = 4\pi$ are related to $\mu$ by (2.31) and the upper bound in (2.39). . . . .	30
2.2	Conventions for dark sector and visible sector mass eigenstates. . . . .	32
4.1	Range of parameters in our model. The AdS curvature is set to $k = 10$ TeV; larger values generically suppress self-interaction effects. The dimensionless brane-localized masses and kinetic terms defined in (4.12) and (4.17) are assumed to be $\mathcal{O}(1)$ , with the exception of $b_{UV}$ which is tuned to zero to reproduce the long-range behavior, (4.4). The early universe bound on $\mu$ is described in Section 4.4. . . . .	75
5.1	Summary of the spectra for a spontaneously broken $U(1)$ model in $\text{AdS}_{d+1}$ resulting from different choices of $\alpha$ . . . . .	137

# Chapter 1

## Introduction

Non-luminous dark matter has been observed to be the dominant contribution to the the universe's matter content. First inferred from observations of galactic rotation curves, the existence of non-luminous dark matter has been strongly supported by observations [2, 3], despite the lack of a definitive experimental signature. As the sensitivity of experiments has improved, combined with the lack of an experimental signal, established paradigms such as the weakly-interacting massive particle (WIMP) have come under tension [286, 8, 9, 6, 185, 1, 35, 79]. As a result new classes of dark matter models, alternatives to the WIMP paradigm, have been proposed.

One avenue considered in this manuscript is to postulate a dark sector comprised two or more states, with one or several of which accounting for the observed abundance of dark matter in the present universe [255, 256, 257, 121, 10, 31]. Dark matter does not couple directly to visible matter in these models. Instead, dark matter couples to one or more states which mediate interactions with the visible sector, alleviating some experimental

constraints. This framework is easily realized by the dark photon portal in which a spin-1 vector boson couples to the Standard Model through kinetic mixing with the hypercharge gauge bosons [183, 151], mediating interactions with the dark sector.

Dark sectors also allow for a richer spectrum of interactions, paving the way for novel phenomena absent from previous studies. One such example is the case of self-interacting dark matter (SIDM). Small-scale structure anomalies such as the core-cusp, too big to fail, and missing satellites problems may be resolved if dark matter self-interacts through a light mediator [293, 292].

I consider the further case where dark matter self-interactions are mediated by a continuum of states instead of one or a few. Such models have been realized in the context of conformal hidden sectors [158, 300] as well as unparticle models [285, 73, 145, 146]. The possibility of novel self-interactions was first identified in the context of a holographic description of a warped dark sector [45]. The resulting dark matter self-interactions inherit a nontrivial dependence on the dark matter relative velocity.

Beyond self-interactions, a continuum of mediators will affect several observables. Frameworks such as the dark photon portal may be reconsidered in the context where the dark photon is represented by a continuum of states, resulting in novel effects on established phenomena.

In this manuscript I explore four possible dark sector models. While experimental probes continue to increase in precision, much about dark matter is still unknown. Our goal is to present novel constructions which contribute to the collective space of dark sector models. I show that through clever model building, constructions which present novel

and previously unexpected phenomena are possible. The models I present are excellent foundations for future studies in new exciting directions.

## Chapter 2

# Vector Self-Interacting Dark Matter

### 2.1 Introduction and Context

Despite strong evidence for the existence of dark matter [2, 4], the lack of a definitive signal in recent experiments puts pressure on the well-studied weakly-interacting massive particle (WIMP) paradigm [286, 8, 9, 6, 185, 1, 35, 79]. One approach beyond this framework is to assume that dark matter belongs to a decoupled sector of particles frequently referred to as dark or hidden sectors with low-mass particles that mediate interactions [255, 256, 257, 121, 10, 31].

A simple realization of this is the dark photon portal in which a low-mass spin-1 vector boson couples to the Standard Model through kinetic mixing with the hypercharge gauge bosons [183, 151]. Instead of annihilating directly into Standard Model par-

ticles, dark matter annihilates into dark photons that subsequently decay into Standard Model particles. Dark photons could be detected by a number of current and future experiments [121, 10, 31]. An automatic feature of dark sector models is the existence of long-range, velocity-dependent self-interactions between dark matter particles coming from exchange of the low-mass mediator. These self-interactions between dark matter particles can address several potential small scale structure tensions between simulations of cold dark matter and astronomical observations [292].

This manuscript introduces a model of spin-1 dark matter that self-interacts through low-mass, spin-1 mediators (dark photons). The dark sector is composed of a  $SU(2)$  gauge group with a scalar sector that enacts two stages of symmetry breaking:

1.  $SU(2) \rightarrow U(1)$  at a scale  $f$ , which sets the scale of the dark matter particles, and
2.  $SU(2) \rightarrow \emptyset$  at a scale  $v \ll f$ , which sets the scale of the dark radiation.

We appeal to the analogy of massive  $W^\pm$  bosons interacting with a *massive* photon, a structure that is similar to the ordinary electroweak sector. The stability of the dark matter is ensured by a residual global  $U(1)$  in the theory. This is the first spin-1 dark sector theory with a massive spin-1 mediator coming from the same multiplet as the dark matter.

Compared to fermionic or spin-0 candidates, vector bosons are a relatively unexplored dark matter candidate [276, 175, 129, 98, 165, 212, 21, 208, 40, 41, 117, 76]. The first proposal of spin-1 dark matter was the Kaluza–Klein photon in the universal extra dimension scenario. This is a spin-1 analog to the supersymmetric neutralino: it is a weakly-interacting massive particle whose existence is related to a symmetry solution of the Higgs hierarchy problem. 5D translation invariance ensures dark matter stability [276],

though the scenario is constrained by collider searches because the visible matter fields also extend into the extra dimension [104].

Non-universal extra dimensional scenarios may avoid collider bounds, but typically require additional features to stabilize dark matter from decaying. Later models explored non-Abelian spin-1 dark matter purely in a hidden sector; these dark sector constructions differ from typical weakly-interacting massive particles in that they do not begin with the assumption that the new particles are related to the naturalness of the Standard Model Higgs sector [10]. Simple constructions with a  $SU(2)$  gauge group provide degenerate, massive spin-1 particles that can be stable due to custodial symmetry [175, 98, 165]. Other models are based on the spontaneous breaking of scale invariance [305, 23, 202, 207, 201, 206, 64, 176]. The scalar field that breaks the gauge symmetry may be used as a portal to the visible sector by mixing with the Standard Model Higgs; the amount of mixing controls the signal at direct detection experiments. A recent exploration with  $SU(3)$  gauge group may resolve a tension in the Hubble constant measurement [212]. Our study focuses a scenario where the triplet of  $SU(2)$  gauge bosons separate into hidden-charged dark matter (analogs of the  $W^\pm$ ) and a massive dark photon (analog of the  $A$ ), which may then kinetically mix with the visible sector photon.

$SU(2)$  sectors admit monopoles when there is an unbroken  $U(1)$  subgroup. This leads to studies of dark sectors that contain both vector dark matter and dark 't Hooft–Polyakov monopoles [21, 208]. This phenomena becomes more subtle in the case we study because the  $U(1)$  global symmetry is Higgsed so that the monopoles confine. We leave a study of this case for future work. An orthogonal direction in the study of non-Abelian



dark sectors is the case where the gauge theory confines. In this phase one has strongly-interacting dark matter composed of glueball-like states [40, 41]. Our model differs from this in that it is Higgsed rather than confined, allowing the dark matter states to be massive spin-1 particles. Alternatively, Ref. [76] recently studied vector strongly interacting dark matter. Our model differs in that it is a simple gauge group with a different scalar content and standard dark sector annihilation modes.

## 2.2 Particles and Symmetries

An  $SU(2)$  gauge field  $W_\mu^a$  couples with strength  $g$  to a two scalar particles: a doublet  $H^i$  and an adjoint scalar  $\Phi = \phi^a T^a$ . In this representation, the  $SU(2)$  transformation is

$$H(x) \rightarrow UH(x) \qquad \Phi(x) \rightarrow U\Phi(x)U^\dagger, \qquad (2.1)$$

where  $U = \exp(i\theta^a T^a)$  is a  $2 \times 2$  special unitary matrix and  $T^a = \frac{1}{2}\sigma^a$  are the generators of  $SU(2)$  in the fundamental representation. In the limit of no interactions, the particles respect a global “flavor” symmetry

$$SU(2)_\Phi \times SU(2)_H \times U(1)_H = SU(2)_V \times SU(2)_A \times U(1)_H, \qquad (2.2)$$

under which the scalar fields transform as

$$SU(2)_\Phi : \Phi \rightarrow U_\Phi \Phi U_\Phi^\dagger \qquad SU(2)_H : H \rightarrow U_H H \qquad U(1)_H : H \rightarrow e^{i\theta_H} H. \qquad (2.3)$$

We gauge the diagonal (vector) subgroup  $SU(2)_V$  of  $SU(2)_\Phi \times SU(2)_H$  composed of transformations with  $U_\Phi = U_H$ . The orthogonal combination is the axial symmetry  $SU(2)_A$ , for which  $U_\Phi = U_H^\dagger$ . The  $U(1)_H$  “Higgs number” symmetry is analogous to hypercharge in the Standard Model.

### 2.2.1 General, Renormalizable Lagrangian

The general, renormalizable Lagrangian satisfying the global symmetries of the particle content is

$$\mathcal{L} = -\frac{1}{4}F_{\mu\nu}^a F^{a\mu\nu} + |D_\mu H|^2 + \text{Tr} |\mathcal{D}_\mu \Phi|^2 - V \quad (2.4)$$

$$V = \frac{\lambda}{4!} (2 \text{Tr} \Phi^2 - f_0^2)^2 + \frac{\lambda'}{4!} (2|H|^2 - v_0^2)^2 + \mu H^\dagger \Phi H + \lambda'' |H|^2 \text{Tr} \Phi^2 . \quad (2.5)$$

$D$  and  $\mathcal{D}$  are covariant derivatives for the fundamental and adjoint of  $\text{SU}(2)$ , respectively. We write the potential  $V$  to imply that the scalars  $\Phi$  and  $H$  obtain vacuum expectation values (vevs) that spontaneously break the symmetries of the theory. This breaking produces a spectrum of Goldstone bosons, three of which are eaten by the massive gauge bosons. The trilinear  $\mu$  term explicitly breaks the global axial  $\text{SU}(2)_A$  symmetry. This gives a mass to the remaining the would-be Goldstone modes. The  $\lambda''$  term mixes the radial modes of the  $H$  and  $\Phi$ . We systematically examine the theory starting from the symmetry breaking  $\lambda$  and  $\lambda'$  terms and subsequently include the effects of the  $\mu$  and  $\lambda''$  terms. Additional quartic terms obeying the global symmetries reduce to the  $\lambda''$  term.<sup>1</sup>

One may also consider additional potential terms that use the pseudo-conjugate field  $\tilde{H}^i \equiv \epsilon^{ij} H^\dagger_j$ , exploiting the pseudoreality of  $\text{SU}(2)$ . Analogously to the Standard Model,  $\tilde{H}$  transforms like  $H$  with respect to  $\text{SU}(2)_H$  but with opposite charge under  $\text{U}(1)_H$ . Any renormalizable potential terms written with  $\tilde{H}$  either reduce to terms in (2.5) or explicitly violate the  $\text{U}(1)_H$  symmetry. We assume the case that this Higgs number symmetry is respected at the Lagrangian level and so we do not include any such terms.

---

<sup>1</sup>For example:  $H^\dagger \Phi^2 H = \frac{1}{2} H^\dagger \{ \Phi, \Phi \} H = \frac{1}{2} H^\dagger \left( \frac{1}{2} \phi^a \phi^b \delta^{ab} \mathbf{1}_{2 \times 2} \right) H = \frac{1}{2} |H|^2 \text{Tr} \Phi^2 .$

### 2.2.2 Spectrum, Symmetry, Stability

A qualitative overview of the model is as follows. The vacuum of the scalar potential spontaneously breaks the global symmetry  $SU(2)_\Phi \times SU(2)_H \times U(1)_H \rightarrow U(1)_{H'}$ , where  $U(1)_{H'}$  is generated by

$$U(1)_{H'} : \quad T_V^3 + \frac{1}{2}T_H, \quad (2.6)$$

analogous to electric charge in the electroweak sector. In what follows, we refer to the *charge* of a dark sector particle with respect to the  $U(1)_V \subset SU(2)_V$  gauge symmetry of the mediator. The gauge bosons eat three of the five Goldstone modes. We suggestively name the remaining two ‘pions,’  $\pi^\pm$ . We take the limit where the triplet vev is much larger than the doublet vev,

$$\langle \text{Tr } \Phi^2 \rangle = \frac{f^2}{2} \quad \gg \quad \langle |H|^2 \rangle = \frac{v^2}{2}. \quad (2.7)$$

Then the particle content in the  $\mu = \lambda'' = 0$  limit are:

1. **Dark matter:**  $W^\pm$  gauge bosons with mass  $\sim gf$ ; primarily eats the Goldstones in the  $\Phi$ .
2. **Mediator:**  $A$  gauge boson with mass  $\sim gv$ , eats the neutral Goldstone in  $H$ .
3. **Dark pions:**  $\pi^\pm$  charged scalars that are mostly the charged Goldstones in  $H$ .

We write  $W^\pm$ ,  $A$ ,  $H$ , and  $\pi^\pm$  to suggest parallels to the Standard Model electroweak gauge fields, Higgs, and charged pions. However, our fields are completely distinct from their visible sector counterparts. For example, there is no  $Z$  boson analog since only  $SU(2)_V$  is gauged.

The key features of this model are:

- The  $W^\pm$  and  $\pi^\pm$  are labeled with respect to their charge with respect to  $A$ . However, this charge is not conserved due to the doublet vev  $\langle H \rangle$ . It cannot be used to stabilize the dark matter. This is a key difference from other  $SU(2) \rightarrow U(1)$  models of vector dark matter [21].
- The stability of  $W^\pm$  is enforced by (1) the unbroken  $U(1)_{H'}$  symmetry and (2) requiring a spectrum where the pion,  $\pi^\pm$ , is heavier than the  $W^\pm$ .
- The  $\mu$ -term in the scalar potential explicitly breaks the  $SU(2)_A$  axial symmetry. This gives a mass to the pion, which is a pseudo-Goldstone boson. This is analogous to the pion masses in chiral perturbation theory and the Higgs mass in composite Higgs models.
- Simultaneously requiring the pion to be heavy and the mediator light is a tuning of a dimensionful, renormalizable parameter. We take this to be  $v_0^2$ .
- The quartic terms set the mass of the radial modes with respect to the vevs. The validity of perturbation theory requires  $\lambda, \lambda', \lambda'' \lesssim 4\pi$  and sets a maximum mass for these modes.

We sketch the spectrum in Fig. 2.1.

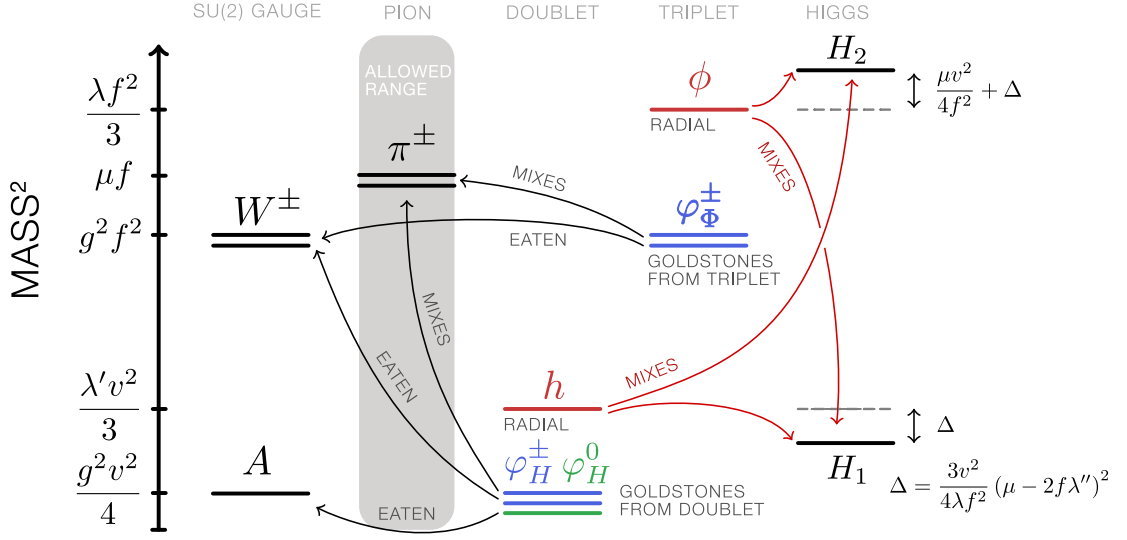


Figure 2.1: Model spectrum. Mass eigenstates are black lines, charged (neutral) Goldstones are blue (green) lines, radial Higgs modes are red lines. Mixing into mass eigenstates indicated by thin lines.

## 2.3 Symmetry Breaking

A linear parameterization of the scalar fields is

$$H = \begin{pmatrix} h_u \\ h_d \end{pmatrix} \quad \Phi = \frac{1}{2} \begin{pmatrix} \phi^3 & \sqrt{2}\phi^+ \\ \sqrt{2}\phi^- & -\phi^3 \end{pmatrix} \quad \phi^\pm \equiv \frac{\phi^1 \mp i\phi^2}{\sqrt{2}}. \quad (2.8)$$

We parameterize the vacuum expectation values of the fields by

$$\langle H \rangle = \begin{pmatrix} 0 \\ v/\sqrt{2} \end{pmatrix} \quad \langle \Phi \rangle = \frac{1}{2} \begin{pmatrix} f \\ -f \end{pmatrix} = fT^3. \quad (2.9)$$

These vevs break the global symmetries  $SU(2)_H \rightarrow \emptyset$  and  $SU(2)_\Phi \rightarrow U(1)$ , respectively.

### 2.3.1 Would-be Goldstones

We parameterize the Goldstone fields as spacetime-dependent transformations of the vacuum by the broken generators [61]:

$$H = e^{i\frac{\varphi_H \cdot T}{v/2}} \langle H \rangle \quad \varphi_H \cdot T = \sqrt{2}\varphi_H^+ T^+ + \sqrt{2}\varphi_H^- T^- + \varphi_H^0 T^3 \quad (2.10)$$

$$\Phi = e^{i\frac{\varphi_\Phi \cdot T}{f}} \langle \Phi \rangle e^{-i\frac{\varphi_\Phi \cdot T}{f}} \quad \varphi_\Phi \cdot T = \sqrt{2}\varphi_\Phi^+ T^+ + \sqrt{2}\varphi_\Phi^- T^- , \quad (2.11)$$

with respect to the  $SU(2)_{H,\Phi}$  generators  $T^\pm = T^1 \pm iT^2, T^3$ . The radial modes are

$$H|_{\text{radial}} = \frac{1}{\sqrt{2}} \begin{pmatrix} 0 \\ h \end{pmatrix} \quad \Phi|_{\text{radial}} = \frac{1}{2} \begin{pmatrix} \phi \\ -\phi \end{pmatrix} . \quad (2.12)$$

### 2.3.2 Gauge Boson Masses

The gauged  $SU(2)_V$  symmetry is the diagonal combination of  $SU(2)_H \times SU(2)_\Phi$ . In our representation, the covariant derivatives on the scalar fields are

$$D_\mu H = \partial_\mu H - igW_\mu^a T^a H \quad \mathcal{D}_\mu \Phi = \partial_\mu \Phi - igW_\mu^a [T^a, \Phi] . \quad (2.13)$$

If the fields acquire vevs (2.9), then the kinetic terms yield the following mass terms for the gauge bosons:

$$\mathcal{L}_{\text{mass}} = m_W^2 W^+ W^- + \frac{1}{2} m_A^2 A^2 \quad m_W^2 = g^2 f^2 + \frac{g^2 v^2}{4} \quad m_A^2 = \frac{g^2 v^2}{4} . \quad (2.14)$$

We identify the massive dark matter  $W^\pm = (W^1 \mp iW^2)/\sqrt{2}$  and mediator (dark photon)  $A = W^3$ . The limit  $v^2 \ll f^2$  yields a spectrum where the dark photon is much lighter than the dark matter. The covariant derivatives with respect to the spin-1 mass eigenstates are

$$D_\mu H = \partial_\mu H - i\frac{g}{\sqrt{2}} (W_\mu^+ T^+ + W_\mu^- T^-) H - igA_\mu T^3 H \quad (2.15)$$

$$\mathcal{D}_\mu \Phi = \partial_\mu \Phi - i\frac{g}{\sqrt{2}} (W_\mu^+ [T^+, \Phi] + W_\mu^- [T^-, \Phi]) - igA_\mu [T^3, \Phi] . \quad (2.16)$$

### 2.3.3 Higgs Mechanism and Leftover Goldstones

Let  $\varphi_V$  be the linear combination of Goldstone bosons associated with  $SU(2)_V$ . Gauging the vector combination  $SU(2)_V$  promotes this global symmetry to a local symmetry. In unitary gauge one performs a local  $SU(2)_V$  transformation to remove  $\varphi_V$  from the theory. It appears solely as the longitudinal polarization of the massive gauge bosons. We express  $\varphi_V$  in terms of the  $\varphi_{H,\Phi}$  by identifying this mixing in the kinetic terms:

$$|DH|^2 + \text{Tr} |\mathcal{D}\Phi|^2 \supset -g \left( \frac{v}{2} \partial\varphi_H^+ + f\partial\varphi_\Phi^+ \right) W^- + \text{h.c.} - g \frac{v}{2} \partial\varphi_H^0 A. \quad (2.17)$$

Only  $\langle H \rangle$  breaks the  $U(1)$  symmetry so that the photon  $A$  eats the only neutral Goldstone. This is in contrast to the charged states for which there are two pairs of charged Goldstones and only one pair of charged gauge bosons. From (2.17) we identify the normalized  $SU(2)_V$  Goldstone  $\varphi_V$  and the orthogonal state  $\varphi_A$ :

$$\varphi_V^\pm = \frac{f\varphi_\Phi^\pm + (v/2)\varphi_H^\pm}{\sqrt{f^2 + (v/2)^2}} \quad \varphi_A^\pm = \frac{f\varphi_H^\pm - (v/2)\varphi_\Phi^\pm}{\sqrt{f^2 + (v/2)^2}}. \quad (2.18)$$

Appendix A.1 presents an illustrative  $U(1)$  example motivating these linear combinations. In unitary gauge,  $\varphi_V^\pm$  only appears as the longitudinal mode of  $W^\pm$ . The ‘axial’ combination  $\varphi_A^\pm$  is an uneaten Goldstone boson that remains in the theory. We refer to these as pions and relabel them  $\pi^\pm$  in anticipation of including explicit symmetry breaking terms to make them massive.

### 2.3.4 Symmetry Breaking with $\lambda, \lambda'$

The simplest form of this model takes only the first two terms in (2.5),

$$V|_{\lambda,\lambda'} = \frac{\lambda}{4!} (2 \text{Tr} \Phi^2 - f_0^2)^2 + \frac{\lambda'}{4!} (2|H|^2 - v_0^2)^2. \quad (2.19)$$

These terms separately break the  $SU(2)_\Phi$  and  $SU(2)_H$  global symmetries. This, in turn, breaks the gauged vector combination of the two and gives mass to the gauge bosons. The vevs  $f$  and  $v$  are trivially related to the Lagrangian parameters  $f_0$  and  $v_0$ ,

$$f = f_0 \qquad v = v_0 . \qquad (2.20)$$

The radial modes  $h$  and  $\phi$  do not mix. Their masses are

$$m_\phi^2 = \frac{\lambda'}{3} f_0^2 \qquad m_h^2 = \frac{\lambda}{3} v_0^2 . \qquad (2.21)$$

### 2.3.5 Symmetry Breaking with $\lambda$ , $\lambda'$ , $\mu$

Introducing the  $\mu$  term in the potential explicitly breaks  $SU(2)_\Phi \times SU(2)_H \rightarrow SU(2)_V$  and gives the  $\pi^\pm$  a mass<sup>2</sup> proportional to  $\mu$ :

$$V|_{\lambda, \lambda', \mu} = \frac{\lambda}{4!} (2 \text{Tr} \Phi^2 - f_0^2)^2 + \frac{\lambda'}{4!} (2|H|^2 - v_0^2)^2 + \mu H^\dagger \Phi H . \qquad (2.22)$$

This shifts the minimum of the potential from (2.20) to the following condition:

$$f^2 = f_0^2 + \frac{3\mu v^2}{2\lambda f} \qquad v^2 = v_0^2 + \frac{3\mu f}{\lambda'} . \qquad (2.23)$$

The  $\mu$  term causes the  $\Phi$  vev to shift the  $H$  vev, and vice versa.

### Tuning for phenomenological hierarchy

Phenomenologically we require that the mediator is light and that the pions are heavier than the dark matter; this forces

$$g^2 v^2 \ll g^2 f^2 \lesssim \mu f . \qquad (2.24)$$

---

<sup>2</sup>In QCD, the quark masses explicitly break chiral symmetry to give mass to the pions.



Assuming  $g \lesssim \mathcal{O}(1)$ , we see that the the vev  $f^2$  is perturbed by a small amount relative to its  $\mu = 0$  value  $f_0^2$ . On the other hand, the hierarchy  $f, \mu \gg v$  and perturbative limit  $\lambda' < 4\pi$  imply that  $v^2$  is shifted by a large amount relative to  $v_0^2$ . Without loss of generality, we assume  $\mu > 0$ . We then require that  $v_0^2$  is negative and tuned to give a small  $v^2 \ll f^2$ .

### Radial mode mixing

The  $\mu$ -term induces mixing between the radial  $\phi$  and  $h$  fields. Expanding (2.22) about the vacuum (2.23) yields a mass matrix  $\mathcal{M}_H$ ,

$$\mathcal{L} \supset \frac{1}{2} \begin{pmatrix} h & \phi \end{pmatrix} \mathcal{M}_H^2 \begin{pmatrix} h \\ \phi \end{pmatrix} \quad \mathcal{M}_H^2 = \begin{pmatrix} \frac{\lambda' v^2}{3} & -\frac{\mu v}{2} \\ -\frac{\mu v}{2} & \frac{\lambda f^2}{3} + \frac{\mu v^2}{4f} \end{pmatrix}. \quad (2.25)$$

The eigenvalues of the mass matrix are

$$m_{1,2}^2 = \frac{1}{2} \text{Tr} \mathcal{M}_H^2 \left( 1 \mp \sqrt{1 - \frac{4 \text{Det} \mathcal{M}_H^2}{(\text{Tr} \mathcal{M}_H^2)^2}} \right). \quad (2.26)$$

We focus on the  $v \ll f \sim \mu$  regime where the eigenvalues are positive<sup>3</sup> and have a large mass splitting. The light and heavy eigenvalues are

$$m_1^2 = \frac{\lambda' v^2}{3} - \frac{3\mu^2 v^2}{4\lambda f^2} + \mathcal{O}\left(\frac{v^4}{f^4}\right) \quad m_2^2 = \frac{\lambda f^2}{3} + \frac{\mu v^2}{4f} + \frac{3\mu^2 v^2}{4\lambda f^2} + \mathcal{O}\left(\frac{v^4}{f^4}\right). \quad (2.27)$$

These correspond to light and heavy radial modes that are a mixture of the  $\phi$  and  $h$  states:

$$\begin{pmatrix} H_1 \\ H_2 \end{pmatrix} = \mathbf{R}_\alpha \begin{pmatrix} h \\ \phi \end{pmatrix} \quad \mathbf{R}_\alpha = \begin{pmatrix} \cos \alpha & \sin \alpha \\ -\sin \alpha & \cos \alpha \end{pmatrix}. \quad (2.28)$$

---

<sup>3</sup>The minimum of the potential has positive squared masses. In (2.26), the possibility of a negative eigenvalue corresponds to the vev in (2.23) becoming a saddle point rather than a minimum. This occurs for large  $\mu$  and is outside the regime of phenomenological interest for this study.

The radial mode mixing angle is related to the model parameters by

$$\tan 2\alpha = \frac{\mu v}{\lambda f^2/3 + \mu v^2/4f - \lambda' v^2/3}. \quad (2.29)$$

### Goldstone mixing

In addition to mixing the radial fields, the  $\mu$  term mixes the charged Goldstones,  $\varphi_\Phi^\pm$  and  $\varphi_H^\pm$ . Expanding (2.22) yields a mass matrix

$$\mathcal{L} \supset \begin{pmatrix} \varphi_\Phi^- & \varphi_H^- \end{pmatrix} \mathcal{M}_G^2 \begin{pmatrix} \varphi_\Phi^+ \\ \varphi_H^+ \end{pmatrix} \quad \mathcal{M}_G^2 = \begin{pmatrix} \frac{\mu v^2}{4f} & -\frac{\mu v}{2} \\ -\frac{\mu v}{2} & \mu f \end{pmatrix}. \quad (2.30)$$

There is a massless mode because  $\text{Det } \mathcal{M}_G^2 = 0$ . This corresponds to the massless Goldstones,  $G^\pm$ , eaten by charged gauge bosons  $W^\pm$ . The massive pions,  $\pi^\pm$ , have a mass-squared given by the trace:

$$m_G^2 = 0 \quad m_\pi^2 = \mu f \left( 1 + \frac{v^2}{4f^2} \right). \quad (2.31)$$

The mass eigenstates are related to the would-be Goldstones,  $\varphi_\Phi^\pm$  and  $\varphi_H^\pm$ , by a rotation

$$\begin{pmatrix} G^\pm \\ \pi^\pm \end{pmatrix} = \mathbf{R}_\beta \begin{pmatrix} \varphi_\Phi^\pm \\ \varphi_H^\pm \end{pmatrix} \quad \mathbf{R}_\beta = \begin{pmatrix} \cos \beta & \sin \beta \\ -\sin \beta & \cos \beta \end{pmatrix}. \quad (2.32)$$

The Goldstone mixing angle,  $\beta$ , satisfies

$$\tan \beta = \frac{v}{2f} \quad \sin \beta = \frac{v/2}{\sqrt{f^2 + v^2/4}} \quad \cos \beta = \frac{f}{\sqrt{f^2 + v^2/4}}, \quad (2.33)$$

where we assume  $0 \leq \beta \leq \pi/2$ . Observe that in the absence of a  $\mu$  term, the mass eigenstates in (2.32) are identical to those defined by (2.18). This shows that the gauging of the vector combination  $\text{SU}(2)_V$  fixes a basis of eaten Goldstones,  $G^\pm$ , and their orthogonal states,  $\pi^\pm$ ; see Appendix A.1. The latter non-linearly realize  $\text{SU}(2)_A$  and pick up an explicit mass when we introduce the  $\mu$  term.

### 2.3.6 Symmetry Breaking with $\lambda, \lambda', \lambda'', \mu$

The most general renormalizable potential (2.5) includes a mixed quartic term  $\lambda''|H|^2\text{Tr}\Phi^2$ . This term shifts the vevs and affects the radial mode mixing but does not induce any further Goldstone interactions since it is manifestly  $\text{SU}(2)_H \times \text{SU}(2)_\Phi \times \text{U}(1)_H$  invariant. The vevs in this scenario are shifted from (2.23):

$$f^2 = f_0^2 + \frac{3v^2}{\lambda} \left( \frac{\mu}{2f} - \lambda'' \right) \quad v^2 = v_0^2 + \frac{3f^2}{\lambda'} \left( \frac{\mu}{f} - \lambda'' \right). \quad (2.34)$$

The  $\lambda''$  term introduces additional interactions and mixing between the radial modes. The radial field mass matrix is

$$\mathcal{M}_H^2 = \begin{pmatrix} \frac{\lambda'v^2}{3} & \lambda''vf - \frac{\mu v}{2} \\ \lambda''vf - \frac{\mu v}{2} & \frac{\lambda f^2}{3} + \frac{\mu v^2}{4f} \end{pmatrix}. \quad (2.35)$$

The eigenvalues of (2.35) are given by (2.26) and yield

$$m_1^2 = \frac{\lambda'v^2}{3} - \frac{3v^2}{4\lambda f^2} (\mu - 2f\lambda'')^2 + \mathcal{O}\left(\frac{v^4}{f^4}\right) \quad (2.36)$$

$$m_2^2 = \frac{\lambda f^2}{3} + \frac{\mu v^2}{4f} + \frac{3v^2}{4\lambda f^2} (\mu - 2f\lambda'')^2 + \mathcal{O}\left(\frac{v^4}{f^4}\right). \quad (2.37)$$

The rotation (2.28) that diagonalizes (2.35) is modified from (2.29) to

$$\tan 2\alpha = \frac{\mu v - 2\lambda''vf}{\lambda f^2/3 + \mu v^2/4f - \lambda'v^2/3}. \quad (2.38)$$

For the remainder of this manuscript we set  $\lambda'' = 0$  since its primary phenomenological effects may be understood as a shift on  $\mu$ .

### 2.3.7 Qualitative Behavior

The parameters of interest realize the spectrum in Fig. 2.1. The qualitative behavior of the theory is the limit where the longitudinal  $W$  modes are predominantly the

triplet Goldstones and

- $\alpha = 0$  : the light Higgs is predominantly the doublet neutral Goldstone,
- $\beta = 0$  : the charged pions are predominantly the doublet charged Goldstones.

### 2.3.8 Vacuum Stability

The stability of the scalar vacuum requires that the eigenvalues of  $\mathcal{M}_H^2$  are both positive. Alternatively, both the trace and determinant of  $\mathcal{M}_H^2$  must be positive. It is clear from (2.35) that  $\text{Tr } \mathcal{M}_H^2 > 0$ . Therefore, it is sufficient to enforce that  $\det \mathcal{M}_H^2 > 0$  to guarantee that the vacuum is stable. This implies the inequality

$$\frac{\lambda'}{9} \left( \lambda + \frac{3\mu}{f} \frac{v^2}{4f^2} \right) > \left( \lambda'' - \frac{\mu}{2f} \right)^2. \quad (2.39)$$

For a fixed  $v \ll f$  hierarchy, this implies that the choice of the trilinear mass scale is restricted to

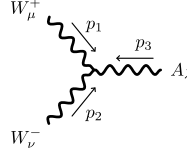
$$\frac{g^2}{2} \lesssim \frac{\mu}{2f} \lesssim \left( \frac{\lambda\lambda'}{9} \right)^{1/2} - \lambda''. \quad (2.40)$$

The lower bound is the requirement that the pions are heavier than the dark matter while the upper bound enforces the stability of the vacuum. If one chooses  $\mu$  such that the upper bound is violated, the vacuum with  $v \ll f$  is a saddle point and the true vacuum of the theory is one where the proposed hierarchy is not realized.

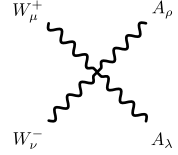
## 2.4 Feynman Rules for Light States

We summarize the dark sector Feynman rules for the dark matter and the low-mass states. The dark matter and dark photon have interactions analogous to the Standard

Model  $W$  and  $Z$  bosons and are thus given by

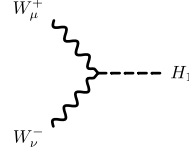


$$= -ig \left[ g^{\mu\nu} (p_1 - p_2)^\lambda + g^{\nu\lambda} (p_2 - p_3)^\mu + g^{\lambda\mu} (p_3 - p_1)^\nu \right] \quad (2.41)$$

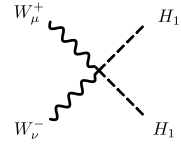


$$= -ig^2 \left[ 2g^{\mu\nu} g^{\lambda\rho} - g^{\mu\lambda} g^{\nu\rho} - g^{\mu\rho} g^{\nu\lambda} \right] . \quad (2.42)$$

The Feynman rules for the dark matter interactions with the light radial mode are



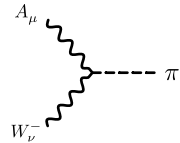
$$= igm_W g^{\mu\nu} (\cos \alpha \sin \beta + 2 \sin \alpha \cos \beta) \quad (2.43)$$



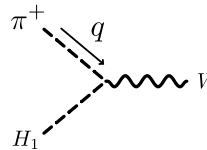
$$= \frac{ig^2}{4} (5 - 3 \cos 2\alpha) g^{\mu\nu} . \quad (2.44)$$

With respect to the general renormalizable spin-1 dark matter Lagrangian parameterization in [102, 67, 66], these rules correspond to  $b_5 = g$  and  $b_6 = ig$ , with other identifications straightforward.

Symmetry also allows the low-mass states to interact with a dark pion and dark matter particle with the opposite  $U(1)_{H'}$  charge. The Feynman rules are given by



$$= \frac{g}{2} m_W \sin 2\beta g_{\mu\nu} \quad (2.45)$$



$$= gq_\nu (2 \sin \alpha \sin \beta - \cos \alpha \cos \beta) . \quad (2.46)$$

These interactions allow the dark pions to decay at tree level.

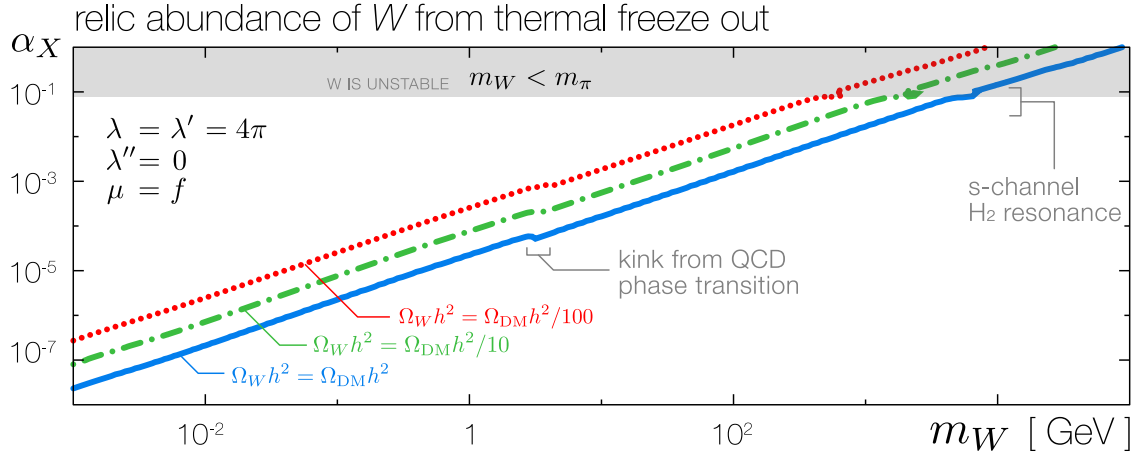


Figure 2.2: The  $W$  relic abundance from thermal freeze out as a function of the  $W$  mass and fine structure constant. We plot lines where the  $W$  saturates the entire dark matter density (solid/blue) or only a 10% (dash-dotted/green) or 1% fraction (dotted/red). We take  $\lambda = \lambda' = 4\pi$ ,  $\lambda'' = 0$  and  $\mu = f$ . The shaded region is excluded in order to prevent dark matter decay.

## 2.5 Relic Abundance and Annihilation

Dark matter annihilation is dominated by  $s$ -wave processes that persist in the zero-relative-velocity limit. We sketch the primary  $W^+W^- \rightarrow AA$  diagrams in Fig. 2.3. The largest  $s$ -wave channels are  $W^+W^-$  annihilating to  $AA$  and  $H_1H_1$ . The  $AH_1$  final state vanishes in the  $m_A/m_W \rightarrow 0$  limit. Note that we assume that the entropy produced in dark matter annihilation is eventually dumped into the visible sector through the portal

interactions in Section 2.8. The relevant annihilation cross sections are:

$$\sigma_{v_{AA}} = \frac{\pi\alpha_X^2}{36m_W^2} \left\{ 152 + \frac{4m_W^4}{(m_W^2 + m_\pi^2)^2} + \frac{3(-4m_W^2 + m_2^2 + 2m_\pi^2)^2}{4(m_2^2 - 4m_W^2)^2} + \frac{2m_W^2(-4m_W^2 + m_2^2 + 2m_\pi^2)}{(m_W^2 + m_\pi^2)(4m_W^2 - m_2^2)} \right\} \quad (2.47)$$

$$\sigma_{v_{H_1H_1}} = \frac{\pi\alpha_X^2}{144m_W^2} \left\{ 3 + \frac{12m_\pi^4}{(m_2^2 - 4m_W^2)^2} - \frac{16m_\pi^2m_W^2}{(m_2^2 - 4m_W^2)(m_W^2 + m_\pi^2)} + \frac{16m_W^4}{(m_W^2 + m_\pi^2)^2} \right\} . \quad (2.48)$$

We define the dark fine structure constant

$$\alpha_X = \frac{g^2}{4\pi} . \quad (2.49)$$

In the decoupling limit where both  $m_\pi$  and  $m_2 \rightarrow \infty$ , (2.47) matches the calculation for a spin-1 dark matter particle annihilating into massless dark photons in Ref. [21]. For completeness, we list the  $s$ -wave annihilation cross sections going into final states with the heavy Higgs,  $H_2$ , though these are typically kinematically suppressed. The relevant final states are  $H_2H_2$  and  $AH_2$ ; these are only allowed when  $m_W > m_2$  and  $m_W > m_2/2$  respectively. The  $H_1H_2$  mode vanishes in the  $m_A/m_W \rightarrow 0$  limit.

$$\sigma_{v_{H_2H_2}} = \frac{2\pi\alpha_X^2}{9m_W^2} \sqrt{1 - \frac{m_2^2}{m_W^2}} \frac{864m_W^8 + 31m_2^8 - 248m_2^6m_W^2 + 820m_2^4m_W^4 - 1296m_2^2m_W^6}{(-6m_2^2m_W^2 + 8m_W^4 + m_2^4)^2} \quad (2.50)$$

$$\sigma_{v_{AH_2}} = \frac{8\pi\alpha_X^2}{9m_W^4} (4m_W^2 - m_2^2) . \quad (2.51)$$

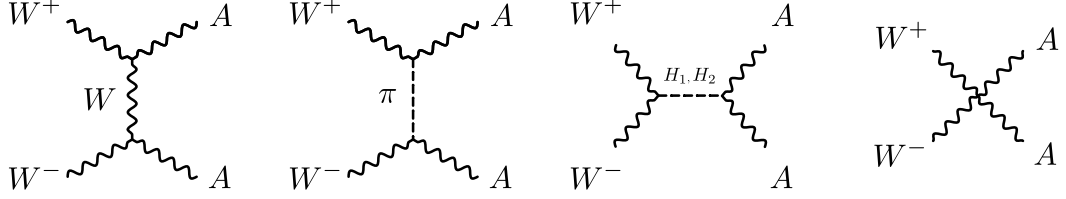


Figure 2.3: Diagrams contributing to  $W^+W^- \rightarrow AA$  annihilation. Not shown: crossed ( $u$ -channel) diagrams and annihilation to scalars.

We assume that the relic abundance is set by non-relativistic freeze out. The freeze-out temperature and final relic abundance is [214]

$$x_f = \ln \left[ 0.038 \sqrt{\frac{g}{g_*}} M_{Pl} m_W \langle \sigma v \rangle \right] - \frac{1}{2} \ln^2 \left[ 0.038 \sqrt{\frac{g}{g_*}} M_{Pl} m_W \langle \sigma v \rangle \right] \quad (2.52)$$

$$\Omega h^2 = 2 \times 1.07 \times 10^9 \frac{x_f \text{ GeV}^{-1}}{\sqrt{g_*(x_f)} M_{Pl} \langle \sigma v \rangle}, \quad (2.53)$$

where we include an explicit factor of two in (2.53) to account for a given dark matter particle,  $W^\pm$ , only being able to annihilate with its anti-particle,  $W^\mp$ . This is compared to  $\Omega h^2 = 0.12$  [287, 283].

Fig. 2.2 shows the coupling  $\alpha_X = g^2/4\pi$  that reproduces the observed dark matter relic abundance assuming thermal freeze out for benchmark parameters. For fermionic dark matter annihilating into much lighter dark photons, a numerical estimate for the target fine structure constant is  $\alpha_{X,\text{fermion}}^{\text{th}} \cong 0.035 (m_X/\text{TeV})$  (see e.g. [230]). Comparing the  $m_A \rightarrow 0$  fermionic  $XX \rightarrow AA$  cross section to (2.47):

$$\langle \sigma_{XX \rightarrow AA} v \rangle^{\text{fermion}} \approx \frac{\pi \alpha_X^2}{m_X^2} \quad \langle \sigma_{WW \rightarrow AA} v \rangle \approx \frac{38}{9} \frac{\pi \alpha_X^2}{m_X^2}. \quad (2.54)$$

We thus estimate the target  $\alpha_X$  in our model by rescaling the fermionic target by  $(38/9)^{-1/2} \approx$



0.5:

$$\alpha_X^{\text{th}} \cong 0.017 \left( \frac{m_W}{\text{TeV}} \right) . \quad (2.55)$$

This estimate ignores the contributions from  $H_1$  final states or possible  $H_2$  resonances (see Fig. 2.4).

Implicit in our assumption is that the dark photon,  $A$ , is sufficiently in equilibrium with the Standard Model. We thus assume

$$\Gamma_A \geq H(x_f \cong 20) \quad (2.56)$$

where  $\Gamma_A$  is the dark photon decay width and  $H(x_f)$  is the Hubble rate evaluated at freeze-out. This places a lower bound on the kinetic mixing with the visible sector,  $\varepsilon$  in (2.65) [257]:

$$\varepsilon^2 \left( \frac{m_A}{10 \text{ MeV}} \right) \gtrsim 10^{-11} \left( \frac{m_W}{50 \text{ GeV}} \right)^2 . \quad (2.57)$$

This is not strictly necessary. One simple direction is to assume a dark sector with a completely different initial temperature at reheating [133]. More generally, the full ‘phase space’ of thermal histories for dark sectors with mediators is an exciting direction that only recently been studied [77, 39, 36, 218, 122, 115]. Alternatively, one may pursue models where UV dynamics produce asymmetric dark matter within our scenario [197, 294]. These possibilities are beyond the scope of the present work. Here we focus on the simple benchmark scenario where the  $W$  abundance is produced through standard thermal freeze out by annihilation into mediators. Explorations of the alternative scenarios are especially interesting and we leave them for future work.

### 2.5.1 Sommerfeld Enhancement

In principle, (2.47) – (2.51) receive an overall Sommerfeld enhancement factor [182, 190, 65]. This enhancement is only significant for non-relativistic freeze out for large masses  $m_W \gtrsim 100$  GeV, which we do not consider here [293]. We leave an analysis of indirect detection of non-relativistic annihilation in the present day for future work as this depends on the details of the choice of portal interactions to the Standard Model.

### 2.5.2 Bound State Formation

The interactions of the  $W^\pm$  mediated by the dark photon  $A$  and radial modes  $H_1$  and  $H_2$  yield Yukawa potentials that may admit bound state solutions when the mass of the mediator  $m_{\text{med}}$  is less than the inverse Bohr radius [252],

$$m_{\text{med}} \lesssim \frac{\alpha_i m_W}{2}, \quad (2.58)$$

where  $\alpha_i$  is the appropriate fine structure constant. The relic abundance may be depleted if a significant fraction of the dark matter is forms bound states. The fine structure constant for interactions mediated by  $A$  is  $\alpha_X$ . The corresponding fine structure constants for the potentials those mediated by  $H_1$  and  $H_2$  are

$$\alpha_{H_1} = \alpha_X \left( \sin \alpha \cos \beta + \frac{1}{2} \cos \alpha \sin \beta \right)^2 \quad \alpha_{H_2} = \alpha_X \left( \cos \alpha \cos \beta - \frac{1}{2} \sin \alpha \sin \beta \right)^2. \quad (2.59)$$

In the regime where  $v \ll f$ ,  $\alpha, \beta \ll 1$  so that  $\alpha_{H_1} \ll \alpha_{H_2} \sim \alpha_X$ .  $W^\pm$  cannot form bound states from the exchange of  $H_2$  because  $m_2 \gtrsim m_W$  so that (2.58) does not hold.

The case in which bound states form from the exchange of  $A$  or  $H_1$  is less clear.

The condition for a thermal relic to form a bound state is approximately

$$\frac{m_{\text{med}}}{m_W} \lesssim 0.0085 \left( \frac{m_W}{\text{TeV}} \right). \quad (2.60)$$

Thus, lighter dark matter requires a smaller ratio  $m_{\text{med}}/m_W$  to form a bound state. Because  $\alpha_{H_1} \ll \alpha_X$  in the regime of interest, the dark matter cannot form bound states from the exchange of  $H_1$ . When  $m_A \lesssim m_W \alpha_X / 2$ , bound state formation is possible for sufficiently low velocities. Following the analysis in Ref. [130], we estimate that only a negligible fraction of the dark matter forms bound states ahead of freeze-out.

## 2.6 Relating Dark Matter and Dark Pion Masses

In the  $v \ll f$  limit of phenomenological interest, the properties of the dark matter  $W^\pm$  and the pions  $\pi^\pm$  are related to one another. Fig. 2.4 shows the allowed region for  $m_\pi \approx \sqrt{\mu} f$  and  $\alpha_X = g^2/4\pi$  for a sample of vevs,  $f$ . The dark matter mass is  $m_W \approx \sqrt{4\pi\alpha_X} f$ . The triangular regions are bounded by requiring

1. a relic abundance less than or equal to the total dark matter abundance (Section 2.5),
2. the  $W^\pm$  is the lightest charged particle in the dark sector (Section 2.3.5), and
3. the tree-level stability of the vacuum (Section 2.3.8).

Observe the following features in Fig. 2.4:

- As the symmetry breaking scale  $f$  is increased, the  $W$  mass increases so that the required coupling to saturate the dark matter relic abundance increases, the minimum

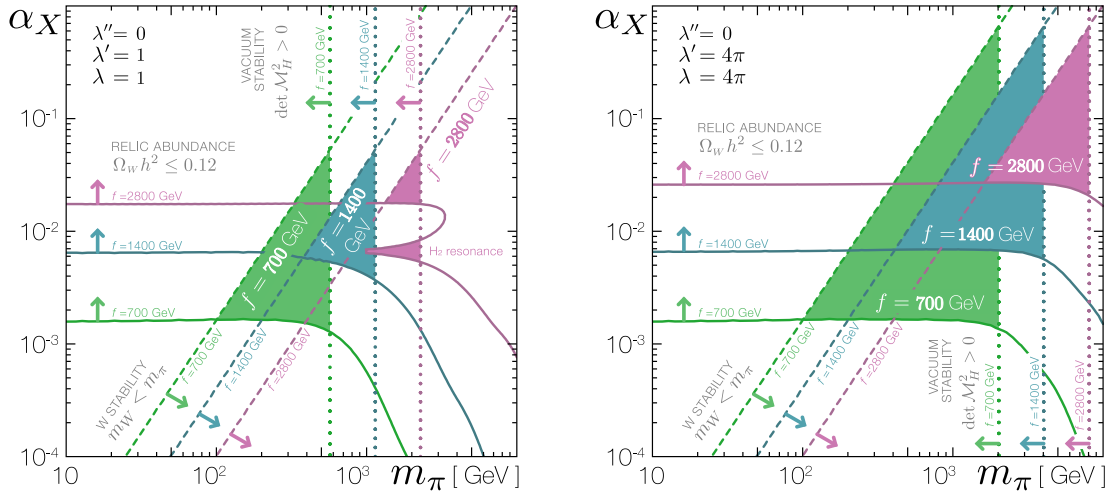


Figure 2.4: Shaded regions correspond to values of the dark fine structure constant  $\alpha_X = g^2/4\pi$  and the pion mass  $m_\pi \approx \mu f$  that (i) do not overclose the universe [solid lines], (ii) have a stable  $W$  [dashed lines], and (iii) have a stable vacuum [dotted lines]. Colors correspond to choices of  $f = 700$  GeV (green, lower-left),  $f = 1400$  GeV (teal, middle),  $f = 2800$  GeV (magenta, upper-right). We take  $\lambda'' = 0$  for simplicity. LEFT:  $\lambda = \lambda' = 1$ . RIGHT:  $\lambda = \lambda' = 4\pi$ .

pion mass increases to maintain the particle spectrum increases, and the bound on the stability of the scalar vevs (2.39) shifts to larger  $\mu$  and hence larger  $m_\pi$ . Note that the stability bound is modified if  $\lambda'' > 0$ .

- In the left-hand plot ( $\lambda = \lambda' = 1$ ), for  $f = 2800$  GeV, the relic abundance bound exhibits a resonance in the annihilation diagram with an  $s$ -channel heavy Higgs,  $H_2$ . This is a useful reminder that the dynamics  $H_2$  may be dominant in certain annihilation channels even though it will not affect the other observational probes discussed in this manuscript.
- Comparing the left-hand ( $\lambda = \lambda' = 1$ ) and right-hand left-hand ( $\lambda = \lambda' = 4\pi$ ) plots, the  $W$  stability lines are unchanged. The other two bounds shift according to the  $\lambda^{(\prime)}$ -dependence of the radial mode masses, (2.36–2.37), and the dependence of the annihilation rate and vacuum stability condition on these masses.
- In the unstable  $W$  region ( $m_W > m_\pi$ ), the relic abundance curves are flat and independent of the pion mass. This corresponds to the leading terms in (2.48–2.47) that are  $m_\pi$ -independent. Note that the left- and right-handed plots differ in this flat region since  $m_1$  depends on  $\lambda'$  via (2.36) so that increasing  $\lambda'$  decreases the phase space for  $W^+W^- \rightarrow H_1H_1$ , resulting a slightly larger  $\alpha_X$  required to annihilate enough  $W$ s.
- In the stable  $W$  region ( $m_W < m_\pi$ ) the  $m_\pi$  dependence of the annihilation cross sections (2.47–2.48) manifests itself. In this regime, the left- and right-hand plots differ in  $m_\pi$  dependence because of the  $\lambda$ -dependence through the heavy Higgs mass, (2.37).

## 2.7 Self-Interacting Dark Matter

The dark sector furnished by our framework automatically realizes the self-interacting dark matter (SIDM) paradigm. Ref. [63] first proposed that dark matter may exist in a separate sector with self-interactions. Refs. [280, 95] identified that the self-interactions may affect the density profiles of dark matter halos and thus allow observational tests of the dark matter self-interaction cross section. More recently, the seminal work in Refs. [130, 131, 48, 293] connected particle physics models of dark sectors (dark matter with low-mass mediators) to observed small scale structure anomalies tied to the dark matter density profiles of dwarf galaxies. We refer to Ref. [292] for a review.

The exchange of dark photons,  $A$ , generates a long range, velocity-dependent, self-interaction between the  $W^\pm$  dark matter particles. At low energies, these self-interactions produce a Yukawa potential,

$$V(r) = \pm \frac{\alpha_X}{r} e^{-m_A r} . \quad (2.61)$$

Since the force mediator is a vector boson, particle–antiparticle interactions produce an attractive potential while particle–particle interactions produce a repulsive potential. The self-interaction potential also receives contributions from the exchange of the radial modes,  $H_1$  and  $H_2$ , that are purely attractive. We assume that both of these contributions are negligible:

The diagram shows two Feynman diagrams for the self-interaction of  $W^\pm$  particles. The left diagram shows the exchange of radial modes  $H_1, H_2$  between two  $W^\pm$  particles, represented by a dashed vertical line. The right diagram shows the exchange of a dark photon  $A$  between two  $W^\pm$  particles, represented by a wavy vertical line. The two diagrams are separated by a double less-than sign ( $\ll$ ), indicating that the  $H_1, H_2$  exchange is much smaller than the  $A$  exchange. The equation is labeled (2.62).

$$\begin{array}{ccc} \begin{array}{c} W^\pm \\ \diagdown \quad \diagup \\ \text{---} \\ \diagup \quad \diagdown \\ W^\pm \end{array} & \ll & \begin{array}{c} W^\pm \\ \diagdown \quad \diagup \\ \text{---} \\ \diagup \quad \diagdown \\ W^\pm \end{array} . \end{array} \quad (2.62)$$

The heavy Higgs,  $H_2$ , is typically much heavier so that the Yukawa suppression causes the force to be short ranged. The light Higgs,  $H_1$ , is assumed to be heavier than the dark photon but may have a mass of the same order of magnitude. In this case, we note that the  $H_1$  exchange diagram is suppressed by a factor of  $(m_A/m_W)^2$  relative to  $A$  exchange. This suppression is clear in the Feynman rule (2.43) where we note that  $\sin \alpha \sim \sin \beta \sim v/f$  from (2.29) and (2.33).

The long-ranged potential (2.61) is the same as that generated by more conventional spin-1/2 or spin-0 models of self-interacting dark matter so that the phenomenology is qualitatively similar. A benchmark model in the conventional scenario is a 15 GeV dark matter with a 17 MeV mediator [200]. The target cross section for this scenario is  $\sigma \sim 1 \text{ cm}^2 (m_X/g)$  for dwarf-scale velocities; this flattens the dark matter density in galactic cores [298, 269, 307]. This potential manifests a velocity dependence depending on the value of the transfer momentum compared to the mass of the mediator. This velocity-dependence suppresses the effect of self-interactions for large systems such as colliding galaxy clusters, where there is little evidence for self-interactions.

We compare the effects of the long-ranged dark matter self-interaction in our model with respect to the standard SIDM benchmark. One difference in our scenario is that we assume that dark matter is symmetric: it is composed of equal parts of  $W^+$  and  $W^-$ . Cosmological constraints on the matter power spectrum constrain the early-universe annihilation of dark matter in the standard self-interacting dark matter scenario [187]<sup>4</sup>. As such, the most viable SIDM models typically assume that the dark matter is asymmetric

---

<sup>4</sup>We leave an exploration of these constraints for future work; in this manuscript we focus on the presentation of the core model with thermal freeze out.

Model	$\alpha_X = g^2/4\pi$	$m_A$	$m_W$	$m_\pi^{\max} (\lambda^{(\prime)} = 1)$	$m_\pi^{\max} (\lambda^{(\prime)} = 4\pi)$
SIDM	$1.35 \times 10^{-6}$	0.095 MeV	0.06 GeV	12 GeV	42 GeV
WIMP-like	$10^{-3}$	6 MeV	60 GeV	440 GeV	1.6 TeV

Table 2.1: Benchmark models: a model realizing self-interacting dark matter targets (SIDM, solid/**red** in Fig. 2.5) and a model that realizes thermal freeze out with a weak-scale dark matter mass (WIMP-like, dash-dotted/**green** in Fig. 2.5). The SIDM benchmark corresponds to  $g = 4.2 \times 10^{-3}$ ,  $v = 46$  MeV,  $f = 15$  GeV. The WIMP-like benchmark corresponds to  $g = 0.11$ ,  $v = 107$  MeV, and  $f = 535$  GeV. The maximum pion mass for  $\lambda = \lambda' = 1$  and  $\lambda = \lambda' = 4\pi$  are related to  $\mu$  by (2.31) and the upper bound in (2.39).

to avoid these bounds. This assumption, in turn, implies that dark matter self-scatters are purely repulsive and avoid resonances.

In this manuscript, we focus on benchmark models of symmetric vector self-interacting dark matter with both attractive and repulsive interactions. We plot the velocity-dependence of the self-interaction cross section,  $\langle\sigma v\rangle$ , in Fig. 2.5. This reproduces the data from Fig. 1 of Ref. [200] overlaid with curves based on our model. The methodology for producing these cross section curves is based on Ref. [293]; we present a self-contained summary in Appendix B.6. The two benchmark parameters models are presented here with parameters in Table 2.1:

1. **The solid/**red** curve is an estimated fit to the inferred self-interaction cross sections for the astrophysical systems.** The dark matter mass  $m_W$  is chosen to be 60 MeV in order to satisfy constraints on cluster scales [200, 187]. The coupling is then fixed by (2.55). This model fits the SIDM targets and is able to explain the dark matter abundance from thermal freeze out.
2. **The dash-dotted/**green** curve is a model constrained to the observed dark**



**matter relic density for a weak scale mass.** The coupling and dark matter mass are three orders of magnitude stronger than that of the SIDM fit. This case is a reasonable fit for the inferred SIDM cross sections from dwarfs and low surface brightness spiral galaxies, but falls orders of magnitude short of the inferred cross section from galaxy cluster profiles.

In addition to these two benchmark models, we present two illustrative curves to highlight important physics:

3. **The dotted/blue curve shows a fit assuming only a repulsive potential.** This model reproduces the best fit curve from Ref. [200] with the same model parameters. The spin of the dark matter candidate makes no appreciable difference since the long-range self-interaction potential is identical. However, since we consider symmetric dark matter, the assumption of a purely repulsive potential is unphysical.
4. **The dashed/yellow curve shows the same model parameters as the dotted/blue curve, but with both attractive and repulsive interactions.** If one simply turns on the attractive contribution to the dotted/blue curve, one can see the effect of resonances. The cross section increases rapidly for low velocities and is a poor fit for the data. Comparing to the dash-dotted/green curve, we see that a modest shift in the model parameters is sufficient to move off of the resonance.

## 2.8 Portal Interactions

We discuss renormalizable portal interactions between the dark sector and the Standard Model. In this context, our convention of naming particles by their Standard

Description	DARK SECTOR		STANDARD MODEL	
	Symbol	Name	Symbol	Name
Charged SU(2) gauge boson	$W^\pm$	dark matter	$\mathcal{W}^\pm$	$W$ -boson
Light neutral gauge boson	$A$	dark photon	$\mathcal{A}$	photon
Heavy neutral gauge boson			$\mathcal{Z}$	$Z$ -boson
Light radial (Higgs) mode	$H_1$	dark Higgs	$\mathfrak{h}$	Higgs boson
Heavy radial (Higgs) mode	$H_2$	heavy Higgs		
Charged pseudo-Goldstone	$\pi^\pm$	dark pion	$\Pi^\pm$	charged pion
Neutral pseudo-Goldstone			$\Pi^0$	neutral pion

Table 2.2: Conventions for dark sector and visible sector mass eigenstates.

Model analogs can be ambiguous. For consistency and clarity, we write the visible sector fields in script font; see Table 2.2.

The dark sector doublet  $H$  and triplet  $\Phi$  may have renormalizable interactions with the Standard Model Higgs  $\mathcal{H}$  through mixed quartics:

$$\mathcal{L} \supset \lambda_{H\mathcal{H}} |H|^2 |\mathcal{H}|^2 + \lambda_{\Phi\mathcal{H}} (\text{Tr } \Phi^2) |\mathcal{H}|^2 . \quad (2.63)$$

This leads to Higgs portal interactions of the type described in [21]<sup>5</sup>. In this manuscript we instead focus on the limit where the Higgs portal interactions are negligible<sup>6</sup> compared to the dimension-5 operator,

$$\mathcal{L} \supset \frac{2}{\Lambda} (\Phi^a F_{\mu\nu}^a) \mathcal{B}^{\mu\nu} , \quad (2.64)$$

where  $\mathcal{B}^{\mu\nu}$  is the Standard Model hypercharge field strength and  $\Lambda$  encodes the combination of couplings and a UV scale at which this term is generated by additional dynamics, for example heavy particles running in a loop. The vev  $\langle \Phi \rangle = f T^a$  induces a kinetic mixing

<sup>5</sup>Our scenario differs slightly in that the low-mass dark Higgs is a mixture that is mostly composed of the radial mode of a doublet rather than a triplet.

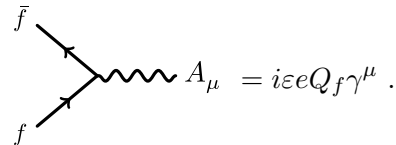
<sup>6</sup>In the limit where this interaction is taken to be zero, the  $H_1$  to  $AA$  is at loop level.

between the dark photon and the visible photon [74]:

$$\mathcal{L} \supset \frac{\varepsilon}{2 \cos \theta_W} F_{\mu\nu} \mathcal{B}^{\mu\nu} \rightarrow \frac{\varepsilon}{2} F_{\mu\nu} \mathcal{F}^{\mu\nu} , \quad (2.65)$$

where  $\mathcal{F}_{\mu\nu}$  is the visible sector photon field strength. We have omitted a mixing term with the  $Z$ -boson field strength which exists in principle but is negligible in the limit where the dark photon is much lighter than the electroweak scale,  $m_A \ll m_Z$ ; we refer to [191] or the appendix of [132] for a detailed derivation. We ignore the limit where additional symmetry breaking leads to dark  $Z$  phenomenology [97]. By focusing on this kinetic mixing scenario [183, 152, 213], we study the hitherto unexplored case of vector dark matter interacting through a low-mass vector mediator.

The dark photons in our scenario are identical to the standard set up in how they interact with visible sector fields and, thus, how experiments may search for them [31, 10]. The effective Feynman rule to fermions  $f$  with electric charge  $Q_f$ , for example, is



$$= i \varepsilon e Q_f \gamma^\mu . \quad (2.66)$$

We thus refer to recent reviews to summarize those bounds [31, 10]. It is sufficient to note that for the range of dark photon masses of interest there is always a sufficiently small  $\varepsilon$  (large  $\Lambda$ ) such that the basic phenomenology is valid. In the small mixing limit, mediators are very long lived and may be targets for recently proposed indirect detection techniques [270, 279, 210, 162]

To demonstrate the phenomenology of kinetic mixing, we examine the bounds on our scenario coming from direct detection experiments. The  $W$ -nucleon ( $N$ ) scattering

amplitude,  $i\mathcal{M}_N$ , is

$$= \frac{g\varepsilon e Q_N}{q^2 - m_A^2} \varepsilon_\mu(p) \varepsilon_\nu^*(p') \bar{u}(k') [g^{\mu\nu} (\not{p} + \not{p}') - 2p'^\mu \gamma^\nu - 2p^\nu \gamma^\mu] u(k) ,$$

(2.67)

where we recall that here  $g$  is the dark sector gauge coupling in (2.41–2.42). This interaction maps simply to the non-relativistic  $\mathcal{O}_1^{(\text{NR})}$  (spin-independent) operator [127, 140, 78, 102, 66, 67]. In the notation of Refs. [102, 67], the interactions (2.41) and (2.66) map onto effective couplings  $b_5 = g$  and  $h_3 = \varepsilon e Q_q$  so that the non-relativistic effective coupling to nucleons is

$$c_1^N \equiv -\frac{b_5 h_3^N}{m_A^2} \quad \text{from which we define} \quad c_p \equiv |c_1^N| = \frac{\varepsilon e g}{m_A^2} . \quad (2.68)$$

We have used the fact that the dark photon coupling to nucleons,  $h^N$ , is proportional to the sum of the valence charges of the quarks due to the conservation of the electric current.

We compare the effective coupling  $c_p$  to the most stringent bounds on spin-independent dark matter–nucleon scattering: XENON 1T [13] and DarkSide 50 [5]. The results are presented in Fig. 2.6. For a given mediator mass  $m_A$  and dark gauge coupling  $g$ , this sets an effective bound on the size of the kinetic mixing parameter  $\varepsilon$  or, alternatively, the effective scale  $\Lambda$  of the dimension-5 operator, (2.64). For very small values of  $\varepsilon$  one may realize unique thermal histories that are beyond the scope of this study [77, 39, 218, 122, 115]. We remark that in the event of a discovery of dark matter scattering at direct detection experiments, Refs. [102, 67] show that vector dark matter interacting through a vector mediator may be disentangled from other candidate models through its recoil spectrum.

## 2.9 Conclusions

This manuscript presents the first model of a stable, vector dark matter with a low-mass vector mediator. We present a full theory with the required scalar sector to enact the necessary symmetry breaking pattern and explain the stabilization mechanism from symmetry principles. This model can be understood as the Higgsed phase of a Yang–Mills hidden sector, in contrast to the confined glueball-dark matter phase explored in Refs. [40, 41]. We present the basic phenomenology assuming that the dark matter abundance is produced by thermal freeze out. We present benchmark parameters for self-interacting dark matter solutions to small scale astrophysical anomalies where we observe a slight tension between the parameters required for a thermal relic and those that can fit the inferred self-interaction cross section across a range of systems from dwarfs to clusters. We leave detailed self-interacting dark matter fits for small scale structure anomalies to future work as this is likely to require additional model building to navigate cosmological bounds and abundance [187]. We also present bounds from direct detection assuming that the vector mediator is the primary portal to the Standard Model, in contrast to similar theories of vector dark matter that assumed a Higgs portal.

Our model is a minimal framework for a spin-1 dark sector that can be mapped on to standard dark sector phenomenology. This model offers many directions for further exploration. Within the perturbative regime of this theory, we identified possibilities for producing the dark matter abundance beyond the thermal freeze out assumption. This connects to recent and ongoing work on the phase space of dark sectors which thermalize through a portal interaction [133, 77, 39, 218, 122, 115]. Depending on the production

mechanism, dark matter may be symmetric or asymmetric, which in turn feeds into the self-interaction phenomenology by affecting the possibility of self-interaction resonances. The model contains an additional light mediator ( $H_1$ ) and an additional charged particle ( $\pi^\pm$ ) that we assumed to be negligible in this work. One can imagine an interplay of the two mediators for  $t$ -channel processes such as self-interactions or direct detection, or alternatively inelasticity coming from a small splitting between the  $\pi^\pm$  and  $W^\pm$ . One may alternatively push  $m_W > m_\pi$  so that the stable dark matter candidates are charged scalars with derivative interactions to a dark photon. Finally, we remark that in the non-perturbative regime the model also furnishes dark sector 't Hooft–Polyakov monopoles [21, 208]. Our model simply realizes the regime where the Abelian force associated with the monopoles is Higgsed, therefore the monopoles are expected to confine. This, in turn, may new dynamics relevant for the dark sector [289, 288].

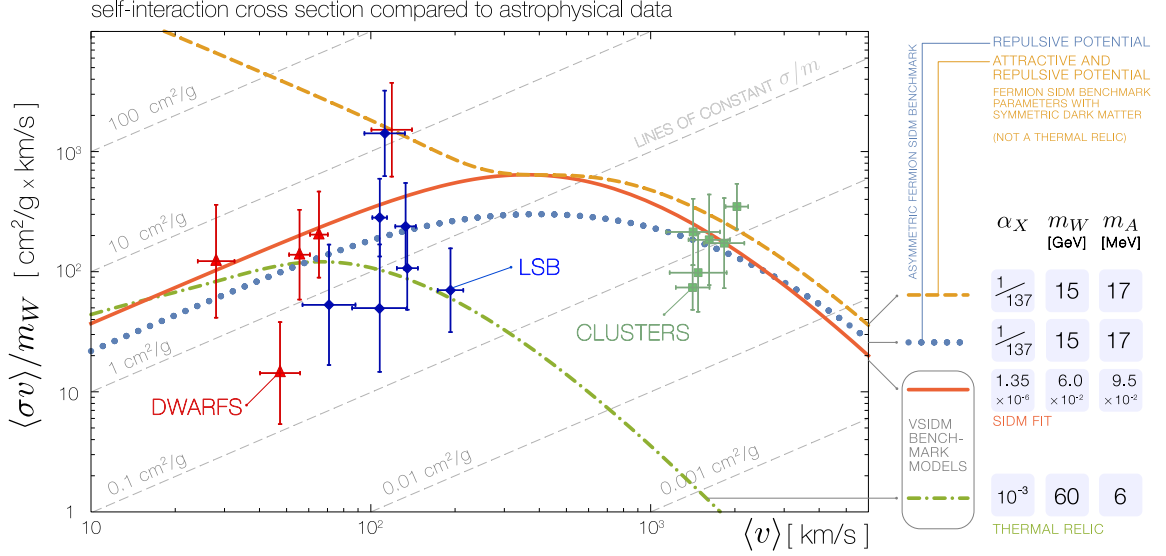


Figure 2.5: Self-interaction cross section as a function of average velocity in our model compared to inferred cross sections for a set of dwarf galaxies, low surface brightness (LSB) spiral galaxies, and galaxy clusters from Ref. [200]. **Benchmark models:** the solid/red curve are a fit to the inferred cross sections from astrophysical data. The  $W^\pm$  are required to have a sub-GeV mass in order to agree with the cluster scale observations [187]. The dash-dotted/green curve corresponds to a fit to the low-velocity data points while maintaining a GeV scale mass. Both benchmark models are subject to the requirement that  $\alpha_X$  is large enough for the  $W^\pm$  to saturate the dark matter relic abundance; see Fig. 2.2. **Illustrative unphysical examples:** the dotted/blue line assumes a *purely repulsive potential* and reproduces the best fit curve from Ref. [200] using the same model parameters. The dashed/yellow line corresponds to the same model parameters but including both attractive and repulsive potentials.

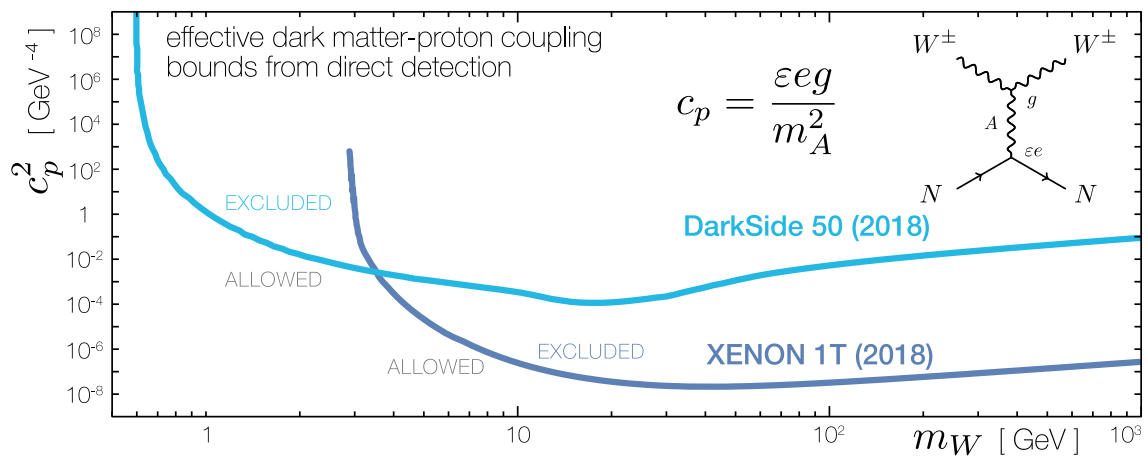


Figure 2.6: Constraints on the effective dark matter–proton coupling,  $c_p^2$ , from direct detection experiments XENON 1T [13] and DarkSide 50 [5].



## Chapter 3

# Vector Portal Pseudo-Goldstone Dark Matter

### 3.1 Introduction

The search for the microscopic description of dark matter is a highly active area of research, situated at the crossroads of particle physics and cosmology. While a massive non-luminous particle is required to resolve the large scale structure of the universe, many of dark matter’s properties remain unknown [2, 3]. A fermionic weakly interacting massive particle (WIMP) has long been a leading candidate for dark matter. As experimental constraints tighten [286, 8, 9, 6, 185, 1, 35, 79], dark matter candidates beyond the WIMP paradigm are considered. One such alternative is to consider additional states beyond the dark matter itself, referred to as a “dark” or “hidden” sector [255, 256, 257, 121, 10, 31]. Typically, a dark sector consists of a stable dark matter candidate, as well as one or more

states that mediate interactions with the visible sector. Often these additional particles are low mass relative to the dark matter. A common framework is the so-called dark photon model where the mediator is a light spin-1 boson. This dark photon may be observable at current and upcoming experiments [121, 10, 31]. Such dark sectors with light mediators automatically admit long-range, velocity-dependent interactions that may resolve several small-scale structure anomalies [292].

Spin-0 particles have long been considered as a dark matter candidate. Models of spin-0 dark matter which couple directly to the Standard Model through a Higgs [278, 239, 51, 81, 233, 184] or  $Z$ -boson portal [120] have been studied extensively. Dark sector models consisting of spin-0 dark matter and a vector [52, 42] or scalar [24] mediator have been considered. The case of pseudo-Goldstone boson dark matter (PGBDM) offers an interesting alternative to these well understood theories. Previously, PGBDM has been studied in the context of composite Higgs models [147]. However in contrast a massive pseudo-Goldstone boson (pGB) from a softly broken  $U(1)$  symmetry has a vanishing direct detection cross section at zero momentum transfer when scattering off nuclei through a Higgs portal interaction [166, 80], circumventing experimental constraints from direct detection experiments. The dark matter in such models remains stable due to a  $\mathbb{Z}_2$  symmetry. These properties have been shown to hold for the fundamental representation of  $SU(N)$  [203], and have been studied in the context of  $B - L$  extensions of the Standard Model [249].

In this manuscript, we consider PGBDM resulting from the spontaneous breaking of a global symmetry group  $SU(2) \times SU(2) \rightarrow SU(2)$ . This symmetry breaking pattern is analogous to chiral symmetry breaking of the flavor symmetry group in which  $SU(2)_L \times$

$SU(2)_R = SU(2)_V \times SU(2)_A$  is broken to the vector subgroup. Here we consider two scalar fields in the fundamental and adjoint representations of a dark sector  $SU(2)$  which, when charged under the vector subgroup, explicitly breaks the axial symmetry. The unbroken  $SU(2)$  subgroup is gauged and spontaneously broken in two steps. First,  $SU(2) \rightarrow U(1)$  at a scale  $f$ . And second,  $U(1) \rightarrow \emptyset$  at a scale  $v \ll f$ . The symmetry structure permits a residual global  $U(1)$  which stabilizes the dark matter, preventing its decay into massless states. The model detailed in this manuscript may also be understood as a phase of the model we present in Ref. [69]. In that work, we developed the first model of spin-1 dark matter with a massive spin-1 mediator which originates from a non-abelian gauge sector. Small explicit breaking terms give a mass to the pseudo-Goldstone states which respect the residual  $U(1)$  and remain in the spectrum. We consider the phase of the theory in which these pseudo-Goldstones are the lightest particles in the spectrum which respect the residual  $U(1)$ . The resulting spectrum consists of two heavy gauge bosons with mass on the scale  $f$ , a dark photon with mass on the scale  $v$ , the two radial modes responsible for SSB, and the two pGB's we consider as dark matter candidates. Unlike previous models of PGBDM, the global symmetry in this model is not softly broken and thus the direct detection cross section resulting from a Higgs portal interaction does not vanish at zero momentum transfer. Instead, we consider the novel case in which the PGBDM interacts with the Standard Model via the dark photon, which couples to the Standard Model hypercharge gauge bosons through kinetic mixing [183, 151]. This scenario is analogous to charged pion dark matter. While PGBDM which couples to the Standard Model through the Higgs portal has been well studied, the case where PGBDM couples to the Standard Model via a spin-

1 mediator charged under an approximate U(1) symmetry has been relatively unexplored. Previous work has considered models of PGBDM in which the dark sector symmetry group is a mirror of the QCD [291] or Standard Model [173, 174] symmetry groups. In the former scenario, resonant scattering between dark matter particles may resolve small-scale structure anomalies as well. In this work we consider a symmetry structure unique from the Standard Model gauge group.

### 3.2 Symmetry Structure

The scalar sector of our theory consists of an SU(2) doublet  $H^i$  and a triplet  $\Phi = \phi_a T^a$  where  $T^a = \sigma^a/2$  are the generators of SU(2) and  $\sigma^a$  are the Pauli matrices. In the limit of no interactions, the full symmetry group of the dark sector is

$$\text{SU}(2)_\Phi \times \text{SU}(2)_H \times \text{U}(1)_H = \text{SU}(2)_V \times \text{SU}(2)_A \times \text{U}(1)_H \quad (3.1)$$

with the field transformations for the dark sector given by

$$\text{SU}(2)_\Phi : \Phi \rightarrow U_\Phi \Phi U_\Phi^\dagger \quad \text{SU}(2)_H : H \rightarrow U_H H \quad \text{U}(1)_H : H \rightarrow e^{i\theta_H} H \quad (3.2)$$

where  $U_{\Phi,H} = \exp\left(i\alpha_{\Phi,H}^a T^a\right)$  is a  $2 \times 2$  special unitary matrix. By analogy to chiral symmetry breaking, we have expressed the full symmetry group in terms of its so called vector and axial subgroups. The vector subgroup corresponds to the transformations where  $U_\Phi = U_H$  while the axial subgroup corresponds to the transformations where  $U_\Phi = U_H^\dagger$ . We gauge the vector subgroup  $\text{SU}(2)_V$ , explicitly breaking  $\text{SU}(2)_A$ . The global  $\text{U}(1)_H$  symmetry corresponds to an accidental ‘‘Higgs number’’ symmetry and behaves similar to Standard Model hypercharge.

### 3.2.1 Lagrangian and Symmetry Breaking Potential

The most general, renormalizable Lagrangian which respects  $SU(2)_V \times U(1)_H$  is:

$$\mathcal{L} = -\frac{1}{4}F_{\mu\nu}^a F^{a\mu\nu} + |DH|^2 + \text{Tr} |\mathcal{D}\Phi|^2 - V(H, \Phi) \quad (3.3)$$

where  $D$  and  $\mathcal{D}$  are the covariant derivatives for  $SU(2)$  in the fundamental and adjoint representations respectively. The potential  $V(H, \Phi)$  is responsible for spontaneously breaking  $SU(2)_V \times U(1)_H \rightarrow U(1)_{H'}$  as well as explicitly breaking  $SU(2)_A$ . The most general renormalizable potential invariant under  $SU(2)_V \times U(1)_H$  can be written in the form

$$V = \frac{\lambda}{4!} (2 \text{Tr} \Phi^2 - f_0^2)^2 + \frac{\lambda'}{4!} (2|H|^2 - v_0^2)^2 + \mu H^\dagger \Phi H + \lambda'' |H|^2 \text{Tr} \Phi^2. \quad (3.4)$$

The first term spontaneously breaks  $SU(2)_\Phi \rightarrow U(1)_\Phi$ , the second term spontaneously breaks  $SU(2)_H \rightarrow \emptyset$ , and the trilinear term explicitly breaks  $SU(2)_A$ . The quartic term proportional to  $\lambda''$  introduces mixing between the doublet and the triplet. Additional quartic terms can all be reduced to the term proportional to  $\lambda''$ . We neglect terms involving the pseudo-conjugate field  $\tilde{H}^i \equiv \epsilon^{ij} H_j^\dagger$ , as they violate the  $U(1)_H$  symmetry which we assume is respected by the Lagrangian. In the following sections we study the symmetry breaking pattern induced by the vacuum expectation values of the scalar fields  $H$  and  $\Phi$ .

### 3.2.2 Spontaneous Symmetry Breaking

We assume the vacuum expectation values (vevs)

$$\langle \Phi \rangle = fT^3 \qquad \langle H \rangle = \frac{1}{\sqrt{2}} \begin{pmatrix} 0 \\ v \end{pmatrix} \quad (3.5)$$

which break  $SU(2)_\Phi \rightarrow U(1)_\Phi$  and  $SU(2)_H \rightarrow \emptyset$  respectively. All three generators of  $SU(2)_H$  are broken by  $\langle H \rangle$  while the  $SU(2)_\Phi$  generator parallel to  $\langle \Phi \rangle$  remains unbroken. The resulting spectrum of states consists of two massive radial modes and five massless Goldstone bosons: two corresponding to the broken generators of  $SU(2)_\Phi$  and three to the broken generators of  $SU(2)_H$ .

While the  $U(1)_H$  symmetry is spontaneously broken by (3.5), the linear combination

$$T_{H'} = T^3 + \frac{1}{2}T_H, \quad (3.6)$$

where  $T_H$  is the generator of  $U(1)_H$ , remains unbroken. In this representation  $T_H = \mathbb{K}_{2 \times 2}$ . We denote the symmetry generated by  $T_{H'}$  as  $U(1)_{H'}$ . While only the vector subgroup,  $U(1)_V$ , spontaneously broken by  $\langle H \rangle$  is gauged, the associated dark photon's interactions respect  $U(1)_{H'}$  as well. We therefore identify the global charge of a dark sector state with respect to this symmetry. This residual symmetry ensures the stability of the lightest charged state.

### 3.2.3 Explicit Symmetry Breaking

By explicitly breaking the global symmetry group, we can remove all of the massless degrees of freedom from the theory. Our dark sector is constructed to contain two sources of explicit global symmetry breaking:

1. Gauge bosons from the explicit gauging of the subgroup  $SU(2)_V$ .
2. Trilinear mixing between the fundamental scalar  $H$  and adjoint scalar  $\Phi$ .

Gauging  $SU(2)_V$  explicitly breaks  $SU(2)_A$  since the covariant derivatives are constructed to only respect the symmetry of the gauged subgroup. As a result three massless Goldstone modes are eaten by vector bosons, becoming their longitudinal components. The remaining two degrees of freedom become pseudo-Goldstone bosons (pGB) associated with  $SU(2)_A$ . In the absence of explicit symmetry breaking terms in the potential the pGBs are massless at tree level. By introducing a trilinear mixing between  $H$  and  $\Phi$  the pGBs pick up a finite mass proportional to the root of the order of parameter responsible for the explicit breaking  $\mu$ . We can see such a term should be allowed by considering a product of irreducible representations of  $SU(2)$ :

$$\mathbf{2} \otimes \bar{\mathbf{2}} \otimes \mathbf{3} = \mathbf{5} \oplus \mathbf{3} \oplus \mathbf{3} \oplus \mathbf{1}, \quad (3.7)$$

noting that the singlet corresponds to the operator  $H^\dagger \Phi H$ . From (3.2) we can see this operator is clearly invariant under transformations where  $U_H = U_\Phi$ , corresponding to an  $SU(2)_V$  singlet. Since  $SU(2)_A$  is not a proper subgroup of  $SU(2)_\Phi \times SU(2)_H$ , operators of this form which break  $SU(2)_\Phi \times SU(2)_H$  may only be singlets under  $SU(2)_V$  or break the symmetry completely. By removing the massless degrees of freedom we have ensured the lightest stable particle in our dark sector is indeed massive, and thus a viable dark matter candidate.

### 3.2.4 Particle Spectrum

Our theory yields a rich spectrum of states. After symmetry breaking, the remaining degrees of freedom consist of three massive gauge bosons, the two scalar radial modes,

and two massive pGB. We take the limit where

$$\langle \text{Tr } \Phi^2 \rangle = \frac{f^2}{2} \quad \gg \quad \langle |H|^2 \rangle = \frac{v^2}{2} \quad (3.8)$$

setting the mass scale of the gauge boson associated with the broken  $U(1)_V$  subgroup much lower than the gauge bosons corresponding to the other two broken generators. Requiring the mediator to be light and remaining gauge bosons to be heavier than the pGBs amounts to the tuning of a dimensionful renormalizable parameter. The resulting particle content can be summarized as follows:

1. **Dark Matter:** Pseudo-Goldstone bosons  $\pi^\pm$  with mass  $\sim \sqrt{\mu}f$ .
2. **Mediators:** Dark photon  $A$  and light radial mode  $H_1$  with masses  $\sim gv$ , and  $\lambda'v$  respectively.
3. **Heavy modes:**  $W^\pm$  gauge bosons and radial mode  $H_2$  with masses  $\sim gf$  and  $\lambda f$  respectively.

Due to  $U(1)_{H'}$  being unbroken, the lightest charged state remains stable. Since both  $W^\pm$  and  $\pi^\pm$  are charged under  $U(1)_{H'}$ , we assume  $m_\pi < m_W + \min(m_1, m_A) \simeq m_W$ . The opposite case in which  $m_W < m_\pi + \min(m_1, m_A)$  has been studied in Ref. [69]. We label our fields, wherever possible, in analogy to those of the Standard Model in order to highlight their similar roles in the symmetry structure of our theory. We sketch the spectrum in Fig. 3.1.



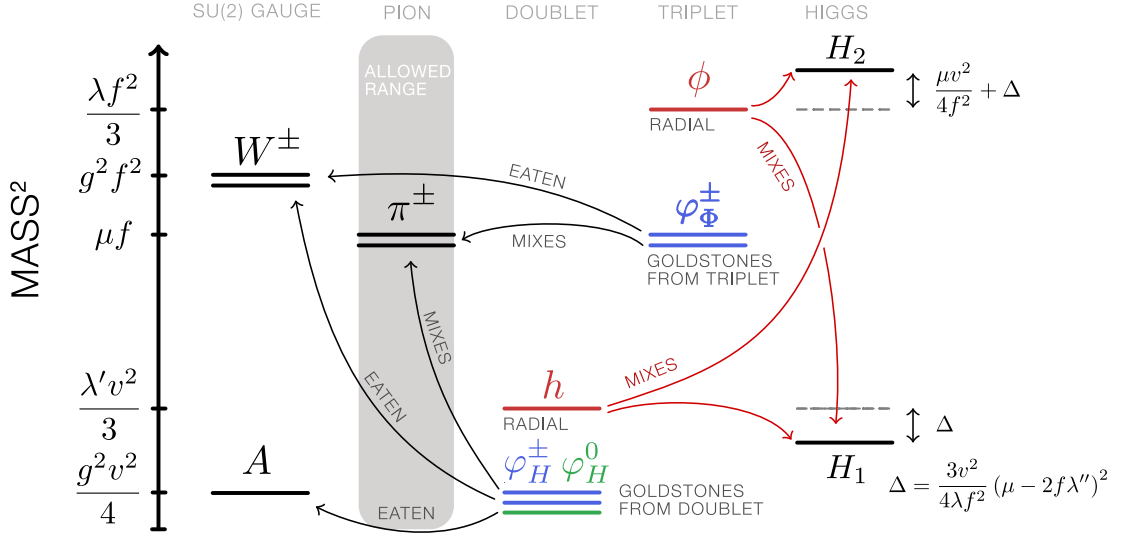


Figure 3.1: Model spectrum. Mass eigenstates are black lines, charged (neutral) Goldstones are blue (green) lines, radial Higgs modes are red lines. Mixing into mass eigenstates indicated by thin lines.

### 3.3 Particles and Mass Spectrum

Following the CCWZ construction [60] we parameterize the scalar fields as rotations of the radial modes by the broken generators

$$\Phi = e^{i\frac{\varphi_\Phi \cdot T}{f}} (\phi + f) T^3 e^{-i\frac{\varphi_\Phi \cdot T}{f}} \quad H = e^{i\frac{\varphi_H \cdot T}{v/2}} \begin{pmatrix} 0 \\ (h+v)/\sqrt{2} \end{pmatrix} \quad (3.9)$$

where we define the broken generators

$$\varphi_\Phi \cdot T = \frac{1}{\sqrt{2}} \varphi_\Phi^+ T^+ + \frac{1}{\sqrt{2}} \varphi_\Phi^- T^- \quad \varphi_H \cdot T = \frac{1}{\sqrt{2}} \varphi_H^+ T^+ + \frac{1}{\sqrt{2}} \varphi_H^- T^- + \varphi_H^0 T^3 \quad (3.10)$$

with  $T^\pm = T^1 \pm iT^2$ . The radial modes  $\phi$  and  $h$  have been expanded about their respective vevs  $f$  and  $v$ . While the scalar fields do mix with the Standard Model Higgs in principle, we consider this coupling to be negligible throughout this work.

### 3.3.1 Gauge Boson Masses

The covariant derivatives for the scalar fields are

$$D_\mu H = \partial_\mu H - igT^a A_\mu^a H \quad \mathcal{D}_\mu \Phi = \partial_\mu \Phi - igA_\mu^a [T^a, \Phi] \quad (3.11)$$

where  $g$  and  $A_\mu^a$  are the  $SU(2)_V$  coupling and gauge field respectively. Evaluating the kinetic terms in the Lagrangian at the vevs gives

$$\mathcal{L} \supset g^2 \left( f^2 + \frac{v^2}{4} \right) W_\mu^+ W_\mu^- + \frac{g^2}{8} v^2 A_\mu A^\mu \quad (3.12)$$

where we have defined the mass eigenstates

$$W^\pm = \frac{1}{\sqrt{2}} (A^1 \mp iA^2) \quad A = A^3 \quad (3.13)$$

such that they are labeled according to their  $U(1)_{H'}$  charges. The gauge boson masses follow directly from (3.12) to be

$$m_W^2 = g^2 \left( f^2 + \frac{v^2}{4} \right) \quad m_A^2 = \frac{g^2 v^2}{4}. \quad (3.14)$$

Even before we diagonalize the potential, the massive pseudo-Goldstone eigenstates can be identified from the kinetic terms of the Lagrangian:

$$|DH|^2 + \text{Tr} |\mathcal{D}\Phi|^2 \supset -g \left( \frac{v}{2} \partial \varphi_H^\pm + f \partial \varphi_\Phi^\pm \right) W^\mp + \text{h.c.} - g \frac{v}{2} \partial \varphi_H^0 A. \quad (3.15)$$

A linear combination of  $\varphi_H^\pm$  and  $\varphi_\Phi^\pm$  is eaten by  $W^\pm$  since both  $\langle \Phi \rangle$  and  $\langle H \rangle$  break  $SU(2)_V$  while  $\varphi_H^0$  is only eaten by  $A$  since the  $U(1)_V$  subgroup is only broken by  $\langle H \rangle$ . We define the eaten Goldstone  $\varphi_V$  and the orthogonal state  $\varphi_A$  as

$$\varphi_V^\pm = \frac{f\varphi_\Phi^\pm + (v/2)\varphi_H^\pm}{\sqrt{f^2 + (v/2)^2}} \quad \varphi_A^\pm = \frac{f\varphi_H^\pm - (v/2)\varphi_\Phi^\pm}{\sqrt{f^2 + (v/2)^2}}. \quad (3.16)$$

$\varphi_A$  is the would-be Goldstone of the spontaneously broken axial symmetry. The Goldstone mode  $\varphi_V^\pm$  is eaten by  $W^\pm$  contributing to its longitudinal polarization. When one ignores the trilinear term in (3.4), the  $\varphi_A^\pm$  is massless at tree level. However, due to the broken axial symmetry, loops of the gauge bosons induce a radiative mass.

### 3.3.2 vevs and Scalar Boson Masses

Minimizing the potential (3.4), we find the vevs to be

$$f^2 = f_0^2 + \frac{3v^2}{\lambda} \left( \frac{\mu}{2f} - \lambda'' \right) \quad v^2 = v_0^2 + \frac{3f^2}{\lambda'} \left( \frac{\mu}{f} - \lambda'' \right). \quad (3.17)$$

The radial modes  $h$  and  $\phi$  mix in this vacuum. In the basis  $\left( h, \phi \right)$ , their mass matrix is given by

$$\mathcal{M}_H^2 = \begin{pmatrix} \frac{\lambda'v^2}{3} & \lambda''vf - \frac{\mu v}{2} \\ \lambda''vf - \frac{\mu v}{2} & \frac{\lambda f^2}{3} + \frac{\mu v^2}{4f} \end{pmatrix}. \quad (3.18)$$

The eigenvalues of (3.18) are

$$m_{1,2}^2 = \frac{1}{2} \text{Tr} \mathcal{M}_H^2 \mp \left| \frac{(\mathcal{M}_H^2)_{12}}{\sin 2\alpha} \right| \quad (3.19)$$

where  $\alpha$  is the angle that parameterizes the orthogonal transformation  $\mathcal{O}_\alpha$  that diagonalizes (3.18). We define the transformation:

$$\begin{pmatrix} H_1 \\ H_2 \end{pmatrix} = \mathcal{O}_\alpha \begin{pmatrix} h \\ \phi \end{pmatrix} \quad \mathcal{O}_\alpha = \begin{pmatrix} \cos \alpha & \sin \alpha \\ -\sin \alpha & \cos \alpha \end{pmatrix} \quad (3.20)$$

where the mixing angle  $\alpha$  is related to the model parameters by

$$\tan 2\alpha = \frac{\mu v - 2\lambda''vf}{\lambda f^2/3 + \mu v^2/4f - \lambda'v^2/3}. \quad (3.21)$$

We can expand (3.19) in the limit  $v \ll f$  yielding the approximate eigenvalues

$$m_1^2 = \frac{\lambda' v^2}{3} - \frac{3v^2}{4\lambda f^2} (\mu - 2f\lambda'')^2 + \mathcal{O}\left(\frac{v^4}{f^4}\right) \quad (3.22)$$

$$m_2^2 = \frac{\lambda f^2}{3} + \frac{\mu v^2}{4f} + \frac{3v^2}{4\lambda f^2} (\mu - 2f\lambda'')^2 + \mathcal{O}\left(\frac{v^4}{f^4}\right) . \quad (3.23)$$

In this limit the masses of the radial modes form a hierarchy such that

$$m_1^2 \sim \lambda' v^2 \ll m_2^2 \sim \lambda f^2 . \quad (3.24)$$

The trilinear term in (3.4) causes the Goldstone modes to mix as well. As we did for the radial modes, we expand (3.4) about the vacuum. In the basis  $\left(\varphi_\Phi^\pm \quad \varphi_H^\pm\right)$  the Goldstone mass matrix is,

$$\mathcal{M}_G^2 = \begin{pmatrix} \frac{\mu v^2}{4f} & -\frac{\mu v}{2} \\ -\frac{\mu v}{2} & \mu f \end{pmatrix} . \quad (3.25)$$

It is easy to see that  $\text{Det } \mathcal{M}_G^2 = 0$ , implying the existence of a zero eigenvalue corresponding to the Goldstone eaten by  $W^\pm$ . The other eigenvalue of (3.25) is simply  $\text{Tr } \mathcal{M}_G^2$ . As we did for the radial modes, we diagonalize  $\mathcal{M}_G^2$  with the orthogonal transformation:

$$\begin{pmatrix} G^\pm \\ \pi^\pm \end{pmatrix} = \mathcal{O}_\beta \begin{pmatrix} \varphi_\Phi^\pm \\ \varphi_H^\pm \end{pmatrix} \quad \mathcal{O}_\beta = \begin{pmatrix} \cos \beta & \sin \beta \\ -\sin \beta & \cos \beta \end{pmatrix} \quad (3.26)$$

where  $\pi^\pm$  is a massive pGB and  $G^\pm$  is the massless Goldstone eaten by  $W^\pm$ . The masses of these states are

$$m_G^2 = 0 \quad m_\pi^2 = \mu f \left(1 + \frac{v^2}{4f^2}\right) . \quad (3.27)$$

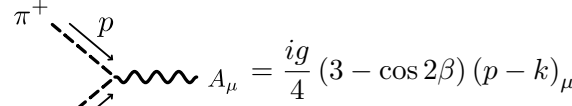
By requiring  $\mathcal{O}_\beta$  diagonalize (3.25), the mixing angle  $\beta$  is found to be

$$\tan \beta = \frac{v}{2f} . \quad (3.28)$$

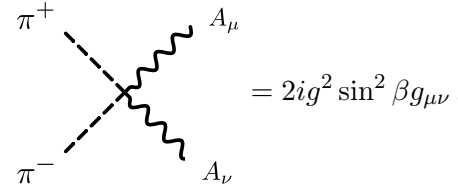
The mass eigenstates defined by (3.26) are identical to the vector and axial states given by (3.16), confirming that  $SU(2)_A$  is indeed broken by both the gauging of  $SU(2)_V$  as well as the trilinear term in (3.4). We identify  $\varphi_V^\pm = G^\pm$  and  $\varphi_A^\pm = \pi^\pm$ .

### 3.4 Feynman Rules for Dark Sector States

We outline the dark sector Feynman rules. Analogous to the interactions between the QCD pion and Standard Model photon, the dark matter interactions with the dark photon are

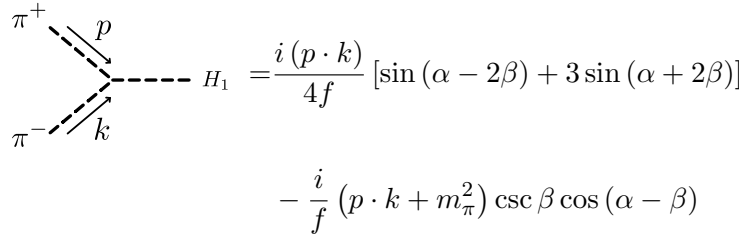


$$A_\mu = \frac{ig}{4} (3 - \cos 2\beta) (p - k)_\mu \quad (3.29)$$

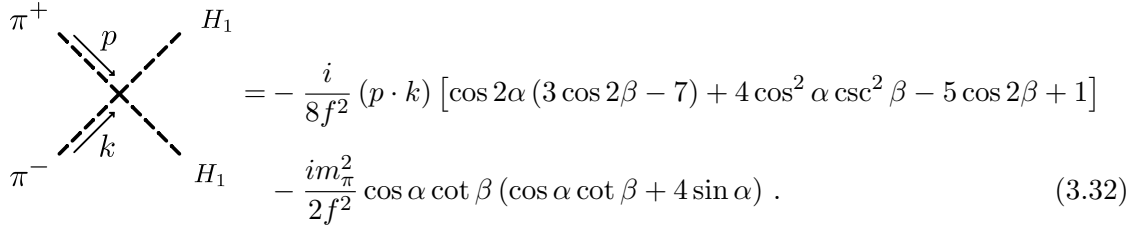


$$= 2ig^2 \sin^2 \beta g_{\mu\nu} . \quad (3.30)$$

The Feynman rules for the dark matter interactions with the light radial mode are

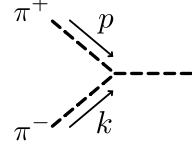


$$H_1 = \frac{i(p \cdot k)}{4f} [\sin(\alpha - 2\beta) + 3 \sin(\alpha + 2\beta)] - \frac{i}{f} (p \cdot k + m_\pi^2) \csc \beta \cos(\alpha - \beta) \quad (3.31)$$

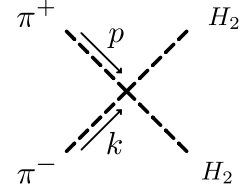


$$H_1 = -\frac{i}{8f^2} (p \cdot k) [\cos 2\alpha (3 \cos 2\beta - 7) + 4 \cos^2 \alpha \csc^2 \beta - 5 \cos 2\beta + 1] - \frac{im_\pi^2}{2f^2} \cos \alpha \cot \beta (\cos \alpha \cot \beta + 4 \sin \alpha) . \quad (3.32)$$

Similarly, the dark matter interactions with the heavy radial mode are

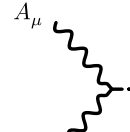


$$= \frac{i(p \cdot k)}{4f} [\cos(\alpha - 2\beta) + 3 \cos(\alpha + 2\beta)] + \frac{i}{f} (p \cdot k + m_\pi^2) \csc \beta \sin(\alpha - \beta) \quad (3.33)$$

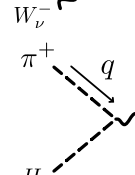


$$= -\frac{i \sin^2 \beta}{2f^2} (p \cdot k) (\sin^2 \alpha \cot^4 \beta + 4 \cos^2 \alpha) - \frac{i m_\pi^2}{2f^2} \sin \alpha \cot \beta (\sin \alpha \cot \beta - 4 \cos \alpha) . \quad (3.34)$$

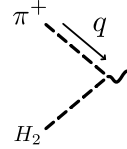
The unbroken  $U(1)_{H'}$  allows for the dark matter  $\pi^\pm$  to interact with a  $W^\pm$  of the opposite  $U(1)_{H'}$  charge and a dark photon or radial mode. The Feynman rules are



$$\pi^+ = \frac{g}{2} m_W \sin 2\beta g_{\mu\nu} \quad (3.35)$$



$$W_\nu^- = g q_\nu (2 \sin \alpha \sin \beta - \cos \alpha \cos \beta) \quad (3.36)$$



$$W_\nu^- = g q_\nu (\sin \alpha \cos \beta + 2 \cos \alpha \sin \beta) . \quad (3.37)$$

These interactions mediate the tree-level decay of the  $W^\pm$ .

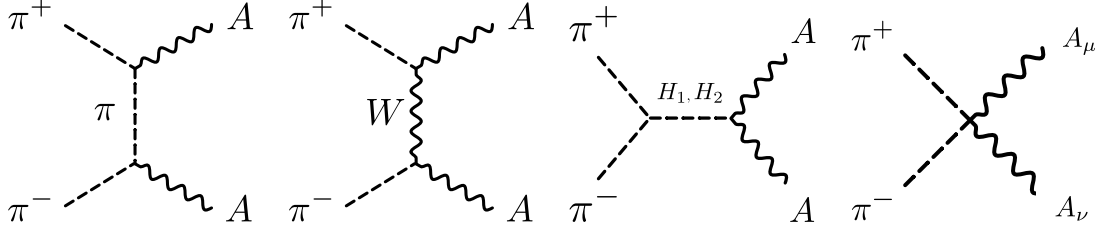


Figure 3.2: Diagrams contributing to  $\pi^+\pi^- \rightarrow AA$  annihilation. Not shown: crossed ( $u$ -channel) diagrams and annihilation to scalars.

### 3.5 Relic Abundance

Dark matter annihilation is dominated by  $s$ -wave processes in the low relative velocity limit. We consider the  $\pi^+\pi^- \rightarrow AA$ ,  $H_1H_1$ , and  $H_2H_2$  channels with all other possibilities being negligible at leading order in  $v/f$ . The diagrams contributing to the  $\pi^+\pi^- \rightarrow AA$  process are shown schematically in Fig. 3.2. To leading order in  $v/f$  the annihilation cross sections are:

$$\sigma v_{AA} = \sigma_0(m_A^2) \left[ \frac{1}{2} + \left( \frac{m_1^2}{4m_A^2} - \frac{m_\pi^2}{2m_W^2} \frac{m_\pi^2 + 5m_W^2}{m_\pi^2 + m_W^2} + X \right)^2 \right] \quad (3.38)$$

$$\sigma v_{H_1H_1} = \sigma_0(m_1^2) \left[ \frac{m_1^2}{2m_A^2} + \frac{m_\pi^2}{2m_W^2} + \frac{2m_\pi^2}{m_\pi^2 + m_W^2} - X \right]^2 \quad (3.39)$$

$$\sigma v_{H_2H_2} = \sigma_0(m_2^2) \left[ \frac{m_\pi^2}{4m_W^2} + \frac{YZ}{4m_W^2} - \frac{m_\pi^2}{m_W^2} Y^2 - \frac{m_\pi^4}{m_W^2} \frac{(3+Y)^2}{(m_2^2 - 4m_\pi^2)} + \frac{3m_2^2}{16m_W^2} \frac{(2m_\pi^2 - Z)}{(m_2^2 - 4m_\pi^2)} \right]^2 \quad (3.40)$$

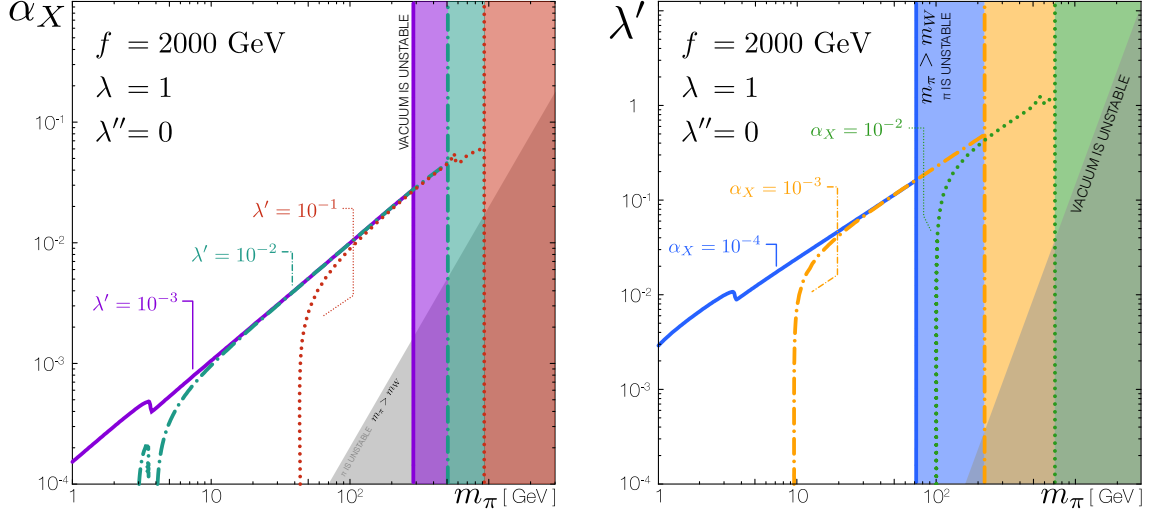


Figure 3.3: The  $\pi$  relic abundance as a function of the  $\pi$  mass and dark fine structure constant/dark Higgs doublet coupling (Left/Right). The solid (purple/blue), dash-dotted (teal/orange), and dotted (red/green) curves represent when the  $\pi$  saturate the dark matter relic abundance for  $\lambda' = 10^{-3}/\alpha_X = 10^{-4}$ ,  $10^{-2}/10^{-3}$ , and  $10^{-1}/10^{-2}$  respectively. The corresponding solid (purple/blue), dash-dotted (teal/orange), and dotted (red/green) vertical lines bound the regions in which the vacuum/ $\pi$  are unstable. The shaded triangular regions denote where the  $\pi$ /vacuum is unstable.

where we have defined the functions

$$\sigma_0(m^2) = \frac{\pi\alpha_X^2}{4m_\pi^2} \sqrt{1 - \frac{m^2}{m_\pi^2}} \quad (3.41)$$

$$X = \frac{m_\pi^2}{2m_W^2} \frac{m_\pi^2 - 2f^2\lambda''}{m_\pi^2 - 4m_\pi^2} \left[ 1 - \frac{2}{m_\pi^2} (m_\pi^2 - 2f^2\lambda'') \right] \quad (3.42)$$

$$Y = \left( 1 - \frac{m_\pi^2 - 2f^2\lambda''}{m_\pi^2} \right) \quad (3.43)$$

$$Z = (m_\pi^2 - 2f^2\lambda'') \quad (3.44)$$

as well as the dark fine structure constant

$$\alpha_X = \frac{g^2}{4\pi}. \quad (3.45)$$



We assume that the dark matter relic abundance is due to freeze-out in the early universe. The freeze-out temperature,  $x_f = m_\pi/T_f$ , and relic abundance,  $\Omega h^2$ , are [214]

$$x_f = \ln \left( 0.054 g_*^{-1/2} M_{Pl} m_\pi \langle \sigma v \rangle \right) - \frac{1}{2} \ln^2 \left( 0.054 g_*^{-1/2} M_{Pl} m_\pi \langle \sigma v \rangle \right) \quad (3.46)$$

$$\Omega h^2 = 2 \times 1.07 \times 10^9 \frac{x_f \text{ GeV}^{-1}}{\sqrt{g_*(x_f)} M_{Pl} \langle \sigma v \rangle} \quad (3.47)$$

where we have included an explicit factor of two in order to account for the fact that the dark matter may only annihilate with its anti-particle. The observed dark matter abundance is satisfied when  $\Omega h^2 = 0.12$  [287, 283].

Fig. 3.3 shows the values of  $\alpha_X$  (left) and  $\lambda'$  (right) which reproduce the observed relic abundance for a set of benchmark parameters. The curve indicating the observed relic abundance for a given  $\lambda'/\alpha_X$  (Left/Right) becomes vertical when terms in the annihilation cross section independent of  $\alpha_X/\lambda'$  (Left/Right) dominate. This imposes an effective lower bound on  $m_\pi$  for a given set of benchmark parameters.

In this scenario we have implicitly assumed that the dark photon,  $A$ , is in equilibrium with the Standard Model thermal bath. We thus require

$$\Gamma_A \geq H(x_f \cong 20) \quad (3.48)$$

where  $\Gamma_A$  is the dark photon decay width and  $H(x_f)$  is the Hubble rate evaluated at the freeze-out temperature. The resulting constraint on the kinetic mixing parameter  $\varepsilon$  in (3.55) is [257]:

$$\varepsilon^2 \left( \frac{m_A}{10 \text{ MeV}} \right) \gtrsim 10^{-11} \left( \frac{m_\pi}{50 \text{ GeV}} \right)^2. \quad (3.49)$$

This assumption is not strictly necessary for a viable model. One may consider the case in which the dark sector is completely secluded, forming a thermal bath separate from the

visible sector with a distinct initial temperature following reheating [133]. The thermal history of dark sectors with mediators has been studied more generally [77, 39, 36, 218, 122, 115]. Another possible scenario is that UV dynamics generate an asymmetry in the  $\pi$  abundance [197, 294]. These situations are beyond the scope of this work and we leave them for future study.

### 3.6 Self-Interactions

Our dark sector automatically yields self-interactions among the  $\pi$ . Dark matter self-interactions were initially identified as a feature of dark sectors [63] and later observed to affect density profiles of dwarf galaxies [280, 95]. More recently, several small-scale structure anomalies have been connected to dark sector models with self-interactions [130, 131, 48, 293]. For a detailed review of the full parameter space of dark matter self-interactions see Ref. [292].

The degree to which self-interactions affect dark matter halo densities depends on the scattering rate,  $\sigma v$  ( $\rho_{\text{DM}}/m_{\text{DM}}$ ). Because the dark matter relative velocity  $v$  and density  $\rho_{\text{DM}}$  are known for the astrophysical systems of interest, the relevant quantity is the ratio of the self-interaction cross section to the dark matter mass,  $\sigma/m_{\text{DM}}$ . Dwarf spheroidal galaxies with low relative velocities ( $v \sim 10$  km/s) suffer from small-scale structure anomalies which may be alleviated in the presence of self-interactions [293, 200, 95]. Galaxy clusters, on the other hand, typically have larger relative velocities ( $v \sim 1500$  km/s) and similarly suffer from small-scale structure anomalies which may also be alleviated by self-interactions. The benchmark values for the ratio of the dark matter self-interaction cross section to its mass

are

$$\left(\frac{\sigma}{m_{\text{DM}}}\right)_{\text{dwarf}} \sim 1 \frac{\text{cm}^2}{\text{g}} \quad \left(\frac{\sigma}{m_{\text{DM}}}\right)_{\text{cluster}} \sim 0.1 \frac{\text{cm}^2}{\text{g}}. \quad (3.50)$$

These seemingly inconsistent target cross sections may be achieved in tandem given the cross section has the appropriate velocity dependence.

The desired velocity dependence is achieved for non-relativistic scattering governed by a Yukawa potential. The dominant contribution to  $\pi^\pm$  self interactions results from the exchange of dark photons,  $A$ , and yields a non-relativistic long-range scattering potential

$$V(r) = \pm \frac{\alpha_\pi}{r} e^{-m_A r} \quad \alpha_\pi = \frac{\alpha_X}{4} \quad (3.51)$$

where the positive sign corresponds to particle-particle scattering and the negative sign to particle-antiparticle scattering. While the radial modes,  $H_1$  and  $H_2$ , also contribute to self-scattering, the  $\pi^+\pi^-H_1$  vertex, (3.31), is suppressed in the non-relativistic limit when  $v \ll f^1$ . Therefore we may ignore self-interactions mediated by  $H_1$ . On the other hand,  $m_2 \gg m_A$  implies  $H_2$  mediated self-interactions are sub-dominant compared to interactions mediated by the dark photon,  $A$ , due to the exponential suppression in (3.51) and may be ignored as well.

The benchmark model of SIDM consists of spin-1/2 dark matter with a mass  $\sim 15$  GeV and a spin-1 mediator of mass  $\sim 17$  MeV [200]. The self-interaction potential is assumed to be purely repulsive, implying an asymmetry in the dark matter abundance. Cosmological constraints on dark matter annihilation in early universe typically favor models

<sup>1</sup>Although the  $\csc\beta$  term in (3.31) diverges for  $v \ll f$ , for scattering  $p \cdot k = -m_\pi^2$  and the coefficient of the divergent term vanishes exactly.

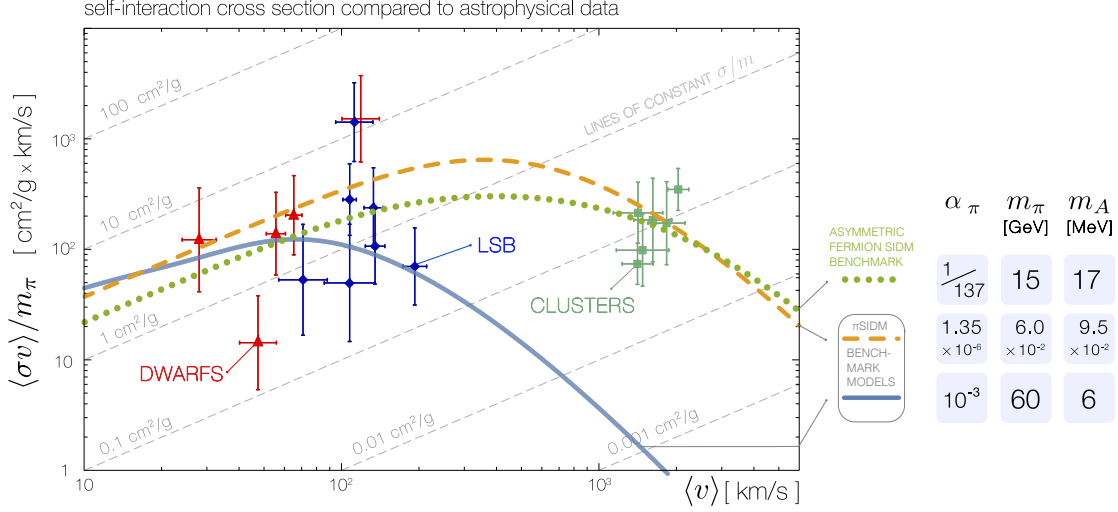


Figure 3.4: Numerical results for the dark matter self-interaction cross section in our model compared to cross sections for a set of dwarf galaxies, low surface brightness (LSB) spiral galaxies, and galaxy clusters from Ref. [200]. The solid/dashed (blue/orange) curves corresponding to benchmarks with symmetric relic abundances, are compared to the dotted (green) curve corresponding to the benchmark model from Ref. [200] with an asymmetric relic abundance. The benchmarks we present are identical to those found for spin-1 dark matter in Ref. [69] with the replacements  $m_W \rightarrow m_\pi$  and  $\alpha_X \rightarrow \alpha_\pi$ .

of asymmetric SIDM, constraining SIDM models with symmetric dark matter abundances to have sub-GeV scale masses [187]. These constraints may be relaxed if we consider cluster scale density profile observations to be satisfied by some other mechanism, allowing for heavier dark matter masses.

Figure 3.4 compares two symmetric benchmark models in the  $\pi$ SIDM framework to the asymmetric case studied in Ref. [200]. We numerically compute the self-interaction cross section following the methodology of Appendix B of Ref. [69], which is based on the procedure originally presented in Ref.[293]. The solid (blue) curve only satisfies dwarf scale observations and corresponds to dark matter with mass  $m_\pi = 60$  GeV, mediator mass  $m_A = 6$  MeV, and coupling  $\alpha_\pi = 10^{-3}$ . On the other hand, the dashed (orange) curve

simultaneously satisfies both dwarf and cluster scale targets, corresponding to dark matter with mass  $m_\pi = 60$  MeV, mediator mass  $m_A = 95$  keV, and coupling  $\alpha_\pi = 1.35 \times 10^{-6}$ . We compare these benchmarks to the dotted (green) curve which reproduces the model from Ref. [200] with  $m_\pi = 15$  GeV,  $m_A = 17$  MeV, and  $\alpha_\pi = 1/137$ . Because we consider contributions to the self-interaction cross section from both the repulsive and attractive potentials, our benchmarks are not necessarily unique due to the fact that an attractive potential displays resonant behavior [293]. In fact, these are the exact same benchmarks we present in Ref. [69] with  $m_W \rightarrow m_\pi$  and  $\alpha_X \rightarrow \alpha_\pi$ . In the standard freeze out scenario, our benchmark models may be fit to the observed relic abundance by tuning the parameters  $\lambda$ ,  $\lambda'$ , and  $f$ . Ultimately, the cause of dark matter halo density profile observations may be the result of contributions from baryonic feedback [49]. Therefore, we may interpret the data in Figure 3.4 as upper bounds on the self-interaction cross section.

### 3.7 Portal Interactions

We consider a renormalizable vector portal interaction between our dark sector to the visible sector. Generally, one may also consider a scalar portal where the dark scalars  $H$  and  $\Phi$  couple to the Standard Model scalar sector through quartic interactions

$$\mathcal{L} \supset \lambda_{H\mathcal{H}} |H|^2 |\mathcal{H}|^2 + \lambda_{\Phi\mathcal{H}} (\text{Tr } \Phi^2) |\mathcal{H}|^2 \quad (3.52)$$

where  $\mathcal{H}$  is the Standard Model Higgs doublet. Models of PGBDM which couple to the visible sector through a Higgs portal have been studied in Refs. [166, 80, 203, 249]. In these models, the direct detection signature vanishes at zero momentum transfer as a result

of a softly broken global symmetry.<sup>2</sup> Because the axial symmetry group of our model is explicitly broken by a term trilinear in the fields, the direct detection cross section does not contain this feature. We consider the limit where the scalar portal is negligible compared to the vector portal in which the  $SU(2)_V$  field strength  $F_{\mu\nu} = F_{\mu\nu}^a T^a$  and the adjoint triplet  $\Phi$  may couple to the Standard model hypercharge field strength  $\mathcal{B}^{\mu\nu}$  through the dimension-5 operator

$$\frac{2}{\Lambda} \text{Tr}(\Phi F_{\mu\nu}) \mathcal{B}^{\mu\nu} \quad (3.53)$$

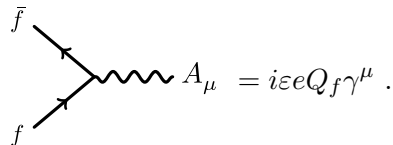
where  $\Lambda$  is the scale of the UV physics which generates this operator. The vev  $\langle \Phi \rangle = f T^3$  induces kinetic mixing between dark photon and visible Standard model photon,

$$\mathcal{L} \supset \frac{\varepsilon}{2 \cos \theta_W} F_{\mu\nu} \mathcal{B}^{\mu\nu} \rightarrow \frac{\varepsilon}{2} F_{\mu\nu} \mathcal{F}^{\mu\nu} , \quad (3.54)$$

where  $\mathcal{F}^{\mu\nu}$  is the visible photon field strength. We do not consider mixing with the Z-boson as its contributions are negligible when the dark photon mass is much below the scale of electroweak symmetry breaking,  $m_A \ll m_Z$ .

The kinetic mixing given by (3.54) induces a coupling between the dark photon and the Standard Model electromagnetic current. This is consistent with the standard dark photon scenario, and may present signatures at present and future experiments [10, 31].

The Feynman rule for the dark photon,  $A$ , and a fermion,  $f$ , with charge  $Q_f$  is



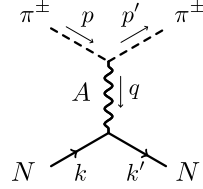
$$A_\mu = i \varepsilon e Q_f \gamma^\mu . \quad (3.55)$$

For bounds on the coupling  $\varepsilon$  we refer to the reviews [10, 31], as our set up is identical to the standard dark photon.

---

<sup>2</sup>In this context, softly broken refers to a symmetry group which is only broken by a mass term.

To demonstrate the bounds on  $\varepsilon$  from direct detection nucleon scattering experiments, we compute the scattering amplitude between dark matter,  $\pi$ , and a charged nucleon,  $N$ ,



$$= \pm \frac{i g \varepsilon e Q_N (3 - \cos 2\beta)}{q^2 - m_A^2} \bar{u}(k') (\not{p} + \not{p}') u(k), \quad (3.56)$$

which maps to a spin-independent operator  $\mathcal{O}_1^{(\text{NR})}$  in the non-relativistic limit [127, 140, 78, 102]. Matching the notation of Ref. [102], we identify

$$h_3 = \varepsilon e Q_q \quad \text{and} \quad g_4 = \frac{g}{4} (3 - \cos 2\beta). \quad (3.57)$$

We define the effective coupling

$$c_1^N = -2 \frac{g_4 h_3^N}{m_A^2} \quad \Longrightarrow \quad c_p \equiv |c_1^N| = \frac{\varepsilon e g}{2m_A^2} (3 - \cos 2\beta) \simeq \frac{\varepsilon e g}{m_A^2} \quad (3.58)$$

where we have assumed the limit  $\tan \beta = v/2f \ll 1$ . Due to the conservation of the electromagnetic charge, the effective coupling  $h_3^N$  for a nucleon,  $N$ , is simply proportional to the charge of the nucleon.

The effective coupling  $c_p$  is constrained by spin-independent dark matter-nucleon scattering from searches such as XENON 1T [13, 14] and DarkSide 50 [5]. We compare the bounds from these searches to the effective coupling  $c_p$  in Fig. 3.5. For a fixed mediator mass  $m_A$  and dark gauge coupling  $g$ , the spin-independent dark matter-nucleon cross section sets an upper bound on the kinetic mixing parameter,  $\varepsilon$ . While beyond the scope of this study, for values of  $\varepsilon$  so small that the dark sector is effectively decoupled from the visible sector,

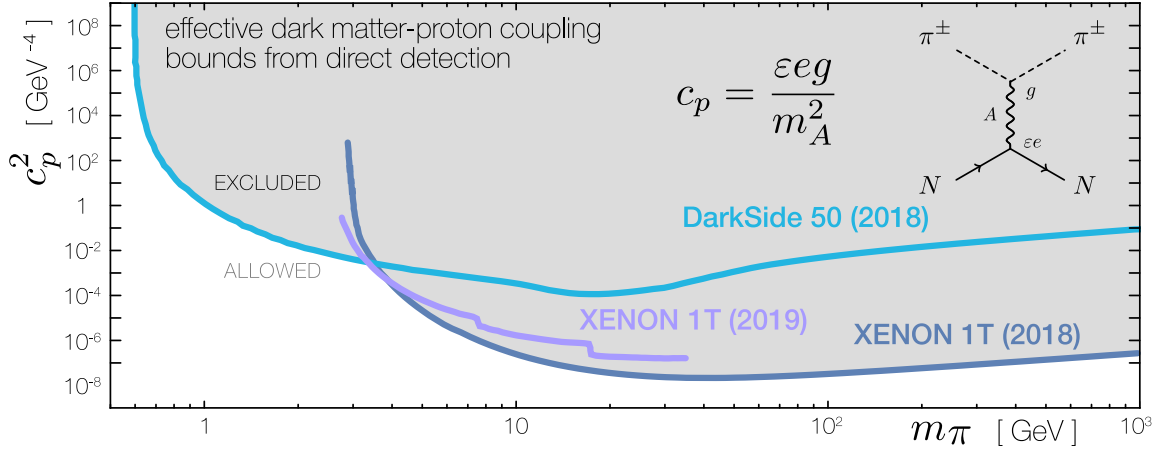


Figure 3.5: Constraints on the effective dark matter–proton coupling,  $c_p^2$ , from direct detection experiments XENON 1T [13, 14] and DarkSide 50 [5].

one may produce thermal histories distinct from the thermal freeze-out scenario [77, 39, 218, 122, 115].

### 3.8 Conclusion

We present a model of pseudo-Goldstone boson dark matter and dark photon mediator. The dark matter mass is finite due to the explicit breaking of the axial subgroup of an  $SU(2) \times SU(2)$  symmetry. Spontaneous symmetry breaking sets the scale of the dark matter and mediator masses, realizing a rich spectrum of states. A residual global  $U(1)$  stabilizes the pseudo-Goldstone states which are assumed to be lightest in the spectrum charged under this symmetry. We find that the pGB states may saturate the observed dark matter relic abundance in the standard thermal freeze-out scenario. For certain benchmark models some small-scale structure anomalies may be resolved by dark matter self-interactions, however the requirement that the dark matter be a thermal relic makes fitting the self-interaction



cross section to observations on dwarf galaxy and cluster scales simultaneously difficult. We leave a precise fit of the self-interaction cross section to observed small-scale structure anomalies for future work. We present direct detection bounds on our PGBDM which is assumed to primarily interact with the visible sector through a vector portal. In general a Higgs portal may be considered. However, such interactions introduce further mixing between the radial modes and thus are beyond the scope of this study.

The model presented in this work offers several avenues for further study. One may consider inelastic scattering off of nucleons, in which a  $\pi^\pm$  up-scatters off of a nucleon producing a  $W^\pm$ . This model may be understood as the phase of the model of spin-1 self-interacting dark matter we present in Ref. [69], where  $m_W > m_\pi$ . Thus, a natural extension of these scenarios is to consider multi-component dark matter in which the observed dark matter abundance consists of a combination of  $\pi^\pm$  and  $W^\pm$ . Such models describe inelastic dark matter which may admit novel phenomenology. Another exciting possibility is to restore the Higgs portal interaction with the visible sector. In this case the direct detection cross section is proportional to the order parameter of explicit symmetry breaking  $\mu$ , resulting in a dependence on the dark matter mass for the direct detection cross section distinct from the vector portal case.

## Chapter 4

# Continuum Mediated Self-Interacting Dark Matter

### 4.1 Introduction

A dark sector is a set of fields that include dark matter and low-mass particles that mediate interactions of the dark matter [255, 256, 257, 121, 10, 31]. If these mediators interact with the Standard Model, their signatures may appear in a suite of laboratory based experiments. Even if these Standard Model interactions are negligible, the mediators induce long-range potentials between dark matter particles that may be tested astronomically [63, 280]. This *self-interacting dark matter* framework has been spurred by the observation that it may address potential small-scale structure tensions between simulations of cold dark matter and astronomical observations [293, 292].

A single mediator typically produces a Yukawa potential between dark matter particles,  $V(r) \sim -e^{-m_\varphi r}/r$ , where  $m_\varphi$  is the mass of the mediator. This long-range behavior can be dramatically altered when the single-mediator exchange picture breaks down, for example when the mediator is represented by a continuum of states. Models of continuum dark sectors have existed for at least a decade in the form of conformal hidden sectors [158, 300] and closely related work on unparticle hidden sectors [285, 73, 145, 146]. The proposal that such models may lead to novel self-interactions was first identified in Ref. [45] for a spin-0 mediator modeled in the holographic description of a warped extra dimension.<sup>1</sup> This paper describes continuum-mediated self-interacting dark matter phenomenology in that benchmark theory. The dynamics of the model generate a long-range potential on the UV brane that scales as a non-integer power of separation,

$$V(r) \sim \frac{1}{r} \left( \frac{1}{\Lambda r} \right)^{\text{non-integer}}, \quad (4.1)$$

where  $\Lambda$  is a cutoff scale.

The long-range forces between dark matter particles allow energy exchange in dark matter halos and create a cored density profile compared to standard cold dark matter  $N$ -body simulations. Observations of small-scale structure anomalies in dwarf spheroidal galaxies are indicative of cored halo profiles and are thus a tantalizing possible signature for dark matter dynamics [293]. Alternative proposals to address these anomalies include

---

<sup>1</sup>In this work we use *continuum* to refer to the discrete set of Kaluza–Klein modes. This could be also referred to as a ‘discretuum,’ as opposed to the ‘continuous continuum’ regime in which the KK modes merge [84] Because a potential is generated by  $t$ -channel diagrams, the mediator field carries spacelike four-momentum. This makes it mostly insensitive to whether the spectral distribution is continuous or discrete and no distinction between these scenarios is necessary.

baryonic feedback on the dark matter halo. Future generations of  $N$ -body simulations may be able to ultimately distinguish between the two scenarios, and it is plausible that nature may even invoke a combination of the two mechanisms. We refer to Ref. [49] for a recent review of the status of these anomalies. A key result of our study is that continuum-mediated interactions leads to a non-integer velocity dependence on the dark matter self-scattering cross section, a quantity that relates the fundamental particle physics parameters of the dark sector to astronomical observations. Schematically,

$$\sigma(v) \sim v^{\text{non-integer}} . \quad (4.2)$$

We proceed as follows. In Section 4.2 we motivate a class of conformal models that generate non-integer potentials of the form (4.1) and specifically highlight a 5D dual picture with a mass gap. We give a precise definition of the gapped, continuum-mediated self-interacting dark matter model in Section 4.3. We discuss experimental constraints beyond self-interactions in Section 4.4; these constraints can be avoided for the types of parameters needed to address small scale structure puzzles in astronomy. The long-range potential is derived in Section 4.5 using spectral techniques. We present closed form expressions using asymptotic limits that we validate numerically. In Section 4.6 we evaluate the figure of merit for astronomical applications, the self scattering transfer cross section. In the so-called Born and classical regimes of dark matter coupling and velocity, we demonstrate novel scaling in the dark matter velocity compared to non-continuum self-interacting models. We confirm the presence of a resonant regime and analyze all regimes numerically. Continuum-mediated self-interactions can explain small-scale structure observations even when the slope of its potential differs significantly from a standard Yukawa potential. In Section 4.7 we show that

Sommerfeld enhancement produces a pattern of resonances that depend on the potential slope and mass gap. We conclude in Section 4.8. The Appendices include a streamlined review of AdS/CFT with a UV brane (Appendix B.1), a calculation of the approximate transfer cross section in the non-perturbative classical regime (Appendix B.4), a proof that there is no Sommerfeld enhancement for a  $1/r^2$  potential (Appendix B.5), and a review of the numerical method used to solve for the transfer cross section (Appendix B.6).

## 4.2 Preliminary Observations

The simplest assumption for dark matter self-interactions is that dark matter currents,  $J_{\text{DM}}$ , interact by exchanging spin-0 or spin-1 mediators at tree-level. In momentum space, the matrix elements take schematically the form

$$\begin{array}{c} \rightarrow \\ \text{---} \\ \rightarrow \end{array} \begin{array}{c} \rightarrow \\ \text{---} \\ \rightarrow \end{array} = J_{\text{DM}}(q) \frac{1}{q^2 - m^2} J_{\text{DM}}(-q). \quad (4.3)$$

The corresponding potential between dark matter currents in position space is Yukawa-like,  $V(r) \sim e^{-mr}/r$ , or Coulomb-like if  $m = 0$ . The mediator mass,  $m$ , cuts off the potential in the infrared and is important for realizing required low-velocity scaling of the dark matter self-scattering cross section for small scale structure anomalies.

The exchange of a single, non-derivatively coupled, weakly-interacting field in (4.3) is the simplest dark matter self-interaction. The resulting  $r^{-1}$  potential is the longest ranged potential allowed by the lower bound on the dimension of the exchanged operator set by unitarity,  $\Delta \geq 1$ . However, it is also plausible that the leading self-interaction is shorter range than  $1/r$  and thus there are a variety of possibilities that have yet to be thoroughly investigated. An extreme example is a zero-range interaction,  $J_{\text{DM}}(q)J_{\text{DM}}(-q)$ , which give

contact-interactions in position space,  $V(r) \sim \delta^{(3)}(r)$ . This possibility is too extreme: the contact interactions produce velocity-independent cross sections that are tightly constrained by the upper bound on dark matter self-scattering at high velocities from observations of galaxy cluster collisions like the Bullet Cluster.<sup>2</sup>

In this work we explore intermediate possibilities where the self-interaction potential has finite range that is shorter than the Yukawa/Coulomb limit. The simplest possibility amounts to a matrix element

$$\begin{array}{c} \text{---} \rightarrow \quad \rightarrow \text{---} \\ | \\ \text{---} \rightarrow \quad \rightarrow \text{---} \end{array} = J_{\text{DM}}(q) \frac{1}{(\sqrt{-q^2})^{4-2\Delta}} J_{\text{DM}}(-q). \quad (4.4)$$

The parameter  $\Delta$  satisfies  $\Delta \geq 1$ , where  $\Delta = 1$  recovers the Coulomb case. The position-space potential scales as  $V(r) \sim r^{-2\Delta+1}$  and becomes steeper near the origin for  $\Delta > 1$  such that the interaction has indeed shorter range than the Coulomb case. The interaction (4.4) is understood to come from the exchange of an operator of dimension  $\Delta$ . Highly non-integer dimensions do not occur in weakly-coupled theories since quantum corrections to the classical scaling dimension are perturbative. However, if the dark sector has strongly-interacting dynamics, then it is likely that the operators have highly non-integer dimension. We focus on a nearly-conformal mediator sector described by a conformal field theory (CFT); this sector may be a gauge theory with large 't Hooft coupling. Currents of elementary dark matter,  $J_{\text{DM}}$ , interact with CFT operators. Even though the mediator sector is strongly-interacting, conformal symmetry constrains the CFT correlation functions and provides a well-controlled framework for calculations. The CFT two-point function has a continuous spectral representation

---

<sup>2</sup>Other short range possibilities include tree-level exchange of a pseudoscalar (see e.g. [123]) and loop-level mediated processes [134, 85], which induce potentials going as  $\propto 1/r^n$  with  $n$  integer and  $\geq 3$ .

tation and so we refer to this scenario as *continuum-mediated self-interacting dark matter*. An analogous description of dark matter–nucleon scattering is used in Ref. [205].

A purely conformal hidden sector does not have a mass gap. This prevents an infrared cutoff that is usually set by the mediator mass. In order to restore the desired exponential damping at long distances, we assume an infrared (IR) mass gap in a slightly more evolved model that is most simply described holographically in five dimensional anti-de Sitter (AdS) space. In this scenario, a 5D field  $\Phi$  propagates in the bulk and interacts with the brane-localized dark matter currents,  $J_{\text{DM}}$ .

The AdS dual of the ungapped amplitude (4.4) is schematically:

$$\text{Diagram (4.5)} \tag{4.5}$$

see Appendix B.1 for relevant details from the AdS/CFT correspondence. In the 5D description of continuum-mediated self-interacting dark matter, dark matter itself is a 4D degree of freedom localized on the UV brane near the AdS boundary. This is identified with an elementary degree of freedom that probes the CFT sector. The mediator continuum is a bulk field coupled to the fields on the boundary. The mass gap in the AdS description is encoded by an infrared (IR) brane localized further away from the AdS boundary:

$$\text{Diagram (4.6)} \tag{4.6}$$

In the 5D description, the mass gap follows from the bulk field having two boundary conditions at finite distance. The exact CFT limit (4.5) is recovered when the IR brane is decoupled by sending it to spatial infinity. The 5D model is shown in Figure 4.1 and is described precisely in the following section.

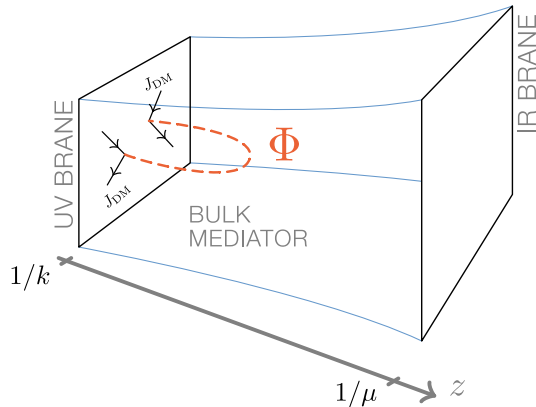


Figure 4.1: Schematic description of the continuum-mediated self-interacting dark matter scenario.

### 4.3 Continuum-Mediated Self-Interactions from AdS

We detail a model in 5D AdS space that realizes the continuum-mediated self-interacting dark matter scenario; the choices of parameters are discussed in the following section. The model is based on the warped dark sector framework [45], which is itself closely related to the Randall–Sundrum 2 model of a warped extra dimension [261].

#### 4.3.1 Geometry and Action

**Geometry.** The metric for the AdS spacetime in conformal coordinates is

$$ds^2 = \left(\frac{1}{kz}\right)^2 (\eta_{\mu\nu} dx^\mu dx^\nu - dz^2) \quad (4.7)$$

where  $k$  is AdS curvature. We restrict to a slice of this AdS space and place UV and IR branes at the endpoints,



$$z_{\text{UV}} \leq z \leq z_{\text{IR}} \qquad z_{\text{UV}} = \frac{1}{k} \qquad z_{\text{IR}} = \frac{1}{\mu} . \quad (4.8)$$

In our model, the scale  $\mu$  characterizes the mass gap of the mediator sector; we take  $\mu \ll k$ .

We assume that some stabilization mechanism prevents the two branes from falling into one another; though we may remain agnostic about the specific choice as the details are not crucial to our study. For concreteness, one may assume the Goldberger–Wise mechanism [161]. We ignore gravitational backreaction effects near the IR brane and approximate the metric to be exactly AdS over the entire space.

The action for the theory includes bulk and brane-localized quadratic terms for the 5D real scalar mediator  $\Phi$ , UV brane-localized quadratic terms for the dark matter  $\chi$ , and interactions between dark matter and mediator:

$$S = \int_{z_{\text{UV}}}^{z_{\text{IR}}} \int d^4x \sqrt{\bar{g}} \mathcal{L}_\Phi + \sqrt{\bar{g}} (\mathcal{L}_\chi + \mathcal{L}_{\text{int}} + \mathcal{L}_\Phi^{\text{UV}}) \delta(z - z_{\text{UV}}) + \sqrt{\bar{g}} \mathcal{L}_\Phi^{\text{IR}} \delta(z - z_{\text{IR}}) , \quad (4.9)$$

where  $\bar{g}$  is the induced metric on the brane, with  $\sqrt{\bar{g}} = (kz)^{-4}$ . Additional terms that do not play a role in the self-interaction phenomenology are the 5D Einstein–Hilbert term, the 4D Standard Model action localized to the UV brane, and possible Standard Model interactions with the mediator. The dark matter Lagrangian terms encode a 4D mass  $m_\chi$  and Yukawa coupling to the bulk mediator:

$$\mathcal{L}_\chi = \bar{\chi} \gamma^\mu \partial_\mu \chi - m_\chi \bar{\chi} \chi \qquad \mathcal{L}_{\text{int}} = \frac{\lambda}{\sqrt{k}} \Phi \bar{\chi} \chi . \quad (4.10)$$

Writing 5D Lorentz indices  $M$ , the bulk mediator Lagrangian is

$$\mathcal{L}_\Phi = \frac{1}{2} [(\partial_M \Phi)(\partial^M \Phi) - M_\Phi^2 \Phi^2] , \quad (4.11)$$

where the bulk mass  $M_\Phi$  is tied to the dimension  $\Delta$  of the operator exchanged between dark matter particles in the CFT picture. The brane-localized Lagrangian terms for the bulk scalar encode mass and kinetic terms:

$$\mathcal{L}_\Phi^{\text{UV}} = \frac{1}{2k} \Phi B_{\text{UV}}[\partial^2] \Phi \quad \mathcal{L}_\Phi^{\text{IR}} = \frac{1}{2k} \Phi B_{\text{IR}}[\partial^2] \Phi \quad B_i[\partial^2] = m_i^2 + c_i \partial^2 + \dots \quad (4.12)$$

The  $B_i[\partial^2]$  are polynomials in the 4D Laplacian  $\partial^2 = \partial_\mu \partial^\mu$ ; the constant term is the brane-localized masses  $m_i^2$ . Higher order terms are typically small and irrelevant for our study.

We remark that the low-energy effective theory also contains a radion that is identified with the dilaton in the 4D theory. This mode is light, but localized on the IR brane and hence has negligible contributions to the dark matter dynamics on the UV brane. We thus do not include it in our analysis as it would produce only a minor shift in the long-range potential.

### 4.3.2 Effective Field Theory Consistency

5D interacting theories are non-renormalizable and are understood to be low-energy effective field theory (EFT) valid up to a cutoff,  $\Lambda$ . The cutoff is tied to the strongest 5D interaction—either gravity or another interaction in the theory. 5D naïve dimensional analysis (NDA) [235, 157, 154, 232, 192], in turn, relates the cutoff to the AdS curvature [84],

$$\Lambda \gtrsim \frac{\ell_5}{\ell_4} k \sim \pi k, \quad (4.13)$$

where the 4D and 5D loop factors are  $\ell_4 = 16\pi^2$  and  $\ell_5 = 24\pi^3$ , respectively.

In our dark sector model, the cutoff sets the dark matter–mediator Yukawa coupling  $\lambda$ . Thus 5D NDA bounds the Yukawa coupling by

$$\lambda \lesssim \sqrt{\frac{\ell_5 k}{\Lambda}} \lesssim 4\pi , \quad (4.14)$$

where we have used (4.13) in the second inequality.

While the 5D theory is valid below  $\Lambda$ , the AdS/CFT dictionary is valid only up to a cutoff scale on the order of  $k < \Lambda$ . From the 4D perspective, a CFT coupled to gravity has a cutoff parametrically smaller than  $M_{\text{Pl}}$  because of the large degrees of freedom of the CFT. This cutoff turns out to be  $k$ , for example by using the species scale conjecture (see e.g. [114]).

Our 5D EFT contains isolated degrees of freedom localized on a brane. In a realistic theory with gravity, localized 4D fields are special modes from 5D bulk fields and are necessarily accompanied by a spectrum of KK modes [136]. We assume an appropriate limit where the observable effects of these modes are negligible.

### 4.3.3 Model Parameters

For the purposes of studying novel, continuum-mediated dark matter self-interactions, we restrict the parameters presented in the 5D model in Section 4.3.1. The AdS curvature,  $k$ , corresponds to the cutoff of the theory, as described in Section 4.3.2. To ensure that the cutoff of the theory is beyond the experimental reach of the Large Hadron Collider to detect, e.g., Kaluza–Klein gravitons, we set  $k$  to be

$$k = 10 \text{ TeV} . \quad (4.15)$$

This sets the position of the UV brane  $z_{\text{UV}} = k^{-1}$  and the upper bound on all other dimensionful parameters in the theory. The AdS curvature is much smaller than the Planck scale, in the spirit of ‘little Randall–Sundrum’ models [100].

The mediator mass,  $M_\Phi$  is related to the dimension  $\Delta$  of the continuum mediator operator and is conveniently described by the dimensionless parameter  $\alpha$ ,

$$\alpha^2 \equiv 4 + \frac{M_\Phi^2}{k^2} = (2 - \Delta)^2 . \quad (4.16)$$

The range of  $\alpha$  corresponds to the  $\Delta_-$  branch of AdS/CFT (see details in Appendix B.1) and can be established as follows. Unitarity of CFT operators requires  $\Delta \geq 1$ , implying  $\alpha \leq 1$ . The Breitenlohner–Freedmann bound for the stability of AdS implies  $\alpha^2 \geq 0$  [46, 47], and we restrict to  $\alpha \geq 0$  without loss of generality. We thus obtain  $0 \leq \alpha \leq 1$ .

Observe that the slope of the resulting long-range potential scales like  $V(r) \sim r^{-1}$  for  $\alpha = 1$  and  $V(r) \sim r^{-3}$  for  $\alpha = 0$ . For potentials more singular than  $r^{-2}$ , solving for the phenomenology becomes computationally intractable and, furthermore, the theory is unlikely to produce the effects relevant for small scale structure anomalies. We thus further restrict the range to  $\alpha \geq 1/2$  to avoid the regime where the long-range potential is steeper than the centrifugal term.

Our theory includes brane-localized masses  $m_i^2 \Phi(x, z_i)^2$  and kinetic terms  $c_i [\partial \Phi(x, z_i)]^2$  for the mediator. It is convenient to parameterize the former into dimensionless variables,

$$b_{\text{IR}} \equiv \frac{m_{\text{IR}}^2}{k^2} + (2 - \alpha) \quad b_{\text{UV}} \equiv \frac{m_{\text{UV}}^2}{k^2} + (2 - \alpha) . \quad (4.17)$$

The IR parameters  $b_{\text{IR}}$  and  $c_{\text{IR}}$  generically have  $\mathcal{O}(1)$  values so we set them all to one. These only have a mild impact on the self-interaction phenomenology. Conversely, we tune

Parameter	Range	What sets the range
Bulk mass	$1/2 \leq \alpha \leq 1$	Calculability, unitarity
Mass gap	$\text{MeV} \lesssim \mu \ll k$	Early universe
Dark matter mass	$\mu \lesssim m_\chi \lesssim k$	Nonlocal potential, EFT validity
Yukawa coupling	$\lambda \leq 4\pi$	EFT perturbativity

Table 4.1: Range of parameters in our model. The AdS curvature is set to  $k = 10$  TeV; larger values generically suppress self-interaction effects. The dimensionless brane-localized masses and kinetic terms defined in (4.12) and (4.17) are assumed to be  $\mathcal{O}(1)$ , with the exception of  $b_{\text{UV}}$  which is tuned to zero to reproduce the long-range behavior, (4.4). The early universe bound on  $\mu$  is described in Section 4.4.

$b_{\text{UV}} = 0$  as required to reproduce the CFT behavior in (4.4) since  $b_{\text{UV}}$  corresponds to a double trace deformation in the conformal theory. The UV brane kinetic coefficient  $c_{\text{UV}}$  is assumed to be  $\mathcal{O}(1)$ , though it is only significant in the limiting case  $\alpha = 1$ .

With these benchmark values in place, the theory is described by the parameters in Table 4.1. The IR scale  $\mu$  defines the mass gap of the theory by setting the scale of the lightest Kaluza–Klein mode and its lower bound is set by dark radiation constraints, described in Section 4.4.

#### 4.3.4 Mediator Propagator and Spectrum

It is convenient to work in position space for the  $z$ -direction but momentum space along 4D Minkowski slices. The mediator field is decomposed as

$$\Phi_p(z) = \int d^4x e^{ip \cdot x} \Phi(x^\mu, z) \quad p \cdot x = p_\mu x^\mu . \quad (4.18)$$

The norm  $p = \sqrt{\eta_{\mu\nu}p^\mu p^\nu}$  is real for timelike  $p^\mu$  and imaginary for spacelike  $p^\mu$ . In these coordinates, the free scalar propagator is the two-point Green's function, see e.g. [136],

$$G_p(z, z') = i \frac{\pi k^3 (zz')^2}{2} \frac{\left[ \tilde{Y}_\alpha^{\text{UV}} J_\alpha(pz_{<}) - \tilde{J}_\alpha^{\text{UV}} Y_\alpha(pz_{<}) \right] \left[ \tilde{Y}_\alpha^{\text{IR}} J_\alpha(pz_{>}) - \tilde{J}_\alpha^{\text{IR}} Y_\alpha(pz_{>}) \right]}{\tilde{J}_\alpha^{\text{UV}} \tilde{Y}_\alpha^{\text{IR}} - \tilde{Y}_\alpha^{\text{UV}} \tilde{J}_\alpha^{\text{IR}}}, \quad (4.19)$$

where  $z_{<,>}$  is the lesser/greater of the endpoints  $z$  and  $z'$ . The quantities  $\tilde{J}^{\text{UV,IR}}$  are

$$\tilde{J}_\alpha^{\text{UV}} = \frac{p}{k} J_{\alpha-1}\left(\frac{p}{k}\right) + B_{\text{UV}}(p^2) J_\alpha\left(\frac{p}{k}\right) \quad \tilde{J}_\alpha^{\text{IR}} = \frac{p}{\mu} J_{\alpha-1}\left(\frac{p}{\mu}\right) + B_{\text{IR}}(p^2) J_\alpha\left(\frac{p}{\mu}\right), \quad (4.20)$$

with similar definitions for  $\tilde{Y}^{\text{UV,IR}}$ . The boundary functions  $B_i(p^2)$  encode brane-localized operators and are defined in (4.12). We refer to (4.19) as the canonical representation of the propagator.

The propagator has an infinite series of isolated poles set by the zeros of  $\tilde{J}_\alpha^{\text{UV}} \tilde{Y}_\alpha^{\text{IR}} - \tilde{Y}_\alpha^{\text{UV}} \tilde{J}_\alpha^{\text{IR}}$  and referred to as Kaluza–Klein (KK) modes. The free propagator can thus equivalently be written as a series

$$G_p(z, z') = i \sum_n \frac{f_n(z) f_n(z')}{p^2 - m_n^2 + i\epsilon}, \quad (4.21)$$

we refer to this particular momentum-space spectral representation as the KK representation of the propagator. Depending on the context, either the canonical or KK representation may be more convenient. Assuming that the UV brane mass parameter is zero,  $b_{\text{UV}} = 0$ , and that the other brane parameters have  $\mathcal{O}(1)$  coefficients, then the KK spectrum for  $p \gg \mu$  is

$$m_n \approx \left( n - \frac{\alpha}{2} + \frac{1}{4} \right) \pi \mu \quad n > 0, \quad (4.22)$$

as can be seen from identifying the poles in the limiting form of the propagator in (4.33). The mass of the lightest mode  $m_0$  depends on the brane-localized parameters and is detailed in Section 4.5.2.

### 4.3.5 Qualitative Description of 4D Near-Conformal Theory

The AdS/CFT correspondence describes the equivalence between a quantum field theory on  $\text{AdS}_{d+1}$  space and a conformal gauge theory with large 't Hooft coupling and large- $N$  in flat  $d$ -dimensional space (for initial works see [234, 168, 302, 143, 229, 144, 106, 105], for some reviews see [7, 306, 248, 198]). AdS bulk fields correspond to CFT operators in a way that is exact (to the best of our knowledge) in the full AdS spacetime and in the presence of a UV brane.

Fields localized on the UV brane are understood to be external fields probing the CFT; these are equivalently called *elementary* states in contrast to CFT degrees of freedom. In the context of our model, dark matter and Standard Model particles are elementary fields. We require that dark matter couples to a scalar operator of the mediator CFT sector; this scalar operator corresponds to the 5D bulk mediator field  $\Phi$ . The mediator CFT two-point correlation function gives the self-interaction amplitude in (4.5).

The understanding of the 4D dual theory is only qualitative in the presence of IR brane cutting off large  $z$  values. The IR brane is interpreted as a spontaneous breaking of the conformal symmetry analogous to confinement in a strongly-interacting gauge theory [19, 87]. The theory is thus only approximately conformal at scales much larger than  $\mu$ , however we follow the common colloquial practice of referring to the 4D theory as a CFT. The scale  $\mu = z_{\text{IR}}^{-1}$  is naturally associated to the mass gap characterizing conformal

symmetry breaking, similar to the QCD confinement scale. KK modes are identified with composite states that are allowed when conformal invariance is broken. In the simplest realization, the composite states are glueballs of adjoint gauge fields.

Either the AdS or CFT description of the theory may be more convenient depending on the context. We primarily focus on the 5D description where the model is concretely defined. The qualitative behavior of this theory is general and captures what is expected for a purely 4D near-conformal mediator; one may view the 5D construction as a simple quantitative tool to describe such a theory.

## 4.4 Phenomenological Constraints

We briefly comment on implications of our model beyond the dark matter self-interaction phenomenology that is our primary focus.

### 4.4.1 Cosmological Dark Radiation

Models of near-conformal dark sectors necessarily introduce large numbers of degrees of freedom. Many of these may be relativistic in the early universe and are thus constrained by big bang nucleosynthesis (BBN) and the cosmic microwave background (CMB). There are at least three ways to avoid the tight constraints on the effective number of relativistic degrees of freedom,  $N_{\text{eff}}$ :

1. The theory may have a sufficiently large mass gap,  $\mathcal{O}(\text{MeV})$ , so that all states are non-relativistic at the relevant times. In this case there is no dark radiation.
2. The relativistic states decay quickly enough that they do not affect BBN or the



CMB [205].

3. The dark sector may be much colder than the Standard Model so that the density of states is suppressed compared to visible matter. This is a natural possibility and has been studied in the context of gravitational interactions in AdS [180, 221, 220]. Dark radiation from a bulk scalar will be studied in an upcoming work [83].

With these features in mind, we focus on  $\mu \gtrsim \mathcal{O}(\text{MeV})$ , but allow for  $\mu$  the possibility of lower scales subject to additional model building to accommodate  $N_{\text{eff}}$  limits.

#### 4.4.2 Fifth Force

Bulk graviton exchange leads to deviations from the Newtonian gravitational potential of the form [261, 159]

$$V_{\text{N}}(r) = -\frac{G_{\text{N}}}{r} \left[ 1 + \mathcal{O}\left(\frac{1}{k^2 r^2}\right) \right]. \quad (4.23)$$

Constraint from fifth force searches set  $k \gtrsim 5 \text{ meV}$  or  $k^{-1} \lesssim 50 \mu\text{m}$  and hence can be ignored; see e.g. [224] for a recent measurement, [44] for a review of  $r^{-3}$  constraints.

#### 4.4.3 Deviations from the Standard Model

Standard Model fields are assumed to be localized on the UV brane. For the purposes of dark matter self interaction phenomenology, we neglect any direct UV-brane interactions between the dark matter and Standard Model and assume that the mediator–Standard Model couplings are negligible. These couplings are phenomenologically relevant, for example in dark matter direct detection experiments [205] or in searches for novel forces

between Standard Model particles [45, 85], but are not directly related to the small scale structure anomalies that are the primary phenomenological focus of this paper.

In principle the brane-localized fields are limits of 5D fields with heavy KK modes [136]. The most significant effects of these modes are deviations in the Standard Model gauge sector: gauge bosons can scatter off 5D gravitons and the gauge couplings pick up an anomalous logarithmic running above the IR scale  $\mu$ . Both of these effects are small enough to be undetected with current data in the limit where  $\Lambda$  is sufficiently close to  $k$ . Since we already assume this in (4.13), the model is safe from these effects.

## 4.5 The Continuum-Mediated Potential

The potential  $V$  between two particles is obtained from the  $t$ -channel scattering amplitude with the external legs taken to the appropriate non-relativistic limit,<sup>3</sup>

$$i\mathcal{M} \equiv -4im_\chi^2 \tilde{V}(|\mathbf{q}|) = -4 \frac{\lambda^2}{k} G_{|\mathbf{q}|}(z_{UV}, z_{UV}), \quad (4.24)$$

with  $t \approx -|\mathbf{q}|^2$  where  $\mathbf{q}$  is the three-dimensional momentum transfer. On the right-hand side we insert the expression from the exchange of a  $t$ -channel bulk mediator between dark matter currents. The position-space potential is related by a Fourier transform

$$V(r) = \int \frac{d^3\mathbf{q}}{(2\pi)^3} \tilde{V}(|\mathbf{q}|) e^{i\mathbf{q}\cdot\mathbf{r}}, \quad (4.25)$$

with  $r = |\mathbf{r}|$ . Even though our effective theory has a cutoff, one may integrate (4.25) to infinite  $|\mathbf{q}|$  under the assumption of a smooth cutoff, as shown in the Appendix B of Ref. [85].

<sup>3</sup>In principle  $u$ -channel diagrams contribute when the scattering particles are identical. This is an  $\mathcal{O}(\text{few})$  effect [194, App. C]. We neglect the  $u$ -channel contribution for simplicity and ease of direct comparison to Ref. [293].

Simply inserting the exact propagator (4.19) is analytically challenging. We proceed by using a spectral representation where the discontinuity of the two-point function is evaluated in the appropriate asymptotic limits from Section 4.5.2.

### 4.5.1 Spectral Representation

The spectral representation for the bulk propagator is [308]

$$G_p(z, z') = \frac{1}{2\pi i} \int_0^\infty d\rho \frac{\text{Disc}_\rho \left[ G_{\sqrt{\rho}}(z, z') \right]}{\rho - p^2}, \quad (4.26)$$

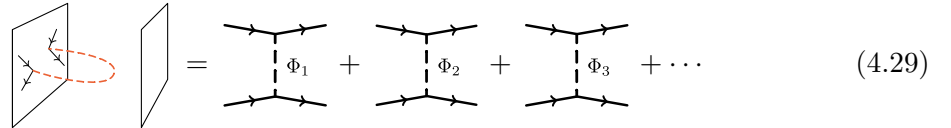
where  $\text{Disc}_\rho [g(\rho)]$  is the discontinuity of  $g(\rho)$  across the branch cut along the real line,  $\rho \in \mathbb{R}^+$ :

$$\text{Disc}_\rho [g(\rho)] = \lim_{\epsilon \rightarrow 0} g(\rho + i\epsilon) - g(\rho - i\epsilon) \quad \epsilon > 0. \quad (4.27)$$

We compute the non-relativistic potential using this spectral representation of the propagator. Performing the  $d^3\mathbf{q}$  integral yields a general representation of the long-range potential:

$$V(r) = -\frac{1}{8\pi^2} \frac{\lambda^2}{k} \int_0^\infty d\rho \text{Disc}_\rho \left[ G_{\sqrt{\rho}}(z_{\text{UV}}, z_{\text{UV}}) \right] \frac{e^{-\sqrt{\rho}r}}{r}. \quad (4.28)$$

**Kaluza–Klein representation.** One may use the KK representation of the free propagator (4.21) in the spectral representation of the potential (4.28); this amounts to identifying the exchange of a 5D bulk scalar with the sum of  $t$ -channel diagrams with each KK mode:



The spectral distribution is  $\text{Disc}_\rho \left[ G_{\sqrt{\rho}}(z, z') \right] = \sum_n f_n(z) f_n(z') 2\pi \delta(p^2 - m_n^2)$ , so that the potential is an infinite sum of Yukawa potentials from each KK mode:

$$V(r) = -\frac{1}{4\pi} \frac{\lambda^2}{k} \sum_n f_n(z_0)^2 \frac{e^{-m_n r}}{r}. \quad (4.30)$$

While this KK representation of  $V$  is exact, it requires knowledge of the entire spectrum of KK masses and wavefunctions.

**Canonical representation.** One may alternatively use the canonical representation of the propagator (4.19) in the spectral representation of the potential (4.28). In this case, one may apply the closed-form asymptotic expressions derived in the following section. These asymptotic expressions carry the same poles as the KK representation. The momentum flowing through the propagator is necessarily spacelike in diagrams that contribute to the potential. Thus we may readily use the asymptotic expressions for large  $|p|$  that are valid away from the poles, (4.34) for  $\alpha < 1$  and (4.39) for  $\alpha = 1$ . We numerically validate this approximation in Section 4.5.5.

## 4.5.2 Propagator Asymptotics

We present the limits of the bulk propagator  $G_p$  for Minkowski momenta  $p$  much smaller and larger than the mass gap,  $\mu$ . We focus on propagation to and from the UV brane where the dark matter currents are localized. These limits illuminate the properties of the theory and yield simplifications for the self-interaction potential.

We treat the  $\alpha < 1$  and  $\alpha = 1$  cases separately; the asymptotic behavior of Bessel functions with near integer order have an extra contribution that is neglected for non-integer order.<sup>4</sup> As a result, one typically cannot obtain the  $\alpha = 1$  asymptotic behavior as the  $\alpha \rightarrow 1$

<sup>4</sup>This is due to the expression for the Bessel function of the second kind with integer index  $\alpha \rightarrow n$ ,

$$Y_n(z) = \frac{1}{\pi} \left. \frac{\partial J_\alpha(z)}{\partial \alpha} \right|_{\alpha=n} + \frac{(-)^n}{\pi} \left. \frac{\partial J_\alpha(z)}{\partial \alpha} \right|_{\alpha=-n} .$$

limit of the  $\alpha < 1$  asymptotic behavior. The  $\alpha = 1$  case is a meaningful benchmark as it is equivalent to the exchange of a single 4D mediator.

**Propagator Asymptotics for  $0 < \alpha < 1$**

**Small momentum asymptotic,  $|p| \ll \mu$ .** For Minkowski momenta much less than the mass gap we find a single 4D pole:

$$G_p(z_{UV}, z_{UV}) = i \frac{2k(1-\alpha)(2\alpha + b_{\text{IR}})}{\alpha(2 + b_{\text{IR}})p^2 - 4\alpha(1-\alpha)b_{\text{IR}}\mu^2} \left(\frac{\mu}{k}\right)^{2-2\alpha}. \quad (4.31)$$

All other poles are heavier than  $\mathcal{O}(\mu)$ . For  $b_{\text{IR}} \lesssim \mathcal{O}(1)$ , the light 4D mode mass is

$$m_0^2 = \frac{4(1-\alpha)b_{\text{IR}}}{2 + b_{\text{IR}}}\mu^2. \quad (4.32)$$

**Large momentum asymptotic,  $|p| \gg \mu$ .** For momenta much larger than the mass gap,

$$G_p(z_{UV}, z_{UV}) = \frac{i}{2k} \frac{\Gamma(\alpha)}{\Gamma(-\alpha + 1)} \left(\frac{4k^2}{p^2}\right)^\alpha S_\alpha(p) \quad S_\alpha(p) = \frac{\sin\left(\frac{p}{\mu} - \frac{\pi}{4}(1 - 2\alpha)\right)}{\sin\left(\frac{p}{\mu} - \frac{\pi}{4}(1 + 2\alpha)\right)}. \quad (4.33)$$

The tower of KK poles are encoded in  $S_\alpha(p)$ . The propagator further simplifies when the momentum has an imaginary part  $\text{Im}(p/\mu) \gtrsim 1$ :

$$G_p(z_{UV}, z_{UV}) = \frac{i}{2k} \frac{\Gamma(\alpha)}{\Gamma(-\alpha + 1)} \left(\frac{4k^2}{-p^2}\right)^\alpha, \quad (4.34)$$

where we have used  $S_\alpha \approx (-1)^\alpha$  in this limit.<sup>5</sup> This includes the case of spacelike momentum. In this limit the conformal scaling appears: recalling that  $\alpha = 2 - \Delta$ , the propagator reproduces the scaling of the amplitude (4.4). Observe that the UV brane kinetic term does

---

<sup>5</sup>Loops from bulk interactions cause heavy KK modes to acquire large widths and give an effective imaginary part to timelike four-momentum in the bulk propagator [135, 84, 82]. This physical imaginary part is important for timelike processes but is not for spacelike processes, hence it is irrelevant for the potential.

not appear in this expression. This reflects the fact that none of the modes are localized near the UV brane.

### Propagator Asymptotics for $\alpha = 1$

**Small momentum asymptotic,  $|p| \ll \mu$ .** For Minkowski momenta much less than the mass gap, we find

$$G_p(z_{\text{UV}}, z_{\text{UV}}) = \frac{(2 + b_{\text{IR}})2ik}{p^2 [(2 + b_{\text{IR}})(2c_{\text{UV}}k + \log(k^2/\mu^2)) - b_{\text{IR}}] - 4b_{\text{IR}}\mu^2} . \quad (4.35)$$

This carries a single 4D pole. The mass of this light mode is

$$m_0^2 = \frac{4b_{\text{IR}}\mu^2}{(2 + b_{\text{IR}}) [2c_{\text{UV}}k + \log(k^2/\mu^2)] - b_{\text{IR}}} . \quad (4.36)$$

This mass is suppressed by  $c_{\text{UV}} + \log(k/\mu)$ , where  $c_{\text{UV}}$  is the coefficient of the UV brane-localized kinetic term and  $\log(k/\mu)$  describes the bulk volume. One may understand (4.36) as a dressing of the zero mode with an IR brane-localized mass.

**Large momentum asymptotic,  $|p| \gg \mu$ .** For momenta much larger than the mass gap,

$$G_p(z_{\text{UV}}, z_{\text{UV}}) = \frac{2ik}{p^2 \left[ 2c_{\text{UV}} - \pi \cot\left(\frac{p}{\mu} + \frac{\pi}{4}\right) - \log\left(\frac{p^2}{4k^2}\right) - 2\gamma \right]} . \quad (4.37)$$

When  $\text{Im}(p/\mu) \gtrsim 1$  the cotangent approaches  $-i$  and the propagator simplifies,

$$G_p(z_{\text{UV}}, z_{\text{UV}}) = \frac{2ik}{p^2 \left[ 2c_{\text{UV}} - \log\left(-\frac{p^2}{4k^2}\right) - 2\gamma \right]} . \quad (4.38)$$

In contrast to the  $\alpha < 1$  case (4.34), the UV brane kinetic term is not negligible. This propagator describes a 4D mode with a logarithmic running of its wavefunction. It is similar to the well known case of a bulk gauge field in AdS. We can absorb a large logarithm by

redefining the brane wavefunction coefficient  $c_{\text{UV}}$  at a physical scale  $p_0$ :

$$\hat{c}_{\text{UV}} = c_{\text{UV}} + [\log(k/p_0) - \gamma] \quad G_p(z_{\text{UV}}, z_{\text{UV}}) = \frac{2ik}{p^2 \left[ 2\hat{c}_{\text{UV}} - \log\left(-\frac{p^2}{p_0^2}\right) \right]}. \quad (4.39)$$

For the astrophysical applications of self-interacting dark matter, the energy transfer ranges over only a few orders of magnitude and the logarithmic running is thus negligible. The  $\alpha = 1$  case thus reproduces the standard single-mediator self-interacting dark matter model and serves as a useful benchmark.

### 4.5.3 Potential, $\alpha < 1$

For bulk masses in the range  $0 < \alpha < 1$  and with generic IR brane mass parameter  $b_{\text{IR}} \sim \mathcal{O}(1)$ , the lightest excitations have mass on the order of  $\mu$ ; see (4.32). Since there is no light mode to contribute to non-analyticities of  $G_p$  for  $|p| < \mu$ , we may apply the  $|p| \gg \mu$  approximation of the propagator to the spectral integral (4.28). The lower limit of the spectral integral is formally the mass of the lightest KK mode,

$$V(r) = -\frac{1}{8\pi^2} \frac{\lambda^2}{k} \int_{m_1^2}^{\infty} d\rho \text{Disc}_\rho \left[ G_{\sqrt{\rho}}(z_{\text{UV}}, z_{\text{UV}}) \right] \frac{e^{-\sqrt{\rho}r}}{r}. \quad (4.40)$$

However, because  $m_1 = \mathcal{O}(\mu)$ , by using the  $\rho \gg \mu^2$  approximation for the propagator (4.34), we introduce some uncertainty in the lower bound of the spectral integral. We verify the validity of this approximation in Section 4.5.5.

The discontinuity across the branch cut along  $\rho > 0$  is

$$\text{Disc}_\rho \left[ \Delta_{\sqrt{\rho}}(z_0, z_0) \right] = \frac{1}{k} \left( \frac{4k^2}{\rho} \right)^\alpha \frac{\Gamma(\alpha)}{\Gamma(1-\alpha)} \sin(\pi\alpha), \quad (4.41)$$

where we have used (4.34). This is valid for  $\text{Im}(p/\mu) \gtrsim 1$ , which we assume because  $p$  is spacelike. Evaluating the integral across the discontinuity using the  $\Gamma$  reflection and

duplication formulas<sup>6</sup> gives the main expression we use in our analysis:

$$V(r) = -\frac{\lambda^2}{2\pi^{3/2}} \frac{\Gamma(3/2 - \alpha)}{\Gamma(1 - \alpha)} \frac{1}{r} \left(\frac{1}{kr}\right)^{2-2\alpha} Q(2 - 2\alpha, m_1 r), \quad (4.42)$$

where  $Q(2 - 2\alpha, m_1 r)$  is the regularized incomplete  $\Gamma$  function,

$$Q(p, z) = \frac{1}{\Gamma(p)} \int_z^\infty dx x^{p-1} e^{-x}. \quad (4.43)$$

For  $r \gg m_1^{-1}$ , the potential is exponentially suppressed at long distances,

$$V(r) \propto -\left(\frac{m_1}{k}\right)^{1-2\alpha} \frac{1}{kr^2} e^{-m_1 r}. \quad (4.44)$$

We see that  $Q(2 - 2\alpha, r)$  takes the place of the  $e^{-mr}$  Yukawa factor that encodes the mass gap in the single-mediator scenario. In turn, this mass gap is a key ingredient for cutting off unwanted long-range dark forces.

It is illustrative to check the behavior in the gapless limit  $\mu \rightarrow 0$ . The large, spacelike momentum approximation of the propagator (4.38) is exact in this limit and potential can be evaluated exactly. We recover the gapless limit in (4.42) the gapless limit is recovered by taking  $m_1 \rightarrow 0$ , giving

$$V_{\text{gapless}}(r) = -\frac{\lambda^2}{2\pi^{3/2}} \frac{\Gamma(3/2 - \alpha)}{\Gamma(1 - \alpha)} \frac{1}{r} \left(\frac{1}{kr}\right)^{2-2\alpha}, \quad (4.45)$$

which matches the result from [45]. The power law behavior obtained matches the proposed scaling in (4.4) with the AdS/CFT identification  $\Delta = 2 - \alpha$ .

#### 4.5.4 Potential, $\alpha = 1$

For bulk mass parameter  $\alpha = 1$  and with generic IR brane mass parameter  $b_{\text{IR}} \sim \mathcal{O}(1)$ , there is a mode lighter than the scale  $\mu$ . The suppression relative to  $\mu$  is the kinetic

<sup>6</sup>Namely:  $\Gamma(1 - z)\Gamma(z) = \pi/\sin(\pi z)$  and  $\Gamma(2z) = \pi^{-1/2} 2^{2z-1} \Gamma(z)\Gamma(z + 1/2)$ .



factor  $(c_{\text{UV}} + \log(k/\mu))^{1/2}$  in (4.36). This is in contrast to the  $\alpha < 1$  case. The spectral integral over the discontinuity in  $G_{\sqrt{\rho}}$  must thus take into account this pole in the  $\rho \ll \mu^2$  regime in addition non-analyticities in the  $\rho \gg \mu^2$  regime. We separate the potential into two pieces accordingly,  $V = V_{\text{light}} + V_{\text{KK}}$ .

**Light mode contribution.** The light mode contributes a simple Yukawa potential:

$$V_{\text{light}} = -\frac{\lambda^2}{4\pi k} f_0(z_{\text{UV}})^2 \frac{e^{-m_0 r}}{r} \quad (4.46)$$

where the profile evaluated on the UV brane is

$$f_0(z_{\text{UV}})^2 = \frac{(2 + b_{\text{IR}})2k}{(2 + b_{\text{IR}}) \left[ 2c_{\text{UV}} + \log\left(\frac{k^2}{\mu^2}\right) \right] - b_{\text{IR}}} \approx \frac{k}{\hat{c}_{\text{UV}} + \log\left(\frac{p_0}{\mu}\right) + \gamma}. \quad (4.47)$$

as can be derived from the pole of the small momentum transfer limit of the propagator (4.35). On the right-hand side we use the assumption that  $b_{\text{IR}} \sim \mathcal{O}(1)$ , apply the  $\mu \ll k$  limit, insert the renormalized brane kinetic term coefficient  $\hat{c}_{\text{UV}}$  defined at the scale  $p_0$  from (4.39).

**KK mode contribution.** The KK mode contribution uses the  $|p| \gg \mu$  asymptotic of the bulk  $\alpha = 1$  propagator (4.39) applied to the large-momentum spectral integral, (4.40).

To obtain an analytically tractable expression we take the limit  $\hat{c}_{\text{UV}} \gg \log(\rho/p_0^2)$  over the range  $\rho \in [m_1^2, r^{-2}]$ ; the upper bound comes from the  $\exp(-\sqrt{\rho}r)$  factor in the spectral integral. The resulting propagator is

$$G_p(z_{\text{UV}}, z_{\text{UV}}) = \frac{ik}{p^2 \hat{c}_{\text{UV}}} \left[ 1 + \frac{\log(-p^2/p_0^2)}{2\hat{c}_{\text{UV}}} + \mathcal{O}\left(\frac{1}{\hat{c}_{\text{UV}}^2}\right) \right]. \quad (4.48)$$

The discontinuity in the spectral integral is

$$\text{Disc}_\rho \left[ G_{\sqrt{\rho}}(z_{\text{UV}}, z_{\text{UV}}) \right] = \frac{2\pi k}{\hat{c}_{\text{UV}}} \delta(\rho) + \frac{k}{\hat{c}_{\text{UV}}^2} \frac{\pi}{\rho} + \mathcal{O}\left(\frac{1}{\hat{c}_{\text{UV}}^3}\right). \quad (4.49)$$

The singular  $\delta(\rho)$  term is outside the range of integration and does not contribute. The leading contribution comes from the  $\mathcal{O}(\hat{c}_{\text{UV}}^{-2})$  term and evaluates to

$$V_{\text{KK}}(r) = -\frac{1}{4\pi r} \frac{\lambda^2}{\hat{c}_{\text{UV}}^2} \Gamma(0, m_1 r). \quad (4.50)$$

**The  $\alpha = 1$  Potential and Limits.** Since we have used the  $\hat{c}_{\text{UV}} \gg \log(\rho/p_0^2)$  limit in the KK potential, we may apply the same approximation to the light mode contribution. This produces the full  $\alpha = 1$  potential

$$V(r) = -\frac{\lambda^2}{4\pi r} \left[ \frac{1}{\hat{c}_{\text{UV}}} \left( 1 - \frac{\log(p_0/\mu) + \gamma}{\hat{c}_{\text{UV}}} \right) e^{-m_0 r} + \frac{\Gamma(0, m_1 r)}{\hat{c}_{\text{UV}}^2} \right] + \mathcal{O}\left(\frac{1}{\hat{c}_{\text{UV}}^3}\right). \quad (4.51)$$

At long distances,  $r \gg m_1^{-1}$ ,

$$\frac{\Gamma(0, m_1 r)}{\hat{c}_{\text{UV}}^2} \rightarrow \frac{1}{\hat{c}_{\text{UV}}^2} \frac{e^{-m_1 r}}{m_1 r}. \quad (4.52)$$

One can explicitly see the exponential suppression from both the light mode and KK mode mass gaps. In the short distance  $r \ll m_1^{-1}$  limit, the incomplete  $\Gamma$  function is  $\Gamma(0, x) \approx -(\log x + \gamma)$  and one has  $e^{-m_0 r} \sim 1$ . Since  $m_0 r \ll 1$ , we obtain

$$V(r) = -\frac{\lambda^2}{\hat{c}_{\text{UV}}} \frac{1}{4\pi r} \left[ 1 - \frac{1}{\hat{c}_{\text{UV}}} \log\left(\frac{r}{r_0}\right) \right] + \mathcal{O}\left(\frac{1}{\hat{c}_{\text{UV}}^3}\right), \quad (4.53)$$

where we introduce the scale  $r_0$

$$\log r_0 = \log p_0 + 2\gamma + \log\left(\frac{m_1}{\mu}\right) \quad (4.54)$$

to absorb  $\mathcal{O}(1)$  coefficients. The explicit  $\mu$  dependence vanishes because the  $\log \mu$  from the light mode and the  $\log m_1 = \log \mu + \mathcal{O}(1)$  from the KK modes cancel.

While (4.53) could be understood as the  $\mu \rightarrow 0$  limit of the  $\alpha = 1$  potential, the  $\hat{c}_{\text{UV}} \gg \log(\rho/p_0^2)$  assumption we used to evaluate the spatial potential formally does not

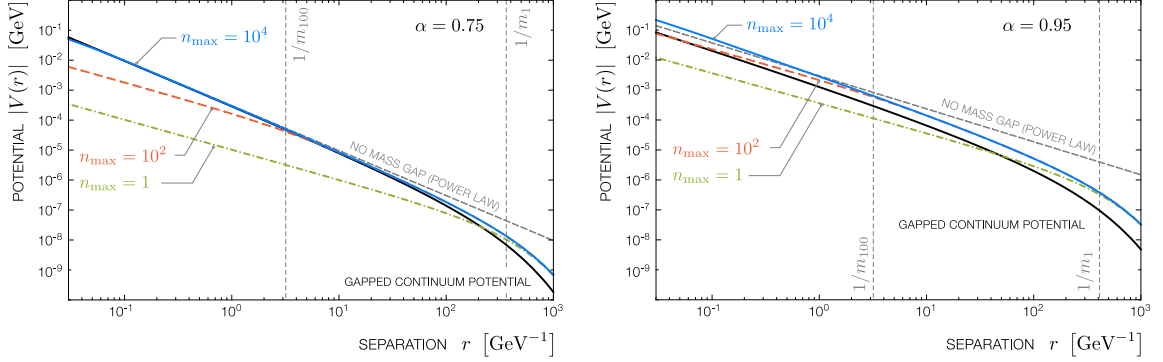


Figure 4.2: Absolute potential  $|V(r)|$  plotted to validate the continuum-mediated potential with a mass gap (black) against a sum over  $n_{\max}$  Kaluza–Klein modes (colored). The potential with  $n_{\max}$  KK modes is valid for separations larger than  $r \gtrsim m_{n_{\max}}^{-1}$ . The disagreement at long separations between the blue and black lines represents our numerical error and does not change the quantitative behavior of integrals over the potential. Also shown: the non-integer power law limit (dashed gray) that is realized in the gap-less limit  $m_1 \rightarrow 0$ .

hold in this limit. Instead the full  $\log^n r$  series would need to be resummed. Nevertheless, we verify that the Fourier transform of the propagator (4.48) matches the potential (4.53). Interestingly, in this limit the contribution from the light mode is replaced by the  $\delta(\rho)$  contribution in the discontinuity across the propagator, (4.49), which is otherwise cut off at finite  $\mu$ . Details of this calculation are presented in Appendix B.2.

The expressions in this section show that the KK mode contribution tends to be small with respect to the light mode for both large and small  $r$ . This logarithmic correction is negligible in our self-interacting dark matter calculations and thus the  $\alpha = 1$  case matches the standard single 4D mediator scenario. It can thus be used as a benchmark comparing to  $\alpha \neq 1$  phenomenology.

### 4.5.5 Validation of Potential

In this study we use the asymptotic approximation of the gapped continuum-mediated potential (4.42). In order to quantify its validity, we compare our approximation to an explicit sum over Kaluza–Klein mediated Yukawa potentials (4.30). This is a meaningful check since a sum over  $n_{\max}$  KK modes is a valid approximation to the full sum on scales longer than the inverse mass of the heaviest mode,  $r \gtrsim m_{n_{\max}}^{-1}$ . We thus test for agreement of the gapped continuum-mediated potential with the sum over a large number of KK in the regime where the latter is valid.

We present our validation in Figure 4.2. The key comparison is between sum over  $n_{\max} = 10^4$  KK modes (blue) and the continuum-mediated potential (black). For values of  $\alpha \lesssim 0.95$ , the sum over  $n_{\max}$  KK modes agrees with the continuum potential in the regime where the finite KK sum is valid,  $r \gtrsim m_{n_{\max}}^{-1}$ . However, at distances longer than the inverse mass gap,  $r \gtrsim m_1^{-1}$ , the curves diverge slightly while maintaining the same qualitative gapped behavior. This discrepancy is caused by the  $|p| \gg \mu$  limit assumed in the derivation of the continuum-mediated potential (4.42). This discrepancy grows when  $\alpha \approx 1$ ; see Footnote 4. Practically, we restrict the continuum-mediated potential for  $\alpha \lesssim 0.95$ . In this range, the large- $\alpha$  discrepancy does not change the qualitative behavior of the continuum-mediated potential, nor the quantitative behavior of integrals of this potential. For larger values of  $\alpha$ , the potential reproduces the well-known case of a single 4D mediator, as described in Section 4.5.4.

Figure 4.2 also demonstrates how a sum of Yukawa potentials can reproduce a potential that goes like a non-integer power of the separation, (4.1). The lightest KK mass sets a long-range length scale,  $m_1^{-1}$ . In the regime  $m_{n_{\max}}^{-1} \lesssim r \ll m_1$ , the sum over Yukawa potentials from  $n_{\max}$  KK modes produces a total potential that matches the power law of (4.45).

## 4.6 Astrophysical Phenomenology

We apply our continuum-mediated model to the phenomenology of self-interacting dark matter for small-scale structure. The quantity that connects particle physics parameters to astronomy is the transfer cross section. We demonstrate the dependence of this cross section on our model parameters and provide representative fits.

### 4.6.1 Review of Self-Interacting Dark Matter Cross Sections

We summarize key results of self-interacting dark matter phenomenology; see Ref. [292] for a detailed review. Long-range dark matter self-interactions affect halo density profiles by thermalizing the inner halo and reducing the central density. The effect of dark matter self-interactions on halos depends on the scattering rate,  $\sigma v(\rho_\chi/m_\chi)$ . Since the dark matter density  $\rho_\chi$  and the relative velocity  $v$  are known for the relevant astrophysical systems, the figure of merit is the ratio of the cross section to the dark matter mass,  $\sigma/m_\chi$ . Dwarf spheroidal galaxies have low relative velocities ( $v \sim 10$  km/s) and exhibit small-scale structure anomalies that could be explained by sufficient self-interactions [200, 293, 95]. On the other hand, galaxy clusters have large relative velocities ( $v \sim 1500$  km/s) and typically

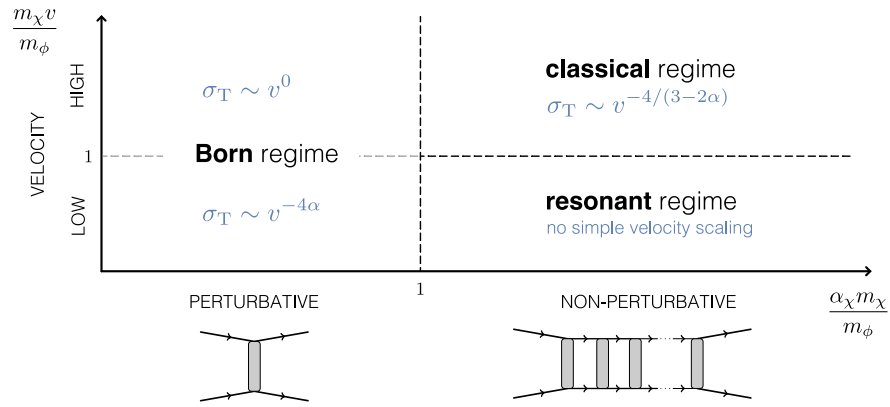


Figure 4.3: Regimes of self-interacting dark matter. The horizontal axis measures whether the ladder of mediator exchanges can be approximated by a single mediator exchange. The vertical axis is a measure of the velocity. The figures of merit are scaled by the ratio of the dark matter mass to the mediator mass (or mass gap) so that the regimes are limits relative to unity. The perturbative regime is described by the Born approximation over the range of all velocities, whereas the non-perturbative regime is separated into a classical regime at high velocities and a resonant regime at low velocities. Blue: asymptotic velocity scaling of the transfer cross section  $\sigma_T$  in the continuum-mediated scenario. No simple scaling exists in the resonant regime. The standard case of a single 4D mediator corresponds to  $\alpha = 1$ .

set upper bounds on these interactions:

$$\left(\frac{\sigma}{m_\chi}\right)_{\text{dwarf}} \sim 1 \frac{\text{cm}^2}{\text{g}} \qquad \left(\frac{\sigma}{m_\chi}\right)_{\text{cluster}} \lesssim 0.1 \frac{\text{cm}^2}{\text{g}} . \quad (4.55)$$

The small-scale target and large-scale upper limit are simultaneously satisfied in self-interacting dark matter models due to the velocity dependence of the cross section. In fact, a more relevant quantity for fitting to astronomical observations is the *transfer cross section*, which is weighted by the amount of transverse momentum transferred between dark matter particles:

$$\sigma_{\text{T}} = \int d\Omega \frac{d\sigma}{d\Omega} (1 - \cos\theta) . \quad (4.56)$$

This accounts for the fact that back-to-back scattering does not change the distribution of energy between halo dark matter particles.<sup>7</sup> The transfer cross section is the figure of merit for determining the effect of self-interactions on the dark matter halo profile. The behavior is classified according to regimes along two axes: perturbativity and relative velocity, see Figure 4.3.

**Perturbativity.** The horizontal axis of Figure 4.3 distinguishes whether the transfer cross section is accurately described by the exchange of a single mediator (perturbative) or otherwise requires a sum over ladder diagrams (non-perturbative). In the former case, one may use the Born approximation. For a 4D dark sector with a single mediator of mass  $m_\phi$  and corresponding potential  $V \sim \alpha_\chi e^{-m_\phi r}/r$ , these regimes correspond to

$$\text{Born: } \frac{\alpha_\chi m_\chi}{m_\phi} \ll 1 \qquad \text{non-perturbative: } \frac{\alpha_\chi m_\chi}{m_\phi} \gg 1 . \quad (4.57)$$

---

<sup>7</sup>A more symmetric treatment is to use the viscosity cross section,  $\sigma_{\text{V}} = \int d\Omega \sin^2\theta d\sigma/d\Omega$ . In order to map to the standard self-interacting dark matter literature, we use  $\sigma_{\text{T}}$  which differs from  $\sigma_{\text{V}}$  by at most an  $\mathcal{O}(1)$  factor [292].

The weighted coupling,  $\alpha_\chi m_\chi/m_\phi$ , measures whether the Hamiltonian eigenstates are distorted from the non-interacting case [272, (7.2.13)]. The sum over ladder diagrams in the non-perturbative regime reproduces the distortions of the asymptotic states relative to the non-interacting eigenstates.

**Velocity.** The horizontal axis of Figure 4.3 distinguishes whether the dark matter relative velocity (kinetic energy) is large enough to ignore the effect of the mediator mass. When the theory is perturbative, the Born approximation may be applied across the entire range of velocities. On the other hand the velocity separates the non-perturbative case into two regimes according to whether the de Broglie wavelength (inverse momentum)  $(m_\chi v)^{-1}$  is comparable to the screening length (inverse mediator mass),  $m_\phi^{-1}$ :

$$\text{resonant: } \frac{m_\chi v}{m_\phi} \ll 1 \qquad \text{classical: } \frac{m_\chi v}{m_\phi} \gg 1 . \qquad (4.58)$$

The *classical regime* is the case where the zeroth-order WKB approximation is valid; this corresponds to the  $\hbar \rightarrow 0$  limit. For a 4D dark sector with a single mediator of mass  $m_\phi$ , the classical regime is the case where the mediator mass is negligible and the theory reproduces the case of Rutherford/Coulomb scattering. In contrast, in the *resonant regime* the Yukawa factor deforms the potential away from the Coulomb limit enough to support quasi-bound states. In this regime, one must numerically solve the Schrödinger equation in a partial wave expansion to determine the transfer cross section [293].

Figure 4.3 shows that  $v < \alpha_\chi$  is a necessary condition for the existence of resonances over some range of  $v$ . Conversely,  $v > \alpha_\chi$  is a sufficient condition for having no resonance for any value of  $v$ .



### 4.6.2 Analytical Behavior of a Continuum Mediator

The transfer cross section from a continuum-mediated potential can be mapped onto the self-interacting dark matter regimes described above and pictured in Figure 4.3.

**Effective coupling.** The condition for perturbativity depends on the dark fine structure constant, which is  $\alpha_\chi = g_\chi^2/4\pi$  for a single 4D mediator. We can identify an effective fine structure constant  $\alpha_\chi^{\text{eff}}$  for our continuum mediator. For bulk mass parameters  $1/2 < \alpha < 1$ ,

$$\alpha_\chi^{\text{eff}} = \frac{\lambda^2 m_1}{4\pi k} \sum_n \frac{f_n^2(z_{\text{UV}})}{m_n} \approx \frac{\lambda^2}{4\pi} \left[ \frac{4}{2\alpha - 1} \frac{1}{\Gamma(1 - \alpha)^2} \right] \left( \frac{m_1}{2k} \right)^{2-2\alpha}. \quad (4.59)$$

This follows from applying the Born approximation condition (4.57) to the sum of Kaluza–Klein potentials (4.30). On the right-hand side we use the spectral representation (4.26) to evaluate the sum. This calculation is detailed in Appendix B.3, where we also discuss the limiting cases where the bulk masses satisfy  $\alpha = 1/2$  and  $\alpha = 1$ . We note that the factor of  $(m_1/k)^{2-2\alpha} \sim (\mu/k)^{2-2\alpha}$  in (4.59) suppresses the effective coupling compared to a naïve estimate  $\lambda^2/4\pi$ .

**Transfer cross section regimes.** The self-interaction regimes in Figure 4.3 are mapped to the continuum-mediated scenario by identifying the mediator mass with the lightest KK mode mass (the mass gap),  $m_\phi \rightarrow m_1$ . We find that the effective coupling  $\alpha_\chi^{\text{eff}}$  replaces  $\alpha_\chi$  in the demarcation of the perturbative (Born) and non-perturbative regimes,

$$\text{Born: } \frac{\alpha_\chi^{\text{eff}} m_\chi}{m_1} \ll 1 \quad \text{non-perturbative: } \frac{\alpha_\chi^{\text{eff}} m_\chi}{m_1} \gg 1. \quad (4.60)$$

We can likewise divide the non-perturbative regime into the classical and resonant regimes:

$$\text{Classical: } \frac{m_\chi v}{m_1} \gg 1 \quad \text{Resonant: } \frac{m_\chi v}{m_1} \ll 1. \quad (4.61)$$

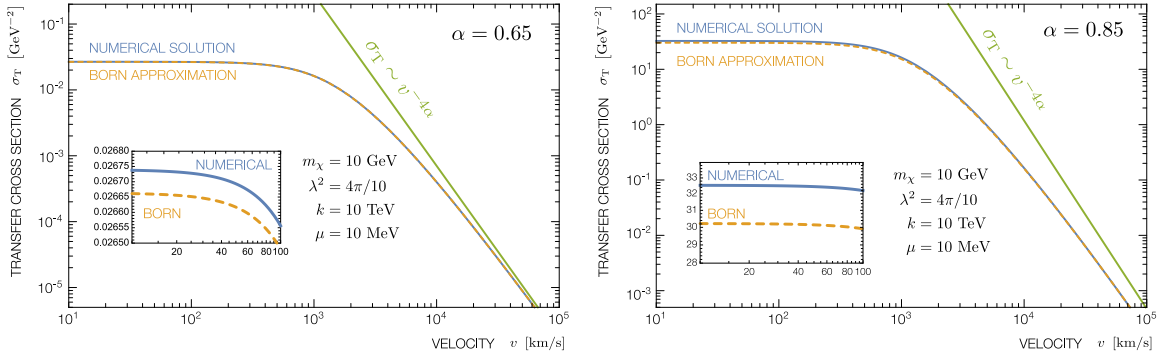


Figure 4.4: Velocity dependence of the transfer cross section in the Born regime. Comparison between the Born approximation and (blue/solid) and the numerical result from a sum of partial waves (orange/dashed). The results asymptotically scale like  $v^{-4\alpha}$  at large velocity (green).

Unlike the case of a Yukawa potential, there are no analytic expressions for the transfer cross section in the entire non-perturbative classical regime.<sup>8</sup> We show the scaling of the transfer cross section for the classical regime in the small mass gap/high velocity limit and give a closed form result in the low velocity regime below, see Appendix B.4.

**Continuum-mediated Born regime.** In the Born regime, the transfer cross section computed perturbatively from the  $1/2 < \alpha < 1$  continuum-mediated potential (4.42) is

$$\left(\frac{d\sigma}{d\Omega}\right)^{\text{Born}} = \frac{(\alpha_\chi^{\text{eff}})^2 m_\chi^2}{4m_1^4} (2\alpha - 1)^2 {}_2F_1(1, \alpha; 1 + \alpha; -|\mathbf{q}|^2/m_1^2)^2, \quad (4.62)$$

where  ${}_2F_1(1, \alpha; 1 + \alpha; -|\mathbf{q}|^2/m_1^2)$  is the hypergeometric function that encodes the mass gap. The transferred three-momentum,  $\mathbf{q}$ , satisfies  $|\mathbf{q}|^2 = \frac{1}{2}m_\chi^2 v^2(1 - \cos\theta)$  where  $\theta$  is the scattering angle in the center of mass frame. We compute the angular integral numerically.

We may examine (4.62) in the limits of large and small transferred three-momentum.

For a transfer momentum much larger than the mass gap,  $|\mathbf{q}| \gg m_1$ , the transfer cross sec-

<sup>8</sup>See Ref. [75] for a discussion of scattering in the limit of no mass gap.

tion is

$$\sigma_{\text{T}}^{\text{Born}} \approx \frac{\lambda^4 m_\chi^2}{16\pi k^4 (1-\alpha)} \left[ \frac{\Gamma(\alpha)}{\Gamma(1-\alpha)} \right]^2 \left( \frac{2k}{m_\chi v} \right)^{4\alpha} \quad |\mathbf{q}| \gg m_1 . \quad (4.63)$$

This matches the result from the gapless potential, (4.45). In the opposite limit,  $|\mathbf{q}| \ll m_1$ , the transfer cross section approaches a constant:

$$\sigma_{\text{T}}^{\text{Born}} \approx \frac{\lambda^4 m_\chi^2}{64\pi^2 \alpha^2 k^4 \Gamma(1-\alpha)^4} \left( \frac{2k}{m_1} \right)^{4\alpha} \quad |\mathbf{q}| \gg m_1 . \quad (4.64)$$

Figure 4.4 compares these asymptotic behaviors to a numerical solution.

Early astrophysical simulations of self-interacting dark matter assumed a constant  $\sigma_{\text{T}}$  and found that the cross sections required to address small-scale structure anomalies were inconsistent with bounds from the upper limits set by galaxy cluster collisions. One of the key insights of Ref. [293] was that suppression of the cross section at transfer momenta relative to a light mediator would alleviate this tension. In the continuum-mediated scenario, we see that the bulk mass parameter  $\alpha$  controls the velocity-scaling in the high-velocity Born limit. This parametric control is not possible for the exchange of a single mediator.

**Continuum-mediated classical regime.** Unlike in the Born regime, in the classical regime closed form results for the transfer cross section do not follow from straightforward calculation. While in the case of a Yukawa potential closed form expressions can be determined for the entire non-perturbative classical regime, see e.g. Ref. [293, eqn. (7)], analytic expressions for the continuum mediated transfer cross section are harder to come by. In the limit of a small mass gap/large velocity, one can determine its velocity dependence. In the opposite low velocity limit, one finds a closed form expression. The calculations are detailed in Appendix B.4.

One can write the transfer cross section in this regime as an integral over the impact parameter  $\rho$ . It is convenient to introduce the dimensionless quantities  $\xi = \rho/\rho_0$ , where  $\rho_0$  is a characteristic length scale defined from the potential (4.42),

$$\sigma_{\text{T}}^{\text{classical}} = 2\pi\rho_0^2 \int_0^\infty [1 - \cos\theta(\xi, m_1\rho_0)] \xi d\xi \quad \rho_0 \equiv \left[ \frac{\lambda^2}{2\pi^{3/2}m_\chi v^2 k^{2-2\alpha}} \frac{\Gamma(3/2 - \alpha)}{\Gamma(1 - \alpha)} \right]^{\frac{1}{3-2\alpha}}. \quad (4.65)$$

When  $m_1\rho_0 \ll 1$ , corresponding to the small mass gap/high velocity limit, the scattering angle  $\theta$  is a function of the ratio  $\xi$  only [75]. In this case, the transfer cross section depends on a non-integer power of the relative velocity,  $-4/(3 - 2\alpha)$ . A finite mass gap induces corrections to this scaling.

While this scaling holds in the small mass gap/high velocity limit of the classical regime, an approximate closed form solution for the transfer cross section can be computed for lower velocities. Following the methodology of Ref. [209], we calculate the transfer cross section in terms of the parameter

$$\beta = \frac{2\alpha_{\chi}^{\text{eff}} m_1}{v^2 m_\chi} (2\alpha - 1). \quad (4.66)$$

In the limit  $\beta \gg 1$ , the transfer cross section is found to approximately be

$$\sigma_{\text{T}}^{\text{classical}} \approx \frac{\pi}{m_1^2} \left[ 1 + \log\left(\frac{\beta}{\log\beta}\right) - \frac{(2\alpha - 1)}{\log\beta} + \frac{(2\alpha - \frac{3}{2})}{\log\left(\frac{\beta}{\log\beta}\right)} \right]^2. \quad (4.67)$$

See Appendix B.4.2 for details. Our analytical result is shown to be in good agreement with the numerical solution to the Schrödinger equation, see Figure 4.5.

**Summary of Velocity Scaling** We summarize the velocity scaling in the different regimes:

$$\sigma_T \sim \begin{cases} v^0 & \text{Born (low velocity)} \\ v^{-4\alpha} & \text{Born (high velocity)} \\ v^{-4/(3-2\alpha)} & \text{Classical} \\ \text{no simple scaling} & \text{Resonant} \end{cases} \quad (4.68)$$

The dependence on the bulk mass parameter  $\alpha$  is a key difference from the standard 4D, single mediator case. The 4D scenario corresponds to  $\alpha = 1$ .

### 4.6.3 Numerical Methodology and Results

To make quantitative statements about the transfer cross section that extend to the classical and resonant regimes, we numerically solve the Schrödinger equation using a partial wave expansion,

$$\sigma_T = \frac{4\pi}{(m_\chi v/2)^2} \sum_{\ell} (\ell + 1) \sin^2(\delta_{\ell+1} - \delta_{\ell}) , \quad (4.69)$$

where  $\delta_{\ell}$  is the scattering phase shifts partial wave  $\ell$ . We follow the methodology of Ref. [293] with a more relaxed numerical algorithm described in Appendix B.6.

For bulk mass parameters  $\alpha \leq 1/2$ , the potential dominates over the repulsive centrifugal barrier for  $r \rightarrow 0$ . In this case one must place a short distance cutoff on  $r$  that encodes data from the UV completion. Practically, the partial wave expansion converges poorly and becomes numerically intractable for potentials more singular than  $r^{-2}$ . As such, we restrict the bulk mass parameter to the range  $1/2 < \alpha < 1$ , where the upper limit is the theoretical upper limit established in Section 4.3.3.

**Realization of the transfer cross section regimes.** The scattering rate density relevant for thermalizing the cores of dark matter halos is the transfer cross section times the dark matter number density,  $\sigma_T n_\chi \sim \sigma_T \rho_\chi / m_\chi$ . The dark matter density  $\rho_\chi$  is a measured input, so a useful figure of merit is the ratio  $\sigma_T / m_\chi$ , for which the typical value required for small-scale structure is  $\sigma_T / m_\chi \sim \mathcal{O}(1)$ .

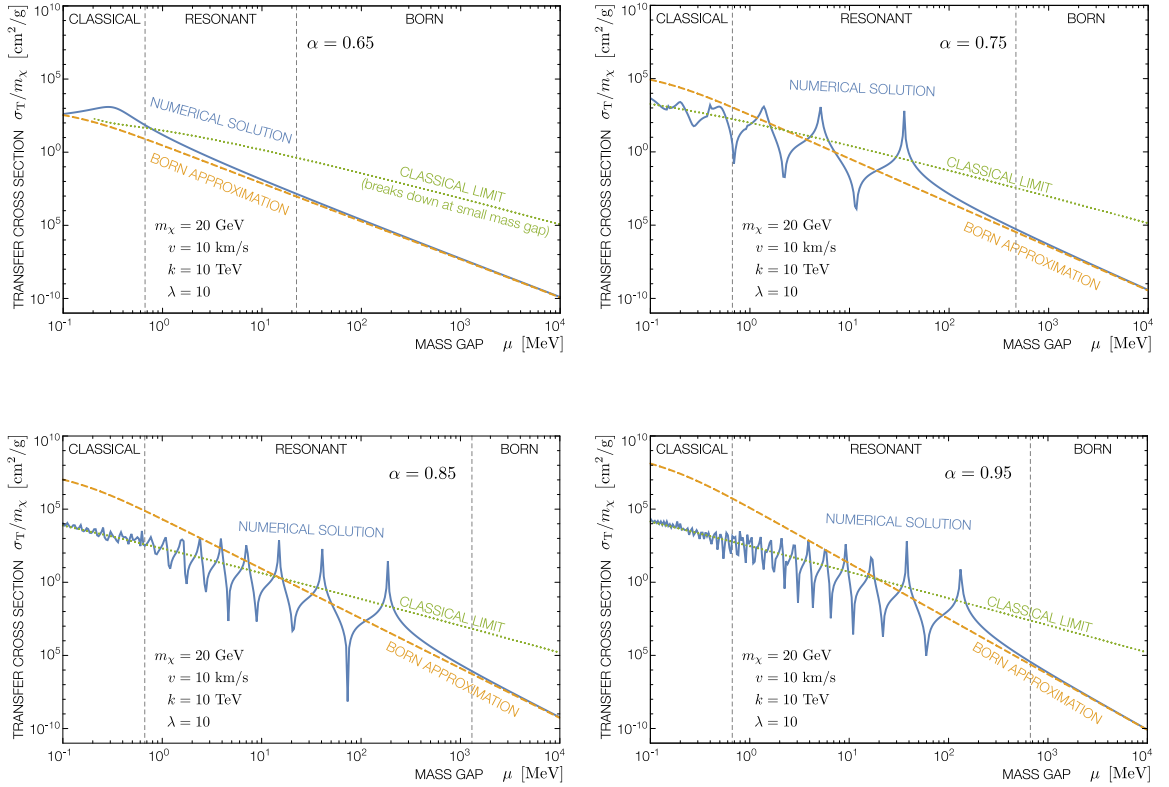


Figure 4.5: Comparison of the numerically calculated transfer cross section to the analytic approximations introduced in Figure 4.3. The general behavior displays distinct regimes, similar to that of a single mediator, see e.g. Ref. [293, Fig. 2]. The blue line is the numerical solution. Orange (dashed)/green (dotted) lines correspond to analytic Born/classical approximations valid in their respective regimes; (4.62) and (4.67) .

To demonstrate the self-interacting dark matter regimes discussed in this section, Figure 4.5 scans the ratio  $\sigma_T / m_\chi$  over the mass gap  $\mu \sim m_1$  for different values of the

bulk mass parameter  $\alpha$ . These one-dimensional plots are slices of the transfer cross section over the two-parameter space of regimes in Figure 4.3. For each of these plots, large values of  $\mu$  correspond to the low-velocity Born regime. Figure 4.5 confirms the agreement with the Born approximation in this limit. As one decreases  $\mu$ , one moves upward and to the right in Figure 4.3, crosses the resonant regime with pronounced peaks in the cross section, and finally enters the classical regime. Figure 4.5 confirms that our approximate analytical results in the classical regime agree with the numerical solution to the Schrödinger equation. For smaller values of  $\alpha$ , our approximation for the transfer cross section in the classical regime breaks down as expected.

**Resonances and the bulk mass parameter.** The resonance structure of transfer cross section can be very sensitive to the bulk mass parameter  $\alpha$ . This parameter has no analog in 4D self-interacting dark matter models with a single mediator and represents a new model degree of freedom to affect phenomenology. The bulk mass feeds into both the overall effective coupling  $\alpha_\chi^{\text{eff}}$  (4.59) and the slope of the potential at short distances (4.42). We demonstrate the  $\alpha$ -sensitivity of the transfer cross section with a set of benchmark parameters in Figure 4.6. The two plots scan over both  $\alpha$  and the relative velocity  $v$  to highlight the interplay in the resonance structure.

We remark that Figure 4.6 plots  $\sigma_{\text{T}} m_\chi^2$  to make it straightforward to use scaling relations to connect results to different parameters. The partial wave expansion (4.69) makes it clear that  $\sigma_{\text{T}} \sim m_\chi^{-2}$ . The additional  $m_\chi$  dependence of the phase shifts  $\delta_\ell$  depend only on the ratios  $m_\chi/m_1$  and  $m_\chi/k$ ; see Appendix A.2. Thus the plots are unchanged by

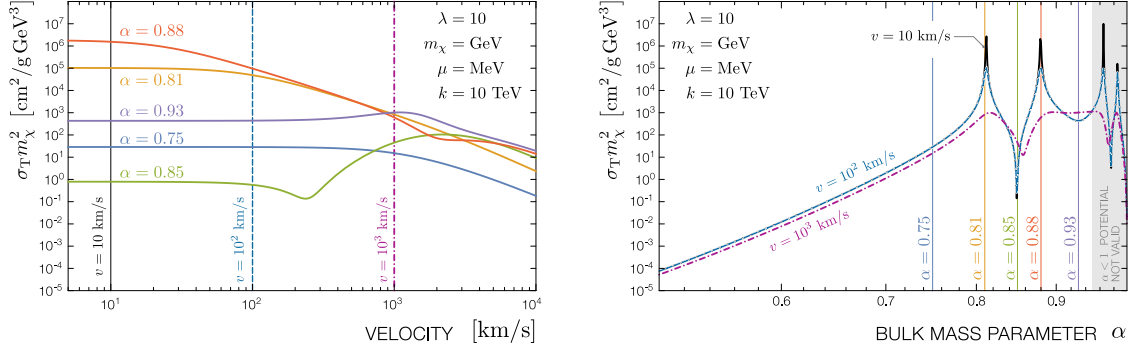


Figure 4.6: Transfer cross section as a function of relative dark matter velocity  $v$  (left) and bulk mass parameter  $\alpha$  (right). The plots demonstrate the presence of resonances and anti-resonances. Vertical markers identify parameters used in the opposite plot.

the following rescaling of parameters by  $\eta$ :

$$m_\chi \rightarrow \eta m_\chi \quad k \rightarrow \eta k \quad \mu \rightarrow \eta \mu . \quad (4.70)$$

This extends the scaling arguments in Ref. [293] to the case of a continuum mediator.

#### 4.6.4 Comparison to Astrophysical Data

The scattering rate,  $\sigma_T v (\rho_\chi/m_\chi)$ , determines the energy transfer in dark matter halos. Figure 4.7 plots the figure of merit  $\sigma_T v/m_\chi$  for a set of benchmark parameters compared to the astronomical data points presented in Ref. [293]. The plot includes a Yukawa potential to represent the 4D single mediator case. These benchmarks correspond to a range of bulk mass parameters  $\alpha$ . The other parameters are set to give fits of comparable  $\chi^2$  to the Yukawa potential. We remark that this is not a scan to minimize  $\chi^2$  and is only meant to demonstrate the range of parameter possibilities that can fit the data. The ultimate cause for the dark matter halo density profile observations may partially (or wholly) include contributions from baryonic feedback, see Ref. [49] for a recent status report. Thus



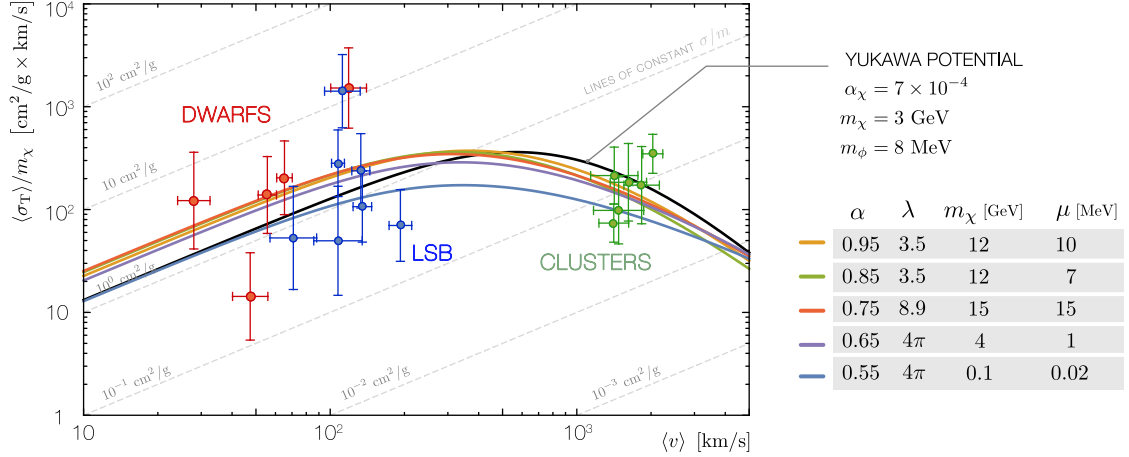


Figure 4.7: Velocity dependence of the thermally averaged transfer cross section. The parameters are chosen to be reasonably fit astronomical data. A benchmark 4D self-interacting dark matter model with a scalar mediator is shown for comparison. The data points for velocities  $v \sim 30\text{--}200$  km/s are determined from the observed rotation curves of dwarf (red) and low-surface brightness galaxies (blue) respectively; points for velocities  $v \gtrsim 10^3$  km/s correspond to galaxy clusters (green) and are determined from stellar line-of-sight velocity dispersion data [200].

one may conservatively interpret the data in Figure 4.7 as upper limits on the transfer cross section for a viable model.

The mass hierarchy between the dark matter and lightest KK mass is comparable to that of the benchmark 4D self-interacting dark matter theory,  $m_\chi/m_\phi \sim \mathcal{O}(10^3)$ . While  $\lambda$  can vary over a few orders of magnitude, the effective coupling  $\alpha_\chi^{\text{eff}}$  remains approximately constant for the benchmarks in Figure 4.7. In the extreme case  $\alpha = 0.55$ , the effective coupling  $\alpha_\chi^{\text{eff}}$  is small compared to the other benchmarks. This is compensated by a small dark matter mass. This interplay between  $\alpha$  (i.e. the bulk mass) and the dark matter–mediator coupling  $\lambda$  may be used, for example, to maintain the fit to data in Figure 4.7 while adjusting a mediator–Standard Model coupling  $\lambda_{\text{SM}}$  to realize other phenomenology.

We remark that while we restrict to the range of bulk mass parameters  $1/2 < \alpha < 1$  for theoretical reasons, we also observe that the model phenomenology gives a mild preference for values away from the lower limit. For small values of  $\alpha \approx 0.55$ , reproducing the desired  $\langle \sigma_{\text{T}v} \rangle / m_\chi$  behavior requires sub-GeV dark matter and a Kaluza–Klein scale of  $\mathcal{O}(10 \text{ keV})$ , which may cause tension with cosmological constraints [94]. On the other hand, for large values of  $\alpha \rightarrow 1$ , one must take care to use the appropriate limiting form of the bulk propagator, as discussed in Section 4.5.2. Since the  $\alpha = 1$  case essentially describes a single 4D mediator, this limit approaches that of ordinary self-interacting dark matter models.

Beyond simply describing the model parameters that reproduce astrophysical data, it is also illustrative to plot a range of model parameters to see how they distort the  $\langle \sigma_{\text{T}v} \rangle / m_\chi$  behavior from the ideal case. Figure 4.8 presents such a scan over the mass gap  $\mu$  and  $m_\chi$  with other parameters fixed.

Varying the mass gap  $\mu$  primarily affects the behavior at low velocities (low momentum transfer), though it leads to an overall rescaling because it is a multiplicative factor in the effective coupling  $\alpha_\chi^{\text{eff}}$  (4.59). Thus for a set of parameters that fit the cluster data well, one can tune the mass gap to help fit the low-velocity data.

The dependence on the dark matter mass  $m_\chi$ , on the other hand, is highly non-trivial. One can see this because the phase shifts in (4.69) depend on the dimensionless combinations  $m_\chi/m_1$  and  $m_\chi/k$ , as described in Appendix A.2. Varying  $m_\chi$  thus affects two independent quantities in the numerical solution of the partial waves.

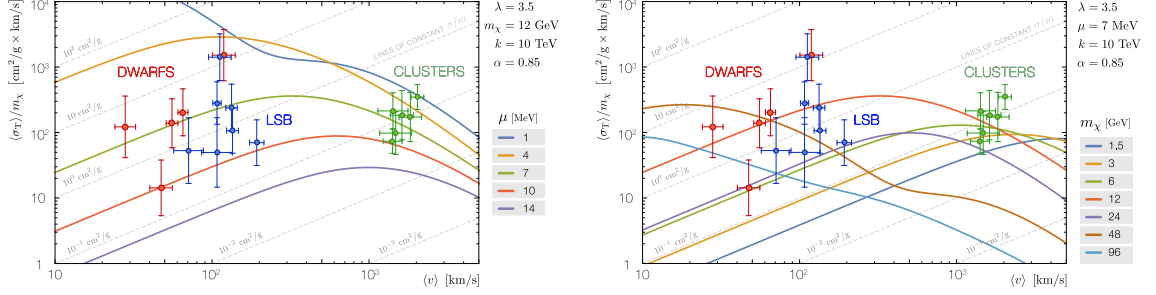


Figure 4.8: Velocity dependence of the thermally averaged transfer cross section, analogous to Figure 4.7, for a range of  $\mu$  and  $m_\chi$  choices to demonstrate the behavior with respect to these parameters.

#### 4.6.5 Comment on Annihilation and Relic Abundance

The purpose of this study is to demonstrate the distinctive self-interaction phenomenology of our model and we have remained agnostic about whether or not dark matter is a relic from thermal freeze out. Thus we have not restricted the dark matter mass  $m_\chi$  and bulk coupling  $\lambda$  to fit that of a thermal relic, even though such a restriction would itself be an interesting benchmark. Indeed, one of the constraints on typical 4D self-interacting dark matter models is that the required self-interactions for small scale structure are generally too large for dark matter to be a thermal relic in the simplest cosmological scenarios. Recent work has shown that in the presence of bulk self-interactions, the high KK-number states of the 5D scalar are not valid asymptotic states due to the breakdown of the narrow width approximation [84]. As a result, the production of KK modes is heavily suppressed by phase space. This can lead to a tantalizing mechanism to suppress the annihilation rate: by increasing the bulk scalar self-interaction—a new parameter in the theory—one may control the total number of effectively allowed final states. We leave this topic for future work.

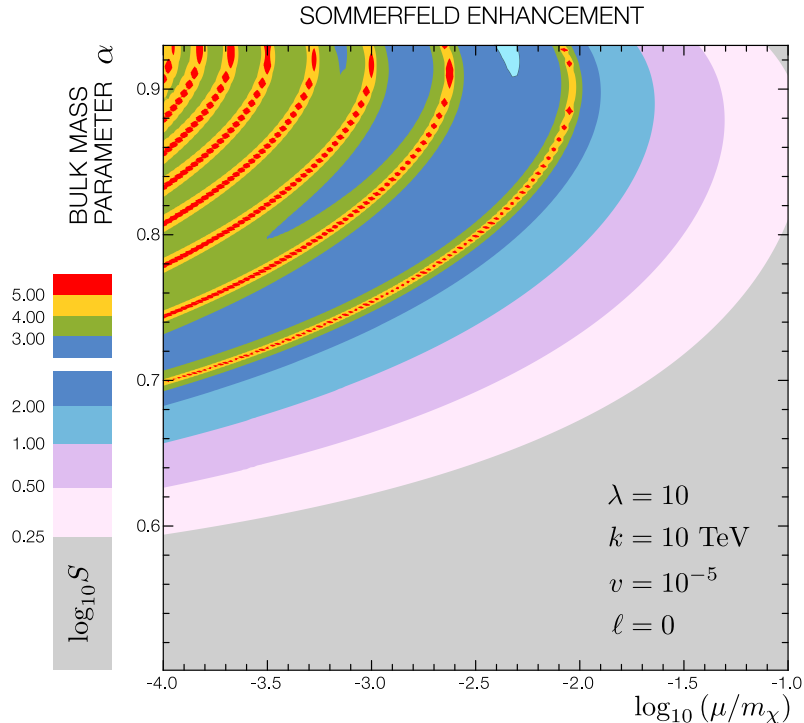


Figure 4.9: Sommerfeld enhancement of the  $\ell = 0$  partial wave for a range of  $\alpha$  and the ratio  $\mu/m_\chi$ . Our approximation of the potential breaks down near  $\alpha = 1$  and hence this region is removed.

## 4.7 Continuum-Mediated Sommerfeld Enhancement

The same dynamics that generate dark matter self-interactions also lead to Sommerfeld enhancements. Sommerfeld enhancements encode the effect of the long-range force on a short-distance process (annihilation) and so depend on the solution to the two-body Schrödinger equation at the origin,  $\Psi(0)$  [182, 18, 222, 190, 189, 65, 177]. In contrast, the dark matter self-interactions that are the main focus of this paper are intrinsically long-ranged.

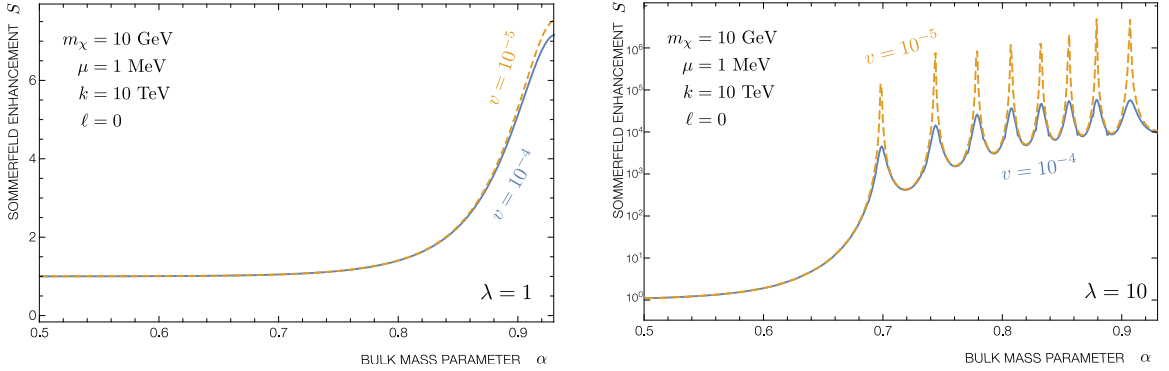


Figure 4.10: Sommerfeld enhancement of the  $\ell = 0$  partial wave as a function of  $\alpha$ .

Diagrammatically both processes involve a ladder of exchanged force mediators between the dark matter initial states. When the potential has a mass gap, the potential supports resonances at large enough coupling.

We investigate the Sommerfeld effect in our continuum-mediated model. The continuum-mediated potentials we consider are shorter-ranged than the  $1/r$  factor in Yukawa potentials. Since the Sommerfeld enhancement is a long range effect, one may expect that the continuum-mediated Sommerfeld effect is suppressed as compared to the Coulomb case. However, the possibility of resonances may compensate for this and a detailed quantitative analysis is required.

Analytical results for Sommerfeld enhancement are only available for Coulomb potentials. More generally, one must use numerical methods to solve for the enhancement from more general potentials, see e.g. Ref. [33]. This method is valid for potentials that scale like  $r^{-1}$  to  $r^{-2}$ , corresponding to bulk masses  $1/2 \leq \alpha \leq 1$  in our continuum-mediated model. Potentials that are strictly steeper than  $r^{-2}$  require a separate treatment because the potential term dominates the centrifugal term at small distances. These potentials require a short-distance cutoff as expected from a low-energy effective theory.

We numerically explore the Sommerfeld enhancement over the range of bulk masses  $1/2 \leq \alpha < 1$  range for a continuum mediator with a mass gap. This is described by the same potential used for self-interactions, (4.42). To avoid the breakdown of asymptotic approximations described in Section 4.5, we restrict to  $\alpha \lesssim 0.9$ . Figure 4.9 shows the Sommerfeld enhancement as a function of  $\alpha$  and  $\mu/m_\chi$  for a benchmark coupling  $\lambda = 10$ . The key result is that Sommerfeld enhancement occur even when  $\alpha < 1$  where the potential is shorter-ranged than a Yukawa potential. The enhancement increases for smaller mass gap relative to the dark matter mass,  $\mu/m_\chi$ . For example for  $\mu/m_\chi = 10^{-4}$  we find  $S \sim 10$  for  $\alpha \sim 0.66$ .

Resonances appear in a nontrivial pattern in the  $\alpha$ - $\mu$  plane. With the assumptions in Figure 4.9, the theory exhibits resonant behavior occurring for bulk masses as low as  $\alpha \sim 0.7$ . These resonances are expected to vanish at lower coupling; this is shown in Figure 4.10 where the Sommerfeld enhancement is plotted for constant  $\mu$ . The large coupling case  $\lambda = 10$  exhibits resonances, while a smaller coupling  $\lambda = 1$  does not. In this case the Sommerfeld effect is found to quickly decrease with  $\alpha$ .

The Sommerfeld enhancement decreases quickly with  $\alpha$  and eventually vanishes near  $\alpha = 1/2$ , corresponding to a  $r^{-2}$  potential. We remark that the enhancement for an ungapped  $V(r) \propto r^{-2}$  potential can be solved exactly. In this case, the centrifugal term has the same scaling as the potential so that the  $\ell = 0$  solution is singular and dependent on the EFT cutoff. To the best of our knowledge, Sommerfeld enhancement for this case has not been discussed in the literature. We present details of this calculation in Appendix B.5. We find  $S = 1$  whenever the dark matter mass is much smaller than the EFT cutoff. In

other words, the  $1/r^2$  potential is too short-ranged to induce any Sommerfeld enhancement, confirming the numerical result in Figure 4.9.

## 4.8 Conclusion

We propose a model where dark matter self-interacts through a continuum of 4D mediators. This generalizes work on self-interacting dark matter that has otherwise focused on the case of a single massive mediator producing a Yukawa potential. A continuum mediator may arise in a strongly-coupled gauge sector. We assume that this mediator sector is nearly conformal so that its features are dictated by symmetry. Applications of the self-interacting dark matter paradigm to small-scale structure anomalies require a mass gap to cut off the potential at long distances. A natural choice to realize this mass gap is to assume that the strongly-coupled sector has a large number of colors so that the theory is described holographically by a brane-localized dark matter interacting with a bulk field in a slice of 5D AdS space.

We present a concrete realization where the 5D continuum mediator is a scalar. We address aspects of effective field theory and constraints from experiments and cosmology. The key parameter that characterizes the hallmark features of our model is  $\alpha$ , which encodes the scalar field's bulk mass and maps onto the conformal dimension  $\Delta$  of the dual scalar operator.

We evaluate the non-relativistic potential induced by a continuum mediator with a mass gap using the spectral representation and asymptotic expressions for the 5D propagator. We obtain simple closed-form expressions for the  $\alpha < 1$  and  $\alpha = 1$  cases and validate

them numerically. The  $\alpha = 1$  case corresponds to a Yukawa potential. At long distances, the potential scales like a non-integer power,  $V \sim r^{2\alpha-3}$ . We focus on the range  $1/2 < \alpha \leq 1$  where calculations are tractable and the potential satisfies constraints from CFT unitarity.

The astronomical phenomenology of dark matter self-interactions depends on the transfer cross section,  $\sigma_T$ . We calculate this quantity in the continuum-mediated scenario and demarcate three types of qualitative behavior—the Born, resonant, and classical regimes. These regimes are qualitatively similar to those of a single 4D mediator, but in the continuum-mediated model the regimes depend on  $\alpha$  in addition to the strength of the dark matter coupling and mass gap.

The velocity-dependence of the transfer cross section allows a self-interacting dark matter model to explain small-scale structure anomalies while avoiding cluster-scale constraints. In contrast to the single 4D mediator, the transfer cross section in the continuum-mediated model exhibits non-integer velocity scaling. For example, in the perturbative Born regime,  $\sigma_T \sim v^{-4\alpha}$  for large velocities. In the non-perturbative classical regime,  $\sigma_T \sim v^{-4/(3-2\alpha)}$  in the small mass gap limit. In contrast, a Yukawa potential in both of these regimes has a transfer cross section scaling of  $\sigma_T \sim v^{-4}$ .

We present benchmark fits of the transfer cross section to astrophysical data. In the extreme case of bulk mass parameters  $\alpha \sim 0.55$ , fits typically require sub-GeV dark matter and sub-MeV mass gaps, which may be cosmologically challenging. Larger values of  $\alpha$  permit higher mass scales so long as the ratio of the dark matter mass to the mass gap is  $m_\chi/\mu \sim 10^3$ . Larger bulk masses cause KK mode profiles to localize away from the UV brane that contains dark matter.



Thus larger bulk masses typically require larger dark matter–mediator couplings between the dark matter and mediator.

Our model necessarily leads to continuum-mediated Sommerfeld enhancement. We demonstrate the pattern of resonances that occur in the  $(\mu, \alpha)$  plane. The enhancements vanish as  $\alpha \rightarrow 1/2$ , consistent with our analytical results for a  $1/r^2$  potential.

We conclude that models of dark matter with continuum mediators introduce novel power-law scalings in self-interaction effects. The bulk mass parameter,  $\alpha$ , has no analog in standard 4D self-interacting dark matter models and is a new way to control the phenomenology. Since the bulk mass controls the localization of the mediator, it naturally plays a role in possible effective couplings to the Standard Model. These observations open new possibilities for dark matter phenomenology.

## Chapter 5

# Holographic Dark Photon

## 5.1 Introduction

Nature may contain hidden sectors beyond the Standard Model (SM): collections of fields with only modest interactions with fields outside their sector [255, 256, 257, 121, 10, 31]. Dark matter may be part of such a hidden sector with additional fields that mediate interactions with ordinary matter. A benchmark example of this type of *dark sector* mediator is the dark photon: a hidden sector with a  $U(1)$  gauge symmetry that kinetically mixes with hypercharge [183, 151].

Most dark sector models contain a small number of mediator fields. An alternative limit is when the dark sector dynamics are described by not only a large number, but a *continuum* of states. This can occur if the mediator is part of a nearly conformal sub-sector or—by holographic duality—if the mediator is a higher-dimensional field in an appropriately warped spacetime. The physics of this type of sector has been explored phenomenologically under the framework of Randall–Sundrum-like models [240, 241], so-called unparticles [285, 73, 145, 146], or conformal hidden sectors [158, 300]. The specific proposal that these dynamics could be connected to a dark sector mediator is presented in Reference [45]. We use the phrase *warped dark sector* to describe this general class of continuum mediator models and specialize to the description with respect to a warped extra dimension. In this paper, we present the theory and phenomenology of a *continuum dark photon*: a continuum spin-1 mediator that interacts with ordinary matter through kinetic mixing.

Quantum fields whose excitations include a continuous range of masses are *generalized free fields* [164]. They are characterized by their Källén–Lehmann spectral representation [195, 226]. The modern manifestation of generalized free fields are bulk fields

in an extra dimension that are holographically related to a large- $N$  strongly coupled theory; the fields are ‘free’ in the sense that the correlation functions factorize into products of two-point functions in the  $N \rightarrow \infty$  limit [113, 116]. In particle physics, Georgi named these continua *unparticles* [156, 155], though earlier models embody some salient features [217, 296, 273]. One may introduce a gap so that the unparticle continuum begins at finite mass [284, 141, 101], in which case we may identify these constructions with hidden valley models [285]. The *unhiggs* proposal draws upon the AdS/CFT correspondence to build a model of unparticle electroweak symmetry breaking [126, 281, 282, 125, 119, 118] (see Ref. [216] for an earlier realization).

The use of warped extra dimensions as a perturbative model for generalized free fields weakly interacting with ordinary particles is sometimes called the AdS/unparticle correspondence [57, 145, 146]. Applications of this approach include models with a Higgs particle plus continuum (quantum critical Higgs) [34], continuum partners in supersymmetry [58, 59, 153], composite Higgs theories [91, 225], continuum dark matter [90, 89], and continuum hidden-sector states [205, 68]. Some phenomenological aspects of continuum mass fields were studied as the limit of densely packed Kaluza–Klein modes. This can occur in little string theory models [12] and in limit of where the widths of Kaluza–Klein modes becomes larger than the mode spacing [84].

A key element of the most recent constructions has been the Cabrer–Gersdorff–Quiros model of a soft-wall background to engineer a gapped continuum spectrum [53, 243].

Early soft-wall constructions focused on holographic realizations of QCD [204, 92], though the technique was quickly realized as a tool models addressing the electroweak hierarchy problem [124, 30, 29].

In this manuscript we model the continuum dark photon as a 5D bulk abelian gauge field in  $\text{AdS}_5$  that interacts with 4D matter localized on a UV brane. Early studies of 5D bulk abelian gauge fields focus on Randall-Sundrum models with an infrared brane that produce a discrete spectrum of Kaluza-Klein excitations of the SM gauge fields [96, 253]. Randall and Schwartz present a systematic derivation of position/momentum space bulk gauge propagators in [258, 259]. This early literature only qualitatively mentions possibility of a bulk Higgs, noting that a bulk vacuum expectation value (vev) is challenging from the point of view of electroweak naturalness [71, 186]. Ref. [99] constructs an explicit model with a bulk Higgs that points out the challenges of analytically solving for the spectrum of the bulk gauge bosons due to the position-dependent vev; the authors of that work construct an approximation based on a brane-localized vev.

An unbroken gauge field in AdS/CFT has been discussed in Refs. [57, 145, 146] as well. In the context of the Randall-Sundrum I model, a bulk (IR-localized) scalar vev has been considered in [99, 55, 15, 16]. Later work explores the more general phenomenology of a hidden sector bulk abelian gauge field with parametrically small interactions with the SM [26, 241, 240]; see Ref. [28] for the case of Yang–Mills gauge fields. These constructions are limited to the cases where the abelian gauge symmetry is either unbroken or broken by the Stückelberg mechanism. Gauge symmetry breaking in an extra dimension can be realized via the implementation of appropriate boundary conditions on the brane(s). This

possibility has for instance been used in [88, 93, 240, 241]. Dark sector models featuring a dark photon in a warped extra dimension have been considered in Refs. [268, 267, 265, 266]. Our study goes beyond this by Higgsing the  $U(1)$  gauge symmetry with a non-trivial bulk vev and taking the limit of an infinite extra dimension so that the bulk fields have a continuum spectrum.

Our simple  $U(1)$  breaking model displays a nontrivial gauge spectrum with possibilities of gapped continuum and discrete modes. Such nontrivial spectra are not unfamiliar, they usually appear in soft-wall models where the metric-dilaton system gives a non-trivial, non-AdS background, see e.g. [204, 171, 172, 29, 124, 53, 299, 243]. In our case, the possible metric backreaction in the deep IR influences the spectrum only at high masses, above a given mass threshold. Below this threshold the metric can be effectively considered as AdS. The nontrivial features of the spectrum are solely the consequence of the presence of the  $U(1)$ -breaking vev over the AdS background.

Spontaneously broken gauge symmetries in AdS open new possibilities for realistic hidden sector model building. The  $AdS_5$  geometry with a Minkowski UV brane naturally lends itself to warped dark sector models [45]. These models describe strongly interacting hidden sectors with low-mass states and weak coupling to the SM

Beyond theoretical motivations, our study will lead to a model of a dark photon whose properties greatly differ from the much-studied standard particle dark photon. Studying well-motivated scenarios other than the standard ones is important to avoid experimental bias and to uncover and motivate possibilities of searches for the dark sector. The holographic continuum dark photon model that we will present can be taken as an

incentive to consider non-standard, well-motivated dark sector candidates in experimental searches.

### 5.1.1 Outline

Our study of a simple broken  $U(1)$  model in AdS spreads into various directions, both theoretical and phenomenological. We thus end this introduction with a guide to the various sections and their relationship.

#### Basics

The model is defined in section 5.2. Basic quantities such as equations of motions and propagators are derived in sections 5.2 and 5.3. In section 5.2 we also evaluate in which conditions and at which location a backreaction of the bulk metric due to the Higgs vev occurs. Throughout this study we do not compute explicitly the backreaction to avoid unnecessarily technical developments, when needed we rather assume the presence of a IR brane that truncates the metric.

#### Holography and related developments

We give the general boundary action in section 5.3.3 and, as an aside, study the notion of Goldstone equivalence theorem arising in the model in Section 5.8. We investigate the explicit form of the boundary action over the parameter space in Section 5.4. This is done either via exact solving or via an approximate WKB method. The knowledge of the location of the backreaction obtained section 5.2 plays a role here. In Section 5.4.2 we present the results of a WKB method that computes the boundary action for a vev

configuration close to the one respecting AdS isometries. We give details for this method in Appendix C.2. This near-AdS WKB method is not the same as the one used to compute the discrete spectrum in section 5.4. Finally, in section 5.9 we study the properties of the dual CFT model in regions of the parameter space where AdS/CFT applies (at least in its standard form). Table 5.1 provides a summary of the main theoretical results.

### Continuum dark photon model

In section 5.5 we lay out a dark photon model based on the  $U(1)$  model in  $\text{AdS}_5$ . We compute basic quantities needed for phenomenology such as the spectral distribution and squared matrix elements for two specific benchmark scenarios. Finite temperature effects in our  $\text{AdS}_5$  model are studied in section 5.6. In particular we show that unwanted cosmological dark radiation from the dark sector is naturally removed if there is a brane in the far IR, leading effectively to a “ultracold freeze-out” of the hidden sector. A subsequent cosmological scenario is presented. In section 5.7.3, we present bounds from an array of experimental and astrophysical data. This partly relies on a technique we introduce to accurately recast bounds on 4D models into bounds on continuum models. Finally, non-standard signatures arising in our dark-photon model are briefly discussed.

#### 5.1.2 Summary of Results

The basic setup is a  $U(1)$  gauge field in  $\text{AdS}_{d+1}$  in the presence of a bulk Higgs with mass  $\mu^2 = (\alpha^2 - \frac{d^2}{4})R^{-2}$ , which develops a vev triggered from the boundary.  $R$  is AdS length.

- Working in the general  $R_\xi$  gauge in the bulk and on the boundary, we provide the most



general brane-to-brane propagators of the vector sector, (5.57), and partly solve the more intricate pseudoscalar sector (*i.e.* the Goldstone and  $A_z$  degrees of freedom), (5.55) and (5.56). We compute the most general boundary action for the set of boundary conditions which allow vector and Goldstone fields on the boundary in Section 5.3.3.

- In Section 5.8 we identify a Goldstone equivalence theorem (GET) for both AdS transition amplitudes and for boundary-localized degrees of freedom, for any  $\alpha$ , expressed in terms of Dirichlet modes of a specific combination of the Goldstone and  $A_z$  fields for the former, (5.158), and their respective boundary components for the latter, (5.160).
- Through a combination of exact solutions and WKB analysis, in Section 5.4 we show that the spectrum may be continuous, continuous with a mass gap, or discrete, depending on the bulk mass parameter  $\alpha$ . Linear Regge behaviour occurs for  $d = 4, \alpha = 0$ . The spectrum also contains a pole corresponding to a  $d$ -dimensional gauge mode which receives mass due to symmetry breaking. A summary is shown in Tab. 5.1.
- The backreaction of the metric due to the bulk vev is found to occur for  $\alpha < \frac{d}{2}$  and its location is estimated in Section 5.4.3. We show that the backreaction influences the discrete spectrum only above a given mass threshold.
- We introduce a WKB method to find EOM solutions in the presence of near-AdS background (*i.e.* for a Higgs vev with  $\alpha$  near  $\frac{d}{2}$ ) in Section 5.4.2 (full details are given in appendix C.2), and find that the resulting boundary action gives rise to an approximate CFT whose parameters evolve logarithmically with the energy scale.

- Turning to CFT duals, in Section 5.9.2 we argue that for  $\alpha \gg \frac{d}{2}$  the CFT sector of the holographic theory is not affected by the  $U(1)$  breaking since the CFT current is conserved. For  $\alpha = \frac{d}{2}$  we argue that the CFT sector of the holographic theory contains an exactly marginal operator which develops a vev due to the mixing with the  $U(1)$ -breaking elementary sector. As a result the  $U(1)$  CFT current is non-conserved and we show that, like in AdS, the anomalous dimension is proportional to the square of the  $U(1)$ -breaking vev, (5.174).
- In Section 5.5 we introduce a simple dark photon model where the  $U(1)$  bulk gauge field kinematically mixes with the brane-localized visible photon. In Appendix C.3 we compute the effect of the dark photon exactly by dressing the visible photon propagator and show explicitly that this is equivalent to a suitable field redefinition of the brane component of the visible photon.
- We derive a simple formula for recasting existing dark photon bounds in the context of our model given by (5.122), and apply it to a set of constraints assuming our dark photon decays invisibly to bulk states in Section 5.7.3. We find that in general, bounds usually associated with larger dark photon masses may extend to the low mass gap regime due to contributions from heavier modes in the spectrum.
- In Section (5.6.5) we consider the case where brane-localized fermionic dark matter freezes out through annihilation into continuum dark photons, and show constraints on the dark matter coupling to the dark photon  $\alpha_\chi$  and dark matter mass  $m_\chi$  such that the dark matter is a thermal relic.

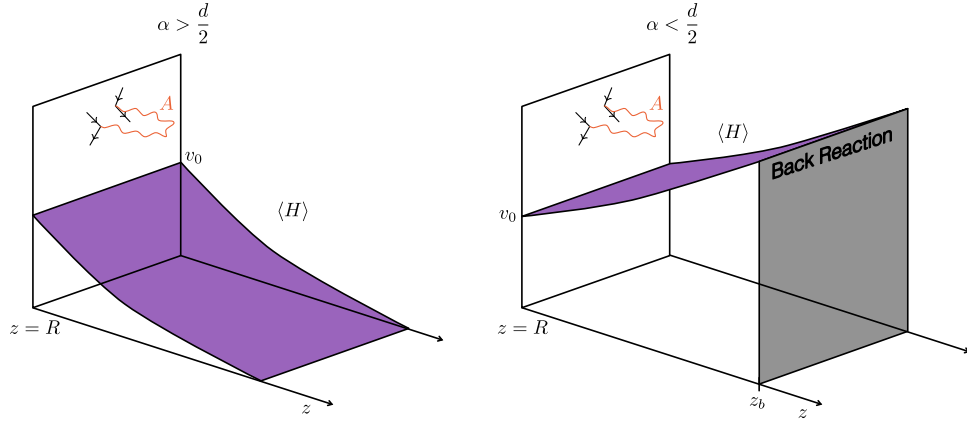


Figure 5.1: The set up for  $\alpha > d/2$  (Left) and  $\alpha < d/2$  (Right). The scalar vev profile as well as the location of the UV brane are shown for both cases. For  $\alpha < d/2$ , an backreaction occurs in the IR due to the non-negligible scalar vev profile.

We find that in the absence of an isolated pole, the preferred value for the dark matter coupling  $\alpha_\chi$  is significantly larger than non-continuum models.

## 5.2 A Broken $U(1)$ in $\text{AdS}_{d+1}$

We lay down the theory of a  $U(1)$  gauge field  $A_M$  propagating in an  $\text{AdS}_{d+1}$  background truncated by a  $d - 1$ -brane (*i.e.* a domain wall or defect) towards the AdS boundary *i.e.* “in the UV”. The  $U(1)$  symmetry is broken by the vacuum expectation value of a bulk scalar  $\Phi$ , which is spontaneously induced by a potential localized to the UV brane. This in turn, induces a non trivial bulk mass for the gauge field which modifies its propagation. The bulk scalar is referred to as the “Higgs field”.

### 5.2.1 Geometry

We consider the Poincaré patch of  $\text{AdS}_{d+1}$  spacetime described in conformal coordinates by the metric

$$ds^2 = g_{MN} dx^N dx^N = \left(\frac{R}{z}\right)^2 (\eta_{\mu\nu} dx^\mu dx^\nu - dz^2). \quad (5.1)$$

where  $\eta_{\mu\nu}$  is the Minkowski metric in  $d$  dimensions:  $\eta = \text{diag}(1, -1, -1, \dots, -1)$ . We take the UV brane located at  $z = R$  except for the cosmological evolution discussed in section 5.6. Spacetime is truncated to the domain  $z \geq R$ .

Depending on the behaviour of the scalar vev in the bulk there can be a non-trivial backreaction of the metric. In this work solving the 5D gravity-scalar is not our focus, we will rather assume that an IR brane truncating the bulk towards the Poincaré horizon (*i.e.* “in the IR”) is present whenever the backreaction becomes nonnegligible. Parametric estimates for the backreaction and IR brane position are given in section 5.2.4.

### 5.2.2 Action and Gauge Fixing

In the coordinates of Eq. (5.1) the  $d + 1$  dimensional action for a  $U(1)$  gauge field  $A_M = (A_\mu, A_z)$  and complex scalar  $\Phi$  can be written as

$$S_{U(1)} = \int d^d x \int_R^\infty dz [\sqrt{g} \mathcal{L} + \sqrt{\bar{g}} \mathcal{L}_{\text{UV}} \delta(z - R)] \quad (5.2)$$

where  $\bar{g}$  is the induced metric on the brane yielding  $\sqrt{\bar{g}} = \left(\frac{R}{z}\right)^d$ . The bulk Lagrangian for the gauge field and scalar is

$$\mathcal{L} = -\frac{1}{4g_{d+1}^2} g^{ML} g^{NP} F_{MN} F_{LP} + g^{MN} (D_M \Phi)^\dagger (D_N \Phi) - \mu^2 \Phi^\dagger \Phi. \quad (5.3)$$

where the covariant derivative is defined as  $D_M = \partial_M - iA_M$ . The scalar has bulk mass  $\mu$ , the gauge field bulk mass is forced to be zero by the gauge symmetry. We assume the brane-localized Lagrangian

$$\mathcal{L}_{\text{UV}} = -\frac{r_{\text{UV}}}{4g_{d+1}^2} \eta^{\mu\rho} \eta^{\nu\sigma} F_{\mu\nu} F_{\rho\sigma} + c_{\text{UV}} R |D_\mu \Phi|^2 - V_{\text{UV}} \quad (5.4)$$

which contains a brane-localized kinetic term for both the gauge field and the scalar. The coefficients of the brane-localized kinetic terms for the gauge field and scalar  $r_{\text{UV}}$  and  $c_{\text{UV}}$  respectively, control the brane-localization of the of said fields. Taking the limit  $r_{\text{UV}}/R, c_{\text{UV}} \rightarrow \infty$ , results in the gauge field and scalar being completely localized to the UV brane..

The brane-localized potential for the scalar is chosen as

$$V_{\text{UV}} = -m_{\text{UV}}^2 R |\Phi|^2 + \lambda_{\text{UV}} R^{d-2} |\Phi|^4, \quad (5.5)$$

This potential spontaneously breaks the  $U(1)$  symmetry by inducing a finite vacuum expectation value for  $\Phi$ . It is convenient to parametrize the scalar field as

$$\Phi(x, z) = \frac{1}{\sqrt{2}} (h(x, z) + v(z)) \exp \left[ i \frac{\pi(x, z)}{v(z)} \right] \quad (5.6)$$

where  $h$  is the radial mode and  $\pi$  is the Goldstone mode such that the expectation value (vev) is given by

$$\langle \Phi(x, z) \rangle = \frac{v(z)}{\sqrt{2}}. \quad (5.7)$$

The vev's dependence on  $z$  is a result of the warped geometry inducing a nontrivial zero-mode for the bulk scalar. On the other hand since the brane is flat, the brane potential is  $x$ -independent as well as the vev.

## Gauge Fixing

After the  $U(1)$  symmetry is spontaneously broken and integrating the action by parts, both the bulk and brane-localized kinetic terms induce mixing between the  $d$ -dimensional gauge field  $A_\mu$ , the  $A_z$  component and the Goldstone  $\pi$ . We cancel these mixing terms using a Fadeev–Popov gauge fixing in the bulk and on the brane. The bulk gauge fixing action is

$$S_{\text{fix}}^{\text{Bulk}} = -\frac{1}{g_{d+1}^2} \int d^d x \int_R^\infty dz \left(\frac{R}{z}\right)^{d-3} \frac{1}{2\xi} \left[ \partial_\mu A^\mu - \xi z^{d-3} \partial_z \left( \frac{1}{z^{d-3}} A_z \right) + \xi \left(\frac{R}{z}\right)^2 g_{d+1}^2 v \pi \right]^2 \quad (5.8)$$

and the brane-localized gauge fixing action

$$S_{\text{fix}}^{\text{UV}} = -\frac{1}{g_{d+1}^2} \int d^d x \frac{g_{d+1}^2}{2\xi_{\text{UV}} R^{d-4}} \left[ \partial_\mu A^\mu + \xi_{\text{UV}} R^{d-4} \left( c_{\text{UV}} R v \pi - \frac{1}{g_{d+1}^2} \frac{R}{z} A_z \right) \right]^2 \Big|_{z=R}. \quad (5.9)$$

## The Full $U(1)$ Action

The complete  $U(1)$  action including gauge fixing is

$$S = S_{U(1)} + S_{\text{fix}}^{\text{Bulk}} + S_{\text{fix}}^{\text{UV}}. \quad (5.10)$$

At any point in the calculations the brane-localized limit  $r_{\text{UV}}/R \rightarrow \infty$ ,  $c_{\text{UV}} \rightarrow \infty$  can be taken, reproducing a  $U(1)$  model in  $d$ -dimensional flat space.

Finally we emphasize that for  $d \geq 3$  the interactions with gravitons in the bulk are non-renormalizable thus the model should be understood as a low-energy effective field theory (EFT). The cutoff scale of the EFT is tied to the  $(d+1)$ -dimensional Planck scale  $M_*$ . Validity of the EFT implies some bounds on the parameters that can be expressed in terms of  $M_*$ , with for example  $g_{d+1}^2 M_*^{d-3} \gtrsim 1$ ,  $RM_* \gtrsim 1$ .

### 5.2.3 Spontaneous Symmetry Breaking

The brane-localized potential  $V_{UV}$  introduced in Eq. (5.5) induces a finite vev for the complex scalar  $\Phi$ . The equation of motion (EOM) for  $\Phi$  is

$$\left[ -\partial^2 + z^{d-1} \partial_z \left( \frac{1}{z^{d-1}} \partial_z \right) - \left( \frac{\mu R}{z} \right)^2 \right] \Phi(x, z) = 0 \quad (5.11)$$

with the boundary condition

$$\left[ \partial_z \Phi - c_{UV} R \partial^2 \Phi + m_{UV}^2 R \Phi - 2\lambda_{UV} R^{d-2} |\Phi|^2 \Phi \right]_{z=R} = 0. \quad (5.12)$$

In the  $x$ -independent configuration corresponding to the VEV  $\langle \Phi(x, z) \rangle = v(z)$ , the vev bulk profile is determined by

$$\left[ z^{d-1} \partial_z \left( \frac{1}{z^{d-1}} \partial_z \right) - \left( \frac{\mu R}{z} \right)^2 \right] v(z) = 0 \quad (5.13)$$

with a boundary condition

$$\partial_z v(z) \Big|_{z=R} = -m_{UV}^2 R v(R) + \lambda_{UV} R^{d-2} v(R)^3. \quad (5.14)$$

The EOM for the vev has the solution

$$v(z) = N_v \left( \frac{z}{R} \right)^{\frac{d}{2} - \alpha} \left[ 1 + A \left( \frac{z}{R} \right)^{2\alpha} \right] \quad (5.15)$$

where we have defined the bulk mass parameter

$$\alpha^2 = \frac{d^2}{4} + \mu^2 R^2. \quad (5.16)$$

In principle  $-\infty < \alpha < \infty$ , here we choose  $\alpha > 0$  such that  $\alpha = \sqrt{\frac{d^2}{4} + \mu^2 R^2}$ . For simplicity

we take  $A \approx 0$  in our analysis.<sup>1</sup> The normalization, determined by (5.14), is

$$N_v = \frac{\frac{d}{2} - \alpha + m_{\text{UV}}^2 R^2}{\lambda_{\text{UV}} R^{d-1}} \quad (5.17)$$

Thus the vev profile we use in this work is

$$v(z) = v_0 \left( \frac{z}{R} \right)^{\frac{d}{2} - \alpha} \quad (5.18)$$

with

$$v_0 = \sqrt{\frac{b_{\text{UV}}}{\lambda_{\text{UV}} R^{d-1}}}, \quad b_{\text{UV}} = \frac{d}{2} - \alpha + m_{\text{UV}}^2 R^2. \quad (5.19)$$

Note that the symmetry breaking is encoded in the boundary condition Eq. (5.14). In the absence of the brane-localized potential, (5.14) would force the normalization of the vev profile to be zero thus preserving the  $U(1)$  symmetry.

### Effective Potential On the UV Brane

From (5.18) we can see that for  $\alpha > \frac{d}{2} + m_{\text{UV}}^2 R^2$ , the vev becomes imaginary and no longer corresponds to the minimum of the potential. In this case the  $U(1)$  symmetry is restored and the corresponding solution for  $N_v$  is trivial. This is due to the fact that the brane-localized potential receives contributions from bulk terms that have been integrated by parts. We can see this by considering that the brane-localized action

$$S_{\text{UV}} = \int d^d x \left[ \Phi^\dagger \partial_z \Phi + m_{\text{UV}}^2 R \Phi^\dagger \Phi - \lambda_{\text{UV}} R^{d-2} \left( \Phi^\dagger \Phi \right)^2 \right] \Big|_{z=R} \quad (5.20)$$

---

<sup>1</sup>For  $\alpha > \frac{d}{2}$  there is no backreaction, thus  $A = 0$  is enforced by requiring  $v(z) \rightarrow 0$  at  $z \rightarrow \infty$ . For  $0 \leq \alpha \leq \frac{d}{2}$  we assume that  $v(z)$  is well behaved on the IR brane, such that  $A \left( \frac{z}{R} \right)^{2\alpha}$  is  $O(1)$ . This implies that it is negligible near the UV brane where the important physics will take place.



where the derivative term is the result of integrating by parts when deriving the bulk EOM. The  $z$ -dependence of the bulk scalar  $\Phi$  is determined by the EOM (5.11). Fourier transforming along the  $d$  Minkowski like directions and making the field decomposition,

$$\Phi(p, z) = R^{\frac{3-d}{2}} K_{\Phi}(z) \Phi_0(p) \qquad K_{\Phi}(z) = \frac{f_{\Phi}(z)}{f_{\Phi}(R)} \qquad (5.21)$$

we find for the bulk profile

$$f(p, z) = N_{\Phi} z^{\frac{d}{2}} H_{\alpha}^{(1)}(pz) \qquad (5.22)$$

where  $p = \sqrt{\eta_{\mu\nu} p^{\mu} p^{\nu}}$  and we have imposed the Hartle-Hawking condition at  $z \rightarrow \infty$ , requiring a positive frequency solution. Therefore,

$$\partial_z \Phi(p, z) \Big|_{z=R} = R^{\frac{3-d}{2}} \left[ \frac{\frac{d}{2} - \alpha}{R} + p \frac{H_{\alpha-1}^{(1)}(pR)}{H_{\alpha}^{(1)}(pR)} \right] \Phi_0(p). \qquad (5.23)$$

The constant term contributes to the potential while the  $p$  dependent term contributes to the brane-to-brane two point function. Fourier transforming back into position space, we see that the brane-localized action becomes

$$S_{\text{UV}} = \int d^d x \frac{1}{R^{d-4}} \left[ \left( \frac{\frac{d}{2} - \alpha}{R^2} + m_{\text{UV}}^2 \right) \Phi_0^{\dagger} \Phi_0 - \lambda_{\text{UV}} \left( \Phi_0^{\dagger} \Phi_0 \right)^2 + \mathcal{O}(\partial^2) \right] \Big|_{z=R} \qquad (5.24)$$

and we can identify the effective potential

$$V_{\text{eff}} = - \left( \frac{\frac{d}{2} - \alpha}{R^2} + m_{\text{UV}}^2 \right) \Phi_0^{\dagger} \Phi_0 + \lambda_{\text{UV}} \left( \Phi_0^{\dagger} \Phi_0 \right)^2. \qquad (5.25)$$

We can now see that for  $\alpha > \frac{d}{2} + m_{\text{UV}}^2 R^2$  the vev is no longer finite, as the sign of the quadratic term in the effective potential goes from positive to negative. Since  $m_{\text{UV}}^2$  is a free parameter, we may tune its value such that the symmetry remains broken for all  $\alpha$ .

### 5.2.4 On Backreaction and IR brane

In our simplified approach to the background, we place an IR brane whenever a strong backreaction due to the vev, if any, would occur in the bulk. We explain in section 5.4.3 why this approach is a good approximation. The existence and location of the backreaction can be estimated by considering Einstein's equation. The cosmological constant of  $\text{AdS}_{d+1}$  is

$$\Lambda = -\frac{d(d-1)}{2R^2} \quad (5.26)$$

We compare  $g_{MN}\Lambda$  to the matter term  $M_*^{1-d}T_{MN}$  where  $M_*$  is the  $d+1$ -dimensional Planck mass. We have

$$T_{MN} = -2\frac{\partial\mathcal{L}}{\partial g^{MN}} + g_{MN}\mathcal{L} = \left(-\eta_{MN}\frac{d}{2}\left(\frac{d}{2}-\alpha\right) - \delta_{zM}\delta_{zN}\left(\frac{d}{2}-\alpha\right)^2\right)\frac{v_0^2}{R^2}\left(\frac{z}{R}\right)^{d-2-2\alpha} \quad (5.27)$$

Focusing on the  $N = M \neq z$  component, we get that the scalar becomes of order of the cosmological constant contribution for

$$\frac{d(d-1)}{2R^2} \sim \frac{d}{2}\left(\frac{d}{2}-\alpha\right)\frac{v_0^2}{R^2}\left(\frac{z_b}{R}\right)^{d-2\alpha}M_*^{1-d} \quad (5.28)$$

which translates as

$$z_b \sim R\left(\frac{(d-1)M_*^{d-1}}{\left(\frac{d}{2}-\alpha\right)v_0^2}\right)^{\frac{1}{d-2\alpha}}. \quad (5.29)$$

for  $\alpha < \frac{d}{2}$ .

For  $\alpha \geq \frac{d}{2}$ , the vev profile decreases fast enough so that no backreaction is induced in the bulk for any  $z > R$ . For  $\alpha < \frac{d}{2}$ , a backreaction occurs. However we see that, even when the vev takes values as large as  $v_0^2 \sim \frac{1}{R^{d-1}}$ , since  $M_* \gg \frac{1}{R}$ , the backreaction becomes

important far away from the brane and there is a finite region  $z \in [R, z_b]$  over which the metric is approximately AdS.

### 5.3 Propagators and Boundary Effective Action

Here we compute the propagators of the model. We then introduce the boundary effective action, which, at leading order, is simply built from brane-to-brane propagators.

The boundary conditions of a  $U(1)$  field are constrained by gauge symmetry. The set of boundary conditions relevant for our case is Neumann boundary conditions for the  $A_\mu$  component and the  $\Phi$  field, and Dirichlet boundary conditions for  $A_z$  (see *e.g.* [297]).

#### 5.3.1 Vector Sector

##### Vector Equation of Motion

Starting from the full  $U(1)$  action Eq. (5.10), we isolate the component of the gauge field transverse to the brane,  $A_\mu$ . To quadratic order in the fields and upon integrating by parts the action for the  $A_\mu$  field is

$$S \supset \frac{1}{g_{d+1}^2} \int d^d x \int_R^\infty dz \frac{1}{2} A_\mu \mathcal{O}^{\mu\nu} A_\nu + \frac{1}{g_{d+1}^2} \int d^d x \frac{1}{2} A_\mu (\mathcal{B}^{\mu\nu} - \eta^{\mu\nu} \partial_z) A_\nu |_{z=R} \quad (5.30)$$

with

$$\mathcal{O}^{\mu\nu} = \left(\frac{R}{z}\right)^{d-3} \left[ \eta^{\mu\nu} \partial^2 - \left(1 - \frac{1}{\xi}\right) \partial^\mu \partial^\nu - \eta^{\mu\nu} z^{d-3} \partial_z \left(\frac{1}{z^{d-3}} \partial_z\right) + \left(\frac{g_{d+1} v(z) R}{z}\right)^2 \right]. \quad (5.31)$$

and

$$\mathcal{B}^{\mu\nu} = r_{UV} \eta^{\mu\nu} \partial^2 - \left( r_{UV} - \frac{g_{d+1}^2}{\xi_{UV} R^{d-4}} \right) \partial^\mu \partial^\nu + c_{UV} R g_{d+1}^2 v_0^2. \quad (5.32)$$

In these notations the gauge field EOM is simply given by

$$\mathcal{O}^{\mu\nu} A_\nu = 0 \quad (5.33)$$

with boundary conditions given by

$$(\mathcal{B}^{\mu\nu} - \eta^{\mu\nu} \partial_z) A_\nu|_{z=R} = 0. \quad (5.34)$$

We Fourier transform along the Minkowski slices,  $A_\mu(x, z) = \int \frac{d^d p}{(2\pi)^d} e^{ip \cdot x} A_\mu(p, z)$  where  $p \cdot x = \eta_{\mu\nu} p^\mu x^\nu$ . We define  $p = \sqrt{\eta_{\mu\nu} p^\mu p^\nu}$ . We decompose the vector field into its transverse and longitudinal parts as

$$A_\mu(p, z) = \left( \eta_{\mu\nu} - \frac{p_\mu p_\nu}{p^2} \right) A_T^\nu(p, z) + \left( \frac{p_\mu p_\nu}{p^2} \right) A_L^\nu(p, z). \quad (5.35)$$

We define the gauge fields bulk mass on the UV brane,

$$m_A^2 = g_{d+1}^2 v_0^2. \quad (5.36)$$

The set of EOM and UV boundary conditions for the transverse and longitudinal parts is found to be

$$\mathcal{O}_T(p^2) A_T^\mu(p, z) = 0 \quad \mathcal{O}_L(p^2) A_L^\mu(p, z) = 0 \quad (5.37)$$

where the operators are defined by

$$\mathcal{O}_T(p^2) = \left( \frac{R}{z} \right)^{d-3} \left[ p^2 + \partial_z^2 - \frac{d-3}{z} \partial_z - m_A^2 \left( \frac{z}{R} \right)^{d-2-2\alpha} \right], \quad \mathcal{O}_L(p^2) = \mathcal{O}_T\left(\frac{p^2}{\xi}\right) \quad (5.38)$$

and the corresponding boundary conditions are

$$(\partial_z + \mathcal{B}_T(p^2)) A_T^\mu(p, z)|_{z=R} = 0 \quad (\partial_z + \mathcal{B}_L(p^2)) A_L^\mu(p, z)|_{z=R} = 0, \quad (5.39)$$

with

$$\mathcal{B}_T(p^2) = r_{UV} p^2 - c_{UV} R g_{d+1}^2 v_0^2 \quad \mathcal{B}_L(p^2) = \mathcal{B}_T\left(\frac{p^2}{\xi}\right). \quad (5.40)$$

## Vector Propagator

We calculate the propagators for the components of  $A_\mu$ . In  $d + 1$  dimensions, the vector propagator is given by the solution to

$$\mathcal{O}^{\mu\rho}\langle A_\rho(x, z)A_\nu(x', z')\rangle = ig_{d+1}^2\delta_\nu^\mu\delta^{(d)}(x - x')\delta(z - z') \quad (5.41)$$

where  $\mathcal{O}^{\mu\nu}$  is defined by (5.31) and satisfies the boundary condition Eq. (5.34). We Fourier transform and decompose the propagator for the gauge field into its transverse and longitudinal parts as

$$\langle A^\mu(p, R)A^\nu(-p, R)\rangle = -i\left(\eta^{\mu\nu} - \frac{p^\mu p^\nu}{p^2}\right)G_p^T(z, z') - i\left(\frac{p^\mu p^\nu}{p^2}\right)G_p^L(z, z') \quad (5.42)$$

where the transverse and longitudinal components of the propagator obey

$$\mathcal{O}_T(p^2)G_p^T(z, z') = g_{d+1}^2\delta(z - z') \quad \mathcal{O}_L(p^2)G_p^L(z, z') = g_{d+1}^2\delta(z - z') \quad (5.43)$$

with boundary conditions

$$(\partial_z + \mathcal{B}_T(p^2))G_p^T|_{z=R} = 0 \quad (\partial_z + \mathcal{B}_L(p^2))G_p^L|_{z=R} = 0. \quad (5.44)$$

### 5.3.2 Scalar Sector

#### Scalar Equations of Motion

Here we focus on the piece of the  $U(1)$  action which contains the radial mode  $h$ , the Goldstone  $\pi$  and the component of the gauge field which is normal to the brane,  $A_z$ . The pseudoscalars  $\pi$  and  $A_z$  are mixed. We introduce the dimensionless Goldstone field

$$a(x, z) = \frac{\pi(x, z)}{v(z)}.$$

The radial mode EOM is identical to the one for  $\Phi$ ,

$$\left(\frac{R}{z}\right)^{d-1} \left[ p^2 + z^{d-1} \partial_z \left( \frac{1}{z^{d-1} \partial_z} \right) - \left( \frac{\mu R}{z} \right)^2 \right] h = 0, \quad (5.45)$$

with boundary conditoin given by

$$\left[ \partial_z h + c_{\text{UV}} p^2 R h - m_h^2 R h - 3 \lambda_{\text{UV}} R^{d-2} v h^2 - \lambda_{\text{UV}} R^{d-2} h^3 \right]_{z=R} = 0 \quad (5.46)$$

where we have defined the brane-localized mass for the radial mode as

$$m_h^2 = \frac{2b_{\text{UV}}}{R^2}. \quad (5.47)$$

In the pseudoscalar sector, varying the action with respect to  $\pi$  and  $A_z$  gives respectively the EOM

$$\begin{aligned} - \left(\frac{R}{z}\right)^{d-1} v^2 \partial^2 a + \partial_z \left[ \left(\frac{R}{z}\right)^{d-1} v^2 (\partial_z a - A_z) \right] \\ + \xi v^2 \left(\frac{R}{z}\right)^{d-1} \left[ z^{d-3} \partial_z \left( \frac{A_z}{z^{d-3}} \right) - g_{d+1}^2 \left(\frac{R}{z}\right)^2 v^2 a \right] = 0, \end{aligned} \quad (5.48)$$

$$\begin{aligned} - \left(\frac{R}{z}\right)^{d-3} \partial^2 A_z + g_{d+1}^2 \left(\frac{R}{z}\right)^{d-1} v^2 (\partial_z a - A_z) \\ + \xi \left(\frac{R}{z}\right)^{d-3} \partial_z \left[ z^{d-3} \partial_z \left( \frac{A_z}{z^{d-3}} \right) - g_{d+1}^2 \left(\frac{R}{z}\right)^2 v^2 a \right] = 0. \end{aligned} \quad (5.49)$$

The boundary conditions obtained from varying in  $\pi$  and  $A_z$  are

$$\left\{ (\partial_z a - A_z) - c_{\text{UV}} R \partial^2 a + c_{\text{UV}} R^{d-3} \frac{\xi_{\text{UV}}}{g_{d+1}^2} (A_z - g_{d+1}^2 c_{\text{UV}} R v_0^2 a) \right\} \Big|_{z=R} = 0 \quad (5.50)$$

$$\left\{ \xi \left[ \partial_z \left( \left(\frac{R}{z}\right)^{d-3} A_z \right) - g_{d+1}^2 v_0^2 a \right] - \frac{\xi_{\text{UV}} R^{d-4}}{g_{d+1}^2} (A_z - g_{d+1}^2 c_{\text{UV}} R v_0^2 a) \right\} \Big|_{z=R} = 0 \quad (5.51)$$

### Solving the pseudoscalar system

The mixed EOM for  $A_z$  and  $\pi$  can be solved by introducing the combinations

$$\chi = \partial_z a - A_z, \quad \Theta = z^{d-3} \partial_z \left( \frac{A_z}{z^{d-3}} - g_{d+1}^2 \left( \frac{R}{z} \right)^2 v^2 a \right). \quad (5.52)$$

Combining the EOM for  $A_z$  and  $\pi$ , we obtain

$$\partial_z \left( \frac{z^{d-1}}{v^2} \partial_z \left[ \frac{v^2}{z^{d-1}} \chi \right] \right) - \partial^2 \chi - g_{d+1}^2 \left( \frac{R}{z} \right)^2 v^2 \chi = 0 \quad (5.53)$$

$$z^{d-3} \partial_z \left( \frac{1}{z^{d-3}} \partial_z \Theta \right) - \frac{1}{\xi} \partial^2 \Theta - g_{d+1}^2 v^2 \left( \frac{R}{z} \right)^2 \Theta = 0. \quad (5.54)$$

For  $\alpha = \frac{d}{2}$ , the  $U(1)$  breaking vev is constant,  $v = v_0$ . Both EOM can be solved exactly. The solutions for  $\chi$  are

$$z^{\frac{d}{2}} I_\nu \left( \sqrt{-p^2} z \right), \quad z^{\frac{d}{2}} K_\nu \left( \sqrt{-p^2} z \right) \quad (5.55)$$

with  $\nu = \sqrt{\left(\frac{d}{2} - 1\right)^2 + m_A^2 R^2}$ . The solutions for  $\Theta$  are

$$z^{\frac{d}{2}-1} I_\nu \left( \frac{\sqrt{-p^2} z}{\sqrt{\xi}} \right), \quad z^{\frac{d}{2}-1} K_\nu \left( \frac{\sqrt{-p^2} z}{\sqrt{\xi}} \right). \quad (5.56)$$

### 5.3.3 Boundary Effective Action

Throughout this work we are interested in the 5D  $U(1)$  model as seen from a brane observer. In field theoretical terms, we assume that a source or a dynamical mode localized on the brane probes the 5D bulk fields. This implies that at the level of the path integral the bulk degrees of freedom can be integrated out, giving rise to a boundary quantum effective action  $\Gamma$ . The boundary effective action is relevant both theoretically and for phenomenological applications.

On the theoretical side, when AdS/CFT applies, the AdS boundary effective action encodes amplitudes which map onto correlators of a dual “holographic” CFT. In particular, an unbroken  $U(1)$  gauge field maps onto a conserved  $U(1)$  CFT current. We will later study when does AdS/CFT apply and what is the fate of the CFT current in the presence of the  $U(1)$ -breaking bulk vev.

As a phenomenological application we could identify the SM fields as the brane-localized degrees of freedom and the bulk modes as a hidden sector beyond the SM (see *e.g.* [45]). In cases where AdS/CFT applies, such effects are equivalently understood in terms of a “conformal hidden sector” compound of a CFT mixed to elementary fields.

Throughout this work we are just interested in the tree-level quadratic piece of  $\Gamma$ . Let us focus on the  $A_\mu$  field. The brane-to-brane propagator for the  $A_\mu$  components takes in general the form

$$G_p^T(R, R) = \frac{g_{d+1}^2}{\mathcal{B}_T(p^2) + \Sigma_T(p^2)}, \quad G_p^L(R, R) = \frac{g_{d+1}^2}{\mathcal{B}_L(p^2) + \Sigma_L(p^2)} \quad (5.57)$$

with  $\Sigma_L(p^2) = \Sigma_T(\frac{p^2}{\xi})$  and  $\mathcal{B}_L(p^2) = \mathcal{B}_T(\frac{p^2}{\xi})$ . Here  $\mathcal{B}(p^2)$  is the boundary operator defined in Eq.(5.40). It is analytical in  $p$ . The  $\Sigma(p^2)$  piece is the inverse of the brane-to-brane propagator for  $\mathcal{B} \rightarrow 0$ . It is in general non-analytical in  $p$ .

We then introduce the boundary value of the field as  $A_{T0}^\mu(p^2) = A_T^\mu(p^2, z = R)$ ,  $A_{L0}^\mu(p^2) = A_L^\mu(p^2, z = R)$ . The effective boundary action is a function of the classical value of these fields,  $\Gamma_A[A_{T/L,0}]$ . At leading order the effective boundary action simply amounts



to plugging the equation of motion into the fundamental action.<sup>2</sup> We find it takes the form

$$\Gamma_A = -\frac{1}{g_{d+1}^2} \int \frac{d^d p}{(2\pi)^d} \frac{1}{2} \left[ A_{T0}^\mu(p) (\mathcal{B}_T(p^2) + \Sigma_T(p^2)) \left( \eta_{\mu\nu} - \frac{p_\mu p_\nu}{p^2} \right) A_{T0}^\nu(-p) \right. \\ \left. + A_{L0}^\mu(p) (\mathcal{B}_L(p^2) + \Sigma_L(p^2)) \left( \frac{p_\mu p_\nu}{p^2} \right) A_{L0}^\nu(-p) \right] \quad (5.58)$$

We refer to the  $\Sigma$  function as the “holographic self-energy”. Notice that taking two functional derivatives in  $A_0$  gives the inverse brane-to-brane propagator Eq. (5.57).

$\Sigma$  can be expressed directly in terms of the solutions of the homogeneous EOM Eq. (5.37). Denoting by  $f_p^T(z)$ ,  $f_p^L(z)$  the solutions which are regular in the bulk (see *e.g.* [138] for details), the holographic self-energy is given by

$$\Sigma(p^2) = \partial_z \log f(p, z)|_{z=R}. \quad (5.59)$$

To the brane observer, the holographic self-energy amounts to having a field with a non trivial spectral distribution — which might be a continuum or a discretum as we will see in next section. The example above is for the vector sector which is our main application.

We also compute the holographic self energy for the Goldstone boson in section 5.3.3.

---

<sup>2</sup>For more details see *e.g.* [302, 248] for AdS, [254] for warped background, [138] for generic manifolds with boundary.

## Boundary-Localized Limit

In the brane-localized limit  $\frac{r_{UV}}{R}, c_{UV} \gg 1$ , the effective boundary action Eq. (5.58) tends to the one of a  $d$ -dimensional flat space free  $U(1)$  model

$$\Gamma_A|_{\frac{r_{UV}}{R}, c_{UV} \gg 1} = -\frac{1}{g_{d+1}^2} \int \frac{d^d p}{(2\pi)^d} \frac{1}{2} \left[ A_{T0}^\mu(p) (r_{UV} p^2 - c_{UV} R m_A^2) \left( \eta_{\mu\nu} - \frac{p_\mu p_\nu}{p^2} \right) A_{T0}^\nu(-p) \right. \\ \left. + A_{L0}^\mu(p) \left( \frac{g_{d+1}^2}{\xi_{UV} R^{d-4}} p^2 - c_{UV} R m_A^2 \right) \left( \frac{p_\mu p_\nu}{p^2} \right) A_{L0}^\nu(-p) \right] \quad (5.60)$$

Up to a re-scaling of the field and gauge fixing parameter  $\xi_{UV}$ , this action describes a  $d$ -dimensional gauge field with squared mass  $\frac{c_{UV} R m_A^2}{r_{UV}}$ .

## Goldstone Boundary Action

We study the Goldstone sector in the  $p \gg g_{d+1} v_0$  limit. A convenient way to implement this limit is to work perturbatively in  $g_{d+1}^2$ . As noted in [86], given the  $\frac{1}{g^2}$  normalization used for the gauge field, the bulk value of  $A_z$  has to be of order  $g_{d+1}^2$  in appropriate units of  $R$ . At leading order in  $g$ , the Goldstone boson EOM becomes very simple and can be solved for any  $\alpha$ . The EOM is

$$-\left(\frac{R}{z}\right)^{d-1} v^2 \partial^2 a + \partial_z \left[ \left(\frac{R}{z}\right)^{d-1} v^2 \partial_z a \right] = 0. \quad (5.61)$$

The solutions are

$$z^\alpha I_\alpha(\sqrt{-p^2} z), \quad z^\alpha K_\alpha(\sqrt{-p^2} z) \quad (5.62)$$

At small  $pz$  the asymptotic solutions behave as  $z^{2\alpha}$  and *cost*. Conversely, for  $\pi = av$ , the asymptotic behaviors are  $z^{\frac{d}{2} \pm \alpha}$ . The holographic self-energy of  $a$  is found to be

$$\Sigma_a(p) = -\sqrt{-p^2} \frac{K_{\alpha-1}(\sqrt{-p^2}R)}{K_\alpha(\sqrt{-p^2}R)} \quad (5.63)$$

$$\approx -\frac{p^2 R}{(2-2\alpha)} - \frac{2}{R} \frac{\Gamma(1-\alpha)}{\Gamma(\alpha)} \left( \frac{-p^2 R^2}{4} \right)^\alpha \quad \text{if } |p|R \ll 1 \quad (5.64)$$

for any  $\alpha$ . We can see that no mass term is generated by the holographic self-energy, in agreement with the shift symmetry of  $a$ . Finally the Goldstone boson boundary action reads

$$S_{\text{Bound},a}^{\text{UV}} = \frac{v_0^2}{2} \int \frac{d^d p}{(2\pi)^d} \left[ a_0(p) (\mathcal{B}_a(p^2) + \Sigma_a(p^2)) a_0(-p) \right] \quad (5.65)$$

with the boundary term

$$\mathcal{B}_a(p^2) = c_{\text{UV}} R p^2 - \xi_{\text{UV}} c_{\text{UV}}^2 R^{d-2} v_0^2. \quad (5.66)$$

## 5.4 The Landscape of Broken $U(1)$ in AdS

$U(1)$ Model in $\text{AdS}_{d+1}$			
	Spectrum	IR Back Reaction	Holographic CFT
$0 \leq \alpha < d/2 - 1$	Discrete $m_n \propto n^{1-\frac{2}{d-2\alpha}}$	Yes	X
$\alpha = d/2 - 1$	Gapped Continuum $m_n > g_{d+1} v_0$		
$d/2 - 1 < \alpha < d/2$	Continuum		
$\alpha = d/2$		No	Non-Conserved Current $\partial_\mu J^\mu \propto v_0^2$
$\alpha \gg d/2$			Conserved Current

Table 5.1: Summary of the spectra for a spontaneously broken  $U(1)$  model in  $\text{AdS}_{d+1}$  resulting from different choices of  $\alpha$ .

In this section we solve the EOM of the  $A^\mu = (A_T^\mu, A_L^\mu)$  component of the gauge field, *i.e.* the component transverse to the brane, and determine the corresponding holographic self-energy. We work in Fourier space, the general equation we solve is Eq. (5.37). Since the solutions for  $A_T$  and  $A_L$  are related by  $p \rightarrow \frac{p}{\sqrt{\xi}}$  we can focus on the solving of the  $A_T^\mu$  component. The solving is done either exactly or approximately over the complete range of Higgs bulk masses,  $\mu^2 \in [-\frac{d^2}{4}, \infty]$ , *i.e.*  $\alpha \in [0, \infty]$ . We also give the boundary effective action for the Goldstone field for any  $\alpha$ .

#### 5.4.1 WKB Approximation

In general there is no analytical solution to the EOM Eq. (5.37), except in particular cases or approximations. An important approximation is the following.

At  $|p|z \gg 1$ , for either timelike or spacelike momentum, we can always apply a standard WKB analysis. This is best done by introducing the rescaled field  $A_\mu = \left(\frac{z}{R}\right)^{\frac{d-3}{2}} \hat{A}_\mu$ . In any dimension,  $\hat{A}_\mu$  satisfies a Schrodinger-like problem  $(\partial_z^2 - V(z))\hat{A}_\mu = -p^2 \hat{A}_\mu$  where

$$V(z) = \frac{\left(\frac{d}{2} - \frac{3}{2}\right)\left(\frac{d}{2} - \frac{1}{2}\right)}{z^2} + g_{d+1}^2 \frac{R^2}{z^2} v^2(z). \quad (5.67)$$

The solution at large  $pz$  can be approximated in an exponential WKB scheme,

$$\exp\left(\pm \int_z dz \sqrt{V(z) - p^2}\right). \quad (5.68)$$

This WKB approximation provides an approximation of the spectrum of the gauge field in the Higgs background. We can already see that two regimes appear.

$\alpha < \frac{d}{2} - 1$  case. The  $p^2$  term dominates in Eq.(5.68) at large  $pz$ . Hence the solutions asymptotically behave as there is no Higgs background. The spectrum is therefore continuous.

$\alpha > \frac{d}{2} - 1$  case. The Higgs vev term dominates in Eq.(5.68) at large  $pz$ . For timelike momentum there is therefore a turning point at  $V(z_c) = p^2$ . This indicates that the spectrum will develop a mass gap.

We proceed with a more detailed analysis of the solutions.

#### 5.4.2 $\alpha \geq \frac{d}{2}$

$\alpha \gg \frac{d}{2}$

For such values of  $\alpha$ , the Higgs vev profile is steeper than all the other terms in the EOM. As a result, the Higgs background affects the boundary condition but not the bulk profile. The solutions to the bulk EOM are given by

$$z^{\frac{d}{2}-1} I_{\frac{d}{2}-1}(\sqrt{-p^2}z), \quad z^{\frac{d}{2}-1} K_{\frac{d}{2}-1}(\sqrt{-p^2}z). \quad (5.69)$$

The  $K$  solution is regular at large  $pz$ . The subsequent holographic self-energy of  $A_\mu$  is

$$\Sigma(p^2) \Big|_{\alpha \gg \frac{d}{2}} = -\sqrt{-p^2} \frac{K_{\frac{d}{2}-2}(\sqrt{-p^2}R)}{K_{\frac{d}{2}-1}(\sqrt{-p^2}R)} \quad (5.70)$$

$$\approx -\frac{2}{R} \frac{\Gamma(2 - \frac{d}{2})}{\Gamma(\frac{d}{2} - 1)} \left( \frac{-p^2 R^2}{4} \right)^{\frac{d}{2}-1} \quad \text{if } |p|R \ll 1, \quad d > 2. \quad (5.71)$$

$$\alpha = \frac{d}{2}$$

In this case the Higgs background contributes exactly as a bulk mass term in the EOM. The solutions to the bulk EOM for spacelike momentum are given by

$$z^{\frac{d}{2}-1} I_\nu(\sqrt{-p^2}z), \quad z^{\frac{d}{2}-1} K_\nu(\sqrt{-p^2}z) \quad (5.72)$$

with

$$\nu = \sqrt{\left(\frac{d}{2} - 1\right)^2 + m_A^2 R^2}. \quad (5.73)$$

The subsequent self-energy of  $A_\mu$  is

$$\Sigma(p^2)\Big|_{\alpha=\frac{d}{2}} = \frac{d - 2(1 + \nu)}{2R} - \sqrt{-p^2} \frac{K_{\nu-1}(\sqrt{-p^2}R)}{K_\nu(\sqrt{-p^2}R)} \quad (5.74)$$

$$\approx \frac{p^2 R}{2(\nu - 1)} + \frac{d - 2(1 + \nu)}{2R} - \frac{2}{R} \frac{\Gamma(1 - \nu)}{\Gamma(\nu)} \left(\frac{-p^2 R^2}{4}\right)^\nu \quad \text{if } |p|R \ll 1. \quad (5.75)$$

$$\alpha = \frac{d}{2} + \epsilon$$

For  $\alpha = \frac{d}{2}$  the Higgs vev amounts to a bulk mass term for the gauge field. We can further study the solutions for  $\alpha$  in the neighbourhood of  $\frac{d}{2}$  using a WKB expansion in the slow variation of the bulk mass term. We define  $\alpha = \frac{d}{2} + \epsilon$  where the correction terms are controlled by  $\epsilon$ . For  $\alpha = \frac{d}{2}$  the Higgs vev amounts to a bulk mass and thus respects the AdS isometries. What we do is therefore a WKB approximation for near-AdS background. We emphasize this is not the same WKB approximation as the one for  $|p|z \gg 1$  described in section 5.4.1.

The details of the near-AdS WKB method calculation are given in App.C.2. We determine the UV brane-to-brane and thus the effective boundary action, with

$$\Sigma(p^2) = \frac{p^2 R}{2\nu^2} - \frac{\nu - d/2 + 1}{R} - \frac{2}{R} \frac{\Gamma(1 - \nu)}{\Gamma(\nu)} \left(\frac{-p^2 R^2}{4}\right)^{\nu - \delta(p)} \left(\frac{pR}{\nu}\right)^{\delta(p)} \quad (5.76)$$

where we have defined

$$\delta(p) = \epsilon \frac{m_A^2 R^2}{\nu} \log \left( \frac{\nu}{pR} \right). \quad (5.77)$$

The coefficient  $\delta(p)$  slowly varies in  $p$ , reflecting the soft breaking of the underlying conformal symmetry. In terms of an approximately conformal dual theory, the correction amounts to a shift in the anomalous dimension given by

$$\Delta\gamma = -\frac{\delta(p)}{2}. \quad (5.78)$$

For  $\epsilon = 0$  ( $\alpha = d/2$ ) the shift to the anomalous dimension  $\Delta\gamma = 0$  and the holographic self-energy matches (5.75).

### 5.4.3 $\alpha < \frac{d}{2}$

For  $\alpha < \frac{d}{2}$  a backreaction of the metric is expected at some point far enough in the bulk, see Sec. 5.2.4. However we will verify in section 5.4.3 that the effect of the backreaction appears only above a certain mass threshold. Thus we can meaningfully solve the EOM with undeformed AdS background as long as we assume that the value of  $p$  is below the threshold.

For arbitrary  $\alpha < \frac{d}{2}$  there is no solution to the EOM. However for large  $|p|z$  we can approximate the solution using the WKB method. The solutions are given in Eq. (5.68). For  $\alpha < \frac{d}{2}$  the Higgs vev term dominates over the bulk mass term at large  $|p|z$  since  $v(z) = v_0 \left(\frac{z}{R}\right)^{\frac{d}{2}-\alpha}$ . In this regime we obtain

$$e^{\pm \int_z dz' \sqrt{V(z')-p^2}} \approx \exp \left( \pm \int_z dz' \sqrt{g_{d+1}^2 \frac{R^2}{z'^2} v^2(z') - p^2} \right). \quad (5.79)$$

This approximation is relevant to determine the spectrum at large  $p$  but cannot be used in the near boundary region, thus it cannot be used to obtain the boundary action. The integral in Eq. (5.79) can be analytically evaluated but is not illuminating. Eq. (5.79) will teach us about the spectrum of the gauge field over the Higgs background.

$$\frac{d}{2} - 1 < \alpha < \frac{d}{2}$$

In this regime the spectrum is a continuum. This is because  $\frac{v^2(z)}{z^2} \rightarrow 0$  for  $z \rightarrow \infty$ , such that there is no WKB turning point. Whenever the vev contribution is negligible with respect to  $p$ , the solutions behave exponentially.<sup>3</sup>

$$\alpha = \frac{d}{2} - 1$$

This particular case can be solved exactly. The solutions are

$$z^{\frac{d}{2}-1} I_{\frac{d}{2}-1} \left( \sqrt{m_A^2 - p^2} z \right), \quad z^{\frac{d}{2}-1} K_{\frac{d}{2}-1} \left( \sqrt{m_A^2 - p^2} z \right). \quad (5.80)$$

The holographic self-energy of  $A_\mu$  takes the form

$$\Sigma(p^2) \Big|_{\alpha=\frac{d}{2}-1} = -\sqrt{m_A^2 - p^2} \frac{K_{\frac{d}{2}-2}(\sqrt{m_A^2 - p^2} R)}{K_{\frac{d}{2}-1}(\sqrt{m_A^2 - p^2} R)} \quad (5.81)$$

$$\approx -\frac{2}{R} \frac{\Gamma(2 - \frac{d}{2})}{\Gamma(\frac{d}{2} - 1)} \left( \frac{(m_A^2 - p^2) R^2}{4} \right)^{\frac{d}{2}-1} \quad \text{if } |(m_A^2 - p^2)| R^2 \ll 1, \quad d > 2 \quad (5.82)$$

where in the expansion we have assumed  $d/2$  is not an integer. When  $d/2$  is an integer (for example when  $d = 4$ ), then a separate calculation must be done using the asymptotic forms of the Bessel functions for integer order.

---

<sup>3</sup>Technically in this regime the field is conformally equivalent to a flat space massless field (see *e.g.* [82], hence the wavefunction is exponential.



For  $\alpha = \frac{d}{2} - 1$  we can see that the spectrum is a *gapped continuum* starting at  $p^2 = m_A^2$ .

$$\alpha < \frac{d}{2} - 1$$

For  $\alpha < \frac{d}{2} - 1$  the Higgs background dominates the potential at large  $z$ . Thus for timelike momentum there is a WKB turning point signaling that spectrum contains discrete poles. These are the normalizable modes determined in the standard WKB matching procedure. They are linear combinations of the WKB solutions in Eq. (5.68).

The spacing of the spectrum is given by

$$\frac{dm_n^2}{dn} = 2\pi \left( \int_{z_0}^{z_c(p)} dz \frac{1}{\sqrt{V(z) - m_n^2}} \right)^{-1} \quad (5.83)$$

where  $z_c > z_0$  corresponds to the turning point,  $V(z_c) = p^2$ .<sup>4</sup> For  $|p| \gg m_A$  the integral is dominated by the region near the turning point. We obtain

$$\int_{z_0}^{z_c(p)} dz \frac{1}{\sqrt{V(z) - p^2}} \approx \frac{\sqrt{\pi} \Gamma(1 + \frac{1}{d-2\alpha-2}) R}{\Gamma(\frac{1}{2} + \frac{1}{d-2\alpha-2}) p} \left( \frac{p^2}{m_A^2} \right)^{\frac{1}{d-2\alpha-2}}. \quad (5.84)$$

It follows that the WKB spectrum for  $m_n \gg g_{d+1} v_0$  behaves as

$$m_n \approx c_\alpha n^{1 - \frac{2}{d-2\alpha}} m_A (m_A R)^{\frac{2}{d-2\alpha} - 1} \quad (5.85)$$

with

$$c_\alpha = \left[ \left( 1 + \frac{2}{d-2\alpha-2} \right) \frac{\sqrt{\pi} \Gamma(\frac{1}{2} + \frac{1}{d-2\alpha-2})}{\Gamma(1 + \frac{1}{d-2\alpha-2})} \right]^{1 - \frac{2}{d-2\alpha}}. \quad (5.86)$$

For example, for  $d = 4$ ,  $\alpha = 0$ , the spectrum behaves as  $m_n^2|_{d=4, \alpha=0} = 4n \frac{m_A}{R}$ .

The spectrum thus has a Regge behaviour. As a cross check we recover this behaviour analytically in next section.

---

<sup>4</sup>A factor of 2 seems to be missing in Eq. 18 of [204].

$\alpha = 0$

In the  $\alpha = 0$  case, there are exact solutions for certain values of  $d$  including  $d = 4$ .

The solutions are

$$e^{-\frac{m_A}{2R}z^2} U\left(-\frac{p^2 R}{4v_0}, 0, \frac{m_A}{R}z^2\right), e^{-\frac{m_A}{2R}z^2} L\left(\frac{p^2 R}{4v_0}, -1, \frac{m_A}{R}z^2\right) \quad (5.87)$$

where  $U$  is the confluent hypergeometric function and  $L$  is the Laguerre polynomial. The regular solution at large  $z$  is the former. For  $m_A R \ll 1$  the holographic self-energy of  $A_\mu$  is found to be

$$\Sigma(p^2) = -m_A - \frac{1}{2} R p^2 \left( \gamma_E + \log(m_A R) + H\left(-\frac{p^2 R}{4m_A}\right) \right) \quad (5.88)$$

where  $\gamma_E$  is the Euler-Mascheroni constant and  $H(x)$  is the analytically continued harmonic number.

For spacelike momentum and  $|p^2|R \gg m_A$ , the harmonic number tends asymptotically to a logarithmic which reproduces exactly the spacelike result with vanishing  $v_0$  (or with  $\alpha \gg \frac{d}{2}$ ). For timelike momentum, the harmonic number develops poles dictated by  $H_{1-r} = H_r + \pi \cotan(\pi r) + \text{finite}$ . The poles occur at integer values for  $r > 1$ . It follows that for  $|p^2|R \gg m_A$  the poles behave as

$$m_n^2 = 4n \frac{m_A}{R}. \quad (5.89)$$

This formula matches exactly the WKB estimate obtained from Eqs. (5.85), (5.86).

## On Backreaction and Spectrum

For  $\alpha < \frac{d}{2}$  the metric has nonnegligible backreaction due to the growth of the Higgs vev in the IR. As explained in section 5.2.4, to take into account this effect we place

an IR brane at the location  $z_b$  where the backreaction would become non negligible. The location of the backreaction  $z_b$  is estimated in Eq. (5.29). Here we study what is the effect of the presence of the IR brane on the gauge field spectrum. In the following estimates we ignore overall numerical factors for simplicity.

What is the effect of the IR brane on the spectrum? Using the WKB approximation, we can readily see that the effect of the IR brane appears when the turning point  $z_c(p)$  reaches  $z_b$ . From the viewpoint of a Schroedinger problem, this amounts to cut the  $V(z)$  potential with a hard wall at  $z = z_b$ . There are thus two regimes.

For  $z_c(p) > z_b$  the modes know about the IR brane. We can thus expect the spectrum in this regime to tend to the typical spectrum for a slice of AdS,  $m_n \propto n$ . In contrast, for  $z_c(p) < z_b$  the modes do *not* know about the IR brane and are thus solely controlled by the Higgs background as dictated by Eq. (5.85). In this regime the details of the backreaction are irrelevant for the spectrum of the gauge field.

The the transition between the two behaviors occurs at a typical value of mass  $m_*$  given by  $z_c(m_*) = z_b$ . We find

$$m_* \sim g_{d+1} M_*^{\frac{d-1}{2}} \left( \frac{v_0^2}{M_*^{d-1}} \right)^{\frac{1}{d-2\alpha}}. \quad (5.90)$$

In terms of mode number, using Eq. (5.85) we find that the condition  $m_n < m_*$  is satisfied for

$$n < (g_{d+1} R)^2 M_*^{d-1} \equiv n_* \quad (5.91)$$

for any  $\alpha \in [0, \frac{d}{2} - 1]$  and any  $d$ . That is, for  $n < n_*$  the spectrum is controlled by the Higgs potential and does not know about the IR brane. For example, for  $d = 4$ ,  $\alpha = 0$ , the

transition is at

$$m_*|_{d=4,\alpha=0} = Rg_5 M_*^{3/2}, \quad n_*|_{d=4,\alpha=0} = g_5^2 R^2 M_*^3. \quad (5.92)$$

What are the allowed values for  $n_*$ ? Since for  $d \geq 3$  we have an EFT we can use that  $g_{d+1}^2 M_*^{d-3} \gtrsim 1$ ,  $RM_* \gg 1$ , therefore  $n_* \gtrsim 1$ . This implies  $n_* \gg 1$ . Thus the Higgs-controlled, backreaction-independent behavior is permitted by EFT on an arbitrarily large interval of mass.

Interestingly, the same transition scale is obtained using a very different approach. We can require the mode spacing induced by the IR brane,  $\Delta m_n|_b = \frac{\pi}{z_b}$ , to be much smaller than the spacing induced by the Higgs background,  $\Delta m_n|_v$ , obtained from Eq. (5.91). Translating  $\frac{\Delta m_n|_v}{\Delta m_n|_b} < 1$  as a constraint on  $n$  gives Eq. (5.91). Plugging into Eq. (5.85) then gives (5.90).

In summary, here we have shown via quantitative WKB-based estimates that the IR brane does not affect the bottom part of the spectrum for masses below the transition value  $m_*$  given by Eq. (5.90).

## 5.5 A Holographic Continuum Dark Photon

In this section we present a dark photon model in AdS<sub>5</sub> based on the  $U(1)$  model studied in the previous sections. Some essential developments needed for phenomenology are performed. In the general analysis of section 5.4 we saw that a variety of phenomenologically distinct possibilities arise from the  $U(1)$  model. Here we focus on two simple benchmark models that arise in specific limits of the model, that we refer to as the *conformal continuum* and the *gapped continuum* dark photon models.

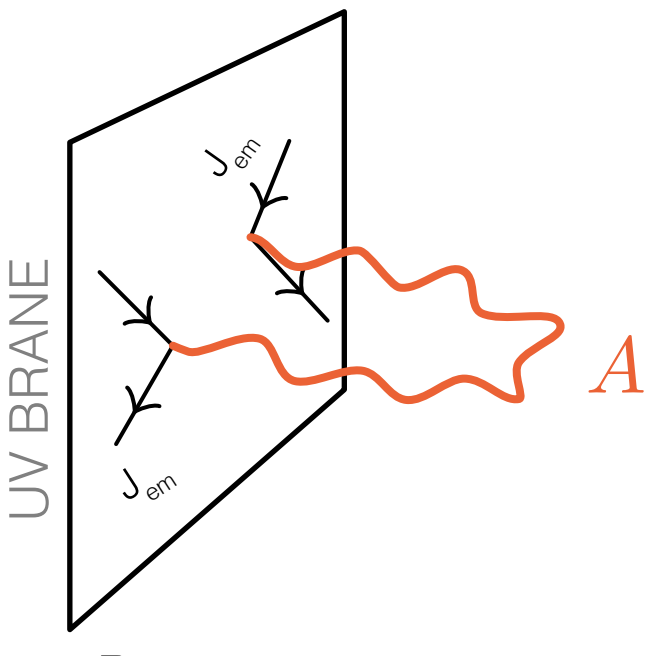


Figure 5.2: The holographic continuum dark photon mediates interactions on the UV brane.

### 5.5.1 Definition

We assume for simplicity that the SM fields are purely brane-localized.<sup>5</sup> The brane-localized visible photon field strength is noted  $\mathcal{F}_{\mu\nu}$  while the dark photon is identified as the bulk  $U(1)$  field  $F_{\mu\nu}$ . We assume a kinetic mixing between the visible photon and the dark photon

$$S_{\text{mix}} = \int d^4x \int_R^\infty dz \frac{\varepsilon}{2} \sqrt{\frac{r_{\text{UV}}}{g_5^2}} F_{\mu\nu} \mathcal{F}^{\mu\nu} \delta(z - R), \quad (5.93)$$

The Feynman rule associated with this kinetic mixing is  $i\varepsilon \sqrt{\frac{r_{\text{UV}}}{g_5^2}} (q^2 \eta_{\mu\nu} - q_\mu q_\nu)$ .

---

<sup>5</sup>Considering exactly localized fields is here a convenient approximation, however in a more realistic setup the localized SM fields should arise as quasilocalized modes from bulk fields. This can have observable consequences which are not the focus of the present study. [136]

### 5.5.2 Dressing the Photon

The photon propagator is dressed by the kinetic mixing insertions. The insertions can be resummed exactly, we find that the dressed photon propagator is

$$\text{Diagram} = \frac{-i}{q^2 (1 - \Pi_A(q^2))} \left( \eta_{\mu\nu} - \frac{q_\mu q_\nu}{q^2} \right) - \frac{i\xi}{q^2} \left( \frac{q_\mu q_\nu}{q^2} \right) \quad (5.94)$$

with

$$\Pi_A(q^2) = \varepsilon^2 r_{UV} q^2 G_q(R, R) . \quad (5.95)$$

The detailed computation is given in App. C.3.

Alternatively, we may notice that the *brane* kinetic Lagrangian can be exactly diagonalized by a field redefinition of the brane component of the photon field,

$$\hat{\mathcal{A}}_0 = \mathcal{A}_0 + \varepsilon \sqrt{\frac{r_{UV}}{g_5^2}} A|_{z=R} . \quad (5.96)$$

In such a basis the visible photon is not dressed by the dark photon, instead the dark photon acquires a  $\varepsilon$ -suppressed coupling to the electromagnetic current. The physical matrix elements with 4D SM fields in external legs must be invariant under this field redefinition, we show in App. C.3 that it is indeed the case. The field redefinition (5.96) results in the shift to the photon's coupling to the electromagnetic current. As a result, the holographic continuum dark photon acquires the interaction

$$\text{Diagram} = i\varepsilon e Q_f \sqrt{\frac{r_{UV}}{g_5^2}} \gamma_\mu , \quad (5.97)$$

resulting in an  $\varepsilon$  suppressed coupling to the electromagnetic current.

### 5.5.3 Benchmark Continuum Models

We limit our study to the  $\alpha = 1$  and  $\alpha = 2$  cases. The  $\alpha = 1$  case features a gapped continuum. The  $\alpha = 2$  case features a continuous spectrum and admits a standard CFT interpretation (see section 5.9). Because of the Ward identity, the longitudinal propagator will never contribute to physical processes in this model. Therefore, we limit our focus to the transverse polarization and denote  $G_p^T \equiv G_p$  for convenience. Our results are easily generalized to the longitudinal case.

The transverse brane-to-brane propagators these models are respectively given by

$$\begin{aligned}
G_p^{\alpha=1}(R, R) &= g_5^2 \left[ r_{\text{UV}} p^2 - c_{\text{UV}} m_A^2 R - \sqrt{m_A^2 - p^2} \frac{K_0(\sqrt{m_A^2 - p^2} R)}{K_1(\sqrt{m_A^2 - p^2} R)} \right]^{-1} \\
&\simeq g_5^2 \left[ r_{\text{UV}} p^2 - c_{\text{UV}} m_A^2 R - \frac{1}{2} (p^2 - m_A^2) R \left( 2\gamma_E + 2 \log \left( \sqrt{p^2 - m_A^2} \frac{R}{2} \right) - i\pi \right) \right]^{-1}
\end{aligned} \tag{5.98}$$

and

$$\begin{aligned}
G_p^{\alpha=2}(R, R) &= g_5^2 \left[ r_{\text{UV}} p^2 - c_{\text{UV}} m_A^2 R - \frac{\nu - 1}{R} - \sqrt{-p^2} \frac{K_{\nu-1}(\sqrt{-p^2} R)}{K_\nu(\sqrt{-p^2} R)} \right]^{-1} \\
&\simeq g_5^2 \left[ \left( r_{\text{UV}} + \frac{R}{2(\nu - 1)} \right) p^2 - c_{\text{UV}} m_A^2 R - \frac{\nu - 1}{R} - \frac{2}{R} \frac{\Gamma(1 - \nu)}{\Gamma(\nu)} \left( \frac{-p^2 R^2}{4} \right)^\nu \right]^{-1}.
\end{aligned} \tag{5.99}$$

The second lines of Eqs. (5.99), (5.98) are obtained for  $pR \ll 1$ , consistent with the cutoff in momentum on the UV brane. We can see that both propagators feature both a continuum part given by the nonanalytical term and an isolated 4D-like pole. The mass of each pole

denoted  $m_\alpha$ , is given by the solutions to the equations

$$r_{\text{UV}}m_1^2 - c_{\text{UV}}m_A^2R - \text{Re} \left[ \frac{\sqrt{m_A^2 - m_1^2} K_0(\sqrt{m_A^2 - m_1^2}R)}{K_1(\sqrt{m_A^2 - m_1^2}R)} \right] = 0 \quad (5.100)$$

$$r_{\text{UV}}m_2^2 - c_{\text{UV}}m_A^2R - \frac{\nu - 1}{R} - \text{Re} \left[ \sqrt{-m_2^2} \frac{K_{\nu-1}(\sqrt{-m_2^2}R)}{K_\nu(\sqrt{-m_2^2}R)} \right] = 0 \quad (5.101)$$

for  $\alpha = 1$  and  $\alpha = 2$  respectively. Even after taking  $pR \ll 1$  (and  $m_A R \ll 1$  for  $\alpha = 1$ ), closed form solutions to (5.100) and (5.101) do not exist. While closed form solutions remain elusive, we may observe that for  $\alpha = 1$ , when  $r_{\text{UV}}/R = c_{\text{UV}}$  the pole is given exactly by  $m_1 = m_A$ . In both cases if  $r_{\text{UV}}/R \sim c_{\text{UV}} \sim \mathcal{O}(1)$ , then the pole mass  $m_\alpha \sim m_A$ . Increasing  $r_{\text{UV}}/R$  ( $c_{\text{UV}}$ ) decreases (increases) the pole mass relative to  $m_A$ .

## Interpretation

Let us understand the physics encoded in these propagators. The non-analytical piece reflects the presence of the AdS bulk modes.<sup>6</sup> We can see that near the resonance pole, the resonance has a *nonzero width* even though we are tree-level. This width can be understood as the resonance being able to decay (or “oscillate”) into the continuum of bulk modes. This feature was first noted in [112]. The CFT interpretation, when it exists, is similar: the resonance can decay into CFT stuff which effectively behaves as a noninteger number of particles. Beyond tree level the propagator is dressed by brane-localized self-energies, that compete with the tree-level imaginary part from the holographic self-energy.

---

<sup>6</sup>The Hilbert space of states in AdS is different from familiar flat 4D space. In AdS states are labelled by their conformal dimension and there is no notion of decay analogous to 4D, instead all states are stable. The dressing of the bulk propagator by bulk loops, rather than inducing unstable states as in 4D, induces a mixing between states with different conformal dimensions (see [137]).



The latter amounts to an *invisible width*. Therefore the physics of the resonances is similar to a particle dark photon with invisible width.

Away from the pole, for  $p^2 \ll m_A^2$ , the resonance is off-shell and can be integrated out. The leading non-analytical piece of the propagator in this limit amounts to a direct coupling to the continuum of AdS bulk states.

### Brane-Localized Limit

The limit of brane-localized dark photon which reproduces exactly the physics of a standard particle dark photon is obtained by letting  $r_{UV} \rightarrow \infty$ . In that limit we can see that only the 4D pole remains in the propagators. A massive dark photon is similarly obtained by simultaneously letting  $r_{UV}, c_{UV} \rightarrow \infty$ .

We notice however that  $r_{UV}, c_{UV}$  are expected to be typically of order one or smaller in units of  $R$  by naïve dimensional analysis. It follows that these holographic dark photon models are qualitatively different from a particle dark photon model.

### Unbroken $U(1)$ limit

For  $m_A \rightarrow 0$  the limit of unbroken  $U(1)$  is recovered (from either propagator), giving

$$G_p(R, R) \simeq \frac{1}{p^2} \frac{g_5^2}{r_{UV} - R \left( \gamma_E + \log \left( \frac{pR}{2} \right) - i \frac{\pi}{2} \right)}. \quad (5.102)$$

#### 5.5.4 Spectral Density and Phase Space

The brane-to-brane propagators, like any 2pt function in 4D flat space, can be written in a spectral representation. Focussing on the transverse brane-to-brane propagator

we have

$$G_p(R, R) = \int \frac{d\mu^2}{2\pi} \frac{\rho_T(\mu^2)}{p^2 - \mu^2 + i\epsilon} \quad (5.103)$$

where  $\rho_T(m^2)$  is the transverse spectral density. The inverse relation is

$$\rho_T(p^2) = -2\text{Im} [G_p(R, R)] . \quad (5.104)$$

Analogous definitions hold for the longitudinal brane-to-brane propagator  $G_p^L(R, R)$  and longitudinal spectral density  $\rho_L(p^2)$  as well. In flat 4D space a free particle state with mass  $M$  has spectral density  $\rho(p^2) = 2\pi\delta(p^2 - M^2)$ , while in an interacting theory the spectral density is continuous beyond the threshold for multiparticle state creation.

In contrast, in our 5D model, the spectral density is continuous even when neglecting interactions of the continuum, reflecting the fact that the Hilbert space of AdS bulk modes is different from the 4D one. Plugging (5.57) into (5.104), the spectral density can be found quite generally to be

$$\rho_T(p^2) = g_5^2 \frac{\text{Im} \Sigma(p^2)}{(\mathcal{B}_T(p^2) + \text{Re} \Sigma(p^2))^2 + \text{Im} \Sigma(p^2)^2} . \quad (5.105)$$

In the case of a gapped continuum, as for  $\alpha = 1$ , it is possible for the pole to be located below the gap scale. In that case an additional term proportional to  $2\pi\delta(p^2 - m_1^2)$  must be

included in the spectral density. The spectral densities for  $\alpha = 1, 2$  assuming  $pR \ll 1$  are

$$\begin{aligned} \rho_T^{\alpha=1}(p^2) &= 2\pi g_5^2 \delta \left( r_{UV} p^2 - c_{UV} m_A^2 R - (p^2 - m_A^2) R \log \left( \sqrt{p^2 - m_A^2} \frac{R}{2} e^{\gamma_E} \right) \right) \Theta(m_A^2 - p^2) \\ &+ \frac{4\pi g_5^2 (p^2 - m_A^2) R}{4 \left( r_{UV} p^2 - c_{UV} m_A^2 R - (p^2 - m_A^2) R \log \left( \sqrt{p^2 - m_A^2} \frac{R}{2} e^{\gamma_E} \right) \right)^2 + \pi^2 R^2 (p^2 - m_A^2)^2} \end{aligned} \quad (5.106)$$

$$\rho_T^{\alpha=2}(p^2) = \frac{g_5^2 \frac{2\pi}{R\Gamma(\nu)^2} \left( \frac{pR}{2} \right)^{2\nu}}{\left( \left( r_{UV} + \frac{R}{2(\nu-1)} \right) p^2 - c_{UV} m_A^2 R - \frac{\nu-1}{R} - \frac{2\pi \cot(\pi\nu)}{R\Gamma(\nu)^2} \left( \frac{pR}{2} \right)^{2\nu} \right)^2 + \frac{4\pi^2}{R^2\Gamma(\nu)^4} \left( \frac{pR}{2} \right)^{4\nu}}. \quad (5.107)$$

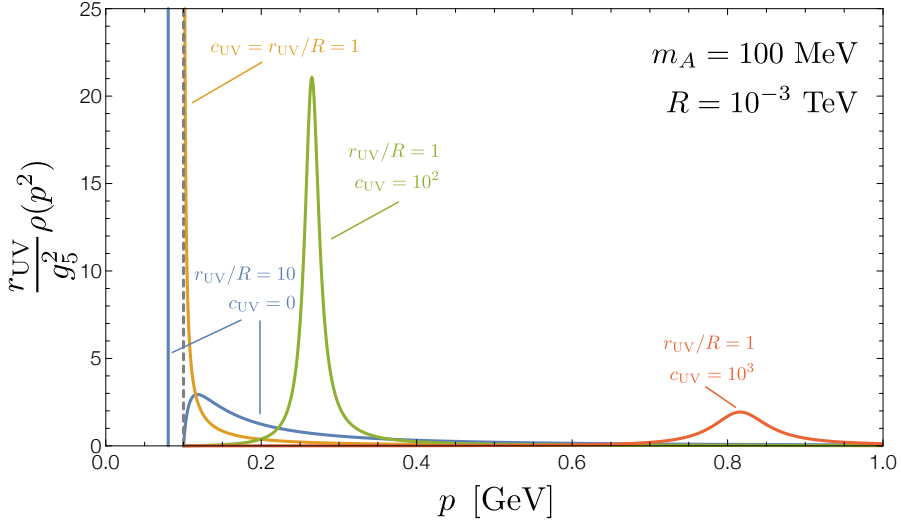


Figure 5.3: Examples of the spectral density for  $\alpha = 1$ . The location of the pole is shifted away from the gap depending on the values of  $c_{UV}$  and  $r_{UV}/R$ .

For  $\alpha = 1$  the continuum is gapped and may have an isolated pole below the gap scale given the solution for the pole mass  $m_1 < m_A$ . When  $r_{UV}/R = c_{UV}$  the propagator has a pole exactly located at  $p^2 = m_A^2$ . As we have discussed previously, for  $r_{UV}/R \sim c_{UV} \sim \mathcal{O}(1)$  the pole mass is approximately  $m_1 \sim m_A$ . When  $r_{UV}/R$  is increased such that

the pole mass passes below the gap scale, the spectral density is an isolated pole below the gap scale and a continuum above. When  $c_{UV}$  is increased on the other hand, the pole mass increases and the width of the resonance broadens. This behavior is shown in Fig. 5.3. The AdS curvature  $R^{-1}$  does not greatly affect the shape of the spectral density in this case. From (5.106) we can see that upto an overall factor, near the gap the continuous piece of the spectral density is only logarithmically dependent on  $R$  and the ratio  $r_{UV}/R$  which is expected to be  $\mathcal{O}(1)$  from NDA. Away from the gap when  $p^2 \gg m_A^2$ , the spectral density goes as  $\sim g_5^2/r_{UV}^2 p^3$  and is independent of  $R$ .

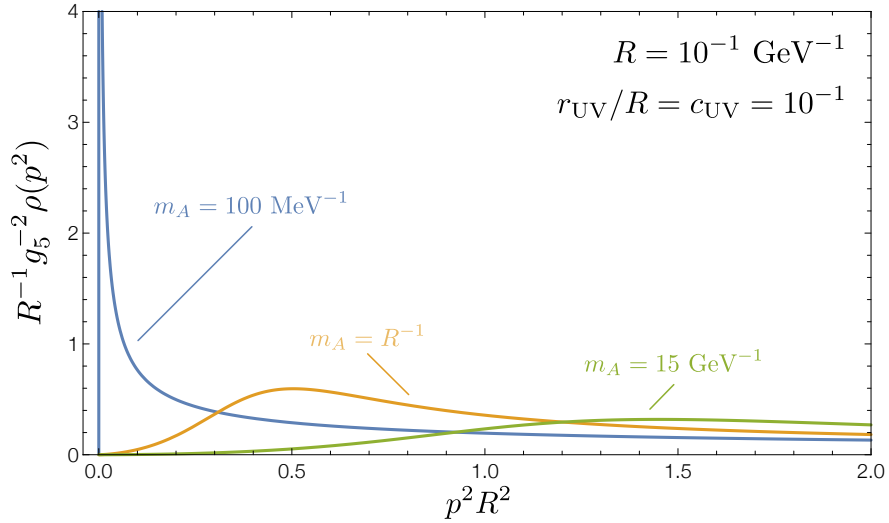


Figure 5.4: Examples of the spectral density for  $\alpha = 2$ . The width of the resonance is determined by the value of  $m_A$  relative to  $R^{-1}$ .

For  $\alpha = 2$ , the continuum is ungapped, it is supported for arbitrary values of  $p$ . The position of the resonance depends on  $m_A$ . The behaviour of the dark photon with  $\alpha = 2$  can be divided into three characteristic regimes: narrow resonance, broad resonance and continuum. For  $m_A \lesssim \frac{1}{R}$ , the resonance is narrow, thus the holographic dark photon

resembles a particle dark photon with an invisible decay width. For  $m_A$  approaching  $\frac{1}{R}$ , the resonance is broad but still has an effect on the observables. Lastly for  $m_A \gtrsim \frac{1}{R}$  the broad resonance is above the cutoff. In that regime the holographic dark photon behaves as a continuum. This behavior is shown in Fig. 5.4.

### 5.5.5 Simplified Continuum Models

There are five parameters in the holographic dark photon model we have defined,  $\varepsilon, R, m_A, c_{UV}, r_{UV}$ . The  $\varepsilon$  mixing coefficient controls the coupling to the SM,  $R$  sets the overall scale, and the three remaining coefficients influences the shape of the spectral distribution and position of the resonance.<sup>7</sup> The  $r_{UV} = 0, c_{UV} = 0$  are typically expected to be of  $O(1)$  or smaller in units of  $R$ . By expecting the propagators or the spectral densities we can see that their impact on the phenomenology is mild. We can thus set them to zero,  $r_{UV} = 0, c_{UV} = 0$ . Furthermore in the  $\alpha = 2$  model we focus on the continuum regime  $m_A \gtrsim \frac{1}{R}$  for which the resonance is integrated out.

We refer to the dark photon models obtained in these conditions as simplified continuum models. The corresponding spectral densities are

$$\rho_T^{\alpha=2}(p^2) = \frac{g_5^2 \frac{2\pi R}{\Gamma(\nu)^2} \left(\frac{pR}{2}\right)^{2\nu}}{(\nu - 1)^2} \quad (\text{Conformal continuum}) \quad (5.108)$$

$$\rho_T^{\alpha=1}(p^2) = \frac{\pi g_5^2 (p^2 - m_A^2)^{-1} R^{-1}}{\log^2 \left( \sqrt{p^2 - m_A^2} \frac{R}{2} e^{\gamma_E} \right) + \pi^2/4} \quad (\text{Gapped continuum}) \quad (5.109)$$

---

<sup>7</sup>The 5D gauge coupling  $g_5$  is irrelevant in our study because it does not affect the processes were the holographic dark photon only interacts with the SM. For these processes the  $g_5$  from Feynman rules and spectral density will always cancel.

### 5.5.6 Continuum Phase Space

By applying the optical theorem to Feynman diagrams with internal continuum dark photon lines, we can deduce the correct phase space for final state dark photons. Using the spectral representation of the propagator (5.103) and that  $\rho_T(p^2)$  is a positive definite function for  $p^2 > 0$ , we can see that each final state continuum dark photon a factor of  $\int \frac{dm^2}{2\pi} \rho_T(m^2)$  must be included when calculating cross sections. We present an explicit example for the production of a continuum dark photon from a brane-localized current.

The matrix element for a  $s$ -channel scattering between two currents can be written

$$\mathcal{M} = i\lambda^2 J_\mu(p, p') \langle A_0^\mu(k) A_0^\nu(-k) \rangle J_\nu^\dagger(p, p') \quad (5.110)$$

where  $\lambda$  is some dimensionless coupling and  $k^2 = (p + p')^2 = s$ . The imaginary part is therefore

$$\text{Im}\mathcal{M} = \lambda^2 \text{tr} \left[ J_\mu(p, p') J_\nu^\dagger(p, p') \right] \text{Im} [i \langle A_0^\mu(k) A_0^\nu(-k) \rangle] . \quad (5.111)$$

From the optical theorem we have

$$\begin{aligned} \sigma &= \frac{\lambda^2}{4s} \left( 1 - \frac{4m_f^2}{s} \right)^{-1/2} \sum_r \text{tr} \left[ J_\mu^r(p, p') J_\nu^{r\dagger}(p, p') \right] \text{Im} [i \langle A_0^\mu(k) A_0^\nu(-k) \rangle] \\ &= \int dk^2 \frac{\lambda^2}{4s} \left( 1 - \frac{4m_f^2}{s} \right)^{-1/2} \sum_r \text{tr} \left[ J_\mu^r(p, p') J_\nu^{r\dagger}(p, p') \right] \text{Im} [i \langle A_0^\mu(k) A_0^\nu(-k) \rangle] \delta(k^2 - s) \end{aligned} \quad (5.112)$$

where  $r$  is some general index for the current. When the current is conserved, the Ward identity holds. The cross section becomes

$$\sigma = \int dk^2 \frac{\lambda^2}{4s} \left(1 - \frac{4m_f^2}{s}\right)^{-1/2} \sum_r \text{tr} \left[ J^{r\mu}(p, p') J_\mu^{r\dagger}(p, p') \right] \text{Im} [G_k(R, R)] \delta(k^2 - s) \quad (5.113)$$

$$= \int \frac{dk^2}{2\pi} \sigma_{4\text{D}}(k^2) \text{Im} [-2G_k(R, R)] \quad (5.114)$$

$$= \int \frac{dk^2}{2\pi} \sigma_{4\text{D}}(k^2) \rho_T(k^2) \quad (5.115)$$

where the 4D cross section

$$\sigma_{4\text{D}}(k^2) = \frac{\pi\lambda^2}{s} \left(1 - \frac{4m_f^2}{s}\right)^{-1/2} \sum_r \text{tr} \left[ -J^{r\mu}(p, p') J_\mu^{r\dagger}(p, p') \right] \delta(k^2 - s) \quad (5.116)$$

is exactly the cross section for production of particle dark photon with invariant mass  $k^2$ .

Therefore we can deduce that for a general process involving a final state dark photon the cross section for the entire continuum is given by

$$\sigma = \int \frac{dk^2}{2\pi} \rho_T(k^2) \sigma_{4\text{D}}(k^2) \quad (5.117)$$

where  $\sigma_{4\text{D}}(k^2)$  is the cross section for a single continuum state. Similarly for two final state dark photons we have

$$\sigma = \int \frac{dk_1^2}{2\pi} \rho_T(k_1^2) \int \frac{dk_2^2}{2\pi} \rho_T(k_2^2) \sigma_{4\text{D}}(k_1^2, k_2^2). \quad (5.118)$$

### 5.5.7 A Recasting Formula for Continuum Models

We show here that the spectral distribution can be used, under mild conditions, directly at the level of the experimental bounds on 4D particles. The method is expressed in terms of dark photon quantities but can have straightforward generalization to other continuum models. Bounds on the particle dark photon parameter space  $(m, \varepsilon_{4D})$  are

typically expressed as  $\varepsilon_{4D} < \varepsilon_{4D,b}(m)$  where  $\varepsilon_{4D,b}(m)$  is the function defining the exclusion region.

We denote a predicted observable as  $O(\varepsilon_{4D}, m)$ . We assume the observable takes the form

$$O(\varepsilon_{4D}, m) = \varepsilon_{4D}^2 R(m). \quad (5.119)$$

Assuming that the observed value of  $O_{\text{obs}}$  does not rely on assumptions on  $m$ , the experimental constraint takes the form  $O_{\text{obs}} = O(\varepsilon_{4D,b}(m), m)$ , which defines the  $\varepsilon_{4D,b}(m)$  function. Specifically, using Eq. (5.119) we get

$$\varepsilon_{4D,b}(m) = \frac{O_{\text{obs}}}{R(m)}. \quad (5.120)$$

We turn to the continuum model. The predicted observable now depends only on  $\varepsilon$ . How do we determine the bound on  $\varepsilon$  using the 4D data? In continuum models the prediction analogous to Eq. (5.119) involves spectral integrals over  $R(m)$ . Here we focus on observables requiring a single spectral integral. Using appropriate conventions without loss of generality we can write

$$O(\varepsilon) = \varepsilon^2 \int \frac{dm^2}{2\pi} \rho(m) R(m). \quad (5.121)$$

The experimental constraints takes the form  $O_{\text{obs}} = O(\varepsilon_b)$ . Using this together with Eq. (5.120), it follows that the bound on  $\varepsilon$ , denoted by  $\varepsilon_b$ , is given by

$$\frac{1}{\varepsilon_b^2} = \int \frac{dm^2}{2\pi} \frac{\rho(m^2)}{\varepsilon_{4D,b}^2(m)}. \quad (5.122)$$

This method is exact and is rather general since it only requires that the experimental observable does not depend on assumptions on  $m$ .



The recasting formula Eq. (5.122) shows that it suffices to know the  $\varepsilon_{4D,b}(m)$  function to obtain the corresponding bound on the continuum model with spectral density  $\rho(m)$ . We use this method in the following.

### 5.5.8 Cutoff scales

The interacting 5D theory is understood as a long distance EFT whose validity breaks down at distances of order  $\Delta X \sim \frac{1}{\Lambda_5}$  where  $\Lambda_5$  is the 5D cutoff. However the validity of the AdS/CFT correspondence breaks down at a larger distance scale,  $\Delta X \sim R$  [7]. From the viewpoint of boundary correlators, this amounts to  $p_{\text{cutoff}} \sim \frac{1}{R}$ . This cutoff also applies to temperature defined on the boundary. As a result, when studying cosmology in the holographic CFT, the highest allowed temperature is  $T_{\text{CFT,cutoff}} \sim \frac{1}{R}$ . In terms of the CFT energy density, the cutoff is

$$\rho_{\text{CFT,cutoff}} \sim \frac{M_{\text{Pl}}^2}{R^2}, \quad (5.123)$$

where one has used  $\rho_{\text{CFT}} \sim cT^4$  with the central charge  $c \sim N^2 \sim (M_{\text{Pl}}R)^2$ . In terms of brane cosmology, this cutoff scale also corresponds to the highest energy density allowing a standard Friedmann equation. For energies higher than  $\rho_{\text{CFT,cutoff}}$ , the Friedmann equation is dominated by a non-standard  $\rho^2$  term and becomes model-dependent [180]. Throughout this work we adopt the viewpoint that the momentum cutoff of the theory is at  $\sim \frac{1}{R}$ .

## 5.6 Finite Temperature and a Cosmological Scenario

Our continuum dark photon model features light degrees of freedom in some sense as dictated by the spectral density. This is important for cosmology since the existence of

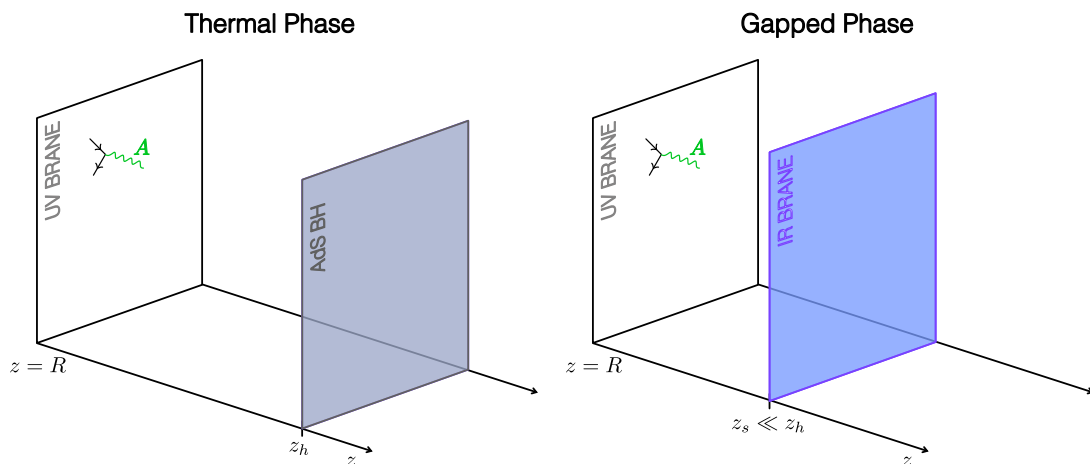


Figure 5.5: Respective geometries for thermal phase with the AdS black hole (Left) and the gapped phase when the background is truncated by an IR brane (Right).

new light degrees of freedom is generically constrained by cosmological observations [238].

Can our model accommodate existing cosmological bounds?

The answer to this question requires a more detailed study of the spacetime background in the far IR. As well known from *e.g.* [169, 180, 221, 220, 87] and as reviewed below, when the UV brane is at finite temperature the metric can become of AdS-Schwarzschild (AdS-S) type [180].

The cosmological evolution of this background as seen from the UV brane is conveniently described by the motion of the UV brane  $z_0(\tau)$  in the bulk, with  $z_h$  remaining constant. This motion effectively acts as a scale factor with  $z_0(\tau) \propto \frac{1}{a(\tau)}$ . In our model we have  $z_0 = R$  at present times, therefore  $\frac{1}{z_0(\tau)} = \frac{a(\tau)}{R}$ . The effective temperature of the black hole horizon as seen from the UV brane is given by  $T_h(\tau) = \frac{1}{\pi R} \frac{z_0(\tau)}{z_h}$ .

At finite temperature the only reason for the bulk black hole not to develop is if the background is truncated by an IR brane or by a singularity (*i.e.* a soft-wall) at

$z_s \ll z_h$ . These two possible backgrounds have to be understood as two different phases.<sup>8</sup>

We consider these two possibilities as the only available ones in our analysis. Taking  $z_s$  as a temperature-independent reference we can say that the bulk has AdS-Schwarzschild for  $T_h \gg \frac{1}{z_s}$ , that we refer to as the thermal phase. For  $T_h \ll \frac{1}{z_s}$ , temperature effects in the bulk are negligible, thus the metric is the one with a IR brane (or a soft-wall) that we refer to as the gapped phase.

We remind that in Section 5.2 we have obtained that for  $\alpha > 2$  the scalar vev does not induce IR backreaction. Thus in this case, at finite temperature one has the AdS-S metric at any temperature, at least as long as the temperature is low enough such that the scalar vev is negligible at  $z_h$ . In contrast for  $\alpha < 2$  an IR backreaction occurs because of the scalar vev. We could but will not study the exact solution of the singularity induced by the vev, here it is enough to assume that a IR brane truncates spacetime at  $z_s$ . The existence of the gapped phase — for  $\alpha$  either smaller or larger than 2 — is an important ingredient for cosmological bounds.

The dual picture of the thermal phase is the one of the SM at temperature  $T$  coupled to a hidden CFT with temperature  $T_h$ . The dual picture of the gapped phase is the one of the SM coupled to a kind of approximate CFT with mass gap of order  $\sim \frac{1}{z_s}$ .

---

<sup>8</sup>This is analogous to the Hawking-Page phase transition. [179] The phase transition is believed to be of first order and may feature supercooling [87, 260, 199, 247, 178, 215, 50, 111, 301, 242]. Our present analysis is only qualitative in regard of the phase transition and its details.

In the cosmology of our model (and more generally of warped braneworlds), the overarching idea is that the presence of the bulk black hole can spoil cosmological bounds because it effectively contributes to dark radiation. This is easily understood in the CFT picture, since hot CFT behaves as radiation.

It follows that there are (at least) two solutions to evade cosmological bounds at late times. Either the hidden sector (*i.e.* the bulk black hole/hidden CFT) remains much colder than the SM thermal bath at late times, or the background transitions to the gapped phase at some intermediate temperature so that the hidden radiation is removed in favor of nonrelativistic degrees of freedom. In the following we discuss cosmological scenarios along these lines. An assumption taken throughout is that the temperature of the hidden sector is zero or negligible at early times. We show the geometry for these solutions in Fig. 5.5.

The cosmology of the related minimal Randall-Sundrum II braneworld model, including the evolution of the bulk black hole, was laid out in a series of increasingly refined analyses in [169, 180, 221, 220]. Here we will use elements of these analyses. In these references also it is assumed that the black hole has negligible temperature at early times.

### 5.6.1 Feeding the Bulk Black Hole

Here we focus on the thermal phase. We explain how the black hole temperature/horizon is fixed by the other quantities of the model.

Let us consider pure AdS. The SM thermal bath is localized on the UV brane, that leaks some amount of energy into the bulk via QFT processes. The produced bulk excitations get strongly interacting in the bulk, at the very least due to AdS gravity. Far enough in the IR a horizon must develop to censor strongly coupled gravity. This is described

by the AdS-Schwarzschild metric. We can say that a bulk black hole forms due to the sustained flux of radiation emitted from the brane.

The leading process for producing bulk modes from boundary-localized modes is a simple  $2 \rightarrow 1$  process. In the minimal version of this finite temperature braneworld scenario, there are only gravitons in the bulk, thus the only process is  $\text{SM} + \text{SM} \rightarrow \text{graviton continuum}$ . In our model there is also the dark photon continuum, therefore there another process is  $\text{SM} + \text{SM} \rightarrow \text{dark photon continuum}$ . The cross section for the  $2 \rightarrow 1$  production of the dark photon continuum has been computed in Eq. (5.150).

The AdS-Schwarzschild metric has only one new parameter: the location of the black hole horizon. This single parameter must encode all the combined effects of the fluxes of energy leaked into the bulk. This was elegantly obtained in [220] in the formalism of the Vaidya metric that describes spacetime around radiative bodies.

For both dark photons and gravitons continuum the process of radiation leaking into the bulk is dominated at early times. Taking the initial SM temperature at the cutoff  $T_i = \frac{1}{R}$  and the corresponding energy density of the SM thermal bath as  $\rho_i = \frac{\pi^2}{30} T_i^4$ ,

The effective Friedmann equation on the moving brane contains the dark radiation term

$$\rho_D(\tau) = 3 \frac{M_{\text{P}}^2}{R^2} \left( \frac{z_0(\tau)}{z_h} \right)^4. \quad (5.124)$$

This explicit expression in terms of  $z_h$  is strictly speaking not necessarily to determine the observable fraction of dark radiation, but will be needed to estimate whether a transition to the gapped phase occurs and at which SM temperature. Notice this energy scales as the one of a CFT sector,  $\sim \pi^2 N^2 T_{\text{CFT}}^4$ . Here we perform the quantitative calculation from the

AdS side.

$$\Omega_{D,f} = \frac{\rho_{D,f}}{\rho_{SM,f}} = \int_{\tau_i}^{\tau_f} d\tau \frac{\langle \sigma v E \rangle n^2}{\rho}. \quad (5.125)$$

Taking the initial temperature at the cutoff of the theory  $T_i \sim \frac{1}{R}$  and taking the initial energy density of the SM bath to be  $\rho_i \sim g_* T_{SM}^4$ , the fraction of dark radiation created is estimated to be

$$\Omega_{D,f} \sim \left( \frac{g_{*f}}{g_{*i}} \right)^{\frac{1}{3}} (\text{coupling})^2 M_P R \quad (5.126)$$

by dimensional analysis, where the couplings are expressed in units of  $R$ . The  $M_P$  factor comes from the time factor, which is related by  $\tau \propto \frac{M_P}{\sqrt{g_* T_{SM}^2}}$  to the SM temperature. For the QFT processes considered here the integral is dominated by early times so is independent of  $\tau_f$  for  $\tau_f \gg \tau_i$ . For the graviton continuum, the square coupling goes as  $\frac{1}{(M_P R)^2}$ , such that the contribution to  $\Omega_D$  is suppressed by  $\frac{1}{M_P R} \sim \frac{1}{N} \ll 1$ . For the dark photon continuum, the square coupling goes as  $\epsilon^2 \alpha_{e.m.}$ . Therefore, to ensure small enough  $\Omega_{D,f}$  the  $\epsilon$  coupling has to be small enough so that it compensates the  $M_P R \sim N$  factor.

In summary we see that in the thermal phase the QFT fluxes have to be suppressed to ensure that dark radiation at late times remains small. Another possibility to avoid dark radiation is that a mass gap show up in the hidden sector, as shown in next subsection.

### 5.6.2 The Transition Time/Temperature

The transition occurs at time  $\tau_t$  for which the horizon position is of same order as the IR brane position. We assume that supercooling does not significantly change this criterion. In the IR brane phase we take the UV brane at  $z_0 = R$ , as in the rest of the

paper. The condition is then

$$\frac{z_0(\tau_t)}{z_h} \sim \frac{R}{z_s}. \quad (5.127)$$

Using the translation of  $z_h$  in terms of temperature, this also amounts to the condition

$$T_h(\tau_t) \equiv T_{h,t} \sim \frac{1}{\pi z_s}.$$

Putting the condition Eq. (5.127) into Eq. (5.124) gives the amount of dark radiation at the transition time. Using this Eq. (5.125), where one integrates up to final time  $\tau_f = \tau_t$ , gives the fraction of dark energy at the transition time  $\Omega_{D,t}$  generated by the  $2 \rightarrow 1$  processes. For  $\tau_t \gg \tau_i$  it is a constant and we deduce the SM temperature at which the transition takes place,

$$T_{\text{SM},t} \sim \left( \frac{1}{(\text{coupling})^2 M_{\text{P}} R} \frac{g_{*i}^{\frac{1}{3}}}{g_{*f}^{\frac{1}{3}}} \right)^{\frac{1}{4}} \frac{1}{g_{*,f}^{\frac{1}{4}}} \frac{(M_{\text{P}} R)^{\frac{1}{2}}}{z_s} \quad (5.128)$$

The time of transition  $\tau_t$  easily follows. The first parenthesis is larger than 1 as required by  $\Omega_{D,f} \ll 1$  in Eq. (5.125). The main enhancement, however, comes from the large  $\sqrt{M_{\text{P}} R} \sim \sqrt{N} \gg 1$  factor at the numerator.

In the graviton case for example, in terms of  $N$  and  $T_h$  we end up with the scaling

$$\frac{T_{\text{SM},f}}{T_{h,t}} \sim N^{\frac{3}{4}}. \quad (5.129)$$

<sup>9</sup> For the dark photon case the behaviour is

$$\frac{T_{\text{SM},f}}{T_{h,t}} \sim \frac{N^{\frac{1}{4}}}{\varepsilon^{\frac{1}{2}}}. \quad (5.130)$$

The bottom line is that the hidden sector is *much* colder than the SM bath at the timescale

---

<sup>9</sup>We note this is an intermediate scaling between the rough estimates made in [169] that gave either  $\sim \sqrt{N}$  or  $\sim N$ .

where the transition between thermal and gapped phases take place. Accordingly, the corresponding mass gap scale  $\frac{1}{z_s}$  is much lower than  $T_{\text{SM},t}$ .

### 5.6.3 Ultracold Hidden Sector Freeze-out Scenario

Given the above finite temperature results we can now outline a possible cosmological scenario. All the hypotheses made throughout are restated here. We can express the scenarios either in terms of geometric quantities in AdS (brane, black hole, ...) or as a hidden CFT sector with  $N^2$  degrees of freedom.

We trace the cosmological evolution as a function of the temperature of the SM bath, here denoted by  $T_{\text{SM}} \equiv T$ .

- $T_i \sim \frac{1}{R}$

The SM energy density is taken to be  $\rho_i \sim g_* T_i^4$ . The metric is assumed to be pure AdS. Accordingly in the CFT picture, the CFT sector has zero or negligible temperature,  $T_h \sim 0$ .

- $T_i < T < T_h$

The SM bath radiates energy into the hidden sector via QFT  $2 \rightarrow 1$  processes. Radiation back into the SM bath is neglected because the hidden sector is much colder than the SM. The hidden sector strongly interacts with itself, it is in thermal equilibrium with temperature  $T_h > 0$  much lower than  $T_{\text{SM}}$ .

- $T \sim T_t$

A transition between the thermal and gapped phase occurs, whose details are not discussed here. This occurs when the temperature of the hidden sector is of order



the mass gap of the hidden sector,  $T_{h,t} \sim \frac{1}{z_s}$ . In the CFT picture, the CFT at finite temperature transitions into a “gapped CFT” whose details are described in AdS.

- $T_0 < T < T_t$

In the gapped phase — here assumed to be a slice of AdS — the continuum is discretized into narrow KK modes with spacing  $m_{KK} \sim \frac{\pi}{z_s} \sim \pi^2 T_{h,t}$ . We assume that the gapped phase has thermal equilibrium at least for  $T$  nearby  $T_t$ , so that the abundances are determined by thermal distributions. Since  $T_h < \frac{1}{z_s}$  the temperature is substantially lower than the masses, therefore all the modes are now non-relativistic. While the temperature decreases, the abundances of KK modes tend to be Boltzman suppressed and freezes out.

The scenario painted here can more generally be referred to as a *ultracold freeze-out*. The mass gap characterizing the phase transition in the hidden sector can be very small compared to the SM temperature. It could be interesting to investigate the generic implications of this setup.

In our model the continuum gets discretized by the mass gap, but with very small spacing  $\frac{1}{z_s}$ . The resulting dark matter scenario emerging in the gapped phase seems roughly similar to scenarios of dynamical dark matter (see [109, 110] and subsequent works) and continuum dark matter [89], here in the case of a ultracold dark photon field. We do not perform a detailed analysis of continuum dark photon abundances. We leave this as an interesting open direction.

## Ultracold Relativistic Hidden Sector

Letting the mass gap scale go to zero, the gapped phase cannot emerge *i.e.*  $T_t \rightarrow 0$ . In that case we recover a more minimal scenario with no phase transition, in which we are still in the thermal AdS phase at present time. To avoid dark radiation bounds in this scenario we need to make  $\Omega_D$  small enough to evade existing bounds. This is achieved by making  $\varepsilon$  and  $\frac{1}{M_{PR}}$  (*i.e.*  $\frac{1}{N}$ ) small enough. In this scenario the hidden sector is relativistic but is so cold that it avoids cosmological bounds anyways.

### 5.6.4 Dark Photon Radiation

We present a more detailed look at radiation from dark photons in our model. If there is no initial population of dark photons, brane-localized SM fermions may populate the hidden sector through the process  $f\bar{f} \rightarrow A_0$ . The S-matrix element for this process is given by

$$|\overline{\mathcal{M}}|^2 = \frac{16\pi\alpha_{EM}Q_f^2 r_{UV}}{g_5^2} \mu^2. \quad (5.131)$$

The energy density of hidden sector light species in the early universe increases the effective number of neutrino degrees of freedom, and thus is constrained by BBN and CMB observations [142]. On the other hand, energy injection due to the late decay of dark photons at or after BBN (CMB) times places a lower bound on the kinetic mixing parameter  $\varepsilon$  [142]. For a particle dark photon, this typically results in bounded exclusion regions in parameter space. In our model, light modes in the dark photon spectrum may be produced and decay as well. We show that assuming no initial population of dark photons, production of our continuum dark photon does not exceed the typical contribution a particle dark photon.

The Boltzmann equation for the energy density on the UV brane including the emission of dark photons is [180, 221, 220]

$$\frac{d\rho}{dt} + 3H(\rho + p) = -\langle\sigma v E\rangle n^2 = -\int \frac{d\mu^2}{2\pi} \rho_T(\mu^2) \int \frac{d^3 p_m}{(2\pi)^3} \mathbf{C}_\mu \quad (5.132)$$

where the collision operator resulting from fermions annihilating into dark photons is

$$\mathbf{C}[f] = \frac{1}{2} \int \frac{d^3 p_1}{2E_1(2\pi)^3} \frac{d^3 p_2}{2E_2(2\pi)^3} |\mathcal{M}(s)|^2 f_1 f_2 (2\pi)^4 \delta^{(4)}(p_1 + p_2 - p_\mu) \quad (5.133)$$

and the squared matrix element is given by (5.131). The thermal distributions  $f_i$  for the fermions are

$$f_i = \frac{1}{e^{E_i/T} + 1} \simeq e^{-E_i/T} \quad (5.134)$$

where we have assumed Maxwell-Boltzmann statistics. In the case where  $f = e^-$  ( $\bar{f} = e^+$ ) taking  $m_e \rightarrow 0$ , the collision term is can be computed analytically giving

$$\langle\sigma v E\rangle n^2 = \int \frac{d\mu^2}{2\pi} \rho_T(\mu^2) \frac{r_{\text{UV}}}{g_5^2} \frac{2\alpha_{\text{EM}}\varepsilon^2 T \mu^4}{\pi^2} K_2(\mu/T) \quad (5.135)$$

Assuming  $\rho_d \ll \rho$ , the relic abundance for dark radiation is approximately [180]

$$\Omega_d \simeq \int_0^\infty \frac{dT}{H(T)T} \frac{\langle\sigma v E\rangle n^2}{\rho} = \int \frac{d\mu^2}{2\pi} \rho_T(\mu^2) \frac{r_{\text{UV}}}{g_5^2} \frac{1350\sqrt{10}\alpha_{\text{EM}}\varepsilon^2}{\pi^4 g_*^{3/2}} \frac{M_{\text{Pl}}}{\mu} \quad (5.136)$$

In the case where there is a mass gap given by  $\mu_0$  we can compare the ratio of the relic abundance for the continuum dark photon with that of a typical particle dark photon with a definite mass  $m = \mu_0$ . Their ratio is simply

$$\frac{\Omega_d}{\Omega_d^{AD}} \simeq \int \frac{d\mu^2}{2\pi} \rho_T(\mu^2) \frac{r_{\text{UV}}}{g_5^2} \frac{\mu_0}{\mu}. \quad (5.137)$$

In our model for both cases of  $\alpha = 1, 2$  we can verify numerically for a given  $r_{\text{UV}}$  and  $c_{\text{UV}}$  that this ratio never exceeds unity signifying that the amount of dark radiation for a continuum dark photon does not exceed that of a particle dark photon.

### 5.6.5 UV Brane-Localized Dark Matter

An attractive scenario to consider is when the holographic dark photon mediates interactions between dark matter localized to the UV brane and the SM. We consider a simple model where the interaction between the dark matter, a Dirac fermion  $\chi$ , and the holographic dark photon is

$$S_{\chi A} = \int d^4x ig_\chi \sqrt{\frac{r_{\text{UV}}}{g_5^2}} \bar{\chi} \gamma^\mu \chi A_\mu \Big|_{z=R}. \quad (5.138)$$

We assume the dark matter freezes out non-relativistically. The dominant process for dark matter annihilation is  $\chi\bar{\chi} \rightarrow A(\mu)A(\mu')$ . The Boltzmann equation for this process is the standard one,

$$\frac{\partial n_\chi}{\partial t} + 3Hn_\chi = -\langle\sigma v\rangle [n_\chi^2 - (n_\chi^{\text{eq}})^2] \quad (5.139)$$

however the thermally averaged cross section is given by

$$\begin{aligned} \langle\sigma v\rangle &= \frac{1}{(n_\chi^{\text{eq}})^2} \int \frac{d\mu^2}{2\pi} \rho(\mu^2) \int \frac{d\mu'^2}{2\pi} \rho(\mu'^2) \int \frac{d^3p_\chi}{2E_\chi(2\pi)^3} \frac{d^3p_{\bar{\chi}}}{2E_{\bar{\chi}}(2\pi)^3} \frac{d^3p_\mu}{2E_\mu(2\pi)^3} \frac{d^3p_{\mu'}}{2E_{\mu'}(2\pi)^3} \\ &\times (2\pi)^4 \delta^{(4)}(p_\chi + p_{\bar{\chi}} - p_\mu - p_{\mu'}) \sum_{\text{spin}} |\mathcal{M}(\chi\bar{\chi} \rightarrow A(\mu)A(\mu'))|^2 e^{-(E_\chi + E_{\bar{\chi}})/T} \quad (5.140) \end{aligned}$$

where we have assumed Boltzmann statistics for the dark matter. This is simply the thermally averaged cross section for dark matter annihilating into dark photons of mass  $\mu$  and  $\mu'$ , convoluted with the spectral distributions of the final states.

In Fig. 5.6 for the case  $\alpha = 1$ , we show the values of  $\alpha_\chi$  and  $m_\chi$  which saturate the observed dark matter relic abundance,  $\Omega_\chi = 0.12$  [304, 283]. We take  $R = 10^{-3} \text{ TeV}^{-1}$  and  $m_A = 100 \text{ MeV}$ . The requirement on  $\alpha_\chi$  depends on whether or not the resonance in the  $\alpha = 1$  brane to brane propagator lies above or below the mass gap  $m_A$ . When the resonance

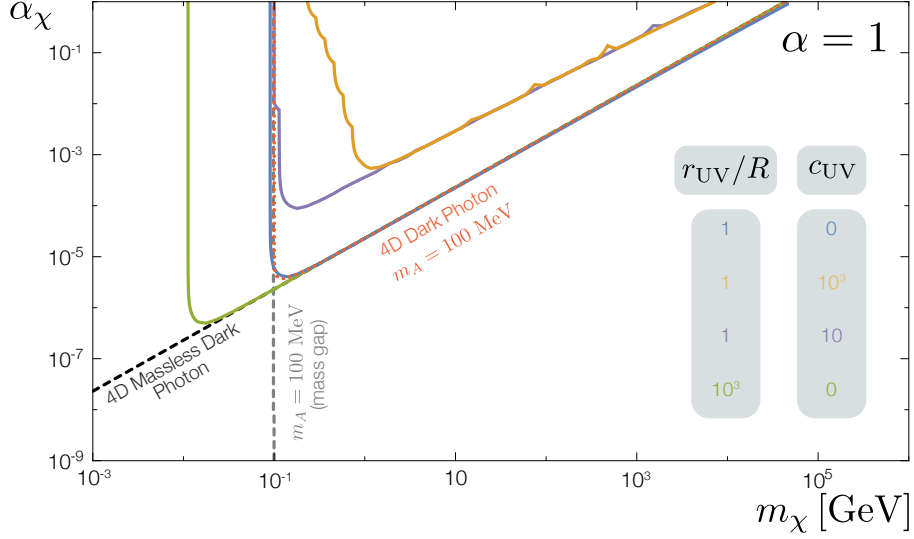


Figure 5.6: Target values of  $\alpha_\chi$  and  $m_\chi$  for non-relativistic freeze out in the case  $\alpha = 1$ . We consider a mass gap  $m_A = 100$  MeV and AdS curvature  $R^{-1} = 10^3$  TeV.

is found to be greater than the mass gap, there is only a continuum and the spectral density is given by (5.106). However if the resonance is found to be below the mass gap, then it is an isolated pole and the holographic dark photon behaves as a particle with a definite mass given by the resonance. This can be seen in the blue and green curves in Fig. 5.6. In both cases the resonance is found to be  $< 100$  MeV providing support to the cross section below the mass gap. For  $r_{UV} = R$  and  $c_{UV} = 0$  the resonance is only slightly below the mass gap and gives similar constraints to the a typical dark photon with mass (dotted red curve),  $m_A = 100$  MeV. On the other hand for  $r_{UV} = 10^3 R$  and  $c_{UV} = 0$  the resonance is well below the gap and the behavior of the holographic dark photon is dominated by the pole. Taking the limit  $r_{UV}/R \rightarrow \infty$  recovers the behavior of a dark photon with mass given by  $c_{UV} m_A R / r_{UV}$  (assuming  $c_{UV} R / r_{UV}$  is finite) or a massless dark photon for  $c_{UV} = 0$ . In contrast for the orange and purple curves, the resonance occurs above the mass gap. In this case the cross section never receives support from the isolated pole and the maximum

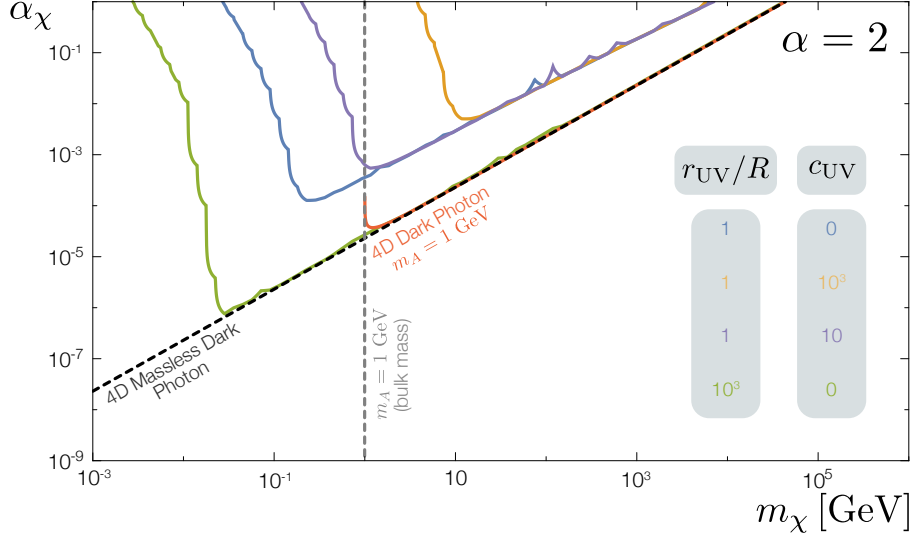


Figure 5.7: Target values of  $\alpha_\chi$  and  $m_\chi$  for non-relativistic freeze out in the case  $\alpha = 2$ . We consider a bulk mass  $m_A = 1$  GeV and AdS curvature  $R^{-1} = 10^3$  TeV.

constraint on  $\alpha_\chi$  for which the dark matter abundance is saturated is relaxed compared to the 4D limit (red dotted curve). Note that for each curve for the holographic dark photon, the constraint on  $\alpha_\chi$  begins to relax near the location of the resonance.

In Fig. 5.7 for the case  $\alpha = 2$  we again show the values of  $\alpha_\chi$  and  $m_\chi$  which saturate the observed dark matter relic abundance,  $\Omega_\chi = 0.12$  [304, 283]. As in the previous case we take  $R = 10^{-3}$  TeV $^{-1}$  however we now consider  $m_A = 1$  GeV. In contrast to the case of  $\alpha = 1$ ,  $m_A$  no longer represents a mass gap rather, it is the value of the bulk mass of the holographic dark photon. Due to the fact that there is no mass gap and the continuum extends all the way to the origin, the resonance present in the  $\alpha = 2$  propagator rather simply determines the location of the resonance peak in the spectral density. This feature is observed in the blue, purple, orange and green curves in Fig. 5.7. Once the mass of the dark matter  $m_\chi$  passes below the resonance, the preferred value of  $\alpha_\chi$  quickly increases similar to

the behavior of the red curve representing a particle dark photon with mass,  $m_A = 1$  GeV, in Fig. 5.7. However unlike a a particle dark photon with a definite mass or the  $\alpha = 1$  case where the continuum vanishes below the mass gap, the dark matter is still free to annihilate into lighter modes and the cross section still has support for dark matter masses below the resonance. We can see from the blue, purple, and orange curves in Fig. 5.7, that annihilation into the continuum may result in a preference for coupling to dark several orders of magnitude larger than that of a particle dark photon. Additionally, the resonance increases with  $c_{UV}$  resulting in heavier dark matter masses being preferred. On the other hand for  $r_{UV}/R = 10^3$  represented by the green curve in Fig. 5.7, the spectrum approaches a narrow peak resembling the distribution for a particle with definite mass. Thus above the resonance the curve closely resembles the target for a massless dark photon.

### Direct Detection

Due to the holographic dark photon's interaction with the electromagnetic current (5.97), the dark matter  $\chi$  may scatter off SM nucleons. In the small momentum transfer limit, interactions between the dark matter and the SM mediated by our dark photon map onto the a spin-independent operator  $\mathcal{O}_1^{(NR)}$  in the standard non-relativistic decomposition [127, 140, 78, 102]. The resulting bounds are identical to non-continuum dark photon models making the replacement for the dark photon's mass  $m^2 \rightarrow -g_5^2 r_{UV}^{-1} G_0(R, R)^{-1}$ . For dark matter masses  $m_\chi \gtrsim 1$  GeV, we refer to the review Ref. [274].

## Self-Interactions

The holographic dark photon may also mediate dark matter self-interactions. Dark matter self-interactions have been identified as a possible solution to several small scale structure anomalies [293, 292]. The case of fermionic dark matter mediated by a 5D bulk scalar has been studied previously and has been shown to yield a scattering cross section with a non-integer dependence on the dark matter relative velocity [68].

The scattering potential is easy to derive using the spectral representation of the brane-to-brane propagator, (5.103) and for general  $\alpha$  is given by

$$V(r) = \pm \frac{\alpha_\chi r_{\text{UV}}}{g_5^2} \int_0^\infty \frac{d\mu^2}{2\pi} \rho_T(\mu^2) \frac{e^{-\mu r}}{r}. \quad (5.141)$$

In the  $pR \ll 1$  limit the spectral integral may be computed analytically. For the case of  $\alpha = 1$  and  $c_{\text{UV}} \neq r_{\text{UV}}/R$

$$V(r)|_{\alpha=1} = \alpha_\chi \frac{2Rr_{\text{UV}}(m_{A^*}(m_{A^*} + 3) + 3)}{m_A^4(r_{\text{UV}} - c_{\text{UV}}R)^2} \frac{e^{-m_{A^*}r}}{r^5}. \quad (5.142)$$

For the case of  $\alpha = 2$  the scattering potential is

$$V(r)|_{\alpha=2} = \alpha_\chi \frac{r_{\text{UV}}}{R} \frac{16\Gamma(2\nu + 2)}{\Gamma^2(\nu)} \frac{1}{(\nu - 1 + c_{\text{UV}}m_A^2 R^2)^2} \frac{1}{r} \left(\frac{R}{2r}\right)^{2\nu+2}. \quad (5.143)$$

The potential for  $\alpha = 1$  has sufficient long range behavior to satisfy SIDM targets however is singular for  $r \rightarrow 0$ . For  $\alpha = 1$ , since  $\nu > 1$ , the potential is singular as well. As discussed for the case of a bulk scalar mediator in Ref. [68], the self-interaction phenomenology of singular potentials becomes numerically intractable and is unlikely to produce effects relevant for small-scale structure anomalies.



## 5.7 Phenomenological Comments and Cross Sections

We consider the phenomenology and relevant cross sections resulting from the holographic dark photon model's coupling to the SM electromagnetic current. The holographic dark photon may present a signature at various dark photon searches. We review the possibility of decay into the electromagnetic spectrum and oscillation into bulk modes as well as present results relevant for various dark photon searches. As discussed in Section 5.6, we can safely ignore BBN and CMB bounds resulting from overabundance and decay into the SM states.

### 5.7.1 Decay Width and Bulk Oscillations

One of the immediate results of the Feynman rule (5.97) is that for  $p^2 > 4m_f^2$ , the holographic dark photon may decay into fermion–anti-fermion pairs. As with other dark photon models which couple to the electromagnetic current, energy injection into the electromagnetic spectrum is a concern. The leading order cause of this effect is decay into electron–positron pairs for  $p^2 > 4m_e^2$  and decay into three photons at 1-loop for  $p^2 < 4m_e^2$ . For a holographic dark photon with mass parameter  $\mu$ , the decay width for these processes are [262, 237]

$$\Gamma_{e^+e^-} = \frac{\alpha_{\text{EM}}\varepsilon^2\mu}{3} \frac{r_{\text{UV}}}{g_5^2} \sqrt{1 - 4\frac{m_e^2}{\mu^2}} \left(1 + 2\frac{m_e^2}{\mu^2}\right) \quad \mu > 2m_e \quad (5.144)$$

$$\Gamma_{\gamma\gamma\gamma} = \frac{17\alpha_{\text{EM}}^4\varepsilon^2}{11664000\pi^3} \frac{r_{\text{UV}}}{g_5^2} \frac{\mu^9}{m_e^8} \quad \mu \ll m_e. \quad (5.145)$$

The numerical solution for  $\Gamma_{\gamma\gamma\gamma}$ , valid for all  $\mu < m_e$ , is presented in Ref. [237].

Analogously, we may determine the associated width induced by the holographic self energy  $\Sigma(p^2)$ . From the optical theorem the width for bulk oscillations is

$$\Gamma_{\text{bulk}} = \frac{1}{\mu} \text{Im} \mathcal{M}(A_0 \rightarrow A_0) . \quad (5.146)$$

From (5.58) we can identify the imaginary part of matrix element as

$$\text{Im} \mathcal{M}(A_0 \rightarrow A_0) = \frac{1}{g_5^2} \text{Im} \Sigma(\mu^2) . \quad (5.147)$$

which for gives a bulk decay width

$$\Gamma_{\text{bulk}}^{\alpha=1} = \frac{1}{g_5^2} \frac{\pi}{2} \mu R \left( 1 - \frac{m_A^2}{\mu^2} \right) \quad (5.148)$$

$$\Gamma_{\text{bulk}}^{\alpha=2} = \frac{1}{g_5^2} \sin \pi \nu \frac{\Gamma(1-\nu)}{\Gamma(\nu)} \left( \frac{pR}{2} \right)^{2\nu-1} \quad (5.149)$$

Therefore when  $r_{\text{UV}} \sim R$  as expected, we can assume  $\Gamma_{\text{bulk}}^{\alpha=1,2} > \Gamma_{e^+e^-}, \Gamma_{\gamma\gamma\gamma}$  due suppression from the kinetic mixing parameter  $\varepsilon$  which is typically  $\ll 1$ . As a result we ignore bounds resulting from overproduction and decay into the electromagnetic spectrum, as we assume the dark photon will decay into bulk modes.

## 5.7.2 Holographic Dark Photon Processes

We review processes which include the holographic dark photon. We leave a detailed discussion of cosmological effects until Section 5.6.

**2  $\rightarrow$  1 Production** The simplest production mechanism is just the 2  $\rightarrow$  1 process where two fermions annihilate to produce the holographic dark photon spectrum. The cross section for this process is

$$\sigma v = \frac{4\pi\alpha_{\text{EM}}Q_f^2 r_{\text{UV}}}{g_5^2} \rho_T(s) \quad (5.150)$$

where  $s$  is the squared center of mass energy.  $2 \rightarrow 1$  production is the primary process by which cosmological holographic dark photons may be produced from the SM. As previously discussed, the dark photon decays invisibly into bulk modes before it can be constrained by BBN and CMB constraints from either overabundance or energy injection into the electromagnetic spectrum.

**Electron–Positron Annihilation** The holographic dark photon may also present a signature from electron–positron annihilation at collider searches such as BaBar and Belle II [163]. Searches for dark photons with invisible decays look for a mono-energetic photon in addition to missing energy. When the spectral density has an isolated pole or the width of the resonance corresponding to the pole mass  $m_\alpha$  is narrow, the holographic dark photon will produce a signal similar to that of a dark photon with a definite mass. On the other hand if the width of the resonance is broad or it is located beyond the experimental sensitivity, all kinematically accessible states in the continuum may be produced. As a result the visible photon will now have a distribution of energies according to the holographic dark photons spectral density.

We present the tree level cross section for the process  $e^+e^- \rightarrow \gamma A_0$ . In the limit where the electron mass  $m_e^2 \ll s$ , the cross section is given by

$$\sigma = \int \frac{d\mu^2}{2\pi} \rho_T(\mu^2) \sigma_{4D}(\mu^2) \quad (5.151)$$

with

$$\sigma_{4D}(\mu^2) = \frac{4\pi\alpha_{\text{EM}}\varepsilon^2 r_{\text{UV}}(s - \mu^2)}{g_5^2 s^4} \left[ -s(s + 2\mu^2) + (s^2 + 2\mu^2 s + 2\mu^4) \log\left(\frac{s}{m_e^2}\right) \right]. \quad (5.152)$$

**Deviation to Coulomb Potential** The holographic dark photon may also mediate interactions between electromagnetic currents, resulting in deviations to the Coulomb potential in the non-relativistic limit. Using the spectral representation of the propagator given by (5.103), the scattering potential is given generally by

$$V(r) = \pm \frac{\alpha_{\text{EM}} \varepsilon^2 r_{\text{UV}}}{g_5^2} \int_0^\infty \frac{d\mu^2}{2\pi} \rho_T(\mu^2) \frac{e^{-\mu r}}{r}. \quad (5.153)$$

where we take the plus (minus) sign for particle–particle (anti-particle) scattering. Using the expressions (5.106) and (5.107), we may calculate the scattering potential in the  $pR \ll 1$  limit. For the case of  $\alpha = 1$

$$V(r)|_{\alpha=1} = \varepsilon^2 Q_f^2 \alpha_{\text{EM}} \frac{2Rr_{\text{UV}}(m_A r(m_A r + 3) + 3)}{m_A^4 (r_{\text{UV}} - c_{\text{UV}} R)^2} \frac{e^{-m_A r}}{r^5}. \quad (5.154)$$

For the case of  $\alpha = 2$  the scattering potential is

$$V(r)|_{\alpha=2} = \varepsilon^2 Q_f^2 \alpha_{\text{EM}} \frac{r_{\text{UV}}}{R} \frac{16\Gamma(2\nu + 2)}{\Gamma^2(\nu)} \frac{1}{(\nu - 1 + c_{\text{UV}} m_A^2 R^2)^2} \frac{1}{r} \left(\frac{R}{2r}\right)^{2\nu+2}. \quad (5.155)$$

Deviations to the Coulomb potential are studied in fifth force searches [25].

**CMB Resonant Conversion** Inter-conversion of photons and dark photons through kinetic mixing or semi-Compton absorption typically constrains low-mass dark photons [262, 238]. These processes are enhanced by matter effects which induce a mass for visible photons. The strongest constraints result from resonant conversion when the photon mass  $\omega \sim m_{\text{dark photon}}$ . For temperatures  $T \lesssim \mathcal{O}(\text{MeV})$  but before recombination, resonant conversion of CMB photons into dark photons may increase the number of light degrees of freedom in the universe, resulting in a positive shift in the effective number of Neutrininos [238]. Since dark photons in our model decay invisibly into bulk modes, we assume these constraints to be negligible.

However for temperature  $T \lesssim 500$  eV, resonant production of low energy photons may result in CMB spectral distortions as well [262, 238]. In our continuum model the visible photon may always be in resonance with a state in the continuum given the mass gap (if it exists) is small enough.

**Stellar Emission** Kinetic mixing between the visible photon and dark photon results in solar emission of dark photons [263]. For low mass dark photons in the resonant case, when  $m_{\text{dark photon}} \ll \omega$  the emission rate is enhanced by a factor of  $\omega^2/m_{\text{dark photon}}^2$ . In our model resonant emission will occur when the mass gap  $m_A \ll \omega$  for  $\alpha = 1$ , or for all  $m_A$  if  $\alpha = 2$ .

### 5.7.3 Phenomenological Signatures and Plots

We present plots resulting from our recasting presented in Section 5.5.7. We consider the cases  $\alpha = 1$  and  $\alpha = 2$  for multiple values of the AdS curvature  $R^{-1}$ .

$\alpha = 1$ : For  $\alpha = 1$  the spectrum is that of a gapped continuum with the mass gap given by the dark photon's bulk mass on the UV brane,  $m_A$ . Following our recasting formula (5.122) we plot the relevant observables for case  $\alpha = 1$  in Fig. 5.8 and 5.9. We choose  $c_{\text{UV}} = 10^3$  and  $r_{\text{UV}} = R$  such that the pole mass  $m_1$  remains above the mass gap, in order to demonstrate the constraints due to the continuum. For  $\alpha = 1$  the spectral density is peaked near the gap and thus the main contribution to constraints is due to states clustered near the mass gap  $m_A$ . Confirming the spectral densities weak dependence on  $R$  in this case, we note that bounds for  $R = 1 \text{ TeV}^{-1}$  and  $R = 10^{-18} \text{ GeV}^{-1}$  from Figures 5.9 and 5.8 are quite similar.

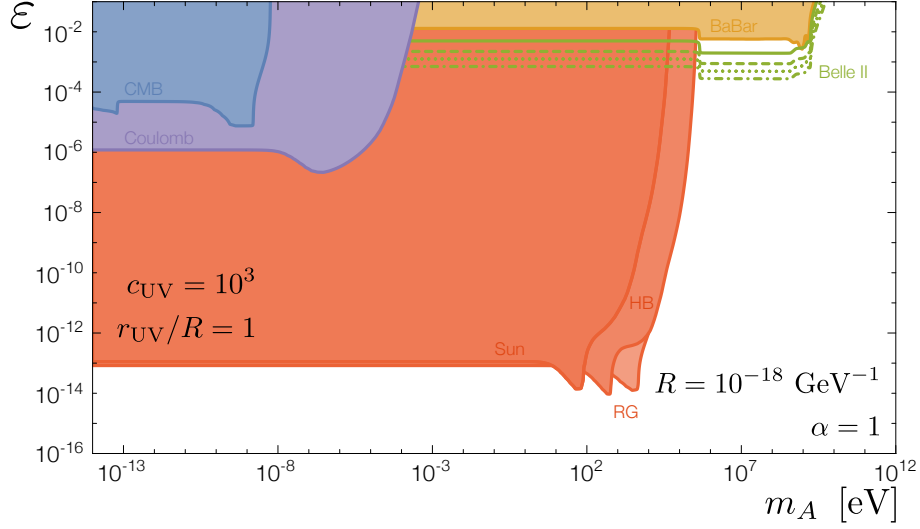


Figure 5.8: We recast constraints on invisibly decaying dark photons according to our formula for  $\alpha = 1$  and  $R = 10^{-18} \text{ GeV}^{-1}$ . There are bounds from BaBar and Belle II projections at large masses [163]. The solid green curve corresponds to a projected luminosity of 0.04%, the dashed green curve corresponds to 1% luminosity, the dotted green curve to 10%, and the dash-dotted green curve to 100%. Note that projections greater than 0.04% are purely speculative and require a detailed analysis. There are bounds due to stellar cooling from the Sun, HB stars, and RG stars [263]. At low masses there are bounds from fifth force experiments searching for deviations to the Coulomb potential [25], as well as from CMB spectral distortions[246]. We take  $r_{UV}/R = 1$  and  $c_{UV} = 10^3$  so that the pole mass remains above the gap scale and does not contribute.

Because all states above the gap with  $\mu^2 \geq m_A^2$  contribute to observables, constraints on  $\varepsilon$  become stronger with a decreasing mass gap. We find that observables corresponding to heavier states generally extend to lower mass gaps, dominating over weaker bounds that otherwise wouldn't have overlapped. This can be seen in Fig. 5.8 and 5.9 by noting that the stellar cooling constraints dominating over CMB resonant conversion and fifth force experiments for a small mass gap.

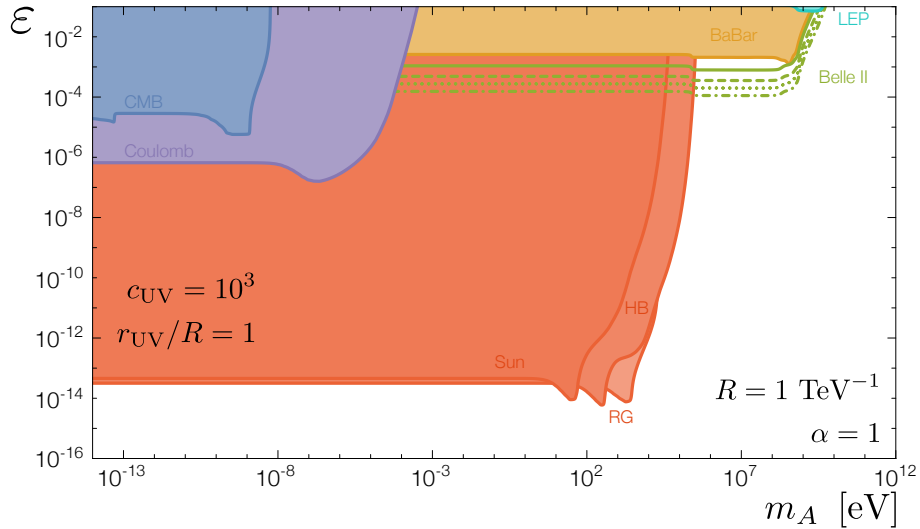


Figure 5.9: We recast constraints on invisibly decaying dark photons according to our formula for  $\alpha = 1$  and  $R = 1 \text{ TeV}^{-1}$ . There are bounds from BaBar and Belle II projections at large masses [163]. The solid green curve corresponds to a projected luminosity of 0.04%, the dashed green curve corresponds to 1% luminosity, the dotted green curve to 10%, and the dash-dotted green curve to 100%. Note that projections greater than 0.04% are purely speculative and require a detailed analysis. There are bounds due to stellar cooling from the Sun, HB stars, and RG stars [263]. At low masses there are bounds from fifth force experiments searching for deviations to the Coulomb potential [25], as well as from CMB spectral distortions[246]. We take  $r_{\text{UV}}/R = 1$  and  $c_{\text{UV}} = 10^3$  so that the pole mass remains above the gap scale and does not contribute.

$\alpha = 2$ : For  $\alpha = 2$  the spectrum is a gapless continuum. In contrast to the  $\alpha = 1$  case, the constraints are highly dependent on the AdS curvature  $R^{-1}$ . The location and width of the resonance is dependent on  $R$  as well as  $m_A$  through the bulk mass parameter  $\nu$ . Because  $m_A$  no longer plays the role of a mass gap in the  $\alpha = 2$  case, when  $m_A$  passes beyond the upper bound of an experiment's sensitivity to the dark photon mass lighter states in the continuum may still contribute. This results in the extension of bounds beyond their typical upper mass threshold for a particle dark photon. This feature is most clearly demonstrated by the stellar emission bounds in Figures 5.11 and 5.10.

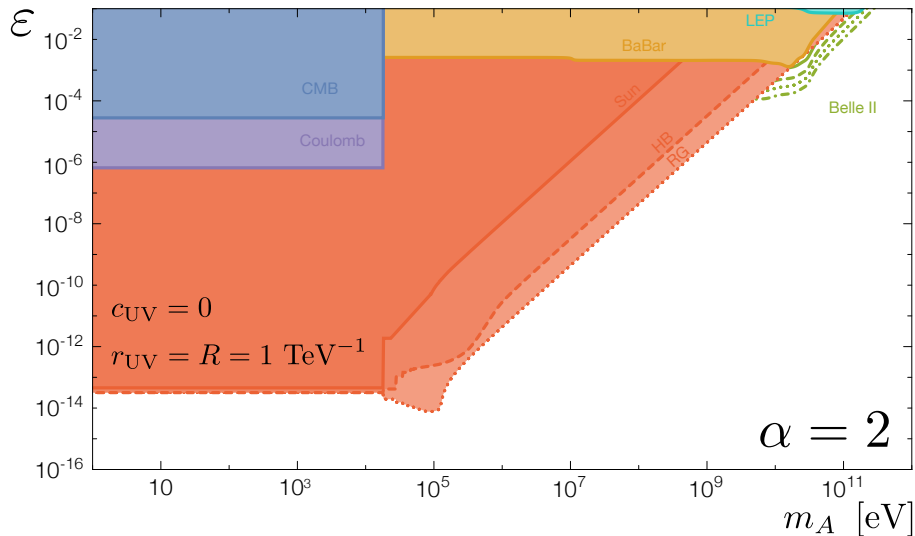


Figure 5.10: We recast constraints on invisibly decaying dark photons according to our formula for  $\alpha = 2$  and  $R = 1 \text{ TeV}^{-1}$ . There are bounds from BaBar, LEP, and Belle II projections at large masses [163]. The solid green curve corresponds to a projected luminosity of 0.04%, the dashed green curve corresponds to 1% luminosity, the dotted green curve to 10%, and the dash-dotted green curve to 100%. Note that projections greater than 0.04% are purely speculative and require a detailed analysis. There are bounds due to stellar cooling from the Sun, HB stars, and RG stars [263]. At low masses there are bounds from fifth force experiments searching for deviations to the Coulomb potential [25], as well as from the resonant conversion of CMB photons into dark photons[246]. We take  $r_{UV}/R = 1$  and  $c_{UV} = 0$ .

## 5.8 On the Goldstone Equivalence Theorem in AdS

In flat space the Goldstone equivalence theorem states that longitudinally polarized gauge fields can be replaced by Goldstone bosons at large momentum in the external legs of  $S$ -matrix elements. This is a consequence of unitarity of the  $S$ -matrix. How does the Goldstone equivalence theorem emerge in our AdS  $U(1)$  model?

To understand how the Goldstone equivalence theorem may appear in our AdS setup, we need to figure out to which kind of objects it applies. In our theory there is gauge



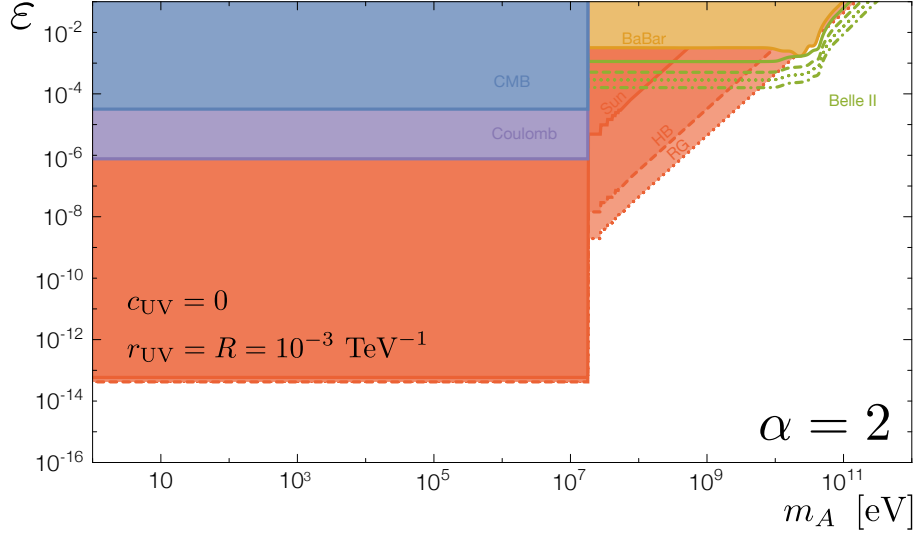


Figure 5.11: We recast constraints on invisibly decaying dark photons according to our formula for  $\alpha = 2$  and  $R = 1 \text{ TeV}^{-1}$ . There are bounds from BaBar and Belle II projections at large masses [163]. The solid green curve corresponds to a projected luminosity of 0.04%, the dashed green curve corresponds to 1% luminosity, the dotted green curve to 10%, and the dash-dotted green curve to 100%. Note that projections greater than 0.04% are purely speculative and require a detailed analysis. There are bounds due to stellar cooling from the Sun, HB stars, and RG stars [263]. At low masses there are bounds from fifth force experiments searching for deviations to the Coulomb potential [25], as well as from the resonant conversion of CMB photons into dark photons[246]. We take  $r_{\text{UV}}/R = 1$  and  $c_{\text{UV}} = 0$ .

fixing on both boundary and bulk. We can therefore expect both a bulk and a boundary Goldstone equivalence theorem, that may apply to different kind of amplitudes.

A convenient way to verify the equivalence theorem in flat space is to take Feynman-t'Hooft gauge and perform a unitary cut on internal gauge and Goldstone lines [251]. Namely, in the Feynman-t'Hooft gauge the timelike contribution to the amplitude goes as  $\frac{k^\mu k^\nu}{m_\lambda^2}$ . It must be cancelled by a corresponding line of the Goldstone  $\pi$ . One then performs a Cutcosky cut on these lines. Unitarity of the full amplitude requires the cancellation  $-|\frac{k_\mu}{m_\lambda} \Gamma_A^\mu|^2 + |\Gamma_\pi|^2 = 0$ . One then uses  $\epsilon_\mu(k) \rightarrow \frac{k_\mu}{m}$  for  $k^2 \gg m^2$ , which establishes the equiv-

alence theorem. This is not a rigorous proof but is enough in the scope of this work. We use a similar method in the following subsections.

### 5.8.1 A Bulk Equivalence Theorem

We first consider the bulk gauge fixing term Eq. (5.8). This term involves both  $\pi$  and  $A_z$ , hence both fields participate to the equivalence theorem. This seems a challenging problem. However, we notice that  $\pi$  and  $A_z$  enter as the  $\Theta$  combination, Eq. (5.52). Thus the bulk equivalence theorem will be express in terms of the  $\Theta$  field.

To avoid any interplay with the boundary gauge fixing, we focus on cutting Dirichlet internal lines. Dirichlet propagators in any warped background can always be represented in a momentum spectral representation (see *e.g.* [138])

$$G_D(p; z, z') = i \int dm^2 \frac{f_{D,m}(z) f_{D,m}(z')}{p^2 - m^2 + i\epsilon}. \quad (5.156)$$

Using the momentum representation Eq. (5.156), unitarity cuts in momentum space are easily implemented in AdS. Taking the Feynman-t'Hooft gauge  $\xi = 1$ , the subsequent steps of the equivalence theorem proof follow similarly to flat space. The combination of the timelike and Goldstone contributions

$$- \left| \frac{k^\mu}{m} f_{D,m}^{A_L} \Gamma_A^\mu(k) \right|^2 + |f_{D,m}^\Theta \Gamma_\Theta(k)|^2 \quad (5.157)$$

appears. To verify whether this combination vanishes, we need to check that the modes of  $A_{L,D}^\mu$  and  $\Theta_D$  are identical. The EOM for  $A_{L,D}^\mu$  is given in Eq. (5.38), the EOM for  $\Theta_D$  is given in Eq. (5.52). We can see that, for any  $d, \alpha$ , the wave operators in both EOM are identical. Thus the solutions and the subsequent set of Dirichlet modes given are identical,

$f_{D,m}^{A_L} = f_{D,m}^\Theta$  for any  $m$ . This ensures that the combination vanishes as required by unitarity.

We then use that  $\epsilon_\mu(k) \rightarrow \frac{k_\mu}{m}$  for  $k^2 \gg m^2$  which establishes

$$\left| \epsilon_\mu(k) f_{D,m}^{A_L} \Gamma_A^\mu(k) \right|^2 \Big|_{p \gg m} \rightarrow |f_{D,m}^\Theta \Gamma_\Theta(k)|^2. \quad (5.158)$$

The bulk equivalence theorem presented here applies to external legs which are Dirichlet modes  $f_{D,m}$ . In pure AdS, Dirichlet modes amount to the AdS *normalizable modes* and the  $\Gamma$  diagrams are referred to as AdS *transition amplitudes* (see *e.g.* [22]).

### 5.8.2 A Boundary Equivalence Theorem

We consider the boundary gauge fixing Eq. (5.9). This gauge fixing affects the boundary degrees of freedom and appears in the boundary action. Let us compare the boundary action for  $S_A^{\text{UV}}$  and  $S_a^{\text{UV}}$ . The fundamental boundary actions match up to an overall factor,  $\mathcal{B}_a = c_{\text{UV}} R^{d-3} \xi_{\text{UV}} \mathcal{B}_{\tilde{G}}$ . The holographic self-energies do not match,  $\Sigma_{A_L} \neq \Sigma_a$ , even for large  $p$ . The standard equivalence theorem, however, applies for  $S$  matrix elements, there are no 1PI insertions on the external legs. Thus here in analogy we will consider diagrams with  $A_{L,0}$  and  $a_0$  in external legs without the  $\Sigma$  insertions. This amounts to a slightly different choice of field basis, analogous to the one introduced in [27] (see discussion in [139]). Without the  $\Sigma$  insertions, the propagators of  $A_{L,0}$  and  $a_0$  take the same form as in flat space.

We take the Feynman-t'Hooft gauge  $\xi = 1$ ,  $\xi_{\text{UV}} = \frac{g_{d+1}^2}{r_{\text{UV}} R^{d-4}}$ , which implies  $\mathcal{B}_{\tilde{G}} = \mathcal{B}_G$ . The propagators for  $A_0^\mu$  and  $a_0$  without the  $\Sigma$  insertions go respectively as  $-i\eta^{\mu\nu} \mathcal{B}_G^{-1}$  and  $i\mathcal{B}_a^{-1}$ . We then proceed with similar steps than the flat space proof. We perform a unitarity cut on the internal gauge and Goldstone lines of a generic amplitude and isolate

the vanishing combination of timelike and Goldstone contributions

$$-\left|\frac{k_\mu}{m_{\mathcal{B}}}\Gamma_A^\mu(k)\right|^2 + \frac{1}{c_{UV}R^{d-3}\xi_{UV}}|\Gamma_a(k)|^2 = 0. \quad (5.159)$$

We have used the relation between  $\mathcal{B}_G$  and  $\mathcal{B}_a$  and introduced the mass  $m_{\mathcal{B}}^2 = \frac{c_{UV}}{r_{UV}}Rg_{d+1}^2v_0^2$  which appears in the polarization sum of  $A_0^\mu$ . Finally we identify as usual the polarization vector  $\epsilon_{\mu,0}(k) \propto \frac{k_\mu}{m_{\mathcal{B}}}$  for  $k^2 \gg m_{\mathcal{B}}^2$ , here associated to the boundary component of the field. If we normalize the polarization such that  $\epsilon_\mu(k) \rightarrow \frac{k_\mu}{v_0}$  we obtain

$$|\epsilon_{\mu,0}(k)\Gamma_A^\mu(k)|^2 \Big|_{p \gg m_{\mathcal{B}}} \rightarrow |\Gamma_a(k)|^2. \quad (5.160)$$

This is a “boundary” version of the equivalence theorem, applying to external legs corresponding to the boundary component of the vector and Goldstone fields.

## 5.9 $U(1)$ Breaking in the Holographic CFT

We now turn to the CFT dual. For  $\alpha \geq \frac{d}{2}$  the Higgs background does not destabilize the AdS metric. We can thus apply AdS/CFT and identify the holographic theory seen by an observer localized on the UV brane *i.e.* on the regulated AdS boundary. AdS/CFT applies for  $pR \ll 1$  [7]. Our goal here is to understand the features encoded in the AdS two-point boundary correlator

$$\langle A_0^\mu(p)A_0^\nu(-p) \rangle = \left( \eta_{\mu\nu} - \frac{p_\mu p_\nu}{p^2} \right) \frac{ig_{d+1}^2}{\mathcal{B}_G(p) + \Sigma(p^2)} \quad (5.161)$$

with  $\alpha \geq \frac{d}{2}$  and  $pR \ll 1$  in terms of a  $d$ -dimensional CFT model with broken  $U(1)$ .

We know that the  $d$ -dimensional theory is a CFT with bilinear coupling to sources. In the presence of a UV brane the sources are understood as dynamical fields and form an

“elementary” sector containing local operators. The CFT sector contains a scalar primary  $\mathcal{O}$  with unit  $U(1)$  charge and conformal dimension  $\Delta_{\mathcal{O}} = \frac{d}{2} + \alpha$  and a  $U(1)$  current  $\mathcal{J}_{\mu}$  with conformal dimension  $\Delta_{\mathcal{J}}$ . CFT unitarity implies that a conserved current has  $\Delta_{\mathcal{J}} = \frac{d}{2} - 1$  and a non-conserved current has dimension

$$\Delta_{\mathcal{J}} = \frac{d}{2} - 1 + \gamma_{\mathcal{J}} \quad (5.162)$$

with  $\gamma_{\mathcal{J}} > 0$  [245].

The elementary sector couples bilinearly to CFT operators. In our case the elementary fields are defined by  $\Phi_0 = \frac{1}{\sqrt{R}}\varphi$ ,  $A_0^{\mu} = B^{\mu}$ , with  $[\varphi] = \frac{d}{2} - 1$ ,  $[B^{\mu}] = 1$ . The  $U(1)$  gauge field has strength  $g$ . The Lagrangian of the  $d$ -dimensional holographic theory with the above content takes the general form

$$\mathcal{L} = \mathcal{L}[\varphi_{\text{CFT}}] + \mathcal{L}_0[\varphi, B^{\mu}] + \frac{b_{\mathcal{J}}}{\Lambda^{\Delta_{\mathcal{J}} - \frac{d}{2} - 1}} B^{\mu} \mathcal{J}_{\mu} + \frac{b_{\mathcal{O}}}{\Lambda^{\Delta_{\mathcal{O}} - \frac{d}{2} - 1}} (\varphi \mathcal{O}^* + h.c.) \quad (5.163)$$

where  $\Lambda$  is the cutoff scale and  $b_{\mathcal{J}}, b_{\mathcal{O}}$  are dimensionless coefficients. We assume  $b_{\mathcal{J}, \mathcal{O}} = \mathcal{O}(1)$ . The  $\Lambda$  cutoff can be identified with the AdS curvature  $\frac{1}{R}$ .

### 5.9.1 $U(1)$ breaking

In the holographic theory defined by Eq. (5.163), the  $U(1)$  breaking occurs via a potential in the elementary Lagrangian  $\mathcal{L}_0$ , giving a nonzero vev for  $\varphi$ . This potential can be identified with the holographic potential derived in Eq. (5.25).

The spontaneous  $U(1)$  breaking in the elementary sector induces a mass for the  $B_{\mu}$  field. By gauge invariance, the elementary  $U(1)$  gauge field must become massless when  $\langle \varphi \rangle \rightarrow 0$  hence

$$m_B \propto g \langle \varphi \rangle. \quad (5.164)$$

It follows that the two-point correlator of  $B_\mu$  takes the form

$$\langle B^\mu(p)B^\nu(-p) \rangle = \left( \eta_{\mu\nu} - \frac{p_\mu p_\nu}{p^2} \right) \frac{ig^2}{Z_B p^2 - m_B^2 + \kappa(-p^2)^{\Delta_{\mathcal{J}} - \frac{d}{2}}}. \quad (5.165)$$

This is an exact result obtained by dressing the free propagator of  $B_\mu$  with bilinear insertions of  $\langle \mathcal{J}^\mu \mathcal{J}^\nu \rangle$ . The  $\kappa$  parameter is proportional to  $\frac{b_{\mathcal{J}}^2}{\Lambda^{2\Delta_{\mathcal{J}} - d - 2}}$ .

As a result of the mixing term  $\varphi \mathcal{O}^* + h.c.$  in Eq. (5.163) the  $U(1)$  breaking is transmitted to the CFT sector. In particular,  $\mathcal{O}$  acquires a  $U(1)$ -breaking vev of order

$$\langle \mathcal{O} \rangle \sim \Lambda^{\Delta_{\mathcal{O}} - \frac{d}{2} + 1} \langle \varphi \rangle. \quad (5.166)$$

If  $\Delta_{\mathcal{O}} \gg d$ , the bilinear mixing is a highly irrelevant operator. Its effect can thus be neglected at energies below the  $\Lambda$  cutoff. If  $\Delta_{\mathcal{O}} = d$ , the bilinear mixing is a classically marginal operator — receiving quantum corrections from the elementary sector. Moreover in that case the CFT contains in general an exactly marginal deformation

$$S_{\text{CFT}} + \omega \int d^d x \mathcal{O}(x) + h.c. \quad (5.167)$$

with  $\omega \in \mathbb{R}$ .<sup>10</sup> Building on the above features we then study the properties of the  $U(1)$  current.

### 5.9.2 Properties of the $U(1)$ Current

The total  $U(1)$  current is given by

$$\mathcal{J}^\mu = \mathcal{J}_{\text{el}}^\mu + \mathcal{J}_{\text{CFT}}^\mu. \quad (5.168)$$

---

<sup>10</sup>In the presence of various exactly marginal deformations, the values of the operators span the “conformal manifold” [32]. Here the conformal manifold is simply  $\mathbb{R}$ .

Since there is spontaneous breaking in the elementary sector, we have  $\partial_\mu \mathcal{J}_{\text{el}}^\mu = 0$  upon using the EOM of the Goldstone boson. In CFT, there is no notion of on-shellness — except for a free field. Hence whenever the symmetry is broken we expect  $\partial_\mu \mathcal{J}_{\text{CFT}}^\mu \neq 0$ . See also [11] for consideration on the Goldstone equivalence theorem along these lines.

Another way to think about this feature is that in AdS, whether the  $U(1)$  symmetry is spontaneously or explicitly broken on the boundary is irrelevant for the bulk fields. The bulk EOM and boundary conditions for  $A_\mu$  are the same for either mechanism. As a result, whether the  $U(1)$  breaking in the elementary sector is spontaneous or explicit should be irrelevant for the corresponding CFT operator  $\mathcal{J}_{\text{CFT}}^\mu$ .

We now proceed to study the  $\Delta_{\mathcal{O}} \gg d$  and  $\Delta_{\mathcal{O}} = d$  cases.

$\Delta_{\mathcal{O}} \gg d$

When  $\alpha \gg \frac{d}{2}$  (*i.e.*  $\Delta_{\mathcal{O}} \gg d$ ), the  $\varphi \mathcal{O}^* + h.c.$  mixing operator is highly irrelevant. Hence at energies much below the  $\Lambda$  cutoff, the vev of  $\mathcal{O}$  is negligible and the CFT current is approximately conserved,

$$\partial_\mu \mathcal{J}_{\text{CFT}}^\mu \Big|_{\Delta_{\mathcal{O}} \gg d, p \ll \Lambda} \approx 0. \quad (5.169)$$

Therefore the dimension of the CFT current is

$$\Delta_{\mathcal{J}}|_{\Delta_{\mathcal{O}} \gg d} = d - 1. \quad (5.170)$$

$\Delta_{\mathcal{O}} = d$

When  $\alpha \gg \frac{d}{2}$  (*i.e.*  $\Delta_{\mathcal{O}} \gg d$ ),  $\mathcal{O}$  is a marginal operator. By dimensional analysis, we expect  $\langle \mathcal{J}_{\text{CFT}}^\mu \rangle \sim \partial^\mu \partial^{-2} \langle \mathcal{O} \rangle$ . This is consistent with the fact that the divergence of the

current is approximately a primary at large momentum [11]. Since the value of  $\langle \mathcal{O} \rangle$  is set by the elementary sector as dictated by Eq. (5.166) we obtain

$$\partial_\mu \langle \mathcal{J}_{\text{CFT}}^\mu \rangle \Big|_{\Delta_{\mathcal{O}}=d, p \ll \Lambda} \sim g \langle \varphi \rangle \Lambda^{\frac{d}{2}+1}. \quad (5.171)$$

What is the anomalous dimension of the CFT current? To determine it we use unitarity of the states created by  $\mathcal{J}_{\text{CFT}}^\mu$ . Using the standard approach to derive unitarity bounds at first level we obtain

$$|P_\mu \mathcal{J}^\mu |0\rangle|^2 = \langle 0 | \mathcal{J}^\nu K_\nu P_\mu \mathcal{J}^\mu |0\rangle = \gamma_{\mathcal{J}} \langle 0 | \mathcal{J}_\mu \mathcal{J}^\mu |0\rangle \quad (5.172)$$

where  $P, K$  are the raising and lowering CFT operators. Using Eq. (5.171) we know that  $P_\mu \mathcal{J}_{\text{CFT}}^\mu \propto \partial_\mu \mathcal{J}_{\text{CFT}}^\mu = g \langle \varphi \rangle \Lambda^{\frac{d}{2}+1} \neq 0$ . Plugging this result into Eq. (5.172), we learn that the anomalous dimension is proportional to the square of the symmetry breaking vev,

$$\gamma_{\mathcal{J}} \propto g^2 |\langle \varphi \rangle|^2 \Lambda^{-d-2} \quad (5.173)$$

where we have introduced appropriate powers of  $\Lambda$  to make the quantity on the r.h.s dimensionless.

### 5.9.3 Comparison to AdS

Finally we compare the  $\langle B^\mu B^\nu \rangle$  correlator from Eq. (5.165), together with the scaling properties derived along this section, to the AdS two-point point boundary correlator Eq. (5.161). We will see that all the features obtained from the CFT model also emerge in AdS.



### $\alpha \gg \frac{d}{2}$ Case

The holographic self-energy is given by Eq. (5.71). The mass appearing in the boundary action is  $\sqrt{c_{\text{UV}}}g_{d+1}v_0$ , which is consistent with the scaling of  $m_B$  given in Eq. (5.164). The AdS Higgs vev is highly localized towards the boundary and approximately does not influence the EOM for  $A_\mu$ . In the CFT this corresponds to the elementary-CFT mixing being a highly irrelevant operator. The holographic action is  $\Sigma(p^2) \propto (-p^2)^{\frac{d}{2}-1}$ . This scaling is consistent with the dimension of the current obtained in Sec. 5.9.2.

### $\alpha = \frac{d}{2}$ Case

The holographic self-energy is given by Eq. (5.75). The mass appearing in the boundary action is  $\sqrt{c_{\text{UV}} + \frac{1}{d-2}}g_{d+1}v_0$ , consistent with Eq. (5.164). The AdS Higgs vev provides an effective bulk mass term for  $A_\mu$ . As a result we have the scaling  $\Sigma(p^2) \propto (-p^2)^\nu$  where  $\nu$  is given by Eq. (5.73). For  $g_{d+1}v_0R \ll 1$  the anomalous dimension  $\gamma_{\text{AdS}}$  appears, with

$$\nu = \frac{d}{2} - 1 + \gamma_{\text{AdS}} \quad \gamma_{\text{AdS}} = \frac{(g_{d+1}v_0R)^2}{d-2}. \quad (5.174)$$

We can see that  $\gamma_{\text{AdS}}$  is proportional to the square of the Higgs vev. Such a scaling is consistent with the anomalous dimension  $\gamma_{\mathcal{J}}$  obtained in the holographic CFT, Eq. (5.173). We can also see that this anomalous dimension is always positive, which is consistent with CFT unitarity bounds.

#### 5.9.4 Summary

The main properties of the dual CFT model obtained here from both AdS and CFT sides are the following. For  $\Delta_{\mathcal{O}} \gg d$  (*i.e.*  $\alpha \gg \frac{d}{2}$  in AdS), the  $U(1)$  breaking in the elementary sector does not affect the  $U(1)$  CFT current. The current is thus conserved *i.e.* has dimension  $\Delta_{\mathcal{J}} = d - 1$ . In contrast, for  $\Delta_{\mathcal{O}} = d$  (*i.e.*  $\alpha = \frac{d}{2}$  in AdS) the  $U(1)$  breaking in the elementary sector affects the CFT sector. The marginal operator develops a  $U(1)$  breaking vev, which in turn shows up in the divergence of the  $U(1)$  CFT current. The current is therefore non-conserved, with dimension  $\Delta_{\mathcal{J}} = d - 1 + \gamma_{\mathcal{J}}$  where  $\gamma_{\mathcal{J}} > 0$ . Using properties of the CFT we can then verify that the anomalous dimension of the current is proportional to the square of the  $U(1)$ -breaking vev, a fact which is also verified from the AdS side.

## 5.10 Conclusions

In this manuscript we present a theory of a  $U(1)$  gauge field in AdS<sub>5</sub>. The  $U(1)$  is spontaneously broken by a bulk Higgs resulting in the gauge field developing a vev dependent on the location in the extra dimension.

We find the general solution for the spin-1 brane-to-brane propagators in the  $R_{\xi}$  gauges and partially solve the pseudoscalar sector pertaining to the bulk Higgs' Goldstone and the  $d + 1$  component of the gauge field  $A_z$ . We compute the boundary action in general for the boundary conditions which allow for the vector and Goldstone fields on the brane and derive a Goldstone equivalence theorem for AdS transition amplitudes and for boundary-localized degrees of freedom, for any  $\alpha$ .

We show that the spectrum is continuous for  $\alpha > d/2 > 1$  and discrete for  $0 \leq \alpha < \frac{d}{2} - 1$ . For the case  $\alpha = \frac{d}{2} - 1$ , the spectrum is continuous with a mass gap. We find that the spectrum has a pole corresponding to a  $d$ -dimensional gauge mode resulting from the spontaneous symmetry breaking of the  $U(1)$  symmetry. When there is a mass gap, this pole may be isolated and dominate the phenomenology.

We estimate the location of the metric's backreaction due to the bulk vev when  $\alpha < \frac{d}{2}$ .

Via a WKB method we develop, we find the solutions to the EOM when  $\alpha = \frac{d}{2} + \epsilon$  for  $\epsilon \ll 1$ . We find that the result is an approximate CFT with logarithmically running parameters.

In the context of CFT dual we argue that the CFT sector is unaffected by the breaking of the  $U(1)$  symmetry when  $\alpha \gg \frac{d}{2}$  since the CFT current is conserved. In the case where  $\alpha = \frac{d}{2}$  an exactly marginal operator in the CFT sector mixes with the elementary  $U(1)$  breaking sector and develops a vev. The resulting CFT current is no longer conserved and there is an anomalous dimension proportional to the vev squared.

We introduce a dark photon model we denote the holographic dark photon in the case  $d = 4$  where The  $U(1)$  gauge field kinetically mixes with the visible photon on UV brane. We compute the exact visible photon propagator dressed with interactions with the holographic dark photon and show that it is equivalent to a field redefinition for the visible photon.

We derive a recasting formula for adapting existing dark photon bounds to our model and show constraints for the cases of  $\alpha = 1$  and  $\alpha = 2$ . We find that for small

mass gap/bulk mass bounds on the continuum dark photon become independent of  $m_A$  due to contributions from heavier states in the continuum. This occurs even for  $m_A$  below experimental sensitivities. In the case  $\alpha = 1$  and  $r_{UV} \sim R$  we find constraints are only logarithmically sensitive to the value of the AdS curvature  $R^{-1}$  which allows for bounds even for  $R^{-1} = 10^{18}$  GeV. Even in the gapless limit, non-trivial behavior remains and the spectral density  $\sim 1/p^2 \log^2(pR)$ . For  $\alpha = 2$ ,  $R^{-1}$  is important for determining the shape of the spectral distribution. In the case  $\alpha = 2$  we also find that bounds may extend to mass gaps beyond the typical upper mass threshold of experiments since lighter states in the continuum may still contribute. The most important bounds for both cases are due to colliders such as BaBar and Belle II.

For nonrelativistic dark matter, we calculate the target values for the dark matter coupling to the holographic dark photon  $\alpha_\chi$  and dark matter mass  $m_\chi$ , which give the correct present day relic abundance. We find that for  $\alpha = 1$  when there is isolated pole it dominates the annihilation cross section. When the pole is larger than the gap scale or, for  $\alpha = 2$  where there is no isolated pole, we find that the preferred coupling is significantly larger than when the pole is isolated due to the cross section being suppressed by the spectral integrals. In all cases the dark photon's brane-localized bulk mass plays a role similar to the mass of the dark photon in a 4D model. When the dark matter mass  $m_\chi < m_A$  the cross section loses support causing the preferred value of  $\alpha_\chi$  to diverge. While similarly imposing a lower cut off on the dark matter mass, the shape of the curve is distinct from the 4D case.

There are several possibilities for future directions. In principle, one should recalculate all dark photon bounds from scratch for the case of the holographic dark photon. Similarly, we neglect to consider bounds from mixing with the  $Z$  – *boson* as they may be significant when the mass scale  $\mu \sim m_Z$ . We leave this for a future more detailed analysis. Additionally, for thermal freeze out we consider a simple benchmark model of dark matter interacting with the holographic dark photon. One may consider a more realistic model of dark matter or further mechanisms by which the dark matter abundance may be set.

## Chapter 6

# Conclusions

In this manuscript we present four concrete possibilities for dark sectors. Each model presents novel behavior, pushing the boundaries of our understanding of dark sectors and their possible signatures.

We show that it is possible to construct a UV complete model of stable spin-1 dark matter with a spin-1 mediator, resulting from the spontaneous symmetry breaking of a single non-abelian gauge symmetry. Additionally, we show that this dark sector satisfies current experimental constraints and may possibly resolve small-scale structure anomalies.

The spectrum of models resulting from the spontaneous symmetry breaking of a non-abelian gauge symmetry is not limited to spin-1 dark matter. We show that it is also possible to construct a model of stable pseudo-Goldstone boson dark matter, with a spin-1 mediator, from the spontaneous symmetry breaking of a single non-abelian gauge symmetry. The pseudo-Goldstone dark matter similarly avoids current experimental constraints and may play a role in resolving small-scale structure anomalies. Through both of these dark

sector models we show that through a cleverly constructed symmetry group, one may realize a variety of dark sectors with novel phenomena.

We expand the self-interacting dark matter framework to consider the possibility that dark matter interactions are mediated by not one or a few states but rather a continuum of states, discovering exciting new self-scattering phenomena. We verify that in the limit of a large number of mediators, a sum of Yukawa potentials reproduces the non-integer power law derived in our continuum model. The self-scattering cross section in our model carries a velocity dependence unseen in previous models of self-interacting dark matter. By simply relaxing the assumption that dark matter self-interactions are mediated by a small number of states, we have shown a robust example of the possibilities of creative model building.

Further delving in to the physics of continuum fields, we present a framework for a continuum dark photon. Utilizing a unique construction of a bulk scalar spontaneously breaking a bulk  $U(1)$  symmetry due to a brane-localized potential, we lay out a model of a continuum dark photon which couples to brane-localized matter. The continuum dark photon introduces interesting tree-level effects not seen in particle dark photon models.

In this manuscript we employ clever and creative model building in order to demonstrate four possible dark sectors, and shed light on the vast space of possible dark sector models as well the types of phenomena to be expected. Additionally each model we present may also serve as a foundation for future, more focused studies, in which several predicted phenomena may be examined in finer detail.

# Bibliography

- [1] M. Ackermann et al. Searching for Dark Matter Annihilation from Milky Way Dwarf Spheroidal Galaxies with Six Years of Fermi Large Area Telescope Data. *Phys. Rev. Lett.*, 115(23):231301, 2015.
- [2] P. A. R. Ade et al. Planck 2015 results. XIII. Cosmological parameters. *Astron. Astrophys.*, 594:A13, 2016.
- [3] N. Aghanim et al. Planck 2018 results. VI. Cosmological parameters. 2018.
- [4] N. Aghanim et al. Planck 2018 results. VI. Cosmological parameters. *Astron. Astrophys.*, 641:A6, 2020. [Erratum: *Astron. Astrophys.* 652, C4 (2021)].
- [5] P. Agnes et al. Darkside-50 532-Day Dark Matter Search with Low-Radioactivity Argon. *Phys. Rev.*, D98(10):102006, 2018.
- [6] R. Agnese et al. New Results from the Search for Low-Mass Weakly Interacting Massive Particles with the CDMS Low Ionization Threshold Experiment. *Phys. Rev. Lett.*, 116(7):071301, 2016.
- [7] Ofer Aharony, Steven S. Gubser, Juan Martin Maldacena, Hirosi Ooguri, and Yaron Oz. Large N field theories, string theory and gravity. *Phys. Rept.*, 323:183–386, 2000.
- [8] D. S. Akerib et al. Improved Limits on Scattering of Weakly Interacting Massive Particles from Reanalysis of 2013 LUX Data. *Phys. Rev. Lett.*, 116(16):161301, 2016.
- [9] D. S. Akerib et al. Results from a search for dark matter in the complete LUX exposure. *Phys. Rev. Lett.*, 118(2):021303, 2017.
- [10] Jim Alexander et al. Dark Sectors 2016 Workshop: Community Report. 2016.
- [11] Nikhil Anand and Sean Cantrell. The Goldstone Equivalence Theorem and AdS/CFT. *JHEP*, 08:002, 2015.
- [12] Ignatios Antoniadis, Asimina Arvanitaki, Savas Dimopoulos, and Amit Giveon. Phenomenology of TeV Little String Theory from Holography. *Phys. Rev. Lett.*, 108:081602, 2012.



- [13] E. Aprile et al. Dark Matter Search Results from a One Ton-Year Exposure of Xenon1T. *Phys. Rev. Lett.*, 121(11):111302, 2018.
- [14] E. Aprile et al. Light Dark Matter Search with Ionization Signals in XENON1T. *Phys. Rev. Lett.*, 123(25):251801, 2019.
- [15] Paul R. Archer. The Fermion Mass Hierarchy in Models with Warped Extra Dimensions and a Bulk Higgs. *JHEP*, 09:095, 2012.
- [16] Paul R. Archer, Marcela Carena, Adrian Carmona, and Matthias Neubert. Higgs Production and Decay in Models of a Warped Extra Dimension with a Bulk Higgs. *JHEP*, 01:060, 2015.
- [17] Paola Arias and Fidel A. Schaposnik. Vortex solutions of an Abelian Higgs model with visible and hidden sectors. *JHEP*, 12:11, 2014.
- [18] Nima Arkani-Hamed, Douglas P. Finkbeiner, Tracy R. Slatyer, and Neal Weiner. A Theory of Dark Matter. *Phys. Rev. D*, 79:015014, 2009.
- [19] Nima Arkani-Hamed, Massimo Porrati, and Lisa Randall. Holography and phenomenology. *JHEP*, 08:017, 2001.
- [20] K. S. Babu, Christopher F. Kolda, and John March-Russell. Implications of generalized  $Z - Z'$  mixing. *Phys. Rev.*, D57:6788–6792, 1998.
- [21] S. Baek, P. Ko, and Wan-Il Park. Hidden Sector Monopole, Vector Dark Matter and Dark Radiation with Higgs Portal. *JCAP*, 1410(10):067, 2014.
- [22] Vijay Balasubramanian, Steven B. Giddings, and Albion E. Lawrence. What do CFTs tell us about Anti-de Sitter space-times? *JHEP*, 03:001, 1999.
- [23] Iason Baldes and Camilo Garcia-Cely. Strong gravitational radiation from a simple dark matter model. *JHEP*, 05:190, 2019.
- [24] Vernon Barger, Paul Langacker, Mathew McCaskey, Michael Ramsey-Musolf, and Gabe Shaughnessy. Complex singlet extension of the standard model. *Physical Review D*, 79(1), Jan 2009.
- [25] D. F. Bartlett and Stefan Lögl. Limits on an electromagnetic fifth force. *Phys. Rev. Lett.*, 61:2285–2287, Nov 1988.
- [26] Brian Batell and Tony Gherghetta. Localized U(1) Gauge Fields, Millicharged Particles, and Holography. *Phys. Rev. D*, 73:045016, 2006.
- [27] Brian Batell and Tony Gherghetta. Holographic mixing quantified. *Phys. Rev. D*, 76:045017, 2007.
- [28] Brian Batell and Tony Gherghetta. Yang-Mills Localization in Warped Space. *Phys. Rev. D*, 75:025022, 2007.

- [29] Brian Batell and Tony Gherghetta. Dynamical Soft-Wall AdS/QCD. *Phys. Rev.*, D78:026002, 2008.
- [30] Brian Batell, Tony Gherghetta, and Daniel Sword. The Soft-Wall Standard Model. *Phys. Rev.*, D78:116011, 2008.
- [31] Marco Battaglieri et al. Us Cosmic Visions: New Ideas in Dark Matter 2017: Community Report. In *U.S. Cosmic Visions: New Ideas in Dark Matter College Park, Md, Usa, March 23-25, 2017*, 2017.
- [32] Connor Behan. Conformal manifolds: ODEs from OPEs. *JHEP*, 03:127, 2018.
- [33] Brando Bellazzini, Mathieu Cliche, and Philip Tanedo. Effective theory of self-interacting dark matter. *Phys. Rev. D*, 88(8):083506, 2013.
- [34] Brando Bellazzini, Csaba Csáki, Jay Hubisz, Seung J. Lee, Javi Serra, and John Terning. Quantum Critical Higgs. *Phys. Rev. X*, 6(4):041050, 2016.
- [35] Lars Bergstrom, Torsten Bringmann, Ilias Cholis, Dan Hooper, and Christoph Weniger. New Limits on Dark Matter Annihilation from AMS Cosmic Ray Positron Data. *Phys. Rev. Lett.*, 111:171101, 2013.
- [36] Nicolas Bernal, Xiaoyong Chu, Camilo Garcia-Cely, Thomas Hambye, and Bryan Zaldivar. Production Regimes for Self-Interacting Dark Matter. *JCAP*, 1603(03):018, 2016.
- [37] Gianfranco Bertone and Dan Hooper. History of dark matter. *Rev. Mod. Phys.*, 90(4):045002, 2018.
- [38] P. Betzios, E. Kiritsis, V. Niarchos, and O. Papadoulaki. Global symmetries, hidden sectors and emergent (dark) vector interactions. *JHEP*, 12:053, 2020.
- [39] Mattias Blennow, Enrique Fernandez-Martínez, and Bryan Zaldivar. Freeze-In Through Portals. *JCAP*, 1401:003, 2014.
- [40] Kimberly K. Boddy, Jonathan L. Feng, Manoj Kaplinghat, Yael Shadmi, and Timothy M. P. Tait. Strongly Interacting Dark Matter: Self-Interactions and keV Lines. *Phys. Rev.*, D90(9):095016, 2014.
- [41] Kimberly K. Boddy, Jonathan L. Feng, Manoj Kaplinghat, and Tim M. P. Tait. Self-Interacting Dark Matter from a Non-Abelian Hidden Sector. *Phys.Rev.*, D89(11):115017, 2014.
- [42] Céline Boehm, Xiaoyong Chu, Jui-Lin Kuo, and Josef Pradler. Scalar dark matter candidates revisited. *Phys. Rev. D*, 103(7):075005, 2021.
- [43] Biswajoy Brahmachari and Amitava Raychaudhuri. Kinetic mixing and symmetry breaking dependent interactions of the dark photon. *Nucl. Phys.*, B887:441–455, 2014.

- [44] Philippe Brax, Sylvain Fichet, and Guillaume Pignol. Bounding Quantum Dark Forces. *Phys. Rev. D*, 97(11):115034, 2018.
- [45] Philippe Brax, Sylvain Fichet, and Philip Tanedo. The Warped Dark Sector. *Phys. Lett. B*, 798:135012, 2019.
- [46] Peter Breitenlohner and Daniel Z. Freedman. Positive Energy in Anti-de Sitter Backgrounds and Gauged Extended Supergravity. *Phys. Lett. B*, 115:197–201, 1982.
- [47] Peter Breitenlohner and Daniel Z. Freedman. Stability in Gauged Extended Supergravity. *Annals Phys.*, 144:249, 1982.
- [48] Matthew R. Buckley and Patrick J. Fox. Dark Matter Self-Interactions and Light Force Carriers. *Phys. Rev.*, D81:083522, 2010.
- [49] James S. Bullock and Michael Boylan-Kolchin. Small-Scale Challenges to the  $\Lambda$ CDM Paradigm. *Ann. Rev. Astron. Astrophys.*, 55:343–387, 2017.
- [50] Don Bunk, Jay Hubisz, and Bithika Jain. A Perturbative RS I Cosmological Phase Transition. *Eur. Phys. J. C*, 78(1):78, 2018.
- [51] C.P. Burgess, Maxim Pospelov, and Tonnies ter Veldhuis. The minimal model of nonbaryonic dark matter: a singlet scalar. *Nuclear Physics B*, 619(1-3):709–728, Dec 2001.
- [52] C. Boehm and P. Fayet. Scalar dark matter candidates. *Nuclear Physics B*, 683(1-2):219–263, Apr 2004.
- [53] Joan A. Cabrer, Gero von Gersdorff, and Mariano Quiros. Soft-Wall Stabilization. *New J. Phys.*, 12:075012, 2010.
- [54] Joan A. Cabrer, Gero von Gersdorff, and Mariano Quiros. Suppressing Electroweak Precision Observables in 5D Warped Models. *JHEP*, 05:083, 2011.
- [55] Giacomo Cacciapaglia, Csaba Csaki, Guido Marandella, and John Terning. The Gaugephobic Higgs. *JHEP*, 02:036, 2007.
- [56] Giacomo Cacciapaglia, Guido Marandella, and John Terning. Colored Unparticles. *JHEP*, 01:070, 2008.
- [57] Giacomo Cacciapaglia, Guido Marandella, and John Terning. The AdS/CFT/Unparticle Correspondence. *JHEP*, 02:049, 2009.
- [58] Haiying Cai, Hsin-Chia Cheng, Anibal D. Medina, and John Terning. Continuum Superpartners from Supersymmetric Unparticles. *Phys. Rev. D*, 80:115009, 2009.
- [59] Haiying Cai, Hsin-Chia Cheng, Anibal D. Medina, and John Terning. SUSY Hidden in the Continuum. *Phys. Rev. D*, 85:015019, 2012.
- [60] Curtis G. Callan, Sidney Coleman, J. Wess, and Bruno Zumino. Structure of phenomenological lagrangians. ii. *Phys. Rev.*, 177:2247–2250, Jan 1969.

- [61] Curtis G. Callan, Jr., Sidney R. Coleman, J. Wess, and Bruno Zumino. Structure of Phenomenological Lagrangians. 2. *Phys. Rev.*, 177:2247–2250, 1969.
- [62] X. Calmet, N. G. Deshpande, X. G. He, and S. D. H. Hsu. Invisible Higgs Boson, Continuous Mass Fields and Unhiggs Mechanism. *Phys. Rev. D*, 79:055021, 2009.
- [63] Eric D. Carlson, Marie E. Machacek, and Lawrence J. Hall. Self-Interacting Dark Matter. *Astrophys. J.*, 398:43–52, 1992.
- [64] Christopher D. Carone and Raymundo Ramos. Classical scale-invariance, the electroweak scale and vector dark matter. *Phys. Rev.*, D88:055020, 2013.
- [65] S. Cassel. Sommerfeld factor for arbitrary partial wave processes. *J. Phys.*, G37:105009, 2010.
- [66] Riccardo Catena, Kåre Fridell, and Vanessa Zema. Direct detection of fermionic and vector dark matter with polarised targets. *JCAP*, 1811(11):018, 2018.
- [67] Riccardo Catena, Kåre Fridell, and Martin B. Krauss. Non-relativistic Effective Interactions of Spin 1 Dark Matter. *JHEP*, 08:030, 2019.
- [68] Ian Chaffey, Sylvain Fichet, and Philip Tanedo. Continuum-Mediated Self-Interacting Dark Matter. 2 2021.
- [69] Ian Chaffey and Philip Tanedo. Vector self-interacting dark matter. *Phys. Rev. D*, 101(7):075005, 2020.
- [70] Jae Hyeok Chang, Rouven Essig, and Samuel D. McDermott. Revisiting Supernova 1987A Constraints on Dark Photons. *JHEP*, 01:107, 2017.
- [71] Sanghyeon Chang, Junji Hisano, Hiroaki Nakano, Nobuchika Okada, and Masahiro Yamaguchi. Bulk Standard Model in the Randall-Sundrum Background. *Phys. Rev. D*, 62:084025, 2000.
- [72] Piotr H. Chankowski, Stefan Pokorski, and Jakub Wagner. Z-prime and the Appelquist-Carrazzone decoupling. *Eur. Phys. J.*, C47:187–205, 2006.
- [73] Chuan-Hung Chen and C.S. Kim. Sommerfeld Enhancement from Unparticle Exchange for Dark Matter Annihilation. *Phys. Lett. B*, 687:232–235, 2010.
- [74] Fang Chen, James M. Cline, and Andrew R. Frey. A New Twist on Excited Dark Matter: Implications for Integral, Pamela/Atic/PPb-Bets, Dama. *Phys. Rev.*, D79:063530, 2009.
- [75] D Chiron and B Marcos. Classical particle scattering for power-law two-body potentials. 1 2016.
- [76] Soo-Min Choi, Hyun Min Lee, Yann Mambrini, and Mathias Pierre. Vector SIMP dark matter with approximate custodial symmetry. *JHEP*, 07:049, 2019.

- [77] Xiaoyong Chu, Thomas Hambye, and Michel H. G. Tytgat. The Four Basic Ways of Creating Dark Matter Through a Portal. *JCAP*, 1205:034, 2012.
- [78] Marco Cirelli, Eugenio Del Nobile, and Paolo Panci. Tools for Model-Independent Bounds in Direct Dark Matter Searches. *JCAP*, 1310:019, 2013.
- [79] Marco Cirelli and Gaele Giesen. Antiprotons from Dark Matter: Current constraints and future sensitivities. *JCAP*, 1304:015, 2013.
- [80] James M. Cline and Takashi Toma. Pseudo-Goldstone dark matter confronts cosmic ray and collider anomalies. *Phys. Rev. D*, 100(3):035023, 2019.
- [81] Timothy Cohen, John Kearney, Aaron Pierce, and David Tucker-Smith. Singlet-doublet dark matter. *Physical Review D*, 85(7), Apr 2012.
- [82] Alexandria Costantino and Sylvain Fichet. Opacity from Loops in AdS. *JHEP*, 02:089, 2021.
- [83] Alexandria Costantino, Sylvain Fichet, and Flip Tanedo. Work in progress.
- [84] Alexandria Costantino, Sylvain Fichet, and Philip Tanedo. Effective Field Theory in AdS: Continuum Regime, Soft Bombs, and IR Emergence. *Phys. Rev. D*, 102(11):115038, 2020.
- [85] Alexandria Costantino, Sylvain Fichet, and Philip Tanedo. Exotic Spin-Dependent Forces from a Hidden Sector. *JHEP*, 03:148, 2020.
- [86] Peter Cox, Tony Gherghetta, and Minh D. Nguyen. A Holographic Perspective on the Axion Quality Problem. *JHEP*, 01:188, 2020.
- [87] Paolo Creminelli, Alberto Nicolis, and Riccardo Rattazzi. Holography and the Electroweak Phase Transition. *JHEP*, 03:051, 2002.
- [88] Csaba Csaki, Christophe Grojean, Hitoshi Murayama, Luigi Pilo, and John Terning. Gauge Theories on an Interval: Unitarity without a Higgs. *Phys. Rev. D*, 69:055006, 2004.
- [89] Csaba Csáki, Sungwoo Hong, Gowri Kurup, Seung J. Lee, Maxim Perelstein, and Wei Xue. Continuum dark matter. *Phys. Rev. D*, 105(3):035025, 2022.
- [90] Csaba Csáki, Sungwoo Hong, Gowri Kurup, Seung J. Lee, Maxim Perelstein, and Wei Xue. Z-Portal Continuum Dark Matter. *Phys. Rev. Lett.*, 128(8):081807, 2022.
- [91] Csaba Csáki, Gabriel Lee, Seung J. Lee, Salvator Lombardo, and Ofri Telem. Continuum Naturalness. *JHEP*, 03:142, 2019.
- [92] Csaba Csaki, Matthew Reece, and John Terning. The AdS/QCD Correspondence: Still Undelivered. *JHEP*, 05:067, 2009.
- [93] Yanou Cui, Tony Gherghetta, and James D. Wells. Emergent Electroweak Symmetry Breaking with Composite W, Z Bosons. *JHEP*, 11:080, 2009.

- [94] Richard H. Cyburt, Brian D. Fields, Keith A. Olive, and Tsung-Han Yeh. Big Bang Nucleosynthesis: 2015. *Rev. Mod. Phys.*, 88:015004, 2016.
- [95] Romeel Dave, David N. Spergel, Paul J. Steinhardt, and Benjamin D. Wandelt. Halo Properties in Cosmological Simulations of Selfinteracting Cold Dark Matter. *Astrophys. J.*, 547:574–589, 2001.
- [96] H. Davoudiasl, J.L. Hewett, and T.G. Rizzo. Bulk Gauge Fields in the Randall-Sundrum Model. *Phys. Lett. B*, 473:43–49, 2000.
- [97] Hooman Davoudiasl, Hye-Sung Lee, and William J. Marciano. ‘Dark’ Z Implications for Parity Violation, Rare Meson Decays, and Higgs Physics. *Phys. Rev.*, D85:115019, 2012.
- [98] Hooman Davoudiasl and Ian M. Lewis. Dark Matter from Hidden Forces. *Phys. Rev.*, D89(5):055026, 2014.
- [99] Hooman Davoudiasl, Ben Lillie, and Thomas G. Rizzo. Off-The-Wall Higgs in the Universal Randall-Sundrum Model. *JHEP*, 08:042, 2006.
- [100] Hooman Davoudiasl, Gilad Perez, and Amarjit Soni. The Little Randall-Sundrum Model at the Large Hadron Collider. *Phys. Lett. B*, 665:67–71, 2008.
- [101] Antonio Delgado, Jose R. Espinosa, and Mariano Quiros. Unparticles Higgs Interplay. *JHEP*, 10:094, 2007.
- [102] James B. Dent, Lawrence M. Krauss, Jayden L. Newstead, and Subir Sabharwal. General Analysis of Direct Dark Matter Detection: from Microphysics to Observational Signatures. *Phys. Rev.*, D92(6):063515, 2015.
- [103] N. G. Deshpande and Xiao-Gang He. Unparticle Realization Through Continuous Mass Scale Invariant Theories. *Phys. Rev. D*, 78:055006, 2008.
- [104] Nicolas Deutschmann, Thomas Flacke, and Jong Soo Kim. Current LHC Constraints on Minimal Universal Extra Dimensions. *Phys. Lett. B*, 771:515–520, 2017.
- [105] Eric D’Hoker, Daniel Z. Freedman, Samir D. Mathur, Alec Matusis, and Leonardo Rastelli. Graviton exchange and complete four point functions in the AdS / CFT correspondence. *Nucl. Phys. B*, 562:353–394, 1999.
- [106] Eric D’Hoker, Daniel Z. Freedman, and Leonardo Rastelli. AdS / CFT four point functions: How to succeed at z integrals without really trying. *Nucl. Phys. B*, 562:395–411, 1999.
- [107] Adriano Di Giacomo and Manu Mathur. Magnetic Monopoles, Gauge Invariant Dynamic Variables and Georgi Glashow Model. *Phys. Lett.*, B400:129–134, 1997.
- [108] Keith R. Dienes, Shufang Su, and Brooks Thomas. Distinguishing Dynamical Dark Matter at the LHC. *Phys. Rev. D*, 86:054008, 2012.

- [109] Keith R. Dienes and Brooks Thomas. Dynamical Dark Matter: I. Theoretical Overview. *Phys. Rev. D*, 85:083523, 2012.
- [110] Keith R. Dienes and Brooks Thomas. Dynamical Dark Matter: II. An Explicit Model. *Phys. Rev. D*, 85:083524, 2012.
- [111] Barry M. Dillon, Basem Kamal El-Menoufi, Stephan J. Huber, and Jonathan P. Manuel. Rapid holographic phase transition with brane-localized curvature. *Phys. Rev. D*, 98(8):086005, 2018.
- [112] S. L. Dubovsky, V. A. Rubakov, and P. G. Tinyakov. Brane world: Disappearing massive matter. *Phys. Rev. D*, 62:105011, 2000.
- [113] Michael Duetsch and Karl-Henning Rehren. Generalized Free Fields and the AdS - CFT Correspondence. *Annales Henri Poincare*, 4:613–635, 2003.
- [114] Gia Dvali and Cesar Gomez. Quantum Information and Gravity Cutoff in Theories with Species. *Phys. Lett. B*, 674:303–307, 2009.
- [115] Cora Dvorkin, Tongyan Lin, and Katelin Schutz. Making Dark Matter Out of Light: Freeze-In from Plasma Effects. *Phys. Rev.*, D99(11):115009, 2019.
- [116] Sheer El-Showk and Kyriakos Papadodimas. Emergent Spacetime and Holographic CFTs. *JHEP*, 10:106, 2012.
- [117] Fatemeh Elahi and Sara Khatibi. Multi-Component Dark Matter in a Non-Abelian Dark Sector. *Phys. Rev. D*, 100(1):015019, 2019.
- [118] Christoph Englert, Dorival Goncalves Netto, Michael Spannowsky, and John Terning. Constraining the Unhiggs with Lhc Data. *Phys. Rev. D*, 86:035010, 2012.
- [119] Christoph Englert, Michael Spannowsky, David Stancato, and John Terning. Unconstraining the Unhiggs. *Phys. Rev. D*, 85:095003, 2012.
- [120] Miguel Escudero, Asher Berlin, Dan Hooper, and Meng-Xiang Lin. Toward (finally!) ruling out  $z$  and higgs mediated dark matter models. *Journal of Cosmology and Astroparticle Physics*, 2016(12):029–029, Dec 2016.
- [121] Rouven Essig et al. Working Group Report: New Light Weakly Coupled Particles. In *Proceedings, 2013 Community Summer Study on the Future of U.S. Particle Physics: Snowmass on the Mississippi (CSS2013): Minneapolis, MN, USA, July 29-August 6, 2013*, 2013.
- [122] Jared A. Evans, Stefania Gori, and Jessie Shelton. Looking for the WIMP Next Door. *JHEP*, 02:100, 2018.
- [123] Pavel Fadeev, Yevgeny V. Stadnik, Filip Ficek, Mikhail G. Kozlov, Victor V. Flambaum, and Dmitry Budker. Revisiting spin-dependent forces mediated by new bosons: Potentials in the coordinate-space representation for macroscopic- and atomic-scale experiments. *Phys. Rev. A*, 99(2):022113, 2019.

- [124] Adam Falkowski and Manuel Perez-Victoria. Electroweak Breaking on a Soft Wall. *JHEP*, 12:107, 2008.
- [125] Adam Falkowski and Manuel Perez-Victoria. Electroweak Precision Observables and the Unhiggs. *JHEP*, 12:061, 2009.
- [126] Adam Falkowski and Manuel Perez-Victoria. Holographic Unhiggs. *Phys. Rev. D*, 79:035005, 2009.
- [127] JiJi Fan, Matthew Reece, and Lian-Tao Wang. Non-Relativistic Effective Theory of Dark Matter Direct Detection. *JCAP*, 1011:042, 2010.
- [128] Marco Farina, Duccio Pappadopulo, Rudderman Joshua T., and Gabriele Trevisan. Phases of Cannibal Dark Matter. *JHEP*, 12:39, 2016.
- [129] Yasaman Farzan and Amin Rezaei Akbarieh. VDM: A model for Vector Dark Matter. *JCAP*, 1210:026, 2012.
- [130] Jonathan L. Feng, Manoj Kaplinghat, Huitzu Tu, and Hai-Bo Yu. Hidden Charged Dark Matter. *JCAP*, 0907:004, 2009.
- [131] Jonathan L. Feng, Manoj Kaplinghat, and Hai-Bo Yu. Halo Shape and Relic Density Exclusions of Sommerfeld-Enhanced Dark Matter Explanations of Cosmic Ray Excesses. *Phys. Rev. Lett.*, 104:151301, 2010.
- [132] Jonathan L. Feng, Jordan Smolinsky, and Philip Tanedo. Detecting Dark Matter Through Dark Photons from the Sun: Charged Particle Signatures. *Phys. Rev.*, D93(11):115036, 2016. [Erratum: *Phys. Rev.*D96,no.9,099903(2017)].
- [133] Jonathan L. Feng, Huitzu Tu, and Hai-Bo Yu. Thermal Relics in Hidden Sectors. *JCAP*, 0810:043, 2008.
- [134] Sylvain Fichet. Quantum Forces from Dark Matter and Where to Find Them. *Phys. Rev. Lett.*, 120(13):131801, 2018.
- [135] Sylvain Fichet. Opacity and effective field theory in anti-de Sitter backgrounds. *Phys. Rev. D*, 100(9):095002, 2019.
- [136] Sylvain Fichet. Braneworld Effective Field Theories — Holography, Consistency and Conformal Effects. *JHEP*, 04:016, 2020.
- [137] Sylvain Fichet. Dressing in AdS and a Conformal Bethe-Salpeter Equation. 6 2021.
- [138] Sylvain Fichet. On holography in general background and the boundary effective action from AdS to dS. *JHEP*, 07:113, 2022.
- [139] Sylvain Fichet, Eugenio Megias, and Mariano Quiros. On Continuum Effective Field Theories and Gravity. 8 2022.
- [140] N. Fornengo, P. Panci, and M. Regis. Long-Range Forces in Direct Dark Matter Searches. *Phys. Rev.*, D84:115002, 2011.



- [141] Patrick J. Fox, Arvind Rajaraman, and Yuri Shirman. Bounds on Unparticles from the Higgs Sector. *Phys. Rev. D*, 76:075004, 2007.
- [142] Anthony Fradette, Maxim Pospelov, Josef Pradler, and Adam Ritz. Cosmological Constraints on Very Dark Photons. *Phys. Rev. D*, 90(3):035022, 2014.
- [143] Daniel Z. Freedman, Samir D. Mathur, Alec Matusis, and Leonardo Rastelli. Comments on 4 point functions in the CFT / AdS correspondence. *Phys. Lett. B*, 452:61–68, 1999.
- [144] Daniel Z. Freedman, Samir D. Mathur, Alec Matusis, and Leonardo Rastelli. Correlation functions in the CFT(d) / AdS(d+1) correspondence. *Nucl. Phys. B*, 546:96–118, 1999.
- [145] Alexander Friedland, Maurizio Giannotti, and Michael Graesser. On the  $RS^2$  Realization of Unparticles. *Phys. Lett. B*, 678:149–155, 2009.
- [146] Alexander Friedland, Maurizio Giannotti, and Michael L. Graesser. Vector Bosons in the Randall-Sundrum 2 and Lykken-Randall Models and Unparticles. *JHEP*, 09:033, 2009.
- [147] Michele Frigerio, Alex Pomarol, Francesco Riva, and Alfredo Urbano. Composite Scalar Dark Matter. *JHEP*, 07:015, 2012.
- [148] C. Fronsdal. Infinite Multiplets and Continuous Mass Spectra. *Conf. Proc. C*, 670828:374–382, 1967.
- [149] C. Fronsdal. Infinite multiplets and the hydrogen atom. *Phys. Rev.*, 156:1665–1677, Apr 1967.
- [150] C. Fronsdal. Progress Report on Infinite Multiplets. *Conf. Proc. C*, 680519:119–132, 1968.
- [151] Peter Galison and Aneesh Manohar. Two z’s or not two z’s? *Physics Letters B*, 136(4):279 – 283, 1984.
- [152] Peter Galison and Aneesh Manohar. Two Z’s Or Not Two Z’s? *Phys. Lett.*, 136B:279–283, 1984.
- [153] Christina Gao, Ali Shayegan Shirazi, and John Terning. Collider Phenomenology of a Gluino Continuum. *JHEP*, 01:102, 2020.
- [154] Howard Georgi. Generalized Dimensional Analysis. *Phys. Lett. B*, 298:187–189, 1993.
- [155] Howard Georgi. Another Odd Thing About Unparticle Physics. *Phys. Lett. B*, 650:275–278, 2007.
- [156] Howard Georgi. Unparticle Physics. *Phys. Rev. Lett.*, 98:221601, 2007.
- [157] Howard Georgi and Lisa Randall. Flavor Conserving CP Violation in Invisible Axion Models. *Nucl. Phys. B*, 276:241–252, 1986.

- [158] Tony Gherghetta and Benedict von Harling. A Warped Model of Dark Matter. *JHEP*, 04:039, 2010.
- [159] Steven B. Giddings, Emanuel Katz, and Lisa Randall. Linearized gravity in brane backgrounds. *JHEP*, 03:023, 2000.
- [160] Gian F. Giudice, Yevgeny Kats, Matthew McCullough, Riccardo Torre, and Alfredo Urbano. Clockwork/Linear Dilaton: Structure and Phenomenology. *JHEP*, 06:009, 2018.
- [161] Walter D. Goldberger and Mark B. Wise. Modulus Stabilization with Bulk Fields. *Phys. Rev. Lett.*, 83:4922–4925, 1999.
- [162] Stefania Gori, Stefano Profumo, and Bibhushan Shakya. Wobbly Dark Matter Signals at Cherenkov Telescopes from Long Lived Mediator Decays. *Phys. Rev. Lett.*, 122(19):191103, 2019.
- [163] Matt Graham, Christopher Hearty, and Mike Williams. Searches for Dark Photons at Accelerators. *Ann. Rev. Nucl. Part. Sci.*, 71:37–58, 2021.
- [164] O. W. Greenberg. Generalized Free Fields and Models of Local Field Theory. *Annals Phys.*, 16:158–176, 1961.
- [165] Christian Gross, Oleg Lebedev, and Yann Mambrini. Non-Abelian Gauge Fields as Dark Matter. *JHEP*, 08:158, 2015.
- [166] Christian Gross, Oleg Lebedev, and Takashi Toma. Cancellation Mechanism for Dark-Matter–Nucleon Interaction. *Phys. Rev. Lett.*, 119(19):191801, 2017.
- [167] F. Gross. *Relativistic Quantum Mechanics and Field Theory*. A Wiley-Interscience publication. Wiley, 1999.
- [168] S. S. Gubser, Igor R. Klebanov, and Alexander M. Polyakov. Gauge theory correlators from noncritical string theory. *Phys. Lett.*, B428:105–114, 1998.
- [169] Steven S. Gubser. AdS / CFT and gravity. *Phys. Rev. D*, 63:084017, 2001.
- [170] Steven S. Gubser and Abhinav Nellore. Mimicking the QCD equation of state with a dual black hole. *Phys. Rev. D*, 78:086007, 2008.
- [171] U. Gursoy and E. Kiritsis. Exploring improved holographic theories for QCD: Part I. *JHEP*, 02:032, 2008.
- [172] U. Gursoy, E. Kiritsis, and F. Nitti. Exploring improved holographic theories for QCD: Part II. *JHEP*, 02:019, 2008.
- [173] Eleanor Hall, Thomas Konstandin, Robert McGehee, and Hitoshi Murayama. Asymmetric Matters from a Dark First-Order Phase Transition. 11 2019.
- [174] Eleanor Hall, Robert McGehee, Hitoshi Murayama, and Bethany Suter. Asymmetric Dark Matter May Not Be Light. 7 2021.

- [175] Thomas Hambye. Hidden Vector Dark Matter. *JHEP*, 01:028, 2009.
- [176] Thomas Hambye and Alessandro Strumia. Dynamical generation of the weak and Dark Matter scale. *Phys. Rev.*, D88:055022, 2013.
- [177] Steen Hannestad and Thomas Tram. Sommerfeld Enhancement of DM Annihilation: Resonance Structure, Freeze-Out and CMB Spectral Bound. *JCAP*, 01:016, 2011.
- [178] Babiker Hassanain, John March-Russell, and Martin Schvellinger. Warped Deformed Throats have Faster (Electroweak) Phase Transitions. *JHEP*, 10:089, 2007.
- [179] S. W. Hawking and Don N. Page. Thermodynamics of Black Holes in anti-De Sitter Space. *Commun. Math. Phys.*, 87:577, 1983.
- [180] Arthur Hebecker and John March-Russell. Randall-Sundrum II Cosmology, AdS / CFT, and the Bulk Black Hole. *Nucl. Phys.*, B608:375–393, 2001.
- [181] A. Hill and J. J. van der Bij. Strongly Interacting Singlet - Doublet Higgs Model. *Phys. Rev. D*, 36:3463–3473, 1987.
- [182] Junji Hisano, Shigeki. Matsumoto, Mihoko M. Nojiri, and Osamu Saito. Non-Perturbative Effect on Dark Matter Annihilation and Gamma Ray Signature from Galactic Center. *Phys. Rev.*, D71:063528, 2005.
- [183] Bob Holdom. Two U(1)'s and Epsilon Charge Shifts. *Phys. Lett.*, 166B:196–198, 1986.
- [184] Laura Lopez Honorez, Emmanuel Nezri, Josep F Oliver, and Michel H G Tytgat. The inert doublet model: an archetype for dark matter. *Journal of Cosmology and Astroparticle Physics*, 2007(02):028–028, Feb 2007.
- [185] Dan Hooper, Chris Kelso, and Farinaldo S. Queiroz. Stringent and Robust Constraints on the Dark Matter Annihilation Cross Section From the Region of the Galactic Center. *Astropart. Phys.*, 46:55–70, 2013.
- [186] Stephan J. Huber and Qaisar Shafi. Higgs Mechanism and Bulk Gauge Boson Masses in the Randall-Sundrum Model. *Phys. Rev. D*, 63:045010, 2001.
- [187] Ran Huo, Manoj Kaplinghat, Zhen Pan, and Hai-Bo Yu. Signatures of Self-Interacting Dark Matter in the Matter Power Spectrum and the Cmb. *Phys. Lett.*, B783:76–81, 2018.
- [188] Masahiro Ibe and Hai-bo Yu. Distinguishing Dark Matter Annihilation Enhancement Scenarios via Halo Shapes. *Phys. Lett.*, B692:70–73, 2010.
- [189] Roberto Iengo. Sommerfeld enhancement for a Yukawa potential. 3 2009.
- [190] Roberto Iengo. Sommerfeld Enhancement: General Results from Field Theory Diagrams. *JHEP*, 05:024, 2009.
- [191] Eder Izaguirre and Itay Yavin. New Window to Millicharged Particles at the Lhc. *Phys. Rev.*, D92(3):035014, 2015.

- [192] Elizabeth E. Jenkins, Aneesh V. Manohar, and Michael Trott. Naive Dimensional Analysis Counting of Gauge Theory Amplitudes and Anomalous Dimensions. *Phys. Lett. B*, 726:697–702, 2013.
- [193] Daniel Kabat and Gilad Lifschytz. CFT Representation of Interacting Bulk Gauge Fields in AdS. *Phys. Rev. D*, 87(8):086004, 2013.
- [194] Felix Kahlhoefer, Kai Schmidt-Hoberg, and Sebastian Wild. Dark Matter Self-Interactions from a General Spin-0 Mediator. *JCAP*, 08:003, 2017.
- [195] Gunnar Kallen. On the Definition of the Renormalization Constants in Quantum Electrodynamics. *Helv. Phys. Acta*, 25(4):417, 1952.
- [196] Ayuki Kamada, Manoj Kaplinghat, Andrew B. Pace, and Hai-Bo Yu. How the Self-Interacting Dark Matter Model Explains the Diverse Galactic Rotation Curves. *Phys. Rev. Lett.*, 119(11):111102, 2017.
- [197] David E. Kaplan, Markus A. Luty, and Kathryn M. Zurek. Asymmetric Dark Matter. *Phys. Rev.*, D79:115016, 2009.
- [198] Jared Kaplan. Lectures on AdS/CFT from the Bottom Up.
- [199] Jared Kaplan, Philip C. Schuster, and Natalia Toro. Avoiding an Empty Universe in RS I Models and Large-N Gauge Theories. 9 2006.
- [200] Manoj Kaplinghat, Sean Tulin, and Hai-Bo Yu. Dark Matter Halos as Particle Colliders: Unified Solution to Small-Scale Structure Puzzles from Dwarfs to Clusters. *Phys. Rev. Lett.*, 116(4):041302, 2016.
- [201] Alexandros Karam and Kyriakos Tamvakis. Dark matter and neutrino masses from a scale-invariant multi-Higgs portal. *Phys. Rev.*, D92(7):075010, 2015.
- [202] Alexandros Karam and Kyriakos Tamvakis. Dark Matter from a Classically Scale-Invariant  $SU(3)_X$ . *Phys. Rev.*, D94(5):055004, 2016.
- [203] Dimitrios Karamitros. Pseudo Nambu-Goldstone Dark Matter: Examples of Vanishing Direct Detection Cross Section. *Phys. Rev.*, D99(9):095036, 2019.
- [204] Andreas Karch, Emanuel Katz, Dam T. Son, and Mikhail A. Stephanov. Linear confinement and AdS/QCD. *Phys. Rev.*, D74:015005, 2006.
- [205] Andrey Katz, Matthew Reece, and Aqil Sajjad. Continuum-mediated dark matter–baryon scattering. *Phys. Dark Univ.*, 12:24–36, 2016.
- [206] Valentin V. Khoze, Christopher McCabe, and Gunnar Ro. Higgs vacuum stability from the dark matter portal. *JHEP*, 08:026, 2014.
- [207] Valentin V. Khoze and Alexis D. Plascencia. Dark Matter and Leptogenesis Linked by Classical Scale Invariance. *JHEP*, 11:025, 2016.

- [208] Valentin V. Khoze and Gunnar Ro. Dark Matter Monopoles, Vectors and Photons. *JHEP*, 10:61, 2014.
- [209] S. A. Khrapak, A. V. Ivlev, G. E. Morfill, and S. K. Zhdanov. Scattering in the Attractive Yukawa Potential in the Limit of Strong Interaction. *Phys. Rev. Lett.*, 90(22):225002, 2003.
- [210] Doojin Kim, Jong-Chul Park, and Seodong Shin. Dark matter “transporting” mechanism explaining positron excesses. *JHEP*, 04:093, 2018.
- [211] Igor R. Klebanov and Edward Witten. AdS / CFT correspondence and symmetry breaking. *Nucl. Phys. B*, 556:89–114, 1999.
- [212] P. Ko and Yong Tang. Residual Non-Abelian Dark Matter and Dark Radiation. *Phys. Lett.*, B768:12–17, 2017.
- [213] I. Yu. Kobzarev, L. B. Okun, and I. Ya. Pomeranchuk. On the possibility of experimental observation of mirror particles. *Sov. J. Nucl. Phys.*, 3(6):837–841, 1966. [*Yad. Fiz.*3,1154(1966)].
- [214] Edward W. Kolb and Michael S. Turner. The Early Universe. *Front. Phys.*, 69:1–547, 1990.
- [215] Thomas Konstandin, Germano Nardini, and Mariano Quiros. Gravitational Backreaction Effects on the Holographic Phase Transition. *Phys. Rev. D*, 82:083513, 2010.
- [216] N. V. Krasnikov. Higgs Boson with Continuously Distributed Mass. *Phys. Lett. B*, 325:430–434, 1994.
- [217] N. V. Krasnikov. Unparticle as a Field with Continuously Distributed Mass. *Int. J. Mod. Phys. A*, 22:5117–5120, 2007.
- [218] Gordan Krnjaic. Freezing In, Heating Up, and Freezing Out: Predictive Nonthermal Dark Matter and Low-Mass Direct Detection. *JHEP*, 10:136, 2018.
- [219] L. D. Landau and E. M. Lifshitz. *Mechanics, Third Edition: Volume 1 (Course of Theoretical Physics)*. Butterworth-Heinemann, 3 edition, January 1976.
- [220] David Langlois and Lorenzo Sorbo. Bulk gravitons from a cosmological brane. *Phys. Rev. D*, 68:084006, 2003.
- [221] David Langlois, Lorenzo Sorbo, and Maria Rodriguez-Martinez. Cosmology of a brane radiating gravitons into the extra dimension. *Phys. Rev. Lett.*, 89:171301, 2002.
- [222] Massimiliano Lattanzi and Joseph I. Silk. Can the WIMP annihilation boost factor be boosted by the Sommerfeld enhancement? *Phys. Rev. D*, 79:083523, 2009.
- [223] Benjamin W. Lee and Steven Weinberg. Cosmological lower bound on heavy-neutrino masses. *Phys. Rev. Lett.*, 39:165–168, Jul 1977.

- [224] J. G. Lee, E. G. Adelberger, T. S. Cook, S. M. Fleischer, and B. R. Heckel. New Test of the Gravitational  $1/r^2$  Law at Separations down to  $52 \mu\text{m}$ . *Phys. Rev. Lett.*, 124(10):101101, 2020.
- [225] Seung J. Lee. Continuum Partners. *Nucl. Part. Phys. Proc.*, 303-305:64–68, 2018.
- [226] H. Lehmann. On the Properties of Propagation Functions and Renormalization Constants of Quantized Fields. *Nuovo Cim.*, 11:342–357, 1954.
- [227] Tongyan Lin. Dark matter models and direct detection. *PoS*, 333:009, 2019.
- [228] Tongyan Lin, Hai-Bo Yu, and Kathryn M. Zurek. On Symmetric and Asymmetric Light Dark Matter. *Phys. Rev.*, D85:063503, 2012.
- [229] Hong Liu and Arkady A. Tseytlin. On four point functions in the CFT / AdS correspondence. *Phys. Rev. D*, 59:086002, 1999.
- [230] Jia Liu, Neal Weiner, and Wei Xue. Signals of a Light Dark Force in the Galactic Center. *JHEP*, 08:050, 2015.
- [231] Abraham Loeb and Neal Weiner. Cores in Dwarf Galaxies from Dark Matter with a Yukawa Potential. *Phys. Rev. Lett.*, 106:171302, 2011.
- [232] Markus A. Luty. Naive Dimensional Analysis and Supersymmetry. *Phys. Rev. D*, 57:1531–1538, 1998.
- [233] Ernest Ma. Verifiable radiative seesaw mechanism of neutrino mass and dark matter. *Physical Review D*, 73(7), Apr 2006.
- [234] Juan Martin Maldacena. The Large N limit of superconformal field theories and supergravity. *Int. J. Theor. Phys.*, 38:1113–1133, 1999. [Adv. Theor. Math. Phys.2,231(1998)].
- [235] Aneesh Manohar and Howard Georgi. Chiral Quarks and the Nonrelativistic Quark Model. *Nucl. Phys. B*, 234:189–212, 1984.
- [236] Donald Marolf and Simon F. Ross. Boundary Conditions and New Dualities: Vector Fields in AdS/CFT. *JHEP*, 11:085, 2006.
- [237] Samuel D. McDermott, Hiren H. Patel, and Harikrishnan Ramani. Dark Photon Decay Beyond The Euler-Heisenberg Limit. *Phys. Rev. D*, 97(7):073005, 2018.
- [238] Samuel D. McDermott and Samuel J. Witte. Cosmological evolution of light dark photon dark matter. *Phys. Rev. D*, 101(6):063030, 2020.
- [239] John McDonald. Gauge singlet scalars as cold dark matter. *Phys. Rev. D*, 50:3637–3649, 1994.
- [240] Kristian L. McDonald and David E. Morrissey. Low-Energy Probes of a Warped Extra Dimension. *JHEP*, 05:056, 2010.

- [241] Kristian L. McDonald and David E. Morrissey. Low-Energy Signals from Kinetic Mixing with a Warped Abelian Hidden Sector. *JHEP*, 02:087, 2011.
- [242] Eugenio Megías, Germano Nardini, and Mariano Quirós. Cosmological Phase Transitions in Warped Space: Gravitational Waves and Collider Signatures. *JHEP*, 09:095, 2018.
- [243] Eugenio Megías and Mariano Quirós. Gapped Continuum Kaluza-Klein spectrum. *JHEP*, 08:166, 2019.
- [244] R. Mertig, M. Böhm, and A. Denner. Feyn calc - computer-algebraic calculation of feynman amplitudes. *Computer Physics Communications*, 64(3):345 – 359, 1991.
- [245] Shiraz Minwalla. Restrictions imposed by superconformal invariance on quantum field theories. *Adv. Theor. Math. Phys.*, 2:783–851, 1998.
- [246] Alessandro Mirizzi, Javier Redondo, and Gunter Sigl. Microwave Background Constraints on Mixing of Photons with Hidden Photons. *JCAP*, 03:026, 2009.
- [247] Germano Nardini, Mariano Quiros, and Andrea Wulzer. A Confining Strong First-Order Electroweak Phase Transition. *JHEP*, 09:077, 2007.
- [248] Horatiu Nastase. Introduction to AdS-CFT. 2007.
- [249] Nobuchika Okada, Digesh Raut, and Qaisar Shafi. Pseudo-Goldstone dark matter in a gauged  $B - L$  extended standard model. *Phys. Rev. D*, 103(5):055024, 2021.
- [250] Duccio Pappadopulo, Rudderman Joshua T., and Gabriele Trevisan. Cannibal Dark Matter. *Phys. Rev.*, D94(3):035005, 2016.
- [251] Michael E. Peskin and Daniel V. Schroeder. *An Introduction to quantum field theory*. Addison-Wesley, Reading, USA, 1995.
- [252] Kalliopi Petraki, Marieke Postma, and Jordy de Vries. Radiative bound-state-formation cross-sections for dark matter interacting via a Yukawa potential. *JHEP*, 04:077, 2017.
- [253] Alex Pomarol. Gauge Bosons in a Five-Dimensional Theory with Localized Gravity. *Phys. Lett. B*, 486:153–157, 2000.
- [254] Eduardo Ponton. TASI 2011: Four Lectures on TeV Scale Extra Dimensions, 2013.
- [255] Maxim Pospelov. Secluded U(1) Below the Weak Scale. *Phys. Rev.*, D80:095002, 2009.
- [256] Maxim Pospelov and Adam Ritz. Astrophysical Signatures of Secluded Dark Matter. *Phys. Lett.*, B671:391–397, 2009.
- [257] Maxim Pospelov, Adam Ritz, and Mikhail B. Voloshin. Secluded WIMP Dark Matter. *Phys. Lett.*, B662:53–61, 2008.

- [258] Lisa Randall and Matthew D. Schwartz. Quantum field theory and unification in AdS5. *JHEP*, 11:003, 2001.
- [259] Lisa Randall and Matthew D. Schwartz. Unification and the Hierarchy from AdS5. *Phys. Rev. Lett.*, 88:081801, 2002.
- [260] Lisa Randall and Geraldine Servant. Gravitational waves from warped spacetime. *JHEP*, 05:054, 2007.
- [261] Lisa Randall and Raman Sundrum. An Alternative to Compactification. *Phys. Rev. Lett.*, 83:4690–4693, 1999.
- [262] Javier Redondo and Marieke Postma. Massive hidden photons as lukewarm dark matter. *JCAP*, 02:005, 2009.
- [263] Javier Redondo and Georg Raffelt. Solar constraints on hidden photons re-visited. *JCAP*, 08:034, 2013.
- [264] Tao Ren, Anna Kwa, Manoj Kaplinghat, and Hai-Bo Yu. Reconciling the Diversity and Uniformity of Galactic Rotation Curves with Self-Interacting Dark Matter. *Phys. Rev. X*, 9(3):031020, 2019.
- [265] Thomas G. Rizzo. Dark Photons, Kinetic Mixing and Light Dark Matter from 5-D. In *53Rd Rencontres De Moriond on Electroweak Interactions and Unified Theories*, pages 227–232, 2018.
- [266] Thomas G. Rizzo. Kinetic Mixing, Dark Photons and an Extra Dimension. Part I. *JHEP*, 07:118, 2018.
- [267] Thomas G. Rizzo. Kinetic Mixing, Dark Photons and Extra Dimensions. Part II: Fermionic Dark Matter. *JHEP*, 10:069, 2018.
- [268] Thomas G. Rizzo and George N. Wojcik. Kinetic Mixing, Dark Photons and Extra Dimensions III: Brane Localized Dark Matter. 6 2020.
- [269] Miguel Rocha, Annika H. G. Peter, James S. Bullock, Manoj Kaplinghat, Shea Garrison-Kimmel, Jose Onorbe, and Leonidas A. Moustakas. Cosmological Simulations with Self-Interacting Dark Matter I: Constant Density Cores and Substructure. *Mon. Not. Roy. Astron. Soc.*, 430:81–104, 2013.
- [270] Ira Z. Rothstein, Thomas Schwetz, and Jure Zupan. Phenomenology of Dark Matter Annihilation into a Long-Lived Intermediate State. *JCAP*, 0907:018, 2009.
- [271] W. Ruhl. Field Representations of the Conformal Group with Continuous Mass Spectrum. *Commun. Math. Phys.*, 30:287–302, 1973.
- [272] Jun John Sakurai. *Modern quantum mechanics; rev. ed.* Addison-Wesley, Reading, MA, 1994.
- [273] Bert Schroer. A Note on Infraparticles and Unparticles. 4 2008.



- [274] Marc Schumann. Direct Detection of WIMP Dark Matter: Concepts and Status. *J. Phys. G*, 46(10):103003, 2019.
- [275] Serif, Ltd. Affinity Designer, Version 1.7. Europe, 2019.
- [276] Geraldine Servant and Timothy M. P. Tait. Is the Lightest Kaluza-Klein Particle a Viable Dark Matter Candidate? *Nucl. Phys.*, B650:391–419, 2003.
- [277] Vladyslav Shtabovenko, Rolf Mertig, and Frederik Orellana. New Developments in FeynCalc 9.0. *Comput. Phys. Commun.*, 207:432–444, 2016.
- [278] Vanda Silveira and A. Zee. Scalar phantoms. *Physics Letters B*, 161(1):136–140, 1985.
- [279] Tracy R. Slatyer and Chih-Liang Wu. General Constraints on Dark Matter Decay from the Cosmic Microwave Background. *Phys. Rev.*, D95(2):023010, 2017.
- [280] David N. Spergel and Paul J. Steinhardt. Observational Evidence for Selfinteracting Cold Dark Matter. *Phys. Rev. Lett.*, 84:3760–3763, 2000.
- [281] David Stancato and John Terning. The Unhiggs. *JHEP*, 11:101, 2009.
- [282] David Stancato and John Terning. Constraints on the Unhiggs Model from Top Quark Decay. *Phys. Rev. D*, 81:115012, 2010.
- [283] Gary Steigman, Basudeb Dasgupta, and John F. Beacom. Precise Relic WIMP Abundance and Its Impact on Searches for Dark Matter Annihilation. *Phys. Rev.*, D86:023506, 2012.
- [284] M. A. Stephanov. Deconstruction of Unparticles. *Phys. Rev. D*, 76:035008, 2007.
- [285] Matthew J. Strassler. Why Unparticle Models with Mass Gaps are Examples of Hidden Valleys. 1 2008.
- [286] Andi Tan et al. Dark Matter Results from First 98.7 Days of Data from the PandaX-II Experiment. *Phys. Rev. Lett.*, 117(12):121303, 2016.
- [287] M. Tanabashi et al. Review of Particle Physics. *Phys. Rev.*, D98(3):030001, 2018.
- [288] John Terning and Christopher B. Verhaaren. Dark Monopoles and  $SL(2, \mathbb{Z})$  Duality. *JHEP*, 12:123, 2018.
- [289] John Terning and Christopher B. Verhaaren. Resolving the Weinberg Paradox with Topology. *JHEP*, 03:177, 2019.
- [290] W. Thirring. Lagrangian Formulation of the Zachariasen Model. *Phys. Rev.*, 126:1209–1212, 1962.
- [291] Yu-Dai Tsai, Robert McGehee, and Hitoshi Murayama. Resonant Self-Interacting Dark Matter from Dark QCD. *Phys. Rev. Lett.*, 128(17):172001, 2022.

- [292] Sean Tulin and Hai-Bo Yu. Dark Matter Self-interactions and Small Scale Structure. *Phys. Rept.*, 730:1–57, 2018.
- [293] Sean Tulin, Hai-Bo Yu, and Kathryn M. Zurek. Beyond Collisionless Dark Matter: Particle Physics Dynamics for Dark Matter Halo Structure. *Phys. Rev.*, D87(11):115007, 2013.
- [294] Michael S. Turner and Bernard J. Carr. Why Should Baryons and Exotic Relic Particles Have Comparable Densities? *Mod. Phys. Lett.*, A2:1–7, 1987.
- [295] Laura G. van den Aarssen, Torsten Bringmann, and Christoph Pfrommer. Is dark matter with long-range interactions a solution to all small-scale problems of  $\Lambda$  CDM cosmology? *Phys. Rev. Lett.*, 109:231301, 2012.
- [296] J. J. van der Bij and S. Dilcher. Heidi and the Unparticle. *Phys. Lett. B*, 655:183–184, 2007.
- [297] D. V. Vassilevich. Heat kernel expansion: User’s manual. *Phys. Rept.*, 388:279–360, 2003.
- [298] Mark Vogelsberger, Jesus Zavala, and Abraham Loeb. Subhaloes in self-interacting galactic dark matter haloes. *MNRAS*, 423(4):3740–3752, Jul 2012.
- [299] Gero von Gersdorff. From Soft Walls to Infrared Branes. *Phys. Rev.*, D82:086010, 2010.
- [300] Benedict von Harling and Kristian L. McDonald. Secluded Dark Matter Coupled to a Hidden CFT. *JHEP*, 08:048, 2012.
- [301] Benedict von Harling and Geraldine Servant. QCD-induced Electroweak Phase Transition. *JHEP*, 01:159, 2018.
- [302] Edward Witten. Anti-de Sitter space and holography. *Adv. Theor. Math. Phys.*, 2:253–291, 1998.
- [303] Wolfram Research, Inc. Mathematica, Version 12.0. Champaign, IL, 2019.
- [304] R. L. Workman and Others. Review of Particle Physics. *PTEP*, 2022:083C01, 2022.
- [305] Seyed Yaser Ayazi and Ahmad Mohamadnejad. Conformal vector dark matter and strongly first-order electroweak phase transition. *JHEP*, 03:181, 2019.
- [306] A. Zaffaroni. Introduction to the AdS-CFT correspondence. *Class. Quant. Grav.*, 17:3571–3597, 2000.
- [307] J. Zavala, M. Vogelsberger, and M. G. Walker. Constraining self-interacting dark matter with the Milky way’s dwarf spheroidals. *MNRAS*, 431:L20–L24, Apr 2013.
- [308] Roman Zwicky. A Brief Introduction to Dispersion Relations and Analyticity. In *Quantum Field Theory at the Limits: From Strong Fields to Heavy Quarks*, pages 93–120, 2017.

# Appendix A

## Vector Self-Interacting Dark Matter

### A.1 Goldstones and Pions: an Abelian Example

We present a simple model to demonstrate the parameterization of the Goldstone degrees of freedom in (2.18) and some of the nuances in the discussion of Section 2.18. Let  $a(x)$  and  $b(x)$  be complex scalar fields with potentials such that  $\langle a(x) \rangle = f_a/\sqrt{2}$  and  $\langle b(x) \rangle = f_b/\sqrt{2}$ . We pass to a non-linear representation,

$$a(x) = \frac{r_a(x)}{\sqrt{2}} e^{i\varphi_a(x)/f_a} \qquad b(x) = \frac{r_b(x)}{\sqrt{2}} e^{i\varphi_b(x)/f_b} . \qquad (\text{A.1})$$

The vevs  $f_a$  and  $f_b$  are order parameters for the breaking patterns

$$\text{U}(1)_a \rightarrow \emptyset \qquad \text{U}(1)_b \rightarrow \emptyset , \qquad (\text{A.2})$$

where  $\text{U}(1)_{a,b}$  correspond to separate rephasing of the  $a$  and  $b$  fields. Focusing on the Goldstone degrees of freedom, we may take  $r_i(x) \rightarrow f_i$ . If the Lagrangian respects the

$U(1)_a \times U(1)_b$  symmetry then the Goldstone fields are independent, massless, free degrees of freedom.

### A.1.1 Gauging a Subgroup Combination

Suppose we gauge a subgroup of  $U(1)_a \times U(1)_b$  under which the  $A$  and  $B$  fields have charges  $q_a$  and  $q_b$  respectively. The covariant derivative of this gauged symmetry is

$$D_\mu = \partial_\mu - igq_i W_\mu , \quad (\text{A.3})$$

where  $g$  is the gauge coupling and  $W_\mu$  is the gauge boson. Ignoring the radial excitations, the kinetic terms for  $a$  and  $b$  yield

$$|Da|^2 + |Db|^2 = \frac{1}{2}(\partial\varphi_a)^2 + \frac{1}{2}(\partial\varphi_b)^2 - g\partial(q_a f_a \varphi_a + q_b f_b \varphi_b) \cdot W + \frac{g^2}{2}(q_a^2 f_a^2 + q_b^2 f_b^2) W^2 . \quad (\text{A.4})$$

We see that the gauge boson  $W$  picks up a mass and eats a linear combination of the Goldstone bosons. We identify the effective order parameter  $f_W$  for the gauge symmetry breaking and the mass of the  $W_\mu$ :

$$f_W^2 = q_a^2 f_a^2 + q_b^2 f_b^2 \quad m_W^2 = g^2 f_W^2 . \quad (\text{A.5})$$

The Goldstone combination that is eaten,  $\varphi_W(x)$ , and its orthogonal combination  $\varphi_X(x)$  are

$$\varphi_W = \frac{q_a f_a}{f_W} \varphi_a + \frac{q_b f_b}{f_W} \varphi_b \quad \varphi_X = \frac{q_b f_b}{f_W} \varphi_a - \frac{q_a f_a}{f_W} \varphi_b . \quad (\text{A.6})$$

Observe that the eaten Goldstone is mostly composed of the field which contributes more to the gauge symmetry breaking. Thus if  $q_a f_a > q_b f_b$ , then  $\varphi_W$  contains more of the  $a$

phase than the  $b$  phase. The orthogonal combination,  $\varphi_X$ , is a bona-fide Goldstone mode in the theory and is composed of mostly the phase of the subdominant source of symmetry breaking.

### A.1.2 Gauging a Vectorlike Combination

Suppose that we gauge  $U(1)_V$ , the diagonal subgroup of  $U(1)_a \times U(1)_b$ . Under  $U(1)_V$ , both  $a$  and  $b$  have the same charge,  $q_a = q_b = 1$ . The analysis above yields

$$f_V^2 = f_a^2 + f_b^2 \quad \varphi_V = \frac{f_a}{f_V}\varphi_a + \frac{f_b}{f_V}\varphi_b \quad \varphi_A = \frac{f_b}{f_V}\varphi_a - \frac{f_a}{f_V}\varphi_b. \quad (\text{A.7})$$

Here  $\varphi_A$  is the Goldstone for the ‘axial’ rotation under which  $a$  and  $b$  transform with opposite phase,  $q_a = -q_b = 1$ , and is orthogonal to the Goldstone for the vector rotation  $\varphi_V$  that is eaten by  $V_\mu$ . This is analogous to the case of electroweak symmetry breaking where the Higgs order parameter for  $SU(2)_L \times U(1)_Y$  is much larger than that of the QCD chiral condensate so that the longitudinal modes of massive electroweak bosons are mostly components of the Higgs doublet. The pions are [pseudo-]Goldstone bosons analogous to the  $\varphi_A$ : they are mostly composed of the phase of the chiral condensate, but contain a small piece of the Higgs doublet that is shifted by the opposite symmetry transformation parameter.

### A.1.3 Which Goldstone is Which?

This presents a puzzle. One is free to describe the symmetry structure of the theory with respect to  $U(1)_a \times U(1)_b$  or  $U(1)_V \times U(1)_A$ . Suppose  $f_a \gg f_b$ . Then in the  $U(1)_a \times U(1)_b$  description, the  $a$  field plays a bigger role in symmetry breaking than the  $b$  field. However,

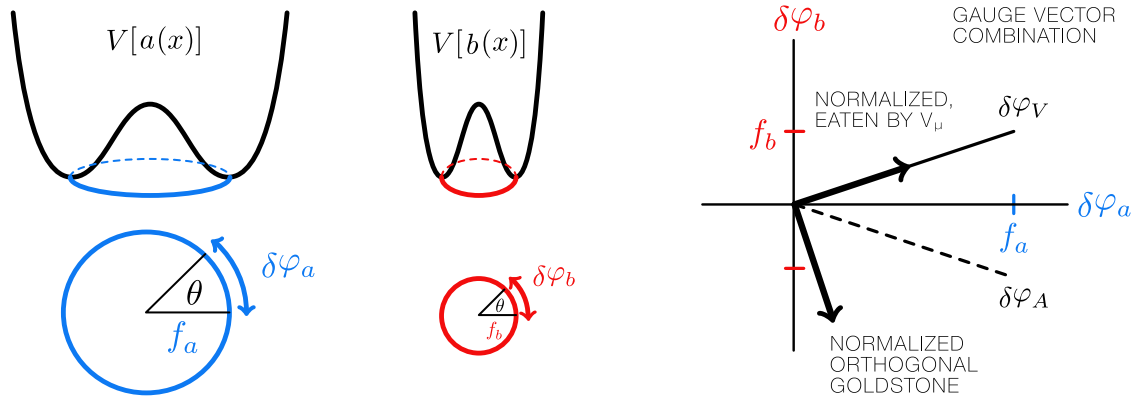


Figure A.1: Fields  $a$  and  $b$  acquire unequal vacuum expectation values  $f_a > f_b$ . The Goldstone excitations with respect to a transformation by parameter  $\theta$  have correspondingly different magnitudes,  $\delta\varphi_a > \delta\varphi_b$ . The Goldstone,  $\delta\varphi_V$ , for a vectorial transformation where  $\theta_a = \theta_b$  is thus *not* orthogonal to the corresponding Goldstone,  $\delta\varphi_A$  for an axial transformation where  $\theta_a = -\theta_b$ .

the vevs each break  $U(1)_V$  and  $U(1)_A$  by the same effective order parameter,  $f_V^2 = f_a^2 + f_b^2$ . Neither  $U(1)_V$  nor  $U(1)_A$  is preferred over the other. Why, then, is it the case in (A.7) that the  $\varphi_V$  eats more  $\varphi_a$  while  $\varphi_A$  eats more of  $\varphi_b$ ? The root of this confusion is illustrated in Fig. A.1: in the absence of gauging, the naïve description of the vector and axial Goldstones are not orthogonal to one another. The choice of gauging a particular combination of the full global symmetry breaks the symmetry and gives ‘priority’ to the eaten Goldstone boson to have a larger admixture of the field that does most of the symmetry breaking.

#### A.1.4 Gauging an Axial Combination

One way to illustrate this point is to observe that if we had instead gauged the axial symmetry,  $q_a = -q_b = -1$ . Let us continue to assume that  $f_a \gg f_b$ . The order parameter for axial symmetry breaking is identical to the vector case so that the axial

symmetry,  $f_A = f_V$ . The only difference from the vector case is that it is now the axial Goldstone,  $\varphi_A$  that is eaten:

$$f_A^2 = f_a^2 + f_b^2 \quad \varphi_A = \frac{f_a}{f_V}\varphi_a - \frac{f_b}{f_V}\varphi_b \quad \varphi_B = \frac{f_b}{f_V}\varphi_a + \frac{f_a}{f_V}\varphi_b . \quad (\text{A.8})$$

Observe that compared to (A.7), the relative admixtures of  $\varphi_{a,b}$  has changed so that the eaten Goldstone (now  $\varphi_A$ ) is *still* mostly composed of the Goldstone ( $\varphi_a$ ) from the dominant source of symmetry breaking. This follows directly from (A.4) where it is clear that the choice of which symmetry is gauged determines which linear combination of fields has more of the  $\varphi_a$  field.

### A.1.5 Gauging both Vector and Axial Symmetry

Another illustrative example is to separately gauge the vector and axial combinations with gauge couplings  $g_V$  and  $g_A$  respectively. We are primarily interested in the case  $g_V = g_A$ , but the two are independent parameters. The kinetic terms then include

$$\begin{aligned} |Da|^2 + |Db|^2 \supset & \partial\varphi_a \cdot (g_V V + g_A A) + \partial\varphi_b \cdot (g_V V - g_A A) \\ & + \frac{f_a^2}{2}(g_V V + g_A A)^2 + \frac{f_b^2}{2}(g_V V - g_A A)^2 . \end{aligned} \quad (\text{A.9})$$

In this case the gauge boson mass matrix is not diagonal. When  $g_V = g_A$  this matrix is diagonalized by writing

$$V = W + Z \quad A = W - Z . \quad (\text{A.10})$$

This transformation is independent of the relative magnitudes of the vevs. The transformation also separates the mixing terms:

$$g\partial\varphi_a \cdot (V + A) + g\partial\varphi_b \cdot (V - A) = g\partial\varphi_a \cdot W + g\partial\varphi_b \cdot Z . \quad (\text{A.11})$$

Thus we are pushed back to the natural basis of Goldstone bosons,  $\varphi_{a,b}$ . The vector and axial gauge bosons are forced to mix in such a way that the mass eigenstates end up being a gauge boson that eats  $\varphi_a$  and a gauge boson that eats  $\varphi_b$ . This is equivalent to the case where one separately gauges the  $U(1)_a$  and  $U(1)_b$  symmetries.

### A.1.6 Global Vector and Axial Goldstones

As a final exercise, one may consider the ungauged theory where one writes the fields in terms of axial and vector Goldstones. In (A.1) one would then identify

$$\varphi_a = \frac{f_a}{\sqrt{2f_a^2 + 2f_b^2}} (\varphi_V + \varphi_A) \quad \varphi_b = \frac{f_b}{\sqrt{2f_a^2 + 2f_b^2}} (\varphi_V - \varphi_A) , \quad (\text{A.12})$$

where the normalizations are chosen so that (1) an excitation along, say, the  $\varphi_V$  direction produces an equal phase transformation on  $a(x)$  and  $b(x)$  and (2) the  $\varphi_{V,A}(x)$  are canonically normalized. Here we see that in the absence of gauging, the  $\varphi_{V,A}$  are treated ‘equally’ despite the unequal vevs. The scenario is identical to the description in terms of  $\varphi_{a,b}$  in that the fields are massless, free excitations.

## A.2 SIDM Methodology

We summarize the methodology for determining the dark matter self-interaction cross section as a function of velocity in Fig. 2.5. We closely follow the procedure in Ref. [293]. The relevant quantity is the transfer cross section,

$$\sigma_T = \int d\Omega (1 - \cos\theta) \frac{d\sigma}{d\Omega} , \quad (\text{A.13})$$

which characterizes interaction cross section weighted by momentum transfer. This regulates the  $\cos\theta \rightarrow 1$  divergence where dark matter scatters do not affect halo shapes. There



is no known analytical expression for the transfer cross section that valid for the entire parameter space though it has been calculated under various approximations for limited parts of parameter space [131, 188, 231, 228, 295, 48]. A large part of the parameter space corresponds to the resonant regime where both quantum mechanical and non-perturbative effects become important, as such a numerical solution to the non-relativistic Schrödinger equation is necessary.

We use a partial wave analysis. The transfer cross section is related to the  $\ell^{\text{th}}$  partial wave phase shift,  $\delta_\ell$ , by

$$\sigma_T = \frac{4\pi}{k^2} \sum_{\ell=0}^{\infty} (\ell + 1) \sin^2 (\delta_{\ell+1} - \delta_\ell) . \quad (\text{A.14})$$

The  $\delta_\ell$ s are, in turn, obtained by solving the radial Schrödinger equation

$$\frac{1}{r^2} \frac{d}{dr} \left( r^2 \frac{dR_\ell}{dr} \right) + \left( k^2 - \frac{\ell(\ell + 1)}{r^2} - m_X V(r) \right) R_\ell = 0 , \quad (\text{A.15})$$

where  $k = m_X v/2$  and  $v$  is the relative velocity of the two-particle dark matter system.  $\delta_\ell$  is found by comparing with the asymptotic solution for  $R_\ell$ :

$$\lim_{r \rightarrow \infty} R_\ell(r) \propto \cos \delta_\ell j_\ell(kr) - \sin \delta_\ell n_\ell(kr) , \quad (\text{A.16})$$

where  $j_\ell$  ( $n_\ell$ ) is the spherical Bessel (Neumann) function of the  $\ell^{\text{th}}$  kind. We define the function  $\chi_\ell \equiv rR_\ell$  and dimensionless variables

$$x \equiv \alpha_X m_X r \qquad a = \frac{v}{2\alpha_X} \qquad b = \frac{\alpha_X m_X}{m_\phi} , \quad (\text{A.17})$$

so that we can rewrite (A.15) as [48]

$$\left( \frac{d^2}{dx^2} + a^2 - \frac{\ell(\ell + 1)}{x^2} \pm \frac{1}{x} e^{-x/b} \right) \chi_\ell(x) = 0 . \quad (\text{A.18})$$

Near the origin, the non-derivative parts of (A.18) are dominated by the angular momentum term. This implies that  $\chi_\ell \propto x^{\ell+1}$  close to  $x = 0$ . We choose a normalization such that  $\chi_\ell(x_0) = 1$  and  $\chi'_\ell(x_0) = (\ell + 1)/x_0$  where  $x_0$  is a point close to the origin chosen to satisfy  $x_0 \ll b$  and  $x_0 \ll (\ell + 1)/a$ . We use  $x_0$  as the lower limit for range in which we numerically solve the Schrödinger equation. Similarly, to define the upper limit of range, we pick a point  $x_m$  satisfying the condition  $a^2 \gg \exp(-x_m/b)/x_m$ . When  $x_m$  satisfies this condition, the potential term is negligible compared to the kinetic term and the solution approaches

$$\chi_\ell(x) \propto x e^{i\delta_\ell} (\cos \delta_\ell j_\ell(ax) - \sin \delta_\ell n_\ell(ax)). \quad (\text{A.19})$$

The phase shift is then

$$\tan \delta_\ell = \frac{ax_m j'_\ell(ax_m) - \beta_\ell j_\ell(ax_m)}{ax_m n'_\ell(ax_m) - \beta_\ell n_\ell(ax_m)} \quad \text{where} \quad \beta_\ell = \frac{x_m \chi'_\ell(x_m)}{\chi_\ell(x_m)} - 1. \quad (\text{A.20})$$

For an initial guess of the range  $(x_0, x_m)$  and the maximum number of partial waves required for convergence,  $\ell_{\max}$ , we calculate  $\delta_\ell$  from (A.20). We then increase  $x_m$  and decrease  $x_0$ , recalculating  $\delta_\ell$  until the differences of successive iterations converge to be within 1%. We then sum (A.14) from  $\ell = 0$  to  $\ell = \ell_{\max}$  to obtain an estimate for  $\sigma_T$ . Next we increment  $\ell_{\max} \rightarrow \ell_{\max} + 1$  and repeat the procedure until successive values of  $\sigma_T$  converge to be within 1% and  $\delta_{\ell_{\max}} < 0.01$ . Ref. [293] iterates  $\ell_{\max}$  until  $\sigma_T$  converged and  $\delta_{\ell_{\max}} < 0.01$  ten consecutive times. We have found that for our analysis that it is sufficient to stop the calculation after one successful convergence. We have found that the ‘‘StiffnessSwitching’’ method from the `NDSolveUtilities` package in *Mathematica* to be particularly useful.

Our model exhibits both attractive and repulsive self-interactions due to dark matter being symmetric and mediated by a vector particle. In this case, one solves the

Schrödinger equation separately for each sign of the potential to extract two transfer cross sections,  $\sigma_T^{(\pm)}$ . The effective transfer cross section is the average of the two.

## Appendix B

# Continuum Mediated Self-Interacting Dark Matter

### B.1 AdS/CFT with UV brane

The AdS/CFT correspondence states that boundary correlators of quantum field theory in  $\text{AdS}_{d+1}$  spacetime are equivalent to correlators of a conformal field theory in  $d$ -dimensional spacetime [7, 306, 248, 198]. For a given bulk field in AdS, the corresponding CFT operator arises through the asymptotic behavior of the field near the AdS boundary. In this appendix we revisit and streamline the two branches of the correspondence in the presence of a UV brane.

#### B.1.1 The Two Branches

A scalar bulk field  $\Phi$  in  $\text{AdS}_5$  corresponds to a scalar operator  $\mathcal{O}$  of a CFT. The conformal dimension of  $\mathcal{O}$  is denoted  $\Delta$ . An analysis of the boundary asymptotics shows that

the relation between AdS bulk mass and  $\Delta$  is given by [234, 168, 302, 143, 229, 144, 106, 105]

$$\Delta(\Delta + d)k^2 = M_\Phi^2, \quad (\text{B.1})$$

or equivalently (4.16). We recall that  $M_\Phi^2 = (\alpha^2 - 4)k^2$  and  $\alpha \geq 0$  by convention. The two roots of (B.1) are

$$\Delta_\pm = 2 \pm \alpha. \quad (\text{B.2})$$

These two roots indicate that the correspondence has two branches; for a given AdS field there can be two CFT duals. Unitarity of the operator implies  $\Delta \geq 1$ . It follows that the  $\Delta_+$  branch exists for  $\alpha \in \mathbb{R}_+$ , but the  $\Delta_-$  branch exists only for  $0 \leq \alpha \leq 1$  [211].

The correspondence is formulated as follows. We define the value of the bulk field on the AdS boundary  $\Phi_0 \equiv \Phi(X^M \rightarrow \text{boundary})$ . Starting from the AdS partition function, one integrates over the bulk degrees of freedom while holding  $\Phi_0$  constant. This defines the boundary effective action

$$\int_{\Phi_0} \mathcal{D}\Phi e^{iS_{\text{AdS}}[\Phi]} = e^{i\Gamma_{\text{AdS}}[\Phi_0]}. \quad (\text{B.3})$$

The two branches of the correspondence are then formulated as follows.

In the  $\Delta_+$  branch, the dual CFT is defined by the correspondence

$$\Gamma_{\text{AdS}}[\Phi_0] \equiv W_{\text{CFT}}[\Phi_0] \quad (\text{B.4})$$

with  $W_{\text{CFT}}[J]$  the generating functional of connected correlators of a CFT where  $J$  is the source of the operator  $\mathcal{O}$  (with  $[\mathcal{O}] = \Delta_+$ ),

$$Z_{\text{CFT}}[J] = \int \mathcal{D}\phi_{\text{CFT}} e^{iS_{\text{CFT}}[\phi_{\text{CFT}}] + \int d^4x \mathcal{O}J} = e^{iW_{\text{CFT}}[J]}. \quad (\text{B.5})$$

In this branch we can observe that the  $\Phi_0$  variable corresponds to the source of the  $\mathcal{O}$  operator.

In the  $\Delta_-$  branch the dual CFT is defined by the correspondence

$$\Gamma_{\text{AdS}}[\mathcal{O}] \equiv \Sigma_{\text{CFT}}[\mathcal{O}] \tag{B.6}$$

with  $\Sigma_{\text{CFT}}[\mathcal{O}_{\text{cl}}]$  the Legendre transform of  $W_{\text{CFT}}[J]$ ,

$$\Sigma_{\text{CFT}}[\mathcal{O}] = W_{\text{CFT}}[J] - \int dx^\mu \mathcal{O} J. \tag{B.7}$$

$\Sigma$  is constructed similarly to an effective action. Its argument is understood to be an expectation value, e.g.  $\mathcal{O}_{\text{cl}}$ , this is left implicit here. In the  $\Delta_-$  branch we can observe that  $\Phi_0$  corresponds to the expectation value of the  $\mathcal{O}$  operator itself.

### B.1.2 The Two Branches with a UV brane

One can truncate AdS with a UV brane and identify  $\Phi_0 = \Phi(X^M \rightarrow \text{UV brane})$ . The above AdS/CFT relations from full AdS remain structurally the same, however fields on a brane away from the boundary can be dynamical, hence the UV brane has a localized action  $S_{\text{UV}}$ . In particular the  $\Phi_0$  variable is in general dynamical instead of being static as in the full AdS case. Thus  $\Phi_0$  is now a 4D field, external to the CFT.

The AdS partition function is

$$\int \mathcal{D}\Phi_0 e^{iS_{\text{UV}}[\Phi_0]} \int_{\Phi_0} \mathcal{D}\Phi e^{iS_{\text{AdS}}[\Phi]} = \int \mathcal{D}\Phi_0 e^{iS_{\text{UV}}[\Phi_0] + i\Gamma_{\text{AdS}}[\Phi_0]}. \tag{B.8}$$

To formulate the 4D theory in terms of a generating functional of connected correlators, one would have to introduce new static sources coupled to  $\Phi_0$  and  $\mathcal{O}$ . Instead we can Legendre

transform and describe the theory directly in terms of an effective action  $\Gamma_{4D}$ . We introduce  $\Gamma_{UV}$ , the effective action generated by  $S_{UV}$ .

Consider the  $\Delta_+$  branch. The 4D theory is identified as in (B.4), appending  $S_{UV}$  on both sides. The  $W_{\text{CFT}}$  is substituted by its Legendre transform using Eq. (B.7), where the  $J$  source is localized on the UV brane and can now be dynamical. It follows that the effective action of the 4D theory is given by

$$\Gamma_{UV}[\Phi_0] + \Gamma_{\text{AdS}}[\Phi_0] \equiv \Gamma_{UV}[\Phi_0] + \Sigma_{\text{CFT}}[\mathcal{O}] + \int d^4x \mathcal{O} \Phi_0 = \Gamma_{4D}[\Phi_0, \mathcal{O}]. \quad (\text{B.9})$$

To illustrate the 4D theory defined by (B.9), consider a dynamical UV brane-localized current  $J_{UV}$  coupled to  $\Phi$  as  $S_{UV} = \int d^4x J_{UV} \Phi_0$ , and evaluate the  $\langle J_{UV} J_{UV} \rangle$  correlator. One finds that the  $J_{UV}$  currents exchange a propagator of  $\Phi_0$ , which is itself dressed by the two-point function of  $\mathcal{O}$ .

In the  $\Delta_-$  branch the effective action of the 4D theory is identified as

$$\Gamma_{UV}[\mathcal{O}] + \Gamma_{\text{AdS}}[\mathcal{O}] \equiv \Gamma_{UV}[\mathcal{O}] + \Sigma_{\text{CFT}}[\mathcal{O}] = \Gamma_{4D}[\mathcal{O}]. \quad (\text{B.10})$$

Consider again the  $\langle J_{UV} J_{UV} \rangle$  correlator from the  $S_{UV} = \int d^4x J_{UV} \Phi_0$  interaction. What we obtain is that the  $J_{UV}$  currents exchange a two-point correlator of  $\mathcal{O}$ . This  $\Delta_-$  branch of the duality is the one used for our model. Identifying the  $J_{UV}$  current as  $J_{\text{DM}}$ , the  $\langle JJ \rangle$  correlator discussed here describes formally the relation given in (4.5).

## B.2 Derivation of Gapless $\alpha = 1$ Potential

In this appendix we show how to evaluate the Fourier transform of (4.48). The first term is a simple pole at the origin and thus gives a Coulomb potential. The next-to-leading

term goes as  $\log(q)/q^2$ . To evaluate its Fourier transform we use

$$\frac{\log q^2}{q^{2n}} = -\partial_\alpha \frac{1}{q^{2\alpha}} \Big|_{\alpha \rightarrow n} \quad (\text{B.11})$$

with  $n = 1$ . The Fourier transform of  $q^{-2\alpha}$  is

$$\frac{1}{(2\pi)^3} \int d^3 \mathbf{q} e^{i\mathbf{q}\mathbf{r}} \frac{1}{q^{2\alpha}} = \frac{1}{(2\pi)^3} \frac{1}{\Gamma(\alpha)} \int d^3 \mathbf{q} e^{i\mathbf{q}\mathbf{r}} \int \frac{dt}{t} t^{\alpha-1} e^{-tq^2} = \frac{1}{(4\pi)^{3/2}} \frac{\Gamma(3/2 - \alpha)}{\Gamma(\alpha)} \left(\frac{4}{r^2}\right)^{3/2-\alpha}. \quad (\text{B.12})$$

We then evaluate the  $\alpha$  derivative and set  $\alpha = 1$ , which gives

$$\frac{1}{(4\pi)^{3/2}} \partial_\alpha \left( \frac{\Gamma(3/2 - \alpha)}{\Gamma(\alpha)} \left(\frac{4}{r^2}\right)^{3/2-\alpha} \right) \Big|_{\alpha \rightarrow 1} = \frac{1}{2\pi} (\gamma + \log r). \quad (\text{B.13})$$

Combining these identities gives (4.53).

### B.3 Validity of the Born Approximation

In order to determine the validity of the Born approximation, consider the wave function for a dark matter particle scattering off of a potential  $V(\mathbf{x})$ ,

$$\psi(\mathbf{x}) \sim e^{i\mathbf{p}\cdot\mathbf{x}} - m_\chi \int d^3 x' \frac{e^{ip|\mathbf{x}-\mathbf{x}'|}}{4\pi|\mathbf{x}-\mathbf{x}'|} V(\mathbf{x}') e^{i\mathbf{p}\cdot\mathbf{x}'}, \quad (\text{B.14})$$

where  $|\mathbf{p}| = m_\chi v/2$  and  $\mathbf{p} \cdot \mathbf{x}' = pr' \cos \theta$ . Near the origin  $|\mathbf{x} - \mathbf{x}'| \approx r'$ , thus the condition for when the Born approximation is valid is

$$\left| \frac{m_\chi}{4\pi} \int d^3 x' \frac{e^{ipr'}}{r'} V(\mathbf{x}') e^{i\mathbf{p}\cdot\mathbf{x}'} \right| \ll 1. \quad (\text{B.15})$$

For a Yukawa potential  $V(r) = \alpha_\chi e^{-m_\phi r}/r$  this condition is simply  $\alpha_\chi m_\chi/m_1 \ll 1$ . At low energies we can replace the exponentials by 1. For a central potential in spherical coordinates the angular integral is trivial. Evaluating (B.15) for a Yukawa potential gives



the condition  $\alpha_\chi m_\chi / m_\phi \ll 1$ . This bound can be equivalently determined by considering the typical momentum flowing through a ladder diagram is of order  $\alpha_\chi m_\chi$  [167, 252]. We evaluate (B.15) for (4.30) and arrive at the result

$$\frac{\lambda^2}{4\pi k} \sum_n \frac{f_n^2(z_{UV})}{m_n} \ll 1. \quad (\text{B.16})$$

In order to make the connection to the Yukawa case more explicit, we define the effective coupling

$$\alpha_\chi^{\text{eff}} = \frac{\lambda^2 m_1}{4\pi k} \sum_n \frac{f_n^2(z_{UV})}{m_n}, \quad (\text{B.17})$$

such that the condition for when the Born approximation is valid becomes

$$\frac{\alpha_\chi^{\text{eff}} m_\chi}{m_1} \ll 1, \quad (\text{B.18})$$

analogous to the Yukawa case.

Recalling that the bulk profiles depend on the bulk mass parameter  $\alpha$ , we note that the sum over KK modes in  $\alpha_{\chi,\text{eff}}$  diverges for  $\alpha \leq 1/2$ . This is consistent with the Schrödinger equation in which, near the origin, the continuum mediated potential (4.42) dominates over the centrifugal barrier for  $\alpha \leq 1/2$ . In order to achieve finite results in the case when  $\alpha \leq 1/2$ , we introduce a smooth cutoff to (B.16) such that

$$\alpha_\chi^{\text{eff}} = \frac{\lambda^2 m_1}{4\pi k} \sum_n \frac{f_n^2(z_{UV})}{m_n} \quad \longrightarrow \quad \alpha_\chi^{\text{eff}}(\Lambda) = \frac{\lambda^2 m_1}{4\pi k} \sum_n \frac{f_n^2(z_{UV})}{m_n} e^{-m_n/\Lambda}, \quad (\text{B.19})$$

where  $\Lambda^{-1}$  is the short distance cutoff. We evaluate the KK sum using the spectral representation of the propagator (4.26) and using the large-momentum asymptotics (4.34). We arrive at the result

$$\alpha_\chi^{\text{eff}} = \frac{\lambda^2}{4\pi\Gamma(1-\alpha)^2} \frac{m_1}{\Lambda} \left(\frac{2k}{\Lambda}\right)^{2\alpha-2} \Gamma\left(1-2\alpha, \frac{m_1}{\Lambda}\right). \quad (\text{B.20})$$

When  $\alpha > 1/2$ , the limit  $\Lambda \rightarrow \infty$  is finite and cutoff independent,

$$\alpha_\chi^{\text{eff}} \Big|_{\alpha > 1/2} = \frac{\lambda^2}{4\pi} \left[ \frac{4}{2\alpha - 1} \frac{1}{\Gamma(1 - \alpha)^2} \right] \left( \frac{m_1}{2k} \right)^{2-2\alpha}. \quad (\text{B.21})$$

This result is identical to evaluating (B.15) for the continuum mediated potential (4.42).

For the special case of a bulk mass parameter  $\alpha = 1/2$ , we find that the effective coupling for the Born approximation is

$$\alpha_\chi^{\text{eff}} = \frac{\lambda^2 m_1}{8\pi^2 k} \log \left( \frac{\Lambda e^{-\gamma}}{m_1} \right). \quad (\text{B.22})$$

The other limit,  $\alpha \rightarrow 1$  requires special care. Because the asymptotic expansions of the canonical propagator used for the  $\alpha < 1$  result break down in this limit, one cannot simply take  $\alpha \rightarrow 1$  in (B.21). Instead, in the case where  $\alpha = 1$ , scattering is governed by the Yukawa potential (4.46) and we can directly apply (4.57) so that

$$\alpha_\chi^{\text{eff}} = \frac{\lambda^2 m_1}{4\pi k} f_0^2(z_{UV}) \quad (\text{B.23})$$

where  $f_0(z_{UV})$  is given by (4.47).

The accuracy of the Born approximation improves at higher energies. This can also be shown from (B.15) by computing the angular integral for a general central potential,

## B.4 Classical Transfer Cross Section

We calculate the transfer cross section in the classical regime and observe its velocity dependence. The angle by which a particle in a central potential is deflected is  $\theta(\rho) = |\pi - 2\varphi(\rho)|$  where [219]

$$\varphi(\rho) = \rho \int_{r_{\min}}^{\infty} \frac{dr}{r^2 \sqrt{1 - \rho^2/r^2 - 4V(r)/m_\chi v^2}} \quad (\text{B.24})$$

and  $\rho$  is the impact parameter. The lower limit of integration  $r_{\min}$  is the largest root of the denominator of (B.24). In contrast to the quantum case, the classical cross section is typically given in terms of the impact parameter rather than the angular variables. In the classical limit, integration over the deflection angle can be troublesome since the solution to (B.24) for  $\varphi(\rho)$  and thus  $\theta(\rho)$  takes values greater than  $\pi$  for cases other than a  $1/r$  potential. On the other hand the impact parameter always ranges between zero and infinity.

The differential cross section is  $d\sigma = 2\pi\rho d\rho$ . The transfer cross section is thus

$$\sigma_{\text{T}}^{\text{classical}} = 2\pi \int_0^\infty [1 - \cos \theta(\rho)] \rho d\rho. \quad (\text{B.25})$$

To connect to the deflection angle, we note that

$$\left( \frac{d\sigma}{d\Omega} \right)^{\text{classical}} = \frac{\rho(\chi)}{\sin \theta} \left| \frac{d\rho}{d\theta} \right| \quad (\text{B.26})$$

where in these variables  $d\Omega = 2\pi d \cos \theta$ . We present calculations for the velocity scaling in the small mass gap/high velocity limit and an analytical result in the low velocity region of the non-perturbative classical regime.

#### B.4.1 Velocity Scaling in the Small Mass Gap/High Velocity Limit

For the sake of this calculation we assume the gapless limit where the potential is

(4.45)

$$V(r) = -\frac{\lambda^2}{2\pi^{3/2}} \frac{\Gamma(3/2 - \alpha)}{\Gamma(1 - \alpha)} \frac{1}{r(kr)^{2-2\alpha}}. \quad (\text{B.27})$$

This approximation also accounts for the high velocity limit where the particle momentum is much greater than the mass gap. Given our potential we can define a characteristic length

scale

$$\rho_0 \equiv \left[ \frac{\lambda^2}{2\pi^{3/2} m_\chi v^2 k^{2-2\alpha}} \frac{\Gamma(3/2 - \alpha)}{\Gamma(1 - \alpha)} \right]^{\frac{1}{3-2\alpha}} \quad (\text{B.28})$$

so that after making the change of variables  $r = \rho/x$ , (B.24) becomes [75]

$$\varphi(\rho) = \int_0^{x_{\max}} \frac{dx}{\sqrt{1 - x^2 + 2(\rho_0 x/\rho)^{3-2\alpha}}} \quad (\text{B.29})$$

where the limit of integration  $x_{\max}$  is the smallest positive root of the denominator. Observe that  $\varphi$  (and by extension  $\chi$ ) and as  $x_{\max}$  are functions of the dimensionless combination  $\rho/\rho_0$  and not  $\rho$  independently. Making the change of variables  $\rho = \rho_0 \xi$ , the transfer cross section is

$$\sigma_{\text{T}}^{\text{classical}} = 2\pi\rho_0^2 \int_0^\infty [1 - \cos \chi(\xi)] \xi d\xi. \quad (\text{B.30})$$

Because  $\chi$  is a function of  $\xi$  and  $\alpha$  only, the integral (B.30) only depends on the bulk mass parameter. We can thus conclude from (B.28) that the velocity dependence of the transfer cross section in the classical regime is  $\sigma_{\text{T}}^{\text{classical}} \sim v^{-4/(3-2\alpha)}$ .

The presence of the mass gap spoils the velocity dependence derived in (B.30). For the gapped potential (4.42), after changing variables, the deflection angle depends on the quantity  $m_1\rho_0$  as well. Thus a small but nonzero  $m_1$  induces corrections to (B.30).

### B.4.2 Low Velocity Classical Regime

We present a closed form result for the transfer cross section in the low velocity region of the non-perturbative classical regime. Following the method of Ref. [209], the transfer cross section is a function of a single unique parameter,

$$\beta = \frac{2\alpha_{\chi}^{\text{eff}} m_1}{m_\chi v^2} (2\alpha - 1). \quad (\text{B.31})$$

The transfer cross section is  $\sigma_T \approx \pi \rho_*^2$  where  $\rho_*$  is found by solving the set of equations

$$\tilde{V}_{\text{eff}}(r_{\text{max}}, \rho_*) = 1 \qquad \left. \frac{d\tilde{V}_{\text{eff}}(r, \rho_*)}{dr} \right|_{r=r_{\text{max}}} = 0 \qquad (\text{B.32})$$

where  $\tilde{V}_{\text{eff}}$  is the effective potential

$$\tilde{V}_{\text{eff}}(r, \rho) = \frac{\rho^2}{r^2} + \frac{4}{m_\chi v^2} V(r) . \qquad (\text{B.33})$$

These conditions correspond to the maximum of the effective potential  $\tilde{V}_{\text{eff}}$ .

We find for  $\beta \gg 1$  that the transfer cross section is approximately

$$\sigma_T^{\text{classical}} \approx \frac{\pi}{m_1^2} \left[ 1 + \log \left( \frac{\beta}{\log \beta} \right) - (2\alpha - 1) \log^{-1} \beta + \left( 2\alpha - \frac{3}{2} \right) \log^{-1} \left( \frac{\beta}{\log \beta} \right) \right]^2 . \qquad (\text{B.34})$$

The accuracy of (B.34) is confirmed in Figure 4.5.

## B.5 Sommerfeld Enhancement from a $1/r^2$ Potential

The Sommerfeld effect amounts to the enhancement of the particle wavefunction at the point where the local annihilation process happens. It comes from the dressing from ladder diagrams generated by a potential  $V(r)$ . The dressed wavefunction is determined by directly solving the Schrödinger equation. The Sommerfeld enhancement factor is defined as  $\sigma = S(p)\sigma_0$  with  $\sigma_0$  the undressed cross section. The method to evaluate the Sommerfeld effect is well known, here we follow [18] (see also [190]).

The Schrödinger equation is

$$-\frac{1}{2M} \Delta \Psi(r) + V(r) \Psi(r) = \frac{p^2}{2M} \Psi(r) . \qquad (\text{B.35})$$

In any solution of the Schrödinger equation with rotational invariance around  $z$ , the solutions can be expanded as

$$\Psi = \sum a_\ell P_\ell(\cos \theta) R_\ell(r). \quad (\text{B.36})$$

The radial wavefunction satisfies

$$-\frac{1}{2Mr^2} \frac{d}{dr} \left( r^2 \frac{dR_\ell}{dr} \right) + \left( V(r) + \frac{\ell(\ell+1)}{2Mr^2} \right) R_\ell(r) = \frac{p^2}{2M} R_\ell(r). \quad (\text{B.37})$$

In the standard approach one uses the fact that angular momentum with  $\ell > 0$  gives  $R_\ell \sim r^\ell$  at small  $r$ , which implies that the  $\ell > 0$  contributions to the wavefunction vanish at the origin. Hence one can focus on the  $\ell = 0$  angular momentum.

For our continuum-mediated potential  $V(r) \propto r^{2\alpha-3}$ , the vanishing of  $\ell > 0$  remains true for any  $\alpha \geq 1/2$ . For  $\alpha > 1/2$ , the  $\ell = 0$  mode gives  $R_\ell \sim \text{constant}$  at small  $r$ . But for  $\alpha = 1/2$ , which is the  $V(r) \propto 1/r^2$  potential of our interest, the  $\ell = 0$  component diverges at small  $r$ . This feature is not an inconsistency. We work in a low-energy EFT so the  $r$  coordinate cannot be zero, it is rather cut at a small value corresponding to the UV cutoff,  $r = r_0$ . In our AdS model the cutoff is at  $r_0 \sim k^{-1}$ . Of course, the subsequent results may be cutoff dependent, but this is not a conceptual problem, this simply reflects that an EFT prediction can depend on the unknown UV physics.

Here we parametrize the  $\alpha = 1/2$  potential as

$$V(r) = -\frac{\kappa}{2r^2}. \quad (\text{B.38})$$

The matching to the physical couplings from the AdS model is  $\kappa = \frac{\lambda^2}{\pi^2 k}$ .

Introducing  $\chi_\ell(r) = rR_\ell(r)$  the Schrödinger equation becomes

$$-\frac{1}{2M} \partial_r^2 \chi_0(r) + V(r) \chi_0(r) = \frac{p^2}{2M} \chi_0(r). \quad (\text{B.39})$$

From this equation, various equivalent methods lead to the Sommerfeld factor, which differs by the boundary conditions chosen for  $\chi$  [18]. We use the following.  $\chi_\ell$  is chosen to satisfy  $\partial_r \chi_\ell = ip\chi_\ell$  at  $r = \infty$ . Using this solution, the Sommerfeld factor is

$$S = \left| \frac{\chi_0(r = \infty)}{\chi_0(r = r_0)} \right|. \quad (\text{B.40})$$

Notice that since we are in an EFT with have replaced the  $r = 0$  by  $r = r_0$ .

The solution satisfying the condition at  $r = \infty$  is found to be

$$\chi_0(r)_\ell \propto \sqrt{r} H_\eta^{(1)}(pr), \quad \eta = \sqrt{\frac{1}{4} - M\kappa}. \quad (\text{B.41})$$

The dimensionful  $\kappa$  coupling is of order of the inverse cutoff of the EFT. The EFT would break at  $M\kappa \sim 1$ , we are rather interested in  $M\kappa \ll 1$ , i.e. the dark matter mass is much lower than the cutoff  $k$ .

Expanding in the small parameter  $M\kappa$  we find

$$\chi_0(r_0) \propto i + \mathcal{O}(pr_0). \quad (\text{B.42})$$

We have that  $pr_0$  is necessarily  $\ll 1$  since  $r_0$  is the inverse cutoff  $k^{-1}$ , and because the non-relativistic approximation requires  $p < M$  and the EFT validity requires  $M < k$ .

It follows that within the range of validity of the EFT, we can simply take  $\eta \approx 1/2$ . The Hankel simplifies to  $H^{(1)}(z) \propto z^{-1/2} e^{iz}$ , thus  $\chi_0(r) \propto e^{ipr}$  for any  $pr$ . The Sommerfeld factor is then exactly  $S = 1$  for any  $p$ .

## B.6 Self-Interacting Dark Matter Numerical Method

We summarize the methodology for determining the dark matter self-interaction cross section. We closely follow the procedure in Ref. [293] however we employ a slightly

more relaxed algorithm. The relevant quantity is the transfer cross section,

$$\sigma_{\text{T}} = \int d\Omega (1 - \cos \theta) \frac{d\sigma}{d\Omega} , \quad (\text{B.43})$$

which characterizes interaction cross section weighted by momentum transfer. This regulates the  $\cos \theta \rightarrow 1$  divergence where dark matter scattering does not affect halo shapes. There is no known analytical expression for the transfer cross section that is valid for the entire parameter space. A large region of the parameter space corresponds to the resonant regime where both quantum mechanical and non-perturbative effects become important, as such a numerical solution to the non-relativistic Schrödinger equation is necessary.

We employ a partial wave analysis. The transfer cross section is related to the  $\ell^{\text{th}}$  partial wave phase shift,  $\delta_\ell$ , by

$$\sigma_{\text{T}} = \frac{4\pi}{p^2} \sum_{\ell=0}^{\infty} (\ell + 1) \sin^2 (\delta_{\ell+1} - \delta_\ell) . \quad (\text{B.44})$$

The  $\delta_\ell$  are, in turn, obtained by solving the radial Schrödinger equation (B.37) taking  $M = m_\chi/2$  and  $p = m_\chi v/2$  where  $v$  is the relative velocity of the two-particle dark matter system.  $\delta_\ell$  is found by comparing with the asymptotic solution for  $R_\ell$ :

$$\lim_{r \rightarrow \infty} R_\ell(r) \propto \cos \delta_\ell j_\ell(pr) - \sin \delta_\ell n_\ell(pr) , \quad (\text{B.45})$$

where  $j_\ell (n_\ell)$  is the spherical Bessel (Neumann) function of the  $\ell^{\text{th}}$  order. We again define the function  $\chi_\ell \equiv rR_\ell$  along with the dimensionless variables

$$x \equiv \alpha_X m_X r \quad a = \frac{v}{2\alpha_X} \quad b = \frac{\alpha_X m_X}{m_1} \quad c = \frac{\alpha_X m_X}{k} , \quad (\text{B.46})$$

so that we can rewrite (B.37) as [48]

$$\left[ \frac{d^2}{dx^2} + a^2 - \frac{\ell(\ell + 1)}{x^2} \pm \frac{2}{\pi^{1/2}} \frac{1}{x} \left( \frac{c}{x} \right)^{2-2\alpha} \frac{\Gamma(3/2 - \alpha)}{\Gamma(1 - \alpha)} Q(2 - 2\alpha, x/b) \right] \chi_\ell(x) = 0 . \quad (\text{B.47})$$



Near the origin for  $\alpha > 1/2$ , the angular momentum term dominates over the potential. This implies that  $\chi_\ell \propto x^{\ell+1}$  close to  $x = 0$ . When  $\alpha \leq 1/2$  and the potential becomes singular, our method breaks down and we cannot determine an initial condition. We choose a normalization for the wavefunctions such that  $\chi_\ell(x_0) = 1$  and  $\chi'_\ell(x_0) = (\ell + 1)/x_0$  where  $x_0$  is a point close to the origin chosen to satisfy  $x_0 \ll b$  and  $x_0 \ll (\ell + 1)/a$ . We take  $x_0$  as the lower limit for the range in which we numerically solve the Schrödinger equation. Similarly, to define the upper limit, we pick a point  $x_m$  satisfying the condition

$$a^2 \gg \frac{2}{\pi^{1/2}} \frac{1}{x} \left(\frac{c}{x}\right)^{2-2\alpha} \frac{\Gamma(3/2 - \alpha)}{\Gamma(1 - \alpha)} Q(2 - 2\alpha, x/b). \quad (\text{B.48})$$

When  $x_m$  satisfies this condition, the potential term is negligible compared to the kinetic term and the solution approaches

$$\chi_\ell(x) \propto x e^{i\delta_\ell} (\cos \delta_\ell j_\ell(ax) - \sin \delta_\ell n_\ell(ax)). \quad (\text{B.49})$$

The phase shift is then

$$\tan \delta_\ell = \frac{ax_m j'_\ell(ax_m) - \beta_\ell j_\ell(ax_m)}{ax_m n'_\ell(ax_m) - \beta_\ell n_\ell(ax_m)} \quad \text{where} \quad \beta_\ell = \frac{x_m \chi'_\ell(x_m)}{\chi_\ell(x_m)} - 1. \quad (\text{B.50})$$

For an initial guess of the range  $(x_0, x_m)$  and the maximum number of partial waves required for convergence,  $\ell_{\max}$ , we calculate  $\delta_\ell$  from (B.50). In Ref. [293]  $x_m$  and  $x_0$  are increased and decreased respectively, recalculating  $\delta_\ell$  until the differences of successive iterations converge to be within 1%. This condition can be quite cumbersome numerically and is *not strictly required* unless one wishes to do a fine grained scan over the parameter space. Instead, we take the value of  $\delta_\ell$  given by our initial guess. This method is sufficient to reproduce the benchmark results in Ref. [200].

We then sum (B.44) from  $\ell = 0$  to  $\ell = \ell_{\max}$  to obtain an estimate for  $\sigma_T$ . Next we increment  $\ell_{\max} \rightarrow \ell_{\max} + 1$  and repeat the procedure until successive values of  $\sigma_T$  converge to be within 1% and  $\delta_{\ell_{\max}} < 0.01$ . Ref. [293] iterates  $\ell_{\max}$  until  $\sigma_T$  converged and  $\delta_{\ell_{\max}} < 0.01$  ten consecutive times. We have found that the “StiffnessSwitching” method from the `NDSolveUtilities` package in *Mathematica* to be particularly useful.

We employ this method to calculate the Sommerfeld enhancements as well. The enhancement factor is [190, 33]

$$S = \left[ \frac{(2\ell + 1)!!}{C} \right]^2 \quad (\text{B.51})$$

where  $C^2$  is

$$C^2 = (\chi_\ell^2(x) - \chi_\ell^2(x - \pi/2a))_{x \rightarrow \infty} . \quad (\text{B.52})$$

# Appendix C

## Holographic Dark Photon

### C.1 Gauge Parameter Boundary Conditions

A general infinitesimal gauge transformation takes the form

$$A_M \rightarrow A_M + \partial_M \alpha(x, z) \qquad a \rightarrow a + \alpha(x, z). \qquad (\text{C.1})$$

The set of boundary conditions for the  $U(1)$  system that are chosen here (Neumann for  $A_\mu$ ,  $a$  and Dirichlet for  $A_z$ ) implies that the gauge transformation parameter  $\alpha(x, z)$  satisfies the boundary conditions

$$(\eta^{\mu\nu} \partial_z - \mathcal{B}^{\mu\nu}) \partial_\mu \alpha|_{z=R} = 0 \qquad (\text{C.2})$$

$$\left\{ -\partial^2 \alpha + c_{\text{UV}} R^{d-4} \frac{\xi_{\text{UV}}}{g_{d+1}^2} (\partial_z - g_{d+1}^2 R v^2) \alpha \right\} \Big|_{z=R} = 0 \qquad (\text{C.3})$$

where  $\mathcal{B}^{\mu\nu}$  is given by (5.32). These conditions allow for a nonvanishing  $\alpha$  on the brane, consistent with the Neumann boundary conditions of  $A_\mu$ ,  $a$ .

## C.2 A WKB Method for Near-AdS Background

For a near-AdS background when  $\alpha \simeq d/2$  we find an approximate solution to the gauge field's equation of motion via a WKB method. We use this solution to calculate the UV brane-to-brane propagator and find a logarithmic running of the anomalous dimension. We put (5.43) in the standard WKB form by changing variables and redefining the bulk profile:

$$y = R \log \left( \frac{z}{R} \right) \qquad f(p, y) = e^{(d/2-1)y/R} \psi(y). \qquad (\text{C.4})$$

The transverse equation of motion is now

$$\psi''(y) + k^2(y)\psi(y) = 0 \qquad (\text{C.5})$$

where we have defined

$$k(y) = \frac{1}{R} \sqrt{p^2 R^2 e^{2y/R} - \left( \frac{d}{2} - 1 \right)^2 - m_A^2 R^2 e^{(d-2\alpha)y/R}}. \qquad (\text{C.6})$$

The standard WKB method gives an approximate solution

$$\psi(y) = C_+ \psi_+(y) + C_- \psi_-(y) \qquad \psi_{\pm}(y) = \frac{1}{\sqrt{k(y)}} \exp \left[ \pm i \int^y dy' k(y') \right] \qquad (\text{C.7})$$

which is valid when

$$\frac{|k'(y)|}{k^2(y)} = \left| \frac{p^2 R^2 e^{2y/R} + (\alpha - d/2) m_A^2 R^2 e^{(d-2\alpha)y/R}}{(p^2 R^2 e^{2y/R} - (d/2 - 1)^2 - m_A^2 R^2 e^{(d-2\alpha)y/R})^{3/2}} \right| \ll 1. \qquad (\text{C.8})$$

This limit is easily satisfied when  $pRe^{y/R} \gg 1$ , corresponding to  $y \rightarrow \infty$ . On the other hand when  $pRe^{y/R} \ll 1$ , corresponding to  $y \rightarrow 0$  and  $pR \ll 1$ , (C.8) is only satisfied when  $\alpha \simeq d/2$ . Note that there exists a turning point  $y_t$  given by the solution to

$$k^2(y_t) = p^2 e^{2y_t/R} - \frac{1}{R^2} \left( \frac{d}{2} - 1 \right)^2 - m_A^2 e^{(d-2\alpha)y_t/R} = 0, \qquad (\text{C.9})$$

where the approximation fails. The full solution is a piece-wise with coefficients determined by matching the asymptotic solutions to the solution near the turning point.

We expand about  $\alpha = d/2 + \epsilon$  where  $\epsilon \ll 1$ . We now have

$$k(y) = \frac{1}{R} \sqrt{p^2 R^2 e^{2y/R} - \nu^2} + \epsilon \frac{m_A^2 y}{\sqrt{p^2 R^2 e^{2y/R} - \nu^2}} \quad (\text{C.10})$$

where we have defined

$$\nu = \sqrt{\left(\frac{d}{2} - 1\right)^2 + m_A^2 R^2}. \quad (\text{C.11})$$

Additionally, we expand the prefactor as

$$\frac{1}{\sqrt{k(y)}} = \exp\left[-\frac{1}{4} \log k^2(y)\right] \simeq R^{1/2} \exp\left\{-\frac{1}{4} \log(p^2 z^2 - \nu^2) - \frac{\epsilon m_A^2 R^2}{2(p^2 z^2 - \nu^2)} \log\left(\frac{z}{R}\right)\right\} \quad (\text{C.12})$$

keeping powers of  $\epsilon$  in the exponential in order to consistently compare the order of the expansion with the phases. To  $\mathcal{O}(\epsilon)$  the turning point is

$$y_t^{(1)} = \frac{R}{2} \log\left(\frac{\nu^2}{p^2 R^2}\right) \left(1 - \epsilon \frac{m_A^2 R^2}{\nu^2}\right). \quad (\text{C.13})$$

For convenience we define the phase

$$\varphi(y) = \int^y dy' k(y') = \varphi^{(0)}(y) + \varphi^{(1)}(y) + \mathcal{O}(\epsilon^2). \quad (\text{C.14})$$

Defining the variable  $x = pRe^{y/R}/\nu$ , we find

$$\varphi^{(0)} = \nu \sqrt{x^2 - 1} - \nu \tan^{-1}\left(\sqrt{x^2 - 1}\right) \quad (\text{C.15})$$

$$\begin{aligned} \varphi^{(1)} = \frac{i\epsilon\zeta m_A^2}{8\nu} \left\{ -4\text{Li}_2\left(\frac{1}{2} - \frac{1}{2}\sqrt{1-x^2}\right) + \log^2(x^2) + 2\log^2\left(\frac{1}{2} + \frac{1}{2}\sqrt{1-x^2}\right) \right. \\ \left. - 4\zeta \tanh^{-1}\left(\sqrt{1-x^2}\right) \log\left(\frac{p^2 R^2}{\nu^2}\right) - 4\log(x^2) \log\left(\frac{1}{2} + \frac{1}{2}\sqrt{1-x^2}\right) \right\} \quad (\text{C.16}) \end{aligned}$$

where

$$\zeta = \begin{cases} 1 & x > 1 \\ -1 & x < 1 \end{cases}. \quad (\text{C.17})$$

Because to  $\mathcal{O}(\epsilon)$ ,  $x_t = pR e^{y_t/R} = 1$ , the value of  $\zeta$  denotes which side of the turning point the solution corresponds to.

We now find the solution to (5.43) near the turning point. In contrast to the standard WKB method in which one would solve the equation of motion after expanding  $k^2(y)$  to linear order in  $(y - y_t)$ , we instead only expand the vev term near the turning point yielding the solutions

$$z^{d/2-1} H_{\nu_t}^{(1)}(pz) \qquad z^{d/2-1} H_{\nu_t}^{(2)}(pz) \quad (\text{C.18})$$

where we have defined

$$\nu_t = \sqrt{(d/2 - 1)^2 + m_A^2 R^2 \left(\frac{z_t}{R}\right)^{d-2\alpha}} = pz_t \quad (\text{C.19})$$

and  $z_t$  is the location of the turning point in  $z$ -coordinates. In order to more easily match onto the turning point solution, we convert the phase  $\varphi(y)$  into  $z$ -coordinates by noting that  $x = pz/\nu$ . In  $z$ -coordinates, the turning point is

$$\nu_t^{(1)} = pz_t^{(1)} = \nu - \epsilon \frac{m_A^2 R^2}{\nu} \log\left(\frac{\nu}{pR}\right). \quad (\text{C.20})$$

The full piece-wise solution is therefore

$$f(z) = \begin{cases} A_+ \frac{z^{d/2-1}}{\sqrt{k(z)}} e^{i\varphi(z)} + A_- \frac{z^{d/2-1}}{\sqrt{k(z)}} e^{-i\varphi(z)} & z < z_t \\ C_1 z^{d/2-1} H_{\nu_t}^{(1)}(pz) + C_2 z^{d/2-1} H_{\nu_t}^{(2)}(pz) & z \simeq z_t \\ B_+ \frac{z^{d/2-1}}{\sqrt{k(z)}} e^{i\varphi(z)} + B_- \frac{z^{d/2-1}}{\sqrt{k(z)}} e^{-i\varphi(z)} & z > z_t \end{cases}. \quad (\text{C.21})$$

### C.2.1 Matching to the Solution Near the Turning Point

In order to determine the coefficients, we expand the WKB solutions in the limits  $z \gg z_t$  and  $z \ll z_t$  and match to the turning point solution in each limit respectively.

Expanding the phase for  $z \gg z_t$ , corresponding to  $pz \gg \nu$ , we find

$$\varphi(z) \simeq pz - \frac{\pi\nu}{2} + \epsilon \frac{m_A^2 R^2}{2\nu} \left[ \pi \log \left( \frac{2\nu}{pR} \right) - i \left( \frac{\pi^2}{12} - \log^2 2 \right) \right]. \quad (\text{C.22})$$

From the Hartle-Hawking condition we can see that we must have  $B_- = C_2 = 0$  since for  $pz \gg \nu$

$$H_\nu^{(1,2)}(x) \sim \sqrt{\frac{2}{\pi x}} e^{\pm i(x - \frac{\nu\pi}{2} - \frac{\pi}{4})}. \quad (\text{C.23})$$

The details of the relation between  $C_1$  and  $B_+$  are ultimately irrelevant to the UV brane-to-brane propagator as they only affect the overall normalization of the homogeneous solution.

On the other hand for  $z \ll z_t$ , similarly corresponding to  $pz \ll \nu$ , the phase is

$$\varphi(z) \simeq -i\nu \left[ \log \left( \frac{2\nu}{pz} \right) - 1 + \epsilon \frac{m_A^2 R^2}{2\nu^2} \left( \log^2 \left( \frac{\nu}{pz} \right) - \log \left( \frac{\nu}{pR} \right) \log \left( \frac{4\nu^2}{p^2 z^2} \right) \right) \right]. \quad (\text{C.24})$$

The prefactor  $1/\sqrt{k(z)}$  may also be expanded for  $pz \ll \nu$  and  $\epsilon \ll 1$  as

$$\frac{1}{\sqrt{k(z)}} \simeq \sqrt{\frac{R}{\nu}} \left( \frac{z}{R} \right)^{\epsilon \frac{m_A^2 R^2}{2\nu^2} \left( 1 + \frac{p^2 z^2}{\nu^2} \right)} \left( 1 + \frac{p^2 z^2}{4\nu^2} \right) e^{-i\pi/4} \quad (\text{C.25})$$

where we have not expanded the  $\epsilon$  dependent power in order to match to the solution near the turning point. The homogeneous solution for  $pz \ll \nu$  is therefore

$$\psi_\pm^{\text{WKB}}(z) \simeq \left( 1 + \frac{p^2 z^2}{4\nu^2} \right) \left( \frac{z}{R} \right)^{\frac{\epsilon m_A^2 R^2}{2\nu^2} \left( 1 + \frac{p^2 z^2}{\nu^2} \right)} \left( \frac{pz}{\nu} \right)^{\mp \nu \pm \frac{\epsilon m_A^2 R^2}{2\nu} \left[ \log \left( \frac{pz}{\nu} \right) - 2 \log \left( \frac{pR}{\nu} \right) \right]} \quad (\text{C.26})$$

where we have absorbed  $z$ -independent factors into the relative constants  $A_\pm$ . We match only the  $z$ -dependent factors at  $\mathcal{O}(\epsilon)$ , taking  $\epsilon \rightarrow 0$  for all other terms. In order to match to

the Hankel function solution near the turning point, we consider only pairs of  $pz$  to be our basis solutions (excluding the power of  $\log(pz/\nu)$ ), while we evaluate other contributions for  $z \simeq z_t^{(0)} = \nu/p$ . The WKB solution is approximately

$$\begin{aligned}\psi_{\pm}^{\text{WKB}}(z \simeq z_t) &\simeq \left(1 + \frac{p^2 z^2}{4\nu^2}\right) \left(\frac{z_t^{(0)}}{R}\right)^{\frac{\epsilon m_A^2 R^2}{\nu^2}} \left(\frac{pz}{2\nu}\right)^{\mp\nu \pm \frac{\epsilon m_A^2 R^2}{\nu} \log\left(\frac{\nu}{pR}\right)} \\ &= \left(1 + \frac{p^2 z^2}{4\nu^2}\right) \left(\frac{pR}{\nu}\right)^{-\frac{\epsilon m_A^2 R^2}{\nu^2}} \left(\frac{pz}{2\nu}\right)^{\mp\nu \pm \frac{\epsilon m_A^2 R^2}{\nu} \log\left(\frac{\nu}{pR}\right)}.\end{aligned}\quad (\text{C.27})$$

In order to match to the WKB solutions, we expand the solution near the turning point for  $pz \ll \nu$ . In this limit the Hankel function is

$$H_{\nu_t}^{(1)}(pz) \simeq -\frac{i}{\pi} \Gamma(\nu_t) \left[1 + \frac{p^2 z^2}{4(\nu_t - 1)}\right] \left(\frac{pz}{2}\right)^{-\nu_t} + \frac{1 + i \cot(\pi\nu_t)}{\Gamma(\nu_t + 1)} \left[1 - \frac{p^2 z^2}{4(\nu_t + 1)}\right] \left(\frac{pz}{2}\right)^{\nu_t}.\quad (\text{C.28})$$

From (C.20) we can see that to  $\mathcal{O}(\epsilon)$  the noninteger power of  $pz$  in the WKB solution matches the solution near the turning point. To leading order in  $pz/\nu$  and  $\epsilon$ , we match the WKB solution to the solution near the turning point and find the coefficients are required to be

$$A_+ = -\frac{i}{\pi} \Gamma(\nu_t) \nu^{-\nu_t} \left(\frac{pR}{\nu}\right)^{\frac{\epsilon m_A^2 R^2}{\nu^2}} C_1 \quad A_- = \frac{1 + i \cot(\pi\nu_t)}{\Gamma(\nu_t + 1)} \nu^{\nu_t} \left(\frac{pR}{\nu}\right)^{\frac{\epsilon m_A^2 R^2}{\nu^2}} C_1.\quad (\text{C.29})$$

### C.2.2 UV Brane-to-Brane Propagator

We use the WKB solution (5.68) to find the UV brane-to-brane propagator. The propagator keeps the general form given by (5.57) with

$$\Sigma(p^2) = \frac{p^2 R}{2\nu^2} - \frac{\nu - d/2 + 1}{R} - \frac{2}{R} \frac{\Gamma(1 - \nu)}{\Gamma(\nu)} \left(\frac{-p^2 R^2}{4}\right)^{\nu - \delta(p)} \left(\frac{pR}{\nu}\right)^{\delta(p)}\quad (\text{C.30})$$



where we have defined

$$\delta(p) = \epsilon \frac{m_A^2 R^2}{\nu} \log\left(\frac{\nu}{pR}\right). \quad (\text{C.31})$$

We find a shift in the anomalous dimension given by

$$\Delta\gamma_{\text{AdS}} = -\frac{\delta(p)}{2}. \quad (\text{C.32})$$

For  $\epsilon = 0$  ( $\alpha = d/2$ ) the shift to the anomalous dimension  $\Delta\gamma_{\text{AdS}} = 0$  and the holographic self-energy matches (5.75).

### C.3 Holographic Dark Photon Model Detailed Calculation

We present a model of a continuum dark photon resulting from a spontaneously broken  $U(1)$  in  $\text{AdS}_5$ . The dark sector is described by (5.2) with  $d = 4$ . Kinetic mixing between the continuum dark photon and the visible photon on the UV brane couples the dark sector to the Standard Model. We calculate the exact visible photon propagator dressed by kinetic mixing with the dark photon, and show that the resulting observables are equivalent to those found from a holographic field redefinition of the visible photon.

The brane-localized kinetic mixing between the visible photon and the warped dark photon is given by

$$S_{\text{KM}} = \int d^4x \int_R^\infty dz \frac{\epsilon}{2} \sqrt{\frac{r_{\text{UV}}}{g_5^2}} F_{\mu\nu} \mathcal{F}^{\mu\nu} \delta(z - R), \quad (\text{C.33})$$

where  $F_{\mu\nu}$  are the vector components of the dark photon field strength, and  $\mathcal{F}_{\mu\nu}$  is the visible photon field strength. The Feynman rule for this interaction is

$$A_\mu \text{---}\text{wavy line}\text{---} A_\nu \quad \xrightarrow{q} \quad = i\epsilon \sqrt{\frac{r_{\text{UV}}}{g_5^2}} (q^2 \eta_{\mu\nu} - q_\mu q_\nu) \quad (\text{C.34})$$



where we have used the identity

$$q_\mu (q^2 \eta^{\mu\rho} - q^\mu q^\rho) = 0 \quad (\text{C.38})$$

and in this case  $\xi$  refers to the gauge fixing parameter of the Standard Model gauge group (not the spontaneously broken dark  $U(1)$ ). Rearranging terms, we can sum (C.37) as a geometric series giving

$$\text{Diagram} = \frac{-i}{q^2 (1 - \Pi(q^2))} \left( \eta_{\mu\nu} - \frac{q_\mu q_\nu}{q^2} \right) - \frac{i\xi}{q^2} \left( \frac{q_\mu q_\nu}{q^2} \right). \quad (\text{C.39})$$

Typically, due to the Ward identity, the terms proportional to  $q_\mu q_\nu$  vanish when contracted with external fermions and therefore do not contribute to S-matrix elements.

For our purposes, we will ignore contributions from Standard Model fields as well as higher order contributions from dark sector particles, and focus only on the contribution to the self-energy resulting from the kinetic mixing between the photon and warped dark photon,  $\Pi_A(q^2)$ . In this case, the 1PI contribution is given by

$$\mu \text{Diagram} \nu = \mu \overset{A}{\text{Diagram}} \nu \equiv i\Pi_A^{\mu\nu} = i(q^2 \eta^{\mu\nu} - q^\mu q^\nu) \Pi_A(q^2). \quad (\text{C.40})$$

Using the Feynman rule given by (C.34) we have

$$i\Pi_A^{\mu\nu} = r_{UV} (i\varepsilon)^2 (q^2 \eta^{\mu\rho} - q^\mu q^\rho) \langle \hat{A}_\rho(q) \hat{A}_\sigma(-q) \rangle (q^2 \eta^{\sigma\nu} - q^\sigma q^\nu) \quad (\text{C.41})$$

where  $\langle \hat{A}_\rho(q) \hat{A}_\sigma(-q) \rangle$  is the tree level brane-to-brane continuum dark photon propagator.

Recalling the definition (5.42),

$$\langle A_\mu(p, z) A_\nu(-p, z') \rangle = -i \left( \eta^{\mu\nu} - \frac{p^\mu p^\nu}{p^2} \right) G_p(z, z') - i \left( \frac{p^\mu p^\nu}{p^2} \right) \tilde{G}_p(z, z'), \quad (\text{C.42})$$

the self-energy can be written as

$$\begin{aligned}
i\Pi_A^{\mu\nu} &= i\varepsilon^2 r_{\text{UV}} (q^2 \eta^{\mu\rho} - q^\mu q^\rho) \left( \eta^{\mu\nu} - \frac{q^\mu q^\nu}{q^2} \right) G_q(R, R) (q^2 \eta^{\sigma\nu} - q^\sigma q^\nu) \\
&= i\varepsilon^2 r_{\text{UV}} (q^2 \eta^{\mu\nu} - q^\mu q^\nu) q^2 G_q(R, R) .
\end{aligned} \tag{C.43}$$

Therefore we have

$$\Pi_A(q^2) = \varepsilon^2 r_{\text{UV}} q^2 G_q(R, R) . \tag{C.44}$$

### C.3.2 Equivalence with Holographic Field Redefinition

Dressing the visible photon propagator with kinetic mixing between the continuum dark photon and visible photon is equivalent to removing (5.93) from the action by diagonalizing the fields. Making the field redefinition

$$\mathcal{A} = \mathcal{A}_0 + \varepsilon \sqrt{\frac{r_{\text{UV}}}{g_5^2}} \mathcal{A}|_{z=R} \tag{C.45}$$

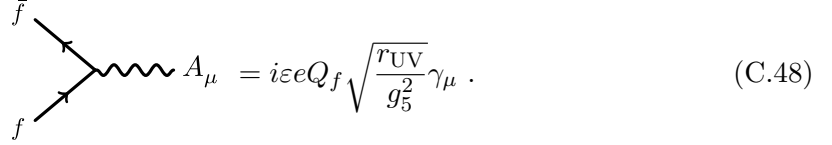
where  $\mathcal{A}_0$  is the visible photon, we find

$$\begin{aligned}
&\int d^4x \int_R^\infty dz \left\{ -\frac{1}{4g_5^2} F_{\mu\nu} F^{\mu\nu} + \delta(z-R) \left[ -\frac{r_{\text{UV}}}{4g_5^2} F_{\mu\nu} F^{\mu\nu} + \frac{\varepsilon}{2} \sqrt{\frac{r_{\text{UV}}}{g_5^2}} F_{\mu\nu} \mathcal{F}^{\mu\nu} - \frac{1}{4} \mathcal{F}_{\mu\nu} \mathcal{F}^{\mu\nu} \right] \right\} \\
&= \int d^4x \int_R^\infty dz \left\{ -\frac{1}{4g_5^2} F_{\mu\nu} F^{\mu\nu} + \delta(z-R) \left[ -\frac{r_{\text{UV}}}{4g_5^2} (1-\varepsilon^2) F_{\mu\nu} F^{\mu\nu} - \frac{1}{4} \mathcal{F}_{0\mu\nu} \mathcal{F}_0^{\mu\nu} \right] \right\} .
\end{aligned} \tag{C.46}$$

We see the mixing has been removed and effectively the brane localized coupling  $r_{\text{UV}} \rightarrow r_{\text{UV}}(1-\varepsilon^2)$ . As a result of the field redefinition (C.45), the visible photon coupling to the electromagnetic current becomes

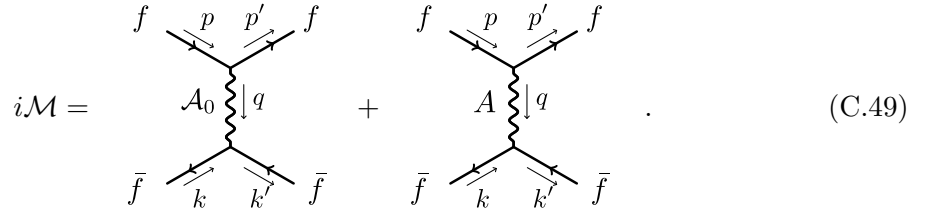
$$\mathcal{A}_\mu j_{\text{EM}}^\mu = \mathcal{A}_{0\mu} j_{\text{EM}}^\mu + \varepsilon \sqrt{\frac{r_{\text{UV}}}{g_5^2}} \mathcal{A}_\mu j_{\text{EM}}^\mu \tag{C.47}$$

inducing a brane-localized coupling between the dark photon and the electromagnetic current. The Feynman rule for a fermion  $f$  with charge  $Q_f$  coupling to the dark photon  $A$  is



$$i\mathcal{M} = ie\epsilon Q_f \sqrt{\frac{r_{UV}}{g_5^2}} \gamma_\mu . \quad (\text{C.48})$$

In order to demonstrate the equivalence of this viewpoint with that of the dressed photon propagator, we consider interactions between the Standard Model electromagnetic currents. The amplitude for fermion–anti-fermion scattering is given by the sum of the diagrams



$$i\mathcal{M} = \text{Diagram 1} + \text{Diagram 2} . \quad (\text{C.49})$$

Using (2.66) and the standard QED photon–fermion interaction, we find for the amplitude

$$i\mathcal{M} = (ieQ_f)^2 \bar{u}(p')\gamma^\mu u(p) \left[ \frac{-i}{q^2} + \frac{-ir_{UV}\epsilon^2}{g_5^2(1-\epsilon^2)} G_q(R, R) \right] \bar{v}(k)\gamma_\mu v(k') \Big|_{r_{UV} \rightarrow r_{UV}(1-\epsilon^2)} \quad (\text{C.50})$$

where we have used  $\bar{u}(p')\gamma^\mu q_\mu u(p) = \bar{v}(k)\gamma^\mu q_\mu v(k') = 0$  and due to the field redefinition we must make the replacement  $r_{UV} \rightarrow r_{UV}(1-\epsilon^2)$ . Recalling (5.57) we may write the amplitude as

$$i\mathcal{M} = \frac{i}{q^2} e^2 Q_f^2 \bar{u}(p')\gamma^\mu u(p) \left[ 1 + \frac{r_{UV}\epsilon^2 q^2}{1-\epsilon^2} \frac{1}{\mathcal{B}_G(q^2) + \Sigma(q^2)} \right] \bar{v}(k)\gamma_\mu v(k') \Big|_{r_{UV} \rightarrow r_{UV}(1-\epsilon^2)} . \quad (\text{C.51})$$

Combining the terms in the bracket over a common denominator gives

$$\begin{aligned}
& \left[ \mathcal{B}_G(q^2) + \Sigma(q^2) + \frac{r_{\text{UV}}\varepsilon^2 q^2}{1 - \varepsilon^2} \right]_{r_{\text{UV}} \rightarrow r_{\text{UV}}(1 - \varepsilon^2)} \\
&= \Sigma(q^2) + r_{\text{UV}}(1 - \varepsilon^2)q^2 - c_{\text{UV}} R m_A^2 + r_{\text{UV}} q^2 \varepsilon^2 \\
&= \Sigma(q^2) + r_{\text{UV}} q^2 - c_{\text{UV}} R m_A^2 \\
&= \mathcal{B}_G(q^2) + \Sigma(q^2). \tag{C.52}
\end{aligned}$$

Finally, plugging into the scattering amplitude we find

$$\begin{aligned}
i\mathcal{M} &= \frac{i}{q^2} e^2 Q_f^2 \bar{u}(p') \gamma^\mu u(p) \left[ \frac{\mathcal{B}_G(q^2) + \Sigma(q^2)}{\mathcal{B}_G(q^2) + \Sigma(q^2) - r_{\text{UV}}\varepsilon^2 q^2} \right] \bar{v}(k) \gamma_\mu v(k') \\
&= \frac{i}{q^2} e^2 Q_f^2 \frac{\bar{u}(p') \gamma^\mu u(p) \bar{v}(k) \gamma_\mu v(k')}{1 - r_{\text{UV}}\varepsilon^2 q^2 G_q(R, R)} \\
&= \frac{i}{q^2} e^2 Q_f^2 \frac{\bar{u}(p') \gamma^\mu u(p) \bar{v}(k) \gamma_\mu v(k')}{1 - \Pi_A(q^2)} \tag{C.53}
\end{aligned}$$

which exactly reproduces the self-energy correction resulting from dressing the undiagonalized photon propagator with brane-localized dark photon interactions. For the rest of this manuscript, we work in the picture where the visible photon and continuum dark photon are diagonalized through a holographic field redefinition.